UNIVERSITY OF BIRMINGHAM

MODELLING AND OPTIMISING PRETRANSPLANT KIDNEY STORAGE

By

Thomas Brendan Smith

A thesis submitted to the University of Birmingham for the degree of

DOCTOR OF PHILOSOPHY

Institute of Metabolism and Systems Research

College of Medical and Dental Sciences

University of Birmingham

February 2020

Abstract

When compared to static cold storage (SCS), the hypothermic machine perfusion (HMP) of pretransplant kidneys confers a therapeutic effect to transplant recipients.

The mechanisms conferring this benefit are not fully understood, however are thought to include a metabolic component. The first experiments in this thesis demonstrated that metabolic differences exist between HMP and SCS stored kidneys.

If properly optimised, HMP potentiates further gains for transplant recipients.

However, the low throughput of organ storage research reduces the rate new HMP protocols are assessed. Therefore, a novel *in vitro* model of organ preservation was created. This model permits high-throughput control of fluid shear stress and oxygenation, and both of these environmental stimuli were found to be independent mediators of cellular survival after simulated preservation. Additionally, oxygen supplementation modulated *de novo* metabolism in hypothermicly stored proximal tubule cells.

When trialled in whole organ models of HMP, high-dose perfusate oxygenation led to increased cortical concentrations of adenosine triphosphate, and also increased the concentrations of citric acid cycle metabolites produced *de novo.*

The final chapters of this thesis chart an international collaborative effort to probe the minimal oxygen delivery strategy capable of inducing *ex vivo* benefit, followed by *in vivo* validation using animal auto-transplantation models.

Dedication

Jeffrey William Smith

When asked about the large scar traversing his chest, my dad would tell us he got it fighting a lion. Much of the effort required to achieve my undergraduate, and all the drive to make a meaningful contribution to organ transplantation research came from the life of this man. This thesis is dedicated to him and to my daughter Christina, thank you for all the smiles.

Acknowledgements

The work documented in my thesis, and forming many of our group's outputs required long hours, countless late nights and weekend work. Therefore, first and foremost I'd like to acknowledge the considerable support of my wife Kalliopy, who has not only helped me through this time, but also borne the brunt of us becoming new parents shortly after the start of my training. My Ph.D. experience would have not have been as productive or as enjoyable without the advice, clinical insight or shared experiences of my good friend and fellow PhD student, Mr. Kamlesh Patel. I'm extremely grateful for all the times you went above and beyond. I owe a debt of gratitude to several key drivers behind our groups research as a whole. I'd like to thank my supervisor, Christian Ludwig for his enthusiasm in the provision of NMR training and practical support. Your innovations in the field of metabolic tracing gave us an unparalleled capability with which to detect changes in metabolism. I'd like to thank Mr. Andrew Ready, whose vision led to the founding of our organ preservation research group and its industrial collaborations and also Mr. Jay Nath, who's example was invaluable while I found my feet as an independent investigator.

Ohema Powell and Tabeer Alam, it was a privilege working with you both and I'd like to express my very sincere appreciation for the different, but equally important ways in which you have continued to help out, even after you had finished your studies.

I would like to extend my thanks to Daniel Tenants' research group, with a special thank you to Dr. Alpesh Thakkar for his provision of mass spectrometry expertise, and also to Haydn Munford and Cristina Escribano Gonzalez for all your help, which has been too extensive to list. The whole-organ work would not have been possible without the support of our industrial partners, Peter DeMuylder and Gunther Vanwezer of Organ Recovery

Systems, USA. I would also like to thank Dr. Tom Darius for some very interesting collaborations, discussions and opportunities.

Prior to COVID-19 spanning the globe, Maria Tabry, my mother in law flew to England to provide support at home while I spent late evenings and finishing off my last projects and writing up. Your help directly contributed to the successes of the final year, I can only apologise you got stuck here for several months during the pandemic restrictions.

Last, but by no means least, I'd like to thank my sister Jennie Smith, brothers Peter and Andrew Smith and particularly my mum, Mary Smith for your lifelong support, which has proven especially invaluable over the last couple of years.

Relevant publications

- Darius T, Vergauwen M, **Smith T**, Gerin I, Joris V, Mueller M, et al. Brief O2 uploading during continuous hypothermic machine perfusion is simple yet effective oxygenation method to improve initial kidney function in a porcine autotransplant model. Am J Transplant [Internet]. 2020 Feb 3;ajt.15800

- **Smith TB**, Nunzio AM De, Patel K, Munford H, Alam T, Powell O, et al. ShearFAST: a user-friendly *in vitro* toolset for high throughput, inexpensive fluid shear stress experiments. bioRxiv. 2020 Feb 2;2020.01.31.929513.

- Darius T, Vergauwen M, **Smith TB**, Patel K, Craps J, Joris V, et al. Influence of different partial pressures of oxygen during continuous hypothermic machine perfusion in a pig kidney ischemia-reperfusion autotransplant model. Transplantation [Internet].2019 Nov 1.

- *Patel K, ***Smith TB**, Neil DAH, Thakker A, Tsuchiya Y, Higgs EB, et al. The Effects of Oxygenation on *Ex vivo* Kidneys Undergoing Hypothermic Machine Perfusion. Transplantation [Internet]. 2019 Feb 103(2):314–22.

- ***Smith TB,** *Patel K, Munford H, Peet A, Tennant DA, Jeeves M, et al. High-Speed Tracer Analysis of Metabolism (HS-TrAM). Wellcome Open Res [Internet]. 2018 Jan 12;3:5.

- Nath J, **Smith TB**, Patel K, Ebbs SR, Hollis A, Tennant DA, et al. Metabolic differences between cold stored and machine perfused porcine kidneys: A 1H NMR based study. Cryobiology [Internet]. 2017 Feb 74:115–20

- Nath J, **Smith TB**, Hollis A, Ebbs S, Canbilen SW, Tennant DA, et al. 13C glucose labelling studies using 2D NMR are a useful tool for determining *ex vivo* whole organ metabolism during hypothermic machine perfusion of kidneys. Transplant Res [Internet]. 2016 Dec 5 5(1):7.

- Ries W, Marie Y, Patel K, Turnbull C, **Smith T**, Jamil N, et al. A simple *ex vivo* model of human renal allograft preservation using the gonadal vein. Ann R Coll Surg Engl [Internet]. 2019 Nov 101(8):609–16.

- Hollis A, Patel K, **Smith TB**, Nath J, Tennant D, Ready A, et al. Manipulating the HIF Pathway in Renal Transplantation, Current Progress and Future Developments. J Clin Exp Transplant [Internet]. 2016 Nov 7 1(2):1–6.

- Nath J, Guy A, **Smith TB**, Cobbold M, Inston NG, Hodson J, et al. Metabolomic Perfusate Analysis during Kidney Machine Perfusion: The Pig Provides an Appropriate Model for Human Studies. Bruns H, editor. PloS One [Internet]. 2014 Dec 12;9(12):e114818.

*Denotes joint 1st authorship.

Declaration

This work has not been submitted, considered or accepeted for any degree other than doctorate of philosophy at the University of Birmingham

Contents

1 Introduction 1

1.1 Chronic kidney disease 1

1.2 Renal Replacement therapy 2

1.2.1 Dialysis 2
1.2.2 Haemodialysis 3
1.2.3 Peritoneal dialysis 3
1.2.4 Kidney Transplantation 4
1.2.5 Transplantation as the gold standard therapy for patients with ESRD 5
1.2.6 Sources of Kidneys 6
1.2.7 Limitations of Transplantation 8

1.3 Pretransplant kidney preservation 12

1.3.1 Static cold storage (SCS) 12
1.3.2 Hypothermic machine perfusion (HMP) 13
1.3.3 The evidence base for the clinical superiority of HMP over SCS 15
1.3.4 Proposed mechanisms governing the beneficial effect of HMP 16

1.4 Organ Preservation Research 20

1.4.1 The double-edged swords in organ preservation research 20
1.4.2 The need for models of organ preservation 21
1.4.3 The call for a novel cell line model in organ preservation research 24

1.5 Designing an *in vitro* screening tool for organ preservation research 26

1.5.1 Selection of a cell lineage relevant to transplantation outcomes. 26
1.5.2 Selection of a cell line representative of primary proximal tubule cells. 27
1.5.3 *In vitro* tools for simulation of complex *ex vivo* environments 32
1.5.4 Combining hypoxia chambers and cell rockers: a novel model of HMP 37
1.5.5 Selection of assays compatible with the high throughput screening tool 38

1.6 Modelling the unknown proximal tubule environment generated by HMP 39

1.7 Environmental stimuli modulating renal physiology 40

1.7.1 Intravascular fluid *in vivo* and *ex vivo* 40
1.7.2 Glomerular filtration *in vivo* and *ex vivo* 41
1.7.3 The proximal tubule *in vivo* and *ex vivo* 45
1.7.4 Modulation of proximal tubule physiology by fluid flow 46
1.7.5 Renal oxygenation *in vivo* and *ex vivo* 50
1.7.6 Chapter Summary: 51
1.7.7 Research hypothesis 53
1.7.8 Statement of aims 53

2 Application of nuclear magnetic resonance spectroscopy 54

2.1 NMR and the atom 54

2.1.1 Nuclear Spin 54
2.1.2 The magnetic moment and gyromagnetic ratio 56
2.1.3 The Boltzmann distribution 57
2.1.4 Larmor Precession 60

2.2 The NMR Experiment 60

2.2.1 The pulse-acquire sequence 60
2.2.2 Fourier Transformation and conversion to the ppm scale 62
2.2.3 The shielding effect of electrons 63
2.2.4 Signal splitting and J-coupling 64

2.3 Rationale for tracer studies in organ preservation research 66

2.3.1 Overview of the HSCQ experiment ... 68
2.3.2 Paired NMR and mass spectrometry analysis ... 70
2.3.3 Chapter summary ... 73
3 Methods and method development ... 74
3.1 *In vitro* methods ... 74
3.1.1 Cell culture ... 74
3.1.2 ShearFAST assisted fluid shear stress experiments. ... 76
3.1.3 Measures of cellular viability, damage and metabolism ... 78
3.1.4 Control of *in vitro* oxygen tensions ... 79
3.1.5 Oxygen sensing *in vitro* and *ex vivo* ... 80
3.2 Method Development ... 81
3.2.1 Controlling oxygen availability *in vitro* with custom hypoxia chamber filling circuits ... 81
3.2.2 Generating hypoxic atmospheres ... 82
3.2.3 Programming of custom oxygen atmospheres ... 85
3.2.4 Concluding statement about the *in vitro* model ... 91
3.3 *Ex vivo* methods ... 92
3.3.1 The paired whole organ model ... 92
3.3.2 Hypothermic machine perfusion ... 93
3.3.3 Tissue homogenisation ... 95
3.4 General methods ... 96
3.4.1 Metabolic analysis using NMR ... 96
3.4.2 NMR experimental parameters ... 97
3.4.3 Metabolite identification and quantification ... 98
3.4.4 Tracer analysis ... 99
3.4.5 HSQC analysis ... 99
3.4.6 Mass spectrometry ... 103
3.4.7 Colorimetric ATP assay. ... 104
3.5 Statistical analysis ... 105
3.5.1 *In vitro* statistics ... 105
3.5.2 *Ex vivo* statistics ... 106
4 ShearFAST: an in vitro toolset for high throughput, inexpensive fluid shear stress experiments. ... 107
4.1.1 Manuscript ... 108
5 Isolating mechanisms of benefit in models of HMP and SCS ... 130
5.1 Comparing metabolic differences between HMP and SCS stored kidneys. 131
5.1.1 Introduction ... 131
5.1.2 Manuscript PAGE 1/6 ... 132
5.2 Manuscript commentary ... 138
5.2.1 Lactate and the hypothermicly stored kidney ... 138
5.2.2 Limitations of this study ... 139
5.3 Assumptions of the systems approach ... 140
5.3.1 Assumption 1-SCS fluid is representative of intraluminal fluid ... 140
5.3.2 Assumption 2- Tissue weight reflect the same biomass between HMP and SCS samples 142
5.3.3 Assumption 3- The metabolic profile of the tissue sampled is reflective of the whole organ 143
6 In vitro dissection and modification of HMP and SCS environments ... 144
6.1.1 Introduction ... 144
6.1.2 Study 1: Identification of environmental stimuli governing cellular viability and metabolism 145
6.1.3 Study 2: Assessing fluid metabolites for their potential as biomarkers *in vitro* ... 145
6.1.4 Study 3: Screening the merits of increased antioxidant provision *in vitro* ... 146

6.2 Methods 147
6.2.1 Study 1: Identification of environmental stimuli governing cellular viability and metabolism 147
6.2.2 Study 2: Assessing fluid metabolites for their potential as biomarkers *in vitro* 152
6.2.3 Study 3: Screening the merits of increased antioxidant provision *in vitro* 152

6.3 Results 153
6.3.1 Study 1: Identification of environmental stimuli governing cellular viability and metabolism 153
6.3.2 Cellular effects of isolated HMP and SCS parameters 154
6.3.3 Study 2: Assessing fluid metabolites for their potential as biomarkers *in vitro* 160
6.3.4 Study 3: Screening the merits of increased antioxidant provision *in vitro* 163
6.3.5 Whole organ assessment of key *in vitro* findings 165

6.4 Discussion 167
6.4.1 Study 1: Identification of environmental stimuli governing cellular viability and metabolism 167
6.4.2 Study 2: Assessing fluid metabolites for their potential as biomarkers *in vitro* 173
6.4.3 Study 3: Screening the merits of increased antioxidant provision *in vitro* 175

6.5 Conclusion 176
7 Metabolic changes in proximal tubule cells submitted to in vitro simulations of kidney donation and preservation 177

7.1 Introduction 177

7.2 Methods 180
7.2.1 Study 1: Assessing RPTEC/TERT1 metabolism of glucose under standard culture 180
7.2.2 Study 2: The effect of warm ischemia on RPTEC/TERT1 glucose metabolism 181
7.2.3 Study 3: Quantifying thermal and pharmacological inhibition of metabolism 182
7.2.4 Study 4: Effect of fluid flow on proximal tubule cell metabolism 183
7.2.5 Study 5: The effect of oxygen availability on proximal tubule metabolism 184

7.3 Results 184
7.3.1 Study 1: Assessing RPTEC/TERT1 metabolism of glucose under standard culture 184
7.3.2 Study 2: The effect of warm ischemia on RPTEC/TERT1 glucose metabolism 187
7.3.3 Study 3: Quantifying thermal and pharmacological inhibition of metabolism 188
7.3.4 Study 4: Effect of fluid flow on proximal tubule cell metabolism 193
7.3.5 Study 5: The effect of oxygen availability on proximal tubule metabolism 195

7.4 Discussion 198
7.4.1 Study 1: Assessing RPTEC/TERT1 metabolism of glucose under standard culture 198
7.4.2 Study 2: The effect of warm ischemia on RPTEC/TERT1 glucose metabolism 199
7.4.3 Study 3: Quantifying thermal and pharmacological inhibition of metabolism 199
7.4.4 Study 4: Effect of fluid flow on proximal tubule cell metabolism 201
7.4.5 Study 5: The effect of oxygen availability on proximal tubule metabolism 202

7.5 Conclusions 203
8 Metabolic and physiological effects of oxygen supplementation during whole organ perfusion. 204

8.1 Manuscript overview 205
8.1.1 Manuscript 207
8.1.2 Discussion 216
8.1.3 Limitations of the study 221
9 The effects of different oxygen delivery strategies during HMP 226

9.1 Introduction 226

9.2 Methods 229
9.2.1 Experiment 1: The effect of a brief period of oxygen uploading at the start of HMP 229
9.2.2 Experiment 2: The effects of brief initial and end ischemic oxygenation strategies. 230

9.2.3 Experiment 3: Profiling the perfusate of kidneys subjected to different oxygenation strategies prior to transplantation 232
9.3 Results 233
9.3.1 Experiment 1: The effect of a brief period of oxygen uploading at the start of HMP 233
9.3.2 Experiment 2: The effects of brief initial and end ischemic oxygenation strategies. 240
9.3.3 Experiment 3: Profiling the perfusate of kidneys subjected to different oxygenation strategies prior to transplantation 243
9.4 Discussion 246
9.4.1 Efficacy of transient oxygenation strategies in the maintenance of perfusate oxygen levels. 246
9.4.2 Effect of oxygen uploading on metabolism 247
9.4.3 Chapter conclusion 250
10 Discussion 251
10.1 Proximal tubule metabolism between donor death and transplantation 252
10.1.1 Therapeutic targets for optimisation using the tiered strategy 253
10.1.2 The effect of oxygen delivery strategy on dissolved oxygen concentrations 254
10.1.3 The effect of oxygen delivery strategy on perfusate flowrate improvement 255
10.1.4 Effect of Oxygenation strategies on tissue damage as assessed by LDH release . 256
10.1.5 The effect of oxygen delivery strategy on metabolism 257
10.2 Further work 257
10.2.1 *In vitro* 257
10.2.2 *Ex vivo* 259
11 Appendices 260
11.1.1 Appendix 1: High Speed Tracing of Metabolism 260
11.2 Introduction 260
11.2.2 Appendix 3: *Ex vivo* glutathione supplementation abstract 277
11.2.3 Appendix 4- Differences in organ characteristics in paired kidneys. 278
11.2.4 Appendix 6 –ShearFAST supplementary data 279
Appendix 9 281
11.2.5 ^{1}H-NMR spectra from a renal cortex 281
11.2.6 1H-NMR spectra from HMP perfusate 282
12 References 283

Figures

Figure number	Title	Page
Figure 1.1.	Schematic of Kolff's artificial kidney- the first working dialysis device	3
Figure 1.2.	Illustration of a transplanted kidney (posterior view)	4
Figure 1.3.	Probability of 5-year survival following RRT	6
Figure 1.4.	Predicted incidence of severe CKD in the UK over the next 20 years	9
Figure 1.5.	Static cold storage	12
Figure 1.6.	HMP using the Organ Recovery Systems LifePort® Kidney Transporter	14
Figure 1.7.	Overview of a tiered strategy for organ preservation research	25
Figure 1.8.	RPTEC/TERT1 cultured in DMEM/HAMS F12 with 10% FBS.	31
Figure 1.9.	Differentiated RPTEC/TERT1 cultured using a custom media formulation	32
Figure 1.10.	Schematic of a standard parallel plate flow chamber	34
Figure 1.11.	A custom mould allowing the generation of a 3D tubule	35
Figure 1.12.	One of two Whitley H35 Hypoxia stations housed in our laboratory.	36
Figure 1.13.	A sealed Billups-Rothenberg hypoxia chamber.	38
Figure 1.14.	The macroscopic internal structure of the human kidney	42
Figure 1.15.	False colour cortical tissue section of a pig kidney after HMP	43
Figure 1.16.	The major subdivisions of the nephron	44
Figure 1.17.	Illustration of the static (top) and perfused (bottom) proximal tubule.	49
Figure 2.1.	Conventional illustration of an atom	55
Figure 2.2.	Unaligned spin 1/2 particles in the absence of a magnetic field	58
Figure 2.3.	An NMR sample enclosed in a receiver coil and solenoid magnet.	58
Figure 2.4.	Different orientations of spin ½ nuclei under an external magnetic field.	59
Figure 2.5.	Nuclear precession around the external magnetic field	61
Figure 2.6.	The NMR pulse-acquire sequence, and its effect on nuclear precession	62
Figure 2.7.	The NOESY Presaturation pulse sequence, adapted from(238).	63
Figure 2.8.	Two 1H-NMR signals arising from the presence of lactate in a sample.	65
Figure 2.9.	Pascals triangle and its prediction of split peak ratios	66
Figure 2.10.	Fine structure of the two lactate signals arising from J Coupling(242)	66
Figure 2.11.	A breakdown of the HSQC pulse sequence.	70
Figure 2.12	The dimensions of the HSQC spectrum	70
Figure 2.13	Overview of an HSQC plot for a single lactic acid signal	71
Figure 2.14.	Different label resolution from HSQC and MID analysis	74
Figure 3.1.	Cell culture apps developed during this PhD: Autocount and PDLCalc	77
Figure 3.2.	The viscosity of chilled preservation solutions	79
Figure 3.3	Hypoxia chamber filling circuit design 1.	84
Figure 3.4.	Monitoring chamber oxygen depletion in Hypoxia chamber filling circuit 1	85
Figure 3.5.	Filling of multiple chambers with a parallel circuit	85
Figure 3.6.	Validating simulation of hypoxic storage	86

Figure 3.7.	Hypoxia chamber filling circuit 2.	87
Figure 3.8.	Endpoint chamber atmosphere modulated by inclusion of oxygen line	88
Figure 3.9.	Fine control of sample oxygen availability using filling circuit 2.	89
Figure 3.10.	The final iteration of the hypoxia chamber filling circuit.	90
Figure 3.11.	Monitoring of hypoxia chamber atmosphere and sample oxygenation.	91
Figure 3.12.	Measurement of chamber atmosphere and sample oxygenation	92
Figure 3.13.	Abattoir set up for procurement of kidneys from freshly sacrificed pigs	93
Figure 3.14.	A porcine kidney attached to an 8mm T-connector using a surgical suture.	94
Figure 3.15.	A bisected porcine kidney after HMP.	96
Figure 3.16.	Example metabolite quantification using Chenomx (Lactate)	100
Figure 3.17.	Referencing the HSQC spectrum to a library signal (carbon 3 of lactate)	102
Figure 3.18.	The split structure of lactate (C3) observed during multiplet analysis.	103
Figure 3.19.	Isotopomer analysis	104
Figure 5.1.	Different staining of HMP and SCS kidneys using trypan blue	142
Figure 6.1.	Installation of a flow-through O2 sensor in the standard LifePort® circuit.	149
Figure 6.2.	Illustration of the generation of 4 separate preservation environments	151
Figure 6.3.	Perfusate oxygen depletion during HMP of porcine kidneys	155
Figure 6.4.	Metabolic differences in cell monolayers stored in UW or UWMPS.	156
Figure 6.5.	Screening the effect of preservation fluid and environment on cell damage	157
Figure 6.6.	The effect of physical environment on cellular viability	159
Figure 6.7.	The effect of the extracellular environment on LDH release in vitro	159
Figure 6.8.	Assessment of correlation between relative cell viability and LDH activity	160
Figure 6.9.	Protective effect of FSS over a range of fluid volumes	161
Figure 6.10.	Correlations between the relative cell viability and fluid metabolic profile	162
Figure 6.11.	Correlation analysis between fluid LDH and metabolic profile	162
Figure 6.12.	The effect of colloid on release of LDH in different oxygen environments.	165
Figure 6.13.	Effect of glutathione supplementation on cellular damage in vitro	165
Figure 6.14.	Cortical glucose levels after 24-hour HMP, or 2 and 24-hour SCS	166
Figure 6.15.	Cortical glutathione in kidneys after 24 hours HMP or SCS	167
Figure 6.16.	Reduction in perfusate LDH by glutathione supplementation ex vivo.	168
Figure 7.1.	RPTEC/TERT1 metabolises glucose under standard culture	187
Figure 7.2.	Simulated warm ischemia generates an anaerobic shift in RPTEC/TERT1	189
Figure 7.3.	NaHS in region of 0.06-0.2mM protects cultured cells at room temperature	190
Figure 7.4.	Modulation of mass isotopic distribution by temperature and NaHS.	193
Figure 7.5.	Effect of storage temperature and NaHS supplementation on LDH release	194
Figure 7.6.	No effect of FSS on metabolic profile during hypothermic preservation.	195
Figure 7.7.	Effect of atmospheric oxygen and oxygen depletion on metabolic profile	196
Figure 7.8.	Oxygen modulates RPTEC/TERT1 metabolism during hypothermic storage	197

Figure 7.9.	Trendline increases in cellular ATP with increases in oxygen availability.	198
Figure 7.10.	The effect of oxygen environment on LDH release in vitro	199
Figure 8.1.	Effect of oxygen tension on relative flow change during HMP	220
Figure 8.2.	Effect of oxygenation and aeration on perfusate metabolic profiles	221
Figure 8.3.	LDH release during HMP with continuous oxygenation or aeration	222
Figure 8.4.	Correlation between perfusate and cortical levels of key metabolites.	223
Figure 8.5.	Species modulates level of oxygen depletion observed during HMP	224
Figure 8.6.	Continuous aeration does not saturate UWMPS O2 carrying capacity.	227
Figure 8.7.	Arterial and venous oxygen levels during oxygenation of a human kidney	227
Figure 9.1.	Overview of oxygen uploading experiment 1.	232
Figure 9.2.	Schematic of two oxygen strategies used in uploading experiment 2.	233
Figure 9.3.	Real-time measures of perfusate oxygenation during brief O2 preloading.	236
Figure 9.4.	Effect of a brief period of oxygenation on perfusate flowrate during HMP	237
Figure 9.5.	The effect of oxygen uploading on Perfusate LDH release	238
Figure 9.6.	Endpoint cortical metabolic profile is unaffected by brief oxygenation	239
Figure 9.7.	De novo metabolism is unaffected by oxygen uploading	241
Figure 9.8.	HSQC analysis of metabolic flux arising from brief oxygen uploading	242
Figure 9.9.	Cortical ATP levels after HMP with and without oxygen preloading	243
Figure 9.10.	Effect of O2 delivery at the start and end of HMP on perfusate O2	244
Figure 9.11.	Relative renal flow rate improvements by different uploading strategies	245
Figure 9.12.	ATP levels in serial cortical biopsies during HMP with oxygen uploading	246
Figure 9.13.	Perfusate lactate concentrations vary with oxygenation strategy	247
Figure 9.14.	Overlay of LDH release between different oxygenation strategies.	248
Figure 9.15.	The effect of oxygen supplementation strategies on perfusate LDH activity	249
Figure 10.1.	Illustration of the tiered strategy for organ preservation research.	256
Figure 10.2.	Oxygenation strategy mediates relative flow rate improvements.	260

Tables

Table 1. The composition of UW and UWMPS solutions (87) 15

Table 2. Nuclear characteristics and spin number 55

Table 3. Chemical shift references used for metabolite quantification 99

Table 4. Modulation of anaerobic metabolism by temperature 190

Table 5. Modulation of TCA cycleprogression by temperature 191

Table 6. Cortical metabolic profiles of HMP, and HMP with brief oxygenation kidneys 236

Table 7. Different flow rates between pairs of kidneys during initiation of HMP 278

Table 8. Differences in weight between paired kidneys prior to initiation HMP 278

Student Supervision

Throughout my PhD, I have functioned as the laboratory supervisor for 6 medical students completing their undergraduate research products in our group. As a result of this, I received a national commendation at the 2017 Papin prize awards held at the University of Warwick for services to undergraduate teaching.

Additionally, I designed and directly supervised the research projects of two students (Tabeer Alam and Ohema Powell):

- Ohema Powell, (1st)
- Tabeer Alam, (2.1)

Abbreviations

° - Degree
°C - Degrees centigrade
± - Plus/minus
^{12}C - Carbon-12
^{13}C - Carbon-13
^{15}N - Nitrogen-15
^{1}H - Proton
Å - Angstrom
ATP - Adenosine triphosphate
AUC - Area under the curve
CI - Cold ischemia
CIT - Cold ischemic time
CKD - Chronic kidney disease
cm^2 - Centimeters squared
CO_2 - Carbon dioxide
COPE - Consortium for organ preservation research
DAMPs - Damage associated molecular patterns
DBD - Donation after brainstem death
DCD - Donation after circulatory death
DGF - Delayed graft function
DSS - 2,2-Dimethyl-2-silapentane-5-sulfonic acid
$dyne/cm^2$ - Dyne per square centimeter
ECD - Expanded criteria donors
ESRD - End stage renal disease
FID - Free induction decay
FSS - Fluid shear stress
g - Gravity OR grams
GCMS - Gas Chromatography Mass spectrometry
GFR - Glomerular filtration rate
GTB - Glomerulotubular balance
H_2S - Hydrogen sulphide
HEPES - 4-2-hydroxyethyl-1-piperazineethanesulfonic acid
HES - Hydroxyethyl starch
HMP - Hypothermic machine perfusion
HPLC - High performance liquid chromatography
HSQC - Heteronuclear single quantum spectroscopy
Hz - Hertz
IGF - Immediate graft function
IGL - Institute George Lopez solution
IRI - Ischemia reperfusion injury
IU/ml - International units per milliliter
kDa - Kilodalton
KIM-1 - Kidney injury molecule-1
KLF2 - Krüppel-like factor 2
kPa - Kilopascals
LDH - Lactate dehydrogenase
MID - Mass isotopic distribution
µl - Microliter
µm - Micrometre
µM - Micromolar
mm - Millimetre
ms - Millisecond
mM - millimolar
Na+ - Sodium cation
nm - Nanometer
nM - Nanomolar
NMR - Nuclear magnetic resonance

NOESY	-	Nuclear Overhauser effect spectroscopy
O_2	-	Oxygen
Pa.s	-	Pascal seconds
PCT	-	Proximal convoluted tubule
PDL	-	Population doubling level
PEG	-	Polyethylene glycol
ppm	-	Parts per million
RCT	-	Randomised controlled trial
ROC%	-	Relative oxygen concentration
ROS	-	Reactive oxygen species
RPM	-	Rotations per minute
RPTEC/ TERT1	-	Renal proximal tubule epithelial cell line.
RRT	-	Renal replacement therapy
SCS	-	Static cold storage
SGLT	-	Sodium glucose transporter
SRB	-	Sulphorhodamine B
TBARS	-	Thiobarbituric acid reactive substances
TCA	-	The citric acid cycle
TGF	-	Tubuloglomerular feedback
TLR4	-	Toll-like receptor 4
UK	-	United Kingdom
UW	-	University of Wisconsin solution
UWMPS	-	University of Wisconsin machine perfusion solution
WI	-	Warm ischemia
WIT	-	Warm ischemic time

1 Introduction

1.1 Chronic kidney disease

In health, our kidneys perform numerous important functions. These include regulation of haematocrit through oxygen mediated erythropoietin release(1), maintenance of whole body fluid balance(2) and blood pH(3).

Despite this, the terms ‘chronic kidney disease’ (CKD) and ‘renal failure’ refer specifically to the malperformance of one critical function, which is the isolation of micromolecular blood components (such as urea) from cellular and macromolecular blood components(4). The process through which the kidney fractionates blood, i.e. glomerular filtration is expanded on later. For now, it is sufficient to state that this process must occur at rate that prevents systemic toxin accumulation, responsible for the considerable morbidity and mortality associated with the uremic syndrome(5).

Measuring glomerular filtration rate (GFR) is the standard clinical test for assessing a patient’s kidney function(6). This may be estimated by quantifying the concentration of creatinine in the patients’ blood, or directly assessed by performing a time course analysis of urinary inulin after intravenous injection(7).

Chronic Kidney disease is diagnosed when GFR falls below 60ml/min/1.73m^2. The range within which a patients GFR falls is used to classify the severity of their kidney disease(4). Disease states which interference with GFR can lead to the development of end stage renal disease (ESRD). The leading genetic cause is autosomal dominant polycystic kidney disease(8). Other disease states implicated include types 1 and 2 diabetes(9), systemic lupus erythromatosus (10,11), IgA nephropathy(12) and hypertension(13).

The point at which a patients GFR is so reduced that it becomes incompatible with life. (i.e. stage-5 CKD) is diagnosed when the GFR reaches less than 15mL/min 1.73m^2(14,15). At this GFR, the patient is incapable of maintaining blood urea and salt/water balance. This is diagnostic of ESRD and the patient requires renal replacement therapy (RRT), designed to replace their lost kidney function.

1.2 Renal Replacement therapy

Renal replacement therapy exists in two forms, i.e. dialysis and renal transplantation.

1.2.1 Dialysis

The advent of dialysis was a major breakthrough for patients with renal insufficiency, prior to which ESRD was a terminal diagnosis. The first functional machine was designed built in secret by Dr. Willem Kolff during the 1940's Nazi occupation of the Netherlands(16) Under that environment, Kolff's prototype was improvised using the local resources available. These included a sewing machine motor to drive gravity assisted fluid flow and sausage skins to serve as a semipermeable membrane (Figure 1.1). Modern dialysis has of course evolved, and is now executed by one of two modalities; i.e. haemodialysis and peritoneal dialysis, however the general mechanisms are the same as those used by Kolff's device.

Dialysis effectively replaces the major function of the kidney, which is the isolation and elimination of toxins from the blood. i.e. glomerular ultrafiltration. Blood is passed along a semi permeable membrane and dialysate is made to flow in opposite direction along the other side of the membrane. Toxins, which are small enough to cross the membrane are isolated from larger components that cannot enter the dialysate(17).

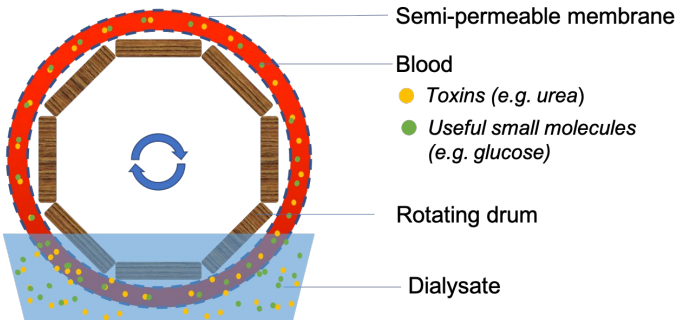

Figure 1.1. Schematic of Kolff's artificial kidney- the first working dialysis device

Kolff's 1942 device involved collection of blood in sausage skins, which were in turn wrapped around the circumference of a drum. Rotation of the drum by the sewing machine engine resulted in the generation of 'blood flow'. Emersion of the drum in a tank containing the dialysate generated counter current flow.

1.2.2 Haemodialysis

Offshoots from the patient's brachial artery and vein are surgically joined, forming an arterial-venous fistula. This allows their blood to continuously flow into a dialysis machine while limiting ischemia in their arm. Following the same principle as Kolff's machine, i.e. through a counter current system, toxins such as urea diffuse down their concentration gradient into the dialysate. The dialysate itself includes electrolytes at near physiological concentrations, in efforts to ensure blood does not become electrolyte depleted(18).

1.2.3 Peritoneal dialysis

Patients receiving peritoneal dialysis have dialysate injected into their peritoneum, which functions as a semipermeable membrane. Toxins accumulate in the peritoneal cavity and the patient may go about their daily life as they dialyse, but remain dependent on dialysate removal and replacement(19).

1.2.4 Kidney Transplantation

Kidney transplantation is the act of surgically implanting a functioning kidney from another person into a patient with ESRD. The renal artery and vein of the donated kidney are sutured onto the patient's external iliac artery, and vein and graft ureter sutured onto the patient's bladder (Figure 1.2). The patient's kidneys are left intact, so that whatever remains of their functions continue to contribute.

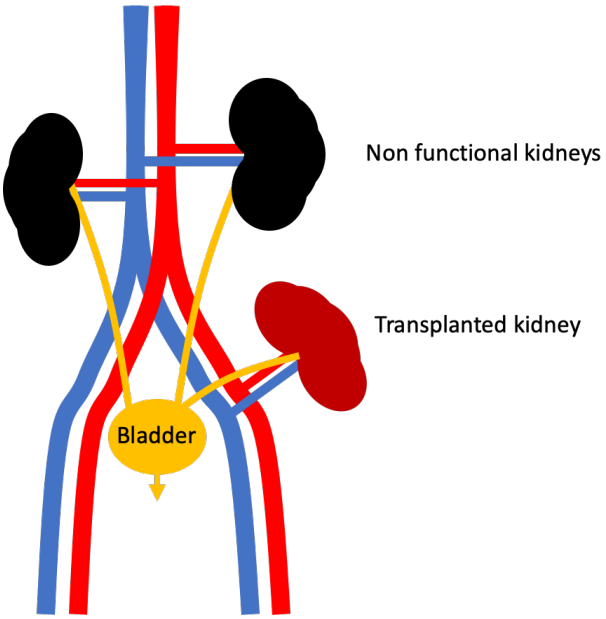

Figure 1.2. Illustration of a transplanted kidney (posterior view)

The patients' blood perfuses the donated kidney, enabling restoration of key renal functions which are not corrected by dialysis. For example, the proximal tubules permit reabsorption of blood glucose, which is lost in dialysis(20), and the donor kidney may act as a regulator of patient erythrocyte manufacture through erythropoietin (EPO) release(21). Patients undergoing dialysis frequently require EPO supplementation(22).

1.2.5 Transplantation as the gold standard therapy for patients with ESRD

Dialysis is a lifesaving therapy for patients with renal failure, illustrated by reports stipulating that patients with ESRD who choose to discontinue dialysis can expect to survive on average for around 7 days(23). Mortality upon withdrawal is linked to uraemia(24), failure to eliminate urea in the urine and corresponding accumulation of toxic metabolites in the blood. Additionally, the absence of renal replacement therapy causes fluid and end electrolyte imbalance, resulting in systemic pathology(5). For example, potassium accumulation is a known factor driving fatal aberrations in cardiac rhythm in patients with CKD(25).

However, the clinical effectiveness of dialysis is affected by factors such the presence of patient comorbidities, hypoalbuminemia, smoker status and age(26).

Dialysis does not significantly extend survival for some patients, typically the elderly and those with multiple comorbidities and in fact may limit quality of life, making a patient 38% more likely to die in hospital than matched patients given palliative care(27).

Additionally, dialysis modalities, whether haemodialysis or peritoneal dialysis exert their own morbidities. The mean patient survival time on haemodialysis is between 4-8 years(28), and each additional year of haemodialysis reduces survival by 6%(29).

This contrasts with the median 10 year lifespan of a well-functioning kidney transplant, a centre wide analysis of graft survival in the UK revealed 98% survive for 1 year post transplant, 87% survive for 5 years and 75% survive for 10 years(30).

Transplantation is therefore considered the gold standard treatment option for patients with end stage renal disease- conferring a well-recognised improvement in patient survival(31–34) (Figure 1.3).

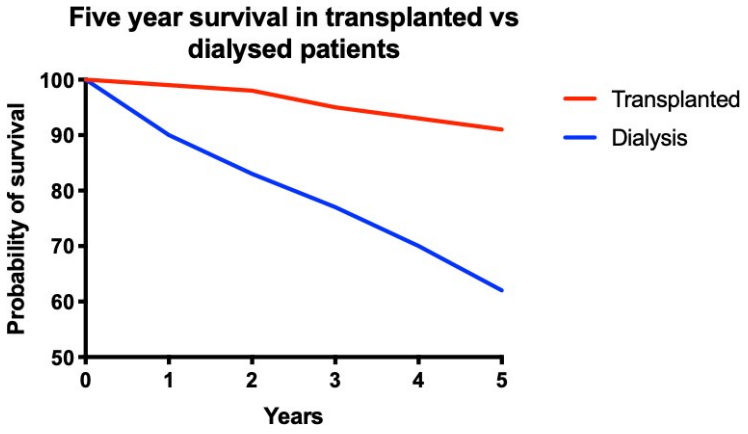

Figure 1.3. Probability of 5-year survival following RRT

Comparative patient survival on dialysis (all modalities-blue) and following kidney transplantation (all donor types- red), adapted from Santos et al (2015)(34).

Patients who receive a transplant, rather than dialysis are likely to have a better quality of life(35) and as mentioned previously, the functional transplant can restore additional renal functions aside from toxin isolation. These include glucose reabsorption and regulation of haematocrit through oxygen regulated erythropoietin release.

Transplantation is also by far the most economical therapy for patients with ESRD, a median 10 year graft survival associated with a well-functioning graft saves the NHS over £241,000 pounds in extra dialysis costs per patient(36).

1.2.6 Sources of Kidneys

1.2.6.1 Deceased donor kidneys

The above justifies the widely held assertion that for appropriate patients, transplantation is the most economically and clinically efficacious treatment arm of renal replacement therapy(37). However, because of the well documented shortage of kidneys suitable for transplant(38), multiple strategies have been implemented in an effort to expand the donor

pool, including the use of donation after circulatory death kidney (DCD)(39) and expanded criteria donor (ECD) kidneys(40).

The number of (DCD) kidneys utilised has been growing over the last decade in the UK, with 272 DCD kidney transplanted by the end of 2006 and 851 transplanted by the end of 2016(41). Kidneys may also be sourced from donors who have undergone brainstem death (i.e. DBD donors). Generally speaking, kidneys sourced from these donors do not experience the same level of warm ischemia as those from DCD donors, however are subject to a cascade of damaging distress signals released during brain death(42). Delayed graft function (DGF) is an undesirable post-transplant complication, which can be defined as the required for dialysis within one after kidney implantation(43). Kidneys sourced from DBD donors have a lower likelihood of developing DGF than those sourced from DCD donors(44). DBD donors are the predominant kidney source in the UK, with 902 DBD kidney transplanted in 2005/2006 and 1134 DBD kidneys used by the end of 2016(41).

1.2.6.2 Extended Criteria donors

The national shortage of transplant quality kidneys donations has led the UK health service to accept kidneys from extended criteria donors (ECD), which are typically from donors who are over 50 years old and may have comorbidities such as hypertension or high serum creatinine(40), factors linked with a general decrease in graft quality and post-transplant outcomes. ECD donations may be DCD or DBD, but organs from extended criteria donors exhibit increased likelihood of developing DGF when compared to standard criteria donors(45,46). The benefits of transplantation over dialysis have led to design of alternative sources. These include the usage the of kidney grafts removed from patients

due to a relatively benign pathology, which may still improve outcomes for those dialysing while on the waiting list(47).

1.2.6.3 Live donor kidneys

Live donors may volunteer one of their kidneys for the UK transplant program. Due to shorter ischemic times and necessarily healthy kidneys(48), these kidneys have superior graft survival and decreased incidence of DGF when compared to all deceased donor kidneys(49). Living donors compose a significant proportion of all transplant kidneys, accounting for around 32% of all kidneys utilised between 2015 and 2016(41).

1.2.7 Limitations of Transplantation

1.2.7.1 Insufficient supply of quality donor organs

While organ donation rates are rising, with a 2% increase in donations in 2019 compared to 2018(50), the main limitation of transplantation is that the current supply of kidneys from all sources does not meet the current and growing patient demand (Figure 1.4). In 2008-2009 it was noted that of all the patients on the transplant list, 41% were still awaiting their kidney transplant after three years and 7% had died during that timeframe while waiting for a suitable organ(51). As such, the optimal treatment of patients with ESRD is intrinsically linked to the availability of quality kidneys.

The number of UK patients starting RRT increased by 2.6% in 2017, compared to 2016(52) and over the next 20 years, the number of UK patients with advanced CKD (i.e. stages 3-5) is expected to double (Figure 1.4)(53).

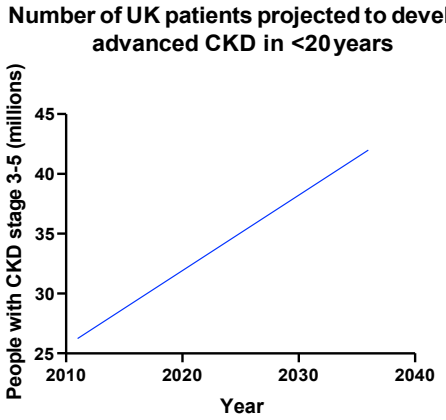

Figure 1.4. Predicted incidence of severe CKD in the UK over the next 20 years

Adapted from data presented by Public Health England (2014) (53)

Additionally, transplantation outcomes are deleteriously impacted by inevitable warm ischemic periods at organ procurement(54,55) and shortly after implantation upon renal perfusion with the recipient's blood(56), known as ischemic reperfusion injury(57).

1.2.7.2 Warm ischemia during kidney procurement

Ischemia stems from a catastrophic reduction in blood supply, which results in inadequate provision of oxygen and metabolic substrates and insufficient removal of waste.

Donation after circulatory death is often preceded by renal hypoperfusion(58,59) and is followed by a mandatory 5 minute 'no touch' policy in the UK(60).

Throughout this time the kidney experiences some level of ischemia, but the organ temperature is still conductive to physiological processes such as anaerobic metabolism(59). With DCD kidneys, the warm ischemic insult manifests prior to donor death and is functionally present when systolic blood pressure falls to 50 mmHg(61). As glomerular filtration requires a pressure of around 75 mmHg(62), the fluid within the post

glomerular structures may become static at this point, and certainly do during the asystole definitive of cardiac arrest.

Therefore, the warm ischemic time includes the period where the organ procurement team wait for the donor to die, and ends upon generation of the cold ischemic time. Over half of the kidneys procured have a functional WI between 30 minutes and 2 hours(63).

The hypoxia inducible factor-1α (HIF-1α) becomes stabilized in hypoxia, triggering translation of genes pertinent to anaerobic metabolism and downregulating transcription of genes involved in aerobic metabolism(64). Consequently, the metabolic profile of DCD kidneys becomes anaerobic in an attempt to replenish intracellular ATP(59,65).

However, in the first hour of warm ischemia, ATP levels in cortical tissue fall by around 90%(66), indicating this switch to anaerobic metabolism does not result in restoration of intracellular ATP levels.

Cells that rely heavily on aerobic metabolism are particularly vulnerable to the damaging effects of warm ischemia. Proximal tubule cells rely on aerobic metabolism to maintain the intracellular ATP(67) which maintains their significant reabsorptive activities and osmotic equilibrium with the extracellular fluid through the action of Na+/K+/ATPase(68–70).

ATP depletion leads to disruption of cytoskeletal filaments(71) loss microvilli, cellular and mitochondrial swelling(72) and cell death. *In vitro* models have demonstrated an ATP dependence on mode of proximal tubule cell death, with initiation of apoptotic and necrotic cell death when ATP levels fall by 70-25% and <15% respectively(73).

The organ acquisition process must therefore be rapid. For DCD kidneys, immediately after the 5-minute ‘no touch’ policy, the kidney is removed from the donor, cannulated and manually cold flushed to remove blood from the vasculature. By cold flushing the kidney upon acquisition, the metabolic requirements of the renal cortex kidney are lowered by up

to 58%(74). This slows ATP depletion through inhibition of ATP dependent processes and instigates the cold ischemic state(75).

Cold ischemia is deleterious(76–78), but delays the immediate insult that would be incurred under warm ischemia(79). As such, induction of cold ischemia may be regarded as a necessary evil in organ preservation.

1.2.7.3 Ischemia reperfusion injury following transplantation

Restoration of blood circulation after transplantation unavoidably generates some degree of ischemia reperfusion injury (IRI), and this process is considered to be critical in the development of negative post-transplant outcomes such as DGF(80) and graft survival(81).

The pathology incurred during ischemia is multifaceted, encompassing metabolic, immunological and mechanical processes. Thermal conductivity of renal tissue during reperfusion permits a global rewarming of the kidney, but delivery of metabolic substrates and oxygen may still be restricted due to patchy revascularisation patterns. Therefore, warm ischemic processes such as the ATP depletion described during organ procurement manifest in a second warm ischemic insult.

In addition, the reintroduction of physiological oxygen drives its own insult. Intracellular antioxidants such as glutathione are depleted during ischemia(82) and oxygen introduction drives generation of reactive oxygen species(83). These damage the cellular actin cytoskeleton and lipid membranes(84), which leads to expression of damage-associated molecular patterns (DAMPs), neutrophil recruitment and progressive development of inflammation(57,85).

Mechanistically, this may cause cellular occlusion of renal vasculature or tubulature, restricting fluid flow(56,57,80). Failure of the proximal tubules to recover from ischemic insult may also contribute to renal pathology following IRI(86).

1.3 Pretransplant kidney preservation

The two main methods by which *ex vivo* kidneys are stored in the period prior to transplantation are static cold storage (SCS) and Hypothermic Machine Perfusion (HMP). Differing from normothermic machine perfusion, which utilises warm blood and active oxygenation to support ongoing metabolism(87), both HMP and SCS utilise wet ice to instigate tissue hypothermia in the region of 4°C. This lowers the nutrient and oxygen requirements of the organ, inhibiting metabolism in renal tissue by up to 58%(74).

1.3.1 Static cold storage (SCS)

In SCS storage, the kidney is immersed in chilled preservation fluid, which is commonly the University of Wisconsin (UW) solution (Table .1) and packed in ice (Figure 1.5).

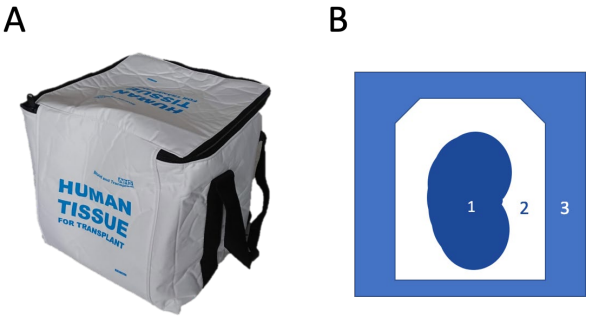

Figure 1.5. Static cold storage

SCS consists of portable polystyrene box (A) in which a human kidney (B1) is submerged in a bag of University of Wisconsin solution (B2) that is kept chilled by crushed ice (B3).

The UW solution was formulated to maintain hydrostatic equilibrium with the tissue(88), but does not include components offering metabolic support (Table .1). An alternative mediation of metabolism was attempted with the UW solution, with the higher concentrations of potassium (125 mmol/L) and lower concentrations of sodium (25mmol/L) implemented to mimic intracellular fluid. This ion ratio is theorised to inhibit ATPase activity, which leads to ATP exhaustion, an inability to maintain osmotic equilibrium and ultimately cell lysis (68). Given its simplicity and portability, SCS is the preservation modality most used in the UK(89).

1.3.2 Hypothermic machine perfusion (HMP)

Prior to Hypothermic machine perfusion (HMP), the kidney is attached via its renal artery to a peristaltic pump, and continuously cold flushed with University of Wisconsin Machine Perfusion Solution (UWMPS), which provides limited metabolic support through inclusion of 10mM glucose (Table .1).

Contrasting with UW, UWMPS was formulated to more closely resemble the extracellular environment, with higher concentrations of sodium (100 mmol/L) compared to potassium (25 mmol/L)(90).

Currently, HMP in the UK is performed using the LifePort® Kidney Transporter (Organ Recovery Systems, USA) (Figure 1.6).

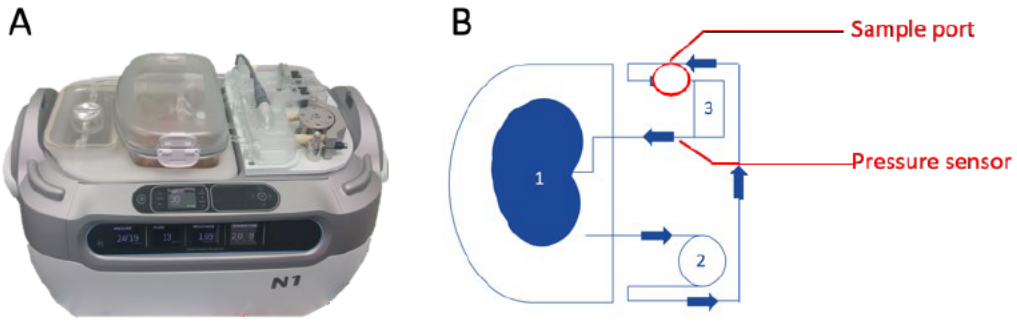

Figure 1.6. HMP using the Organ Recovery Systems LifePort® Kidney Transporter

A kidney (B1) is placed in a fluid reservoir containing UWMPS and attached by its renal artery to the perfusion circuit. The perfusion fluid is kept chilled using wet ice in the cassette holder and is cycled through the circuit at pressure of ~30 mmHg using a peristaltic pump (B2). A sample port allows sterile aspiration of the perfusate and a bubble chamber prevents air from entering the kidney during perfusion (B3). The rotational frequency of the peristaltic pump is modulated with respect to continuous readings from the pressure sensor, which maintains the perfusion pressure selected by the operator.

The LifePort® Kidney Transporter perfuses kidneys at sub-physiological pressures. The standard pressure used for adult kidneys is 30 mmHg, although the LifePort® can maintain perfusion between 10-60 mmHg. Lower pressures, (e.g. 20 mmHg) may be used for small or paediatric kidneys(91). The flow rate of fluid flow circulating through kidneys stored using the LifePort® is inversely proportional by the intrinsic resistance conferred by the kidney. The rate of fluid flow (ml/min), resistance (mmHg), as well as fluid temperature (°C) are displayed on a liquid crystal display interface on the front of the device.

Although hypothermic pretransplant organ preservation has permitted the extended storage of organs(92) and therefore enabled the national transport of deceased donor kidneys, it is only within the last 10 years that the evidence base supporting the routine use of HMP over SCS has been conclusively established(89,93–95). Prior to this realisation, optimisation of HMP storage was not deemed a priority and as such, organ preservation protocols had remained largely unchanged for over 20 years(96)

Constituents	UW (g/l)	UW MPS (g/l)
Hydroxyethyl starch (HES)	50	50
Potassium phosphate monobasic	3.4	3.4
Total glutathione	0.922	0.922
Sodium hydroxide/hydrochloric acid	-	-
Lactobionic acid (as Lactone)	35.83	-
Magnesium sulfate heptahydrate	1.23	-
Raffinose pentahydrate	17.83	-
Adenosine	1.34	-
Allopurinol	0.136	-
Potassium hydroxide	5.61	-
Calcium Chloride (dehydrate)	-	0.068
4-2-hydroxyethyl-1-piperazineethanesulfonic acid (HEPES) free acid	-	2.38
Mannitol	-	5.4
Glucose, beta D (+)	-	1.8
Sodium Gluconate	-	17.45
Magnesium gluconate	-	1.13
Ribose, D(-)	-	0.75
Adenine	-	0.68

Table 1 The composition of UW and UWMPS solutions(97)

1.3.3 The evidence base for the clinical superiority of HMP over SCS

The evidence base for the superiority of HMP over SCS stems largely from observed reductions in the development and severity of what is termed delayed graft function (DGF) after transplantation.

DGF, the requirement for dialysis within one week of transplantation(54) has been shown to correlate with likelihood of acute rejection(98,99) and graft failure(95). Meta-analysis

have estimated a 41% increased risk of rejection within three years for DGF kidneys, falling slightly to 38% in the first year following transplant(100).

Strategies aimed at reducing the incidence of DGF post-transplant may therefore have considerable impact on patients, and reduce the need for repeat transplantation.

A randomised controlled trial (RCT) in 2009 compared the post-transplant outcomes for 336 patients who received a kidney stored by SCS with 336 patients that received one that had been stored by HMP(95). Kidneys in the HMP group were found to function better post-transplant, with a lower incidence of DGF (i.e. in 70 vs 89 patients, adjusted odds ratio 0.57, p <0.01) and a shorter duration of DGF i.e. 10 vs 13 days, p <0.04) when compared to the SCS kidney cohort. A three year follow up from this study demonstrated improved graft survival in HMP stored kidneys over SCS stored kidneys, and a deleterious effect of DGF manifestation on graft survival(94). Recently, these findings were collated in an systematic review, indicating HMP resulted in significant reductions in DGF(101).

However, a factor limiting the application of this finding to UK practice was that the kidneys perfused in the 2009 study underwent HMP immediately after procurement from the donor. In the UK, standard practice at acquisition is to place the kidney in SCS upon transport to the receiving hospital, where it may or may not be perfused at surgical team's discretion. The findings of the 2009 study(95) were reproduced on a large UK dataset(76), which demonstrated decreased incidence of DGF in HMP vs SCS stored kidneys (i.e. 34.2 vs 42% respectively, p<0.001) and reduced duration of DGF (6.1 vs 7.4 days, p<0.003) respectively.

Regardless of storage modality, the cold ischemic time (CIT), i.e. the duration of hypothermic preservation is a notable antagonist in transplantation. However, storage of the kidney by HMP appears to reduce its deleterious effects. For short CIT, (i.e. <10hrs), HMP results in 6% incidence of DGF, compared to the 28% incidence for SCS stored

kidneys(102). Additionally, use of HMP rather than SCS may offer reductions in DGF for extended CIT i.e. (>20 hours)(102), a speculation corroborated by a review of the NHSBT kidney transplantation outcomes dataset(76).

1.3.4 Proposed mechanisms governing the beneficial effect of HMP

Even with marginally longer cold ischemic times, the incidence of DGF in kidneys which underwent HMP is lower than in SCS stored kidneys(76). There are numerous mechanisms proposed to explain the observed benefit of HMP over SCS preservation.

Clearly, the post-transplant benefit delivered by HMP must be generated by environmental differences existing between HMP and SCS, of which there are two possible instigators. Whilst HMP and SCS both utilise hypothermia, they differ in the provision of fluid flow and the composition of perfusion fluid. However, discerning the therapeutic action delivered by these interacting variables is a challenge, and this confounds the identification of therapeutic modifications that could be assessed for their capacity to further benefit the transplant recipient.

1.3.4.1 Vascular conditioning

The beneficial mechanisms behind HMP are likely to be at least partly mechanical. During HMP, the vascular resistance detected gradually drops(103). This is illustrative of improvements in vascular patency, a mechanical reversal of the vasospasm that occurs following hypothermic storage in hyperkaliaemic fluids(104), such as UW(105).

Shear stress mediates the vasodilatory effect of fluid flow through the modulation of nitric oxide release pathways in perfused kidneys(106).

This results in improvements to vascular patency, reflected through the decreasing intrarenal resistance. These may enable a patient's blood to perfuse the transplanted

kidney more fully or more quickly, limiting damage related to the second warm ischemic insult acquired during reperfusion. There is evidence linking higher renal resistance during HMP with a greater likelihood of DGF development post-transplant(103). Furthermore, well-functioning kidneys appear to plateau at minimal resistance within the first three hours of perfusion, whereas kidneys that go on to develop DGF do not plateau within this time period(107,108). Therefore, pressure driven vasodilation of the blood vessels during storage may play a role in minimisation of DGF. Since the presence of flow is exclusive to machine perfusion, SCS kidneys do not benefit from this parameter. However, the presence of flow in HMP may generate other protective parameters which are also absent from SCS, as described below.

1.3.4.2 Active delivery of therapeutic agents and removal of waste

Both UW and UW MPS contain therapeutic agents such as reduced glutathione (Table 1), which is included for its antioxidant properties. However, as demonstrated later in Figure 5.1, it is unlikely that UW permeates the SCS stored kidney effectively. The presence of fluid flow may be required to deliver preservation fluid into the intravascular/intratubular space, thereby permitting its protective function. Additionally, the presence of flow may also serve to dilute and transport accumulating extracellular waste, inflammatory DAMPS or cellular detritus away from the kidney architecture and out into the organ reservoir.

1.3.4.3 Improved metabolic support

Provision of metabolic support through HMP is suspected to contribute to its beneficial effect. A UK study utilised Nuclear Magnetic Resonance (NMR) spectroscopy to quantify perfusate metabolites prior to transplantation. It was found that perfusate metabolic profile had predictive potential for the development of DGF, with a seemingly counterintuitive

increased likelihood of DGF development with lower perfusate glucose concentrations(109) This implies a link between renal glucose handling during storage and functional outcomes. Elsewhere, the role of NMR based perfusate metabolic profiling in the prediction of transplant outcomes has also been proposed(110).

Whether or not kidneys submitted to HMP and SCS have different metabolic profiles, potentiating a metabolic mechanism behind the benefit of HMP was unknown. This was investigated in Chapter 5.

1.3.4.4 Active modulation of renal physiology by fluid flow

Fluid shear stress (FSS), generated *in vivo* by fluid flow across the surface of cell membranes is a known cytoprotective stimulus for the vascular endothelium.

In endothelial cells, FSS has been shown to trigger transcription of an anti-inflammatory phenotype through the action of flow sensitive Krüppel-like factor 2 (KLF2) expression(111). KLF2 is a flow modulated transcription factor that is linked with the regulation of diverse cellular functions. Generation of fluid shear stress during kidney storage has been shown to promote KLF2 expression on the vascular endothelium, which is otherwise lost in static cold storage(112). Upregulation of KLF2 expression by perfusion was also observed by our own group using a gonadal vein model of kidney preservation(113).

1.3.4.5 Inhibition of the innate immune response

Renal ischemia has been shown to upregulate toll like receptor 4 (TLR4) in renal tubular cells(114). Alongside serving as a sentry for invading microorganisms, TLR4 functions as a sensor for local tissue damage. DAMPs activate TLR4, leading to activation of innate immune response(115,116). TLR4 knockout mice are protected from IRI and AKI (117),

indicating lower TLR4 expression following organ storage is desirable. Periods of HMP after SCS result in lower surface expression of TLR4(118) which could confer reduced activation of destructive innate immune responses. As indicated above, DAMPs may also be diluted in the organ reservoir in HMP, but left to accumulate in the intravascular/tubular space within the kidney during static preservation.

HMP has also been shown to downregulate the presence of inflammatory cytokines and leucocyte adhesion molecules(119), potentially granting immunomodulatory protection not offered by SCS storage.

1.4 Organ Preservation Research

1.4.1 The double-edged swords in organ preservation research.

The fact that some aspect of HMP is generating a therapeutic benefit for patients indicates that an optimised organ preservation environment could further improve outcomes for transplant recipients. However, while the aforementioned mechanisms may factor in the perceived benefit of HMP over SCS, how to integrate these into an improved organ preservation protocol is not a trivial question.

Each variable that can be changed in organ perfusion (e.g. perfusion pressure, oxygen availability, fluid composition, temperature etc.) exists on a continuous scale, with the optimal degree likely to be sandwiched between that which is ineffectual because it is inadequate, and deleterious because it is excessive.

For example, although the presence of fluid flow affords vasodilation which is believed to be beneficial(103), higher perfusion pressures result in increases in proximal tubule biomarkers of oxidative stress, suggesting increased tubular damage as a function of higher shear stresses(120).

As an additional example, oxygen supplementation is an area of significant clinical interest in the field of organ preservation, This is more thoroughly discussed in the final chapters of this thesis, however in general, research in this area has focused on establishing the level necessary to exert clinically desirable outcomes while minimising deleterious processes, such as oxidative insult(121–123).

Finding the optimal perfusate composition is likely to be the greatest challenge, with unlimited combinations of possible components and concentrations. The current 10mM glucose present in UW MPS was originally included as a mediator of osmotic pressure(90) however is within the realm of hyperglycaemia which has been shown exerts deleterious oxidative processes in the kidney(124). Compounding the problem are the interactions between independent organ storage variables. For example, If the optimal oxygen delivery strategy became defined, this may necessitate an optimised perfusate to meet new metabolic demands, and an optimised perfusion pressure to deliver oxygen and nutrients throughout the kidney without causing unnecessary mechanical damage in the oxygen dilated vessels(125,126). Modulation of perfusate may impact perfusion parameters through changes in fluid viscosity, and the optimal combinations of all these variables are likely to change with changes in preservation temperature.

Optimisation of organ preservation practices is therefore a significant challenge, which requires the deployment of biological models to address.

1.4.2 The need for models of organ preservation

Understanding whether or not a modification to organ storage protocols is likely to have a beneficial effect on the receiving transplant patient requires large clinical trials.

It is both unethical and impractical to assess each potential modification to organ storage protocols on humans in the first instance, therefore models of organ preservation are

required to provide a strong evidence base for the assessment of refined preservation protocols in humans.

1.4.2.1 Animal models of kidney preservation

Animal models are frequently used in biomedical research, and organ preservation experiments are no exception. Kidneys are commonly sourced from pigs, given their similar size and anatomy to human kidneys(127), however studies utilising alternative animal models have been reported(128). The two kidneys possessed by all animal models permits several research strategies and these are highlighted below.

1.4.2.2 Animal Auto-transplant models

Studies seeking to define clinically superior organ preservation strategies may use an autotransplant model. With this strategy, one kidney is removed from each animal subject, subjected to the storage condition of interest then transplanted back into the same animal with simultaneous removal of the functioning kidney. This is an elegant model, which negates the requirement for immunosuppression, and renders the animal fully reliant on the function of their sole remaining transplanted kidney. Clinically relevant parameters, such as serum creatinine, graft or animal survival may be assessed in this model(125), and with the lack of immune rejection, deterioration in clinical measures is indicative of an inferior preservation protocol. As such, the autotransplant model is a final tool in the preclinical assessment of novel organ preservation strategies-prior to human experimentation.

1.4.2.3 Paired ex vivo perfusion models

A strategy more suited to investigating potential mechanistic effects of novel preservation strategies is to remove both kidneys simultaneously. This permits the utilisation of one

kidney as a ‘control’ which should simulate standard organ preservation as closely as possible. The contralateral kidney may be subjected to the modified preservation protocol and experimentally ascertained physiological changes observed between the pair are assumed to be caused by the difference in preservation protocol.

The auto transplant model is the most clinically translatable, but is a labour and resource intensive tool which is economically and ethically ill-suited for the high throughput screening of novel preservation strategies.

For this reason, much of the whole organ work documented in this thesis utilises a paired porcine kidney model to assess avenues for storage protocol optimisation.

Porcine kidneys may be sourced from local slaughterhouses. Since no animals are harmed for the purposes of research, there are no ethical considerations to the utilisation of this model.

The main limitations to the paired slaughterhouse model are its non-human origin, its relative quality over the standard deceased donor human kidney and the non-representative manner in which the slaughterhouse kidneys are procured, when compared to conventional organ harvesting. Additional limitations include the low throughput nature of this model it’s incompatibility with assessment of *in vivo* functional outcome. Some measure of functional outcome with *ex vivo* kidneys is possible through the use of specialised benchtop reperfusion circuits(87). The *ex vivo* porcine perfusion model is more thoroughly critiqued in in Chapter 5.

One critical variable that is difficult to control is the duration of storage, this results from external factors, such as the distance between donor and receiving hospital.

Despite the utility of hypothermic storage in suppression of cellular function, the cold ischemic time (CIT) is an independent risk factor for development of DGF, with each extra hour of CIT potentially increasing the risk of developing DGF by 8%(102). It is understood

that CIT should be minimised, but practically this is perhaps the most difficult parameter of hypothermic storage to control in clinical practice. Particularly with DCD kidneys, donor and recipient may be individually located anywhere in UK. Combined with the need for procedures such as recipient dialysis or immunological matching, this has resulted in a median CIT of around 15 hours in the UK(7).

This being the case, and with the ultimate goal of finding the optimal preservation protocol for the long-term storage of kidneys, it was logical to instigate extended CIT (i.e. >18 hours) in all of the research documented in this thesis, and vary the other variables with the potential to modulate graft integrity during storage.

1.4.3 The call for a novel cell line model in organ preservation research

To date, all mechanisms proposed for the benefit of HMP over SCS are linked in some way to the presence of fluid flow and fluid composition, which includes dissolved oxygen. However, with so many different combinations of possible storage environment, the discovery of optimal combinations of environmental parameters is likely to take a very long time using whole organ models in isolation.

Following established approaches used for drug discovery (which use high-throughput cell line models inform ever more translatable, but slower experiments using animal models(129) could expedite the identification of improved preservation environments. Figure 1.7 illustrates this proposed workflow below.

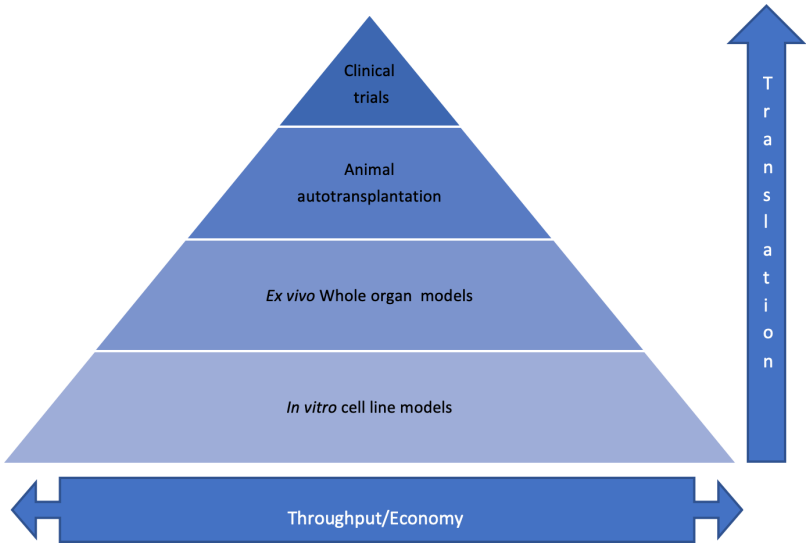

Figure 1.7. Overview of a tiered strategy for organ preservation research

With this tiered strategy, inexpensive, high throughput *in vitro* experiments direct, slower, more resource intensive whole organ experiments. These have indirect measures of benefit- such as identification of beneficial metabolic effects, improved perfusion parameters or reduced biomarker release. Once a lead candidate preservation protocol is established, this is brought forward for auto transplantation experiments. The last stage of this pyramid i.e. human experimentation through clinical trials is subject to the adequate evidence of *in vivo* benefit in the animal auto transplantation study.

Although cell line models cannot fully simulate the complex physiology and cell-cell interactions exhibited by their *in situ* parent cells, these models are unique in that they could allow identification of optimal preservation environments on a defined cell lineage, which is not easily accessible in any other model.

As described later, the gross anatomy and physiology of the kidney dictates that different tissues will experience different preservation environments during HMP. Therefore, when the optimal preservation protocol is realised, it will likely be a finely tuned balance of environmental parameters that best protect structures deemed to be the highest priority.

Cell lines have previously been used in models of organ preservation(130). The usage of multi-well dishes allows for experimentation with different perfusion fluids on scales unparalleled by any other biological model.

However, although tools currently exist which allow for low throughput variation of fluid flow or oxygen availability (Figures 1.10- 1.13), there are no current descriptions of an *in vitro* method through which all the parameters pertinent to the organ preservation environment (e.g. fluid composition, flow, dissolved oxygen content and storage temperature or duration) can be varied with the throughput permitted by multiwell dishes. As such, the bottom *in vitro* tier of the tiered strategy for organ preservation research can be considered undefined.

A primary goal of this thesis was the creation of a complete model of kidney preservation which allows scalable, high throughput variation and assessment of diverse organ storage environments, encompassing all the environmental variable described above. A description of this model is documented in Chapters 3 and 4 and its implementation is documented in Chapter 6 and 7. The background rationalising the design of the *in vitro* model follows below.

1.5 Designing an *in vitro* screening tool for organ preservation research

The capacity of an *in vitro* model to direct modifications to organ storage protocols that have a good chance of proving beneficial to the whole organ is intuitively dependent on the following criteria:

1. The cell lineage selected is relevant to post-transplant outcomes
2. The cell line chosen is representative of its parent cells

3. Relevant environmental parameters such as temperature, fluid composition, flow and oxygen availability are programable in an inexpensive, high throughput manner.
4. Experimental outcomes can be measured in the high throughput, economical manner befitting a screening tool.

How these criteria were used to direct the creation of a novel, useful cell-based screening tool for organ preservation research is described below.

1.5.1 Selection of a cell lineage relevant to transplantation outcomes.

The cell linage most often utilised in kidney preservation research is the proximal tubule cell line(131–133). Given their high metabolic rate, proximal tubule cells rely heavily on continuous oxygenation to support their reabsorptive functions, and as such are among those cells most damaged by ischemia upon cessation of blood flow(134–137).

Ischemia is believed to be a key antagonist in renal transplantation(138), with its deleterious effects on post-transplant outcomes manifesting during organ procurement(139), hypothermic storage(77,78,102,140–142) and particularly during reperfusion(57).

It follows that oxygen environments that protect proximal tubule cells during hypothermic preservation are likely to be sufficient to meet the metabolic requirements of the rest of the kidney during hypothermic storage, although further work using other cell linages is necessary to determine the whether this oxygen level is deleterious to other cell types.

Functionally, damage sustained to proximal tubule results in inadequate reacquisition of filtered solutes, and results in the release of necessary metabolites into the urine(143,144). Accordingly, there are several reports that indicate *in situ* proximal tubule damage during

preservation may be implicated in transplant outcomes. Urinary retinol binding protein, an *in vivo* biomarker of proximal tubular insult(145) is predictive of the rejection of kidneys in transplant recipients with otherwise functional grafts(146).

A potential importance of proximal tubule cell function may be inferred from the observation that glucose absorption by the perfused human kidney appears to be linked to the development of DGF(109). As described later, the *in vivo* proximal tubule is the primary site of glucose reabsorption in the kidney, acquiring 90% of the 180g passing through the kidneys every 24 hours(147,148). Although it is unknown whether this process proceeds under hypothermic storage, it is possible that *ex vivo* proximal tubules in this study were somehow implicated in the glucose reabsorption that appears linked to DGF development. Therefore, the proximal tubule is a key stucture of interest in kidney preservation research.

1.5.2 Selection of a cell line representative of primary proximal tubule cells.

An additional rationale behind the deployment of proximal tubule cells as the basis for a cell line model of kidney preservation is that each *in vivo* proximal tubule cell has the reported potential to spawn a mature proximal tubule. PCT cells are their own progenitor linage(149). Upon tubular insult, mature PCT cells dedifferentiate, migrate to the damaged area and then proliferate, repairing the tubule(150). It follows that given the right culture environment, cultured proximal tubule cells could form a monolayer representative of the *in situ* proximal tubule.

Currently used proximal tubule cell lines applied to organ preservation research include LLK-PK1 and HK-2. The porcine PCT cell line LLK-PK1has been utilised to demonstrate that switching the colloid found in UW (HES) for polyethylene glycol 35kDa resulted in improved protection under hypothermic storage (130). However arguably, the porcine

source of LLK-PL1 confers an unnecessary species deviation from human cellular physiology.

Human kidney-2 cells (HK-2) on the other hand, have been utilised in numerous reports to demonstrate a protective role of thermal conditioning prior to preservation(132) and that malignant cells are more susceptible to hypothermia in UW than benign cells(131).

HK-2 was established prior to 1994 upon recognition that '*no well differentiated PTC line derived from adult human kidneys cells exists'* (151). Primary human cortical cells were immortalised with E6/E7 genes from human papilloma virus (151). However, this cell line is reported to have dysregulated growth signalling through its transforming genes(152). Proximal tubule growth stage is a key determinant of its metabolism, with the proliferative stage characterised by glycolytic metabolism and the mature monolayer metabolic profile dominated by the beta oxidation of fatty acids(153). With the particular focus on metabolic profile optimisation during organ storage in this thesis, representative growth and metabolism forms a key requirement of the cell line model. HK-2 also lacks drug transporters which may mask the effectiveness of drugs screened using the model(154).

RPTEC/TERT1 is a human proximal tubule cell line immortalized through transfection with human telomerase reverse transcriptase(155), an enzyme which constitutively extends telomeric repeats to chromosomal telomers. This delays telomere dependent senescence, '*a major obstacle to the immortalization of human cell lines*'(156), but does not interfere with normal cellular growth or physiology. RPTEC/TERT1 is regarded as one of the most representative human proximal tubule cell lines, possessing drug transporters missing in HK-2(157), and developing dome structures in the mature monolayer (Figure 1.9), an indicator of unidirectional water transport(153).

Like the *in vivo* proximal tubule cells(158,159), mature RPTEC/TERT1 epithelium utilises lactate and fatty acids as substrates for metabolism, but proliferating cells utilise glycolysis(153).

Importantly for a consistent cell line model, RTEC/TERT1 have been documented to retain their representation of primary human PTEC for 90 population doublings(155). These observations indicate RPTEC/TERT1 is a suitable foundation on which to build a consistent, representative *in vitro* model of kidney preservation.

1.5.2.1 Defining culture conditions generating a representative model.

Everycyte GmbH, the supplier from which RPTEC/TERT1 was procured recommend routine culture in their proprietary ProxUp media at volumes of 240µl/cm^2 growth area. This has been reported to result in evidence of desirable indicators of monolayer maturation, including dome formation and cobblestone morphology(160)(Figure 1.9).

However, such ready to use media is ill-suited for usage in a high-throughput metabolic model of pretransplant kidney storage, which also seeks to make use of metabolic tracers. As described later in this chapter, NMR, and particularly ^{13}C NMR, are regarded as a relatively insensitive techniques(161). Larger cell growth areas (i.e. ≥75cm^2) have proven optimal for the sufficient biomass for specialised NMR analysis. This would necessitate purchase of significant volumes of ProxUp media. From an economic perspective this is undesirable, as a high-throughput cell line model of organ preservation requires large numbers of cells, replicates and a cost-effective media to maintain them. More importantly, supplementation of cell culture media with isotopically labelled tracers such as glucose is mandatory for the downstream tracing of metabolism. However, the existing ^{12}C glucose in ProxUP media would further decrease the signal to noise ratio observed in cell extracts. To counteract the suppression of signal induced through ^{12}C glucose competition with ^{13}C

enriched glucose, a new media formulation was required which could be modified to be free of the substrate which later would be supplemented in isotopically labelled form.

1.5.2.2 Selection of custom media for the in vitro model.

The first media trialled was DMEM/HAMS F12(1:1) (Sigma Aldrich, UK) which was supplemented to have a final concentration of 10% foetal bovine serum (ThermoScientific, UK, Cat: V30180.03).

We, and others(162) have observed that use of foetal bovine serum results in poor evidence of proximal tubule cell differentiation, indicated by elongated cells and lack of monolayer generation (Figure 1.8). This violates criterion 2 of the requirements of cell line model of organ preservation, which is that the cells used must be afford the closest representation of their parent cells. The batch to batch variability of serum also confers a level of uncertainty surrounding media composition(163) and its influence on the *in vitro* data acquired.

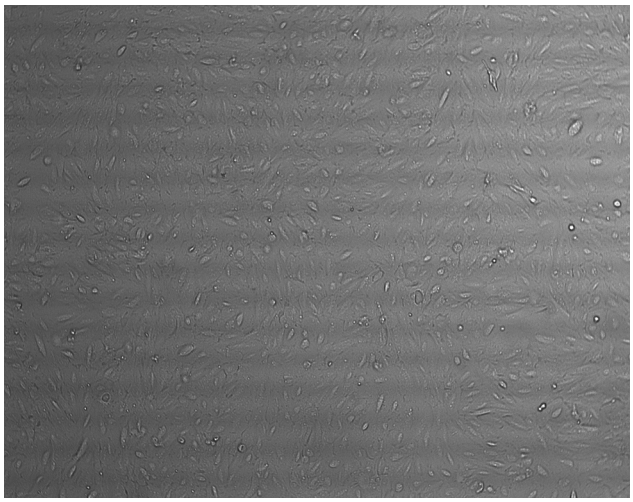

Figure 1.8. RPTEC/TERT1 cultured in DMEM/HAMS F12 with 10% FBS.

These cells show no evidence of differentiation, with elongated fibroblast-like morphology also documented elsewhere(162).

A review of the literature led to the testing of another media formulation which contains important serum components at defined concentrations(153).

Using this customised media, the effect of culture duration on RPTEC/TERT1 metabolic, transcriptomic and proteomic maturation has been extensively characterized and the authors of that study demonstrate striking similarities in growth rate and monolayer maturation between RPTEC/TERT1 and primary proximal tubule cells(153).

In line with the findings of this paper, culture of RPTEC/TERT1 in media based on that described in the above publication generated evidence of monolayer maturation in the form of cobblestone morphology and functional water reabsorption by formation of dome structures(162,164) (Figure 1.9). Interestingly, time course observation of these domes revealed these are not a simple bubble wrap-like structure, but change dynamically over time. The media utilised in this thesis was based on the custom formulation from this publication- and is detailed in Chapter 3.

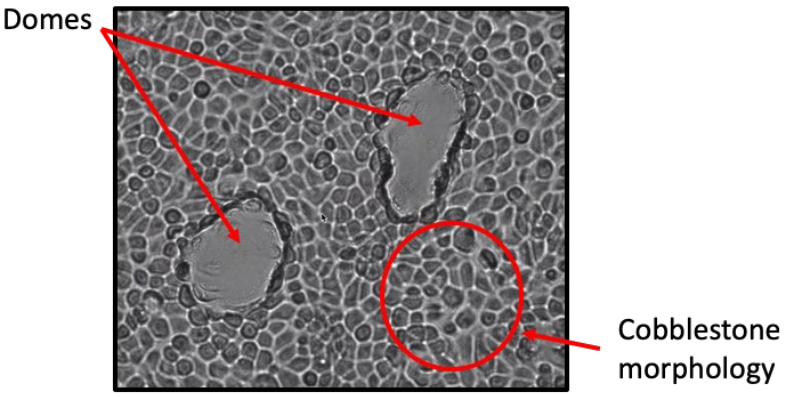

Figure 1.9. Differentiated RPTEC/TERT1 cultured using a custom media formulation

Cobblestone morphology indicates the formation of tight junctions(165) and dome formation indicates functional unidirectional transport of water.

1.5.3 *In vitro* tools for simulation of complex *ex vivo* environments

1.5.3.1 Simulating the fluid flow in vitro

As a whole, cell line research appears to focus on testing of agents that can be physically added to multiwell dishes. The capacity to screen multiple preservation fluids in a single experiment is a central advantage of the use of cell lines in organ preservation research. However, cell line research does not appear to make a large contribution to whole organ research as whole, perhaps due to the requirement for specialised equipment to simulate they environmental stimuli deemed to mediate renal physiology during storage.

The approaches used to simulate key environmental stimuli *in vitro* generally restricts the utilisation of a primary advantage of the cell line mode over the whole organ model, which is its capacity to screen large numbers of different experimental conditions. These *in vitro* methods are briefly described below.

1.5.3.2 Parallel plate flow chambers

Parallel plate flow chambers consist of a chamber in which adherent cells are cultured, with an inlet and outlet tube connected to the chamber by which fluid may pumped across the monolayer and the degree of fluid shear stress mathematically calculated (Figure 1.10). These devices are advantageous in that they confer unidirectional fluid shear stress and also allow for fine control of oxygen tensions in the fluid bathing the cells via an upstream oxygenator. Storage temperature can be controlled by heating or cooling the fluid reservoir.

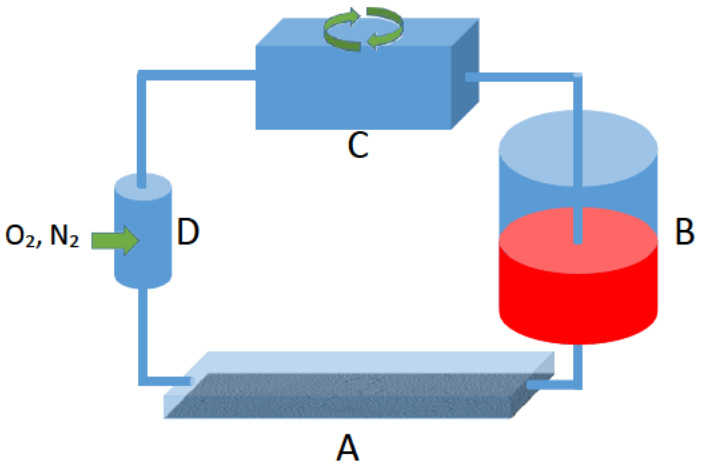

Figure 1.10. Schematic of a standard parallel plate flow chamber

Fluid in a reservoir (B) is actively pumped (C) through an oxygenator (D) before flowing over the cultured cells (A).

However, each replicate requires its own pump, fluid reservoir and flow chamber, making them low throughput and resource intensive. The schematic diagram in Figure 1.10 is in principle very similar to the LifePort® perfusion circuit in design (Figure 1.6), in that multiple flow chambers would be required for parallel experiments. The dilutional effect of this apparatus hinders the detection of secreted biomarker or metabolites, which may already be at low levels due to the hypothermic preservation environment.

Furthermore, the different *in vitro* analytical tools used in this thesis require different numbers of cells. Metabolic profiling may be performed with growth areas of a six well plate (9.6 cm^2) (153) whereas cell viability analysis described later can be executed in 96 well plate. Application of sophisticated NMR tracer techniques requires growth areas of at least 75 cm^2. The low throughput nature and difficulties with scalability associated with parallel plate flow chambers makes them inefficient as screening tools. Therefore alternative *in vitro* methods to simulate the *ex vivo* preservation environment are required.

1.5.3.3 Microfluidic devices

Culture of cells in microfluidics channels continuous perfusion with smaller volumes of liquid and gravity can be replace the requirement for mechanically driven perfusion-negating the ned for sperate pumps. Culture in different ambient temperature and oxygen environments allows for higher throughput environmental studies than parallel plate flow chambers. The emergence of gravity driven organ on a chip technology(166) is an exciting development which potentiates more physiological cell line microenvironments.

Although a 3D proximal tubule microfluidic chip was designed and fabricated for use in this thesis (Figure 1.11) its development was halted with the justification that the capacity to closely simulate luminal flow or 3D tubule structure was not as important as having a scalable model, capable of high throughput simulation of different organ preservation environments and compatible with high throughput assays to determine their effects.

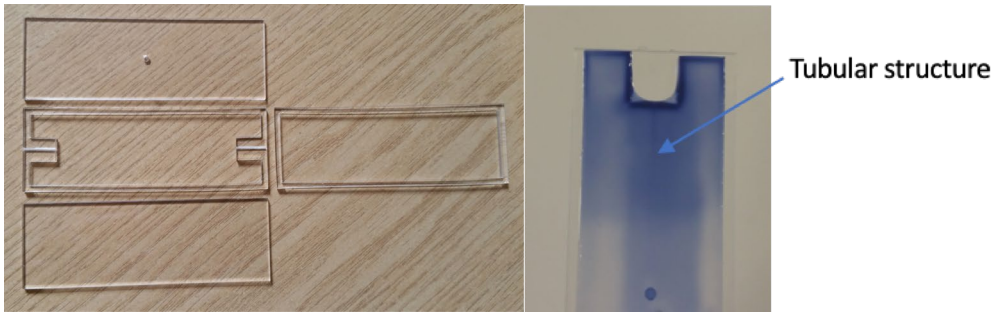

Figure 1.11. A custom mould allowing the generation of a 3D tubule

The diameter of the modelled tubule is roughly comparable to that of the human proximal tubule (i.e.~50 μm(167). The tubular structure is faintly visible after perfusion with trypan blue dye.

1.5.3.4 Cell rocker induced shear stress

Cell rockers are common place in the laboratory environment, and provide a simple, economical means with which to generate repeating cycles of fluid flow in standard laboratory equipment. When adherent cells, cultured on the bottom of a receptacle are

placed on the cell rocker, the supernatant bathing them is subject to fluid flux cycles. This fluid motion causes the cell monolayer to experience some undefined degree of fluid shear stress.

The paper '*Quantifying fluid shear stress in a rocking culture dish'*(168) presents a series of equations which calculates fluid flux over the plate when the volume and viscosity of a given fluid, the dimensions of the dish and the rocking profile (angle, frequency) are known. If the rocking profile is determined and the mathematics of the model executed correctly, cell rockers potentiate shear stress experiments limited only by the number of plates that can be placed on the rocking platform.

The limitations of this approach are that the flow pattern is bidirectional, rather that unidirectional as is found in normal physiology. Furthermore, there is no established means with which to accurately measure the rocking profile and the mathematics must be executed correctly each time an experiment is performed. There is also no established means with which to generate defined oxygen environments or temperatures, which are separate but highly relevant stimuli in current organ preservation research.

1.5.3.5 Tools for controlling oxygen availability in vitro

There are several well established means of submitting cells to defined degrees of hypoxia. Hypoxia stations (Figure 1.12) and parallel plate flow chambers (Figure 1.13) are two commonly used pieces of equipment that allow for fine manipulation of oxygen concentrations in fluid bathing cultured cells. Hypoxia stations allow high throughput experiments using a uniform hypoxic environment, however are incompatible with cell rocker-based induction of shear stress due to space constraints, and are also unsuitable for the simulation of hypothermic storage as they maintain normothermic temperatures.

Simultaneous assessment of the effects of different oxygen environments requires multiple hypoxia stations.

Figure 1.12. One of two Whitley H35 Hypoxia stations housed in our laboratory.

The Whitley Hypoxia station consists of a large, airtight incubator space where cultured cells are kept at physiological temperatures (i.e. 37 °C). The 5% CO_2 atmosphere permits the action of sodium bicarbonate pH buffers, and the oxygen environment is constantly and actively maintained at user defined thresholds. The oxygen environment generated may be controlled a touchscreen interface on the front of the hypoxia station.

An alternative to hypoxia stations and parallel plate flow chambers are hypoxia chambers (Figure 1.13). These are inexpensive, high-throughput, air tight units which are designed to instigate conditions of severe hypoxia/anoxia. Cell culture ware is placed in the chamber, which is then sealed and flushed with large quantities of nitrogen gas. This expels the atmosphere within the chamber and replaces it with theoretically anoxic environment. However, there are no reported means with which to finely tune the oxygen environment inside a hypoxia chamber.

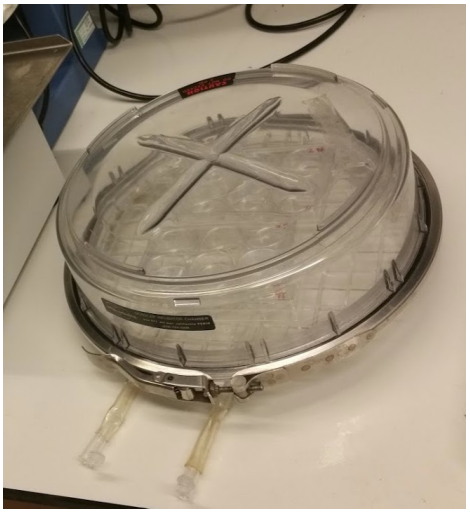

Figure 1.13. A sealed Billups-Rothenberg hypoxia chamber.

This simple unit may be rendered airtight using a metal clasp and sealing the two ports on the front. Roughly the size of a dinner plate, these are large enough to store multiple tissue culture multiwell plates, but small and light enough to fit inside a standard cell culture incubator and in this thesis, to be placed on a cell rocker for simultaneous shear stress induction using the ShearFAST assisted cell rocker model.

1.5.4 Combining hypoxia chambers and cell rockers: a novel model of HMP.

Chapter 3 describes the creation and validation of a simple method which the oxygen atmosphere within a hypoxia chamber can be programmed. Chapter 4 describes the development and validation of ShearFAST, a smartphone application which uses the positional sensors of a smartphone to measure the rocking profile set on a cell rocker, and integrates these measurements into a calculator permitting determination of the shear stress generated when the user inputs the other known experimental parameters. These two developments are compatible with each other, allowing high throughput instigation of different extracellular environments.

Together, these form an inexpensive, high throughput method which also permits simultaneous instigation of other factors such as fluid composition and temperature.

1.5.5 Selection of assays compatible with the high throughput screening tool

The capacity to generate diverse cellular environments *in vitro* is best complemented with high throughput economical assays with which to infer their effects. The following section introduces the assays selected for use in this thesis. In general, the sulphorhodamine B, and lactate dehydrogenase assays were selected for use as indicators the protective potential of a given preservation environment, and NMR was deployed when inferences of metabolic modulation by a tested preservation environment was desired. NMR is discussed in Chapter 2.

1.5.5.1 The Sulphorhodamine B (SRB) assay

The Sulphorhodamine B (SRB) assay was designed for application in high throughput *in vitro* drug screening(169), and the economical, scalable properties of this method make it an ideal assay with which to close in on optimal pretransplant preservation conditions.

The SRB assay functions on the principle that live cells bound to the plastic of culture ware can be likened to microscopic packets of protein. Sulphorhodamine B is bright purple dye that binds to amino acids under slightly acidic conditions(170).

Cellular detachment and/or lysis of the bound cells results in net loss of protein bound to the cultureware, and a corresponding decrease in the concentration of dye immobilised on the plastic. When dyed monolayers are washed with acid, the bound dye is retained (Figure 6.5). The dye is however soluble under basic conditions, therefore colorimetric detection of the absorbance of dye retained on cells and resuspended in base is proportional to the protein content remaining on the dish after an experiment. Higher absorbance of light at 510nm is indicative of increased cellular viability.

1.5.5.2 The lactate dehydrogenase (LDH) assay

The colorimetric lactate dehydrogenase (LDH) assay is a well-established, inexpensive approach with which to assess the relative merits of one preservation condition over the other. This assay uses fluid samples such as the cell culture supernatant, and therefore is complimentary to SRB analysis of cellular integrity which uses the cellular monolayers. Another reason this assay was selected for *in vitro* analysis that LDH is also detectable in HMP perfusate (Figure 9.5), potentiating a translatable biomarker between *in vitro* and *ex vivo* models.

Lactate dehydrogenase is an intracellular enzyme which plays a vital role in the interconversion of glycolytic endpoint metabolites. Assessment of LDH in the blood is a well-established clinical tool, and *in vitro*, is an indicator of membrane damage and ongoing cell death. The biochemical mechanism of the assay is reviewed elsewhere(171).

1.6 Modelling the unknown proximal tubule environment generated by HMP

The selection of the proximal tubule as a key structure of interest in kidney preservation is rationalised above. While the environmental stimuli that govern proximal tubule, function and integrity *in vivo* are well established we really know very little about the proximal tubule environment generated by HMP or how this impacts cellular physiology.

The following section utilises current understanding of renal physiological processes in health to speculate over the types of environments that could be conceivably generated by current HMP protocols.

While it is beyond the scope of this thesis to define the proximal tubule environment during hypothermic preservation, combining the tools described in Chapters 3 and 4 allows for high throughput, simulation of the relevant environmental extremes.

In this manner, an optimal preservation environment can be defined *in vitro*. Then, it falls to the researcher how to deliver the optimal environment predicted *in vitro* to *ex vivo* proximal tubule during preservation.

The following is an introduction to renal physiology in health, which allows speculation over the possible proximal tubule environments generated during *ex vivo* preservation. and conjecture over on the types of modifications HMP protocols that could be beneficial to the proximal tubule. This literature review begins with a description of the blood flowing through the kidney.

1.7 Environmental stimuli modulating renal physiology

1.7.1 Intravascular fluid *in vivo* and *ex vivo*

Blood is a complicated, non-Newtonian water-based fluid, composed of cellular, polymer (e.g. protein), monomer (e.g. glucose, lactate) and simple molecular constituents (e.g. ions, dissolved gases) and metabolic waste.

By far, the most numerous cell type within human blood is the red blood cell, or erythrocyte. This is a highly specialised cell type which has the primary function of increasing the oxygen carrying capacity of the blood.

Although oxygen is soluble in water, the majority of the oxygen transported in the bloodstream is bound to haemoglobin (98%), with the remaining 2% is dissolved in the plasma(172).

Erythrocytes effectively raise the oxygen carrying capacity of the blood by acting as containers for haemoglobin, a dynamic protein which has itself evolved to harvest O_2 or CO_2 from environments where either gas is abundant, and release them in environments where the counterpart gas prevails. As shown in Table 1, the metabolic support offered by commonly used preservation fluids both in terms of metabolic substrate provision, and in terms of oxygen carrying capacity is far lower than that of blood.

Although hypothermia is used during *ex vivo* preservation, and is known to supress metabolic rate(173), it is unclear whether metabolic support offered by clinically used preservation fluids meets the metabolic demands of the hypothermicly stored organ. Research into the use of perfusate oxygen carriers, such as haemoglobin and active oxygenation during HMP(174) is testament to the uncertainty that the current preservation fluids are cable of transporting sufficient oxygen during standard organ preservation.

1.7.2 Glomerular filtration *in vivo* and *ex vivo*

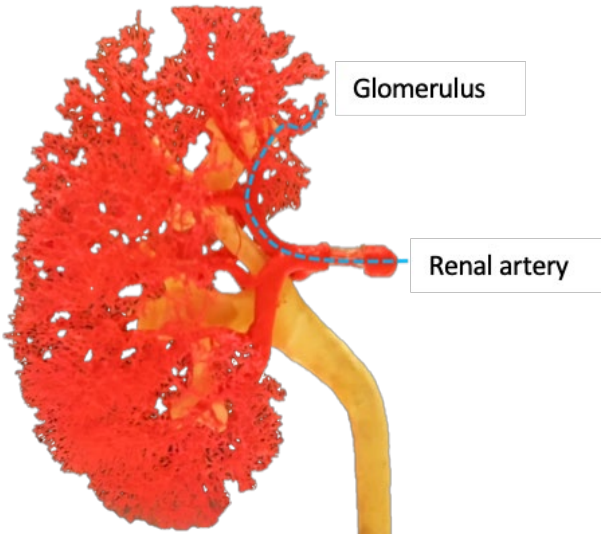

Figure 1.14. The macroscopic internal structure of the human kidney

The vascular structure of a human kidney (red) with the collecting ducts visible in yellow

Blood enters the kidney through the renal artery (Figure 1.14) which drains from the descending aorta. The blood flows; via interlobular and arcuate arteries and afferent arterioles to millions of glomeruli; fenestrated, tightly knotted bundle of capillaries which reside within the renal cortex. The glomerulus (Figure 1.15) is commonly depicted as the starting point of the nephron (Figure1.16), the functional unit of the kidney.

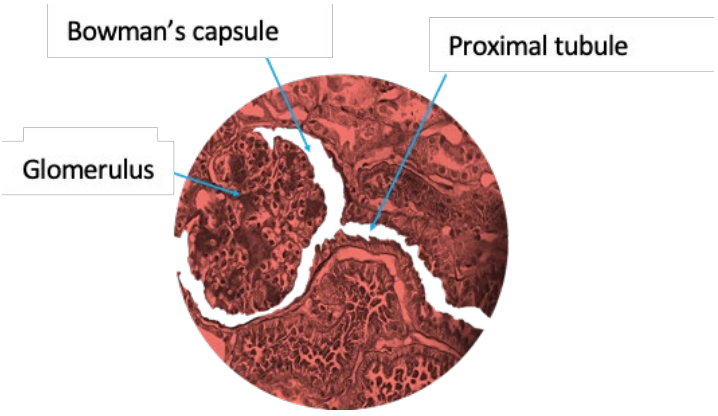

Figure 1.15 False colour cortical tissue section of a pig kidney after HMP

The efferent arteriole, which the glomerulus drains into has a smaller diameter than the afferent arteriole supplying it and *in vivo*, the intraluminal pressure difference between blood entering and leaving the glomerulus is between 10-15 mmHg(175,176).

This intraglomerular pressure pushes the blood components first through the glomerular fenestrations, which are between 60-70nm in diameter and then through relatively abundant smaller podocyte slits (sized between 45- 50 Å radii) and less abundant larger slits (sized between 75 -115 Å radii)(177).

Alongside selection based on component charge, this creates a glomerular ultrafiltrate which is generally devoid of components larger than albumin(178,179).

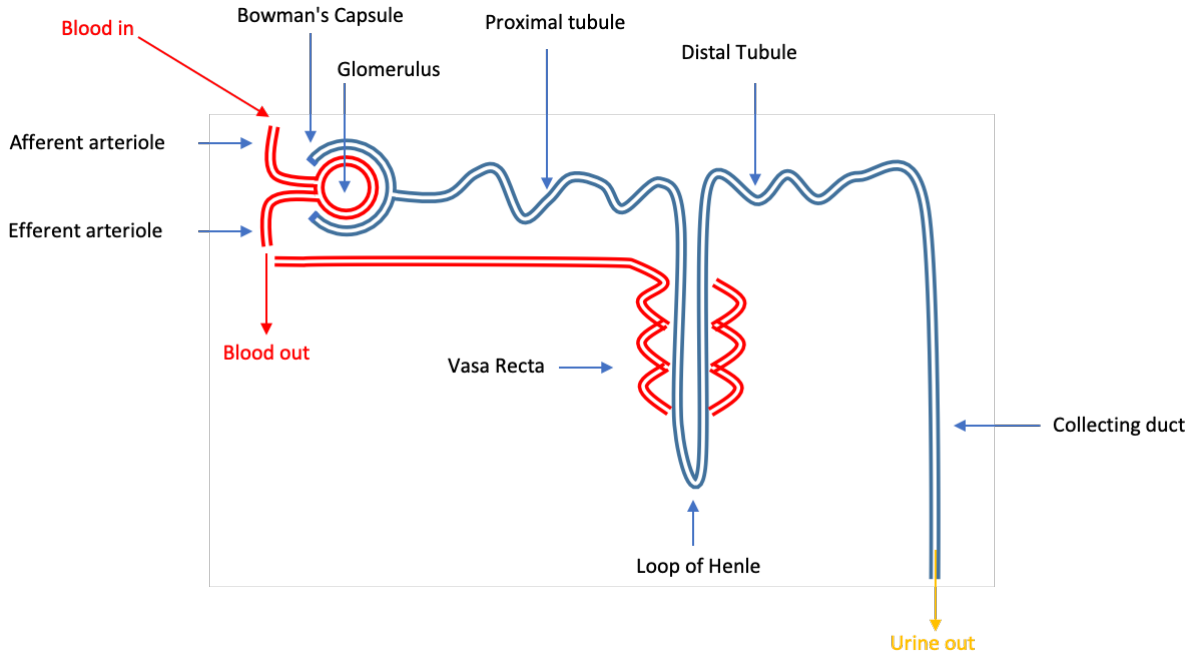

Figure 1.16. The major subdivisions of the nephron

The schematic highlights key structures of the nephron, which function in concert to fulfil diverse renal functions, ranging from ultrafiltration (Glomerulus), selective reabsorption of glucose (proximal tubule) fine control of water and ion balance (Loop of Henle, distal tubule) and excretion of waste (collecting duct). The thesis will focus primarily on cortical tissues and in particular the proximal tubule, which is reviewed in greater detail later.

The glomerular filtration rate (GFR), a clinical measure of the volume of fluid passing through the nephron is highly variable and is subject to change due to circadian rhythm(180), changes in blood pressure(181) or in response to feedback from the downstream nephron (i.e. Tubuloglomerular feedback- TGF)(182).

In health, glomerular filtration effectively results in retention of all cellular matter within the glomerulus, which then returns to systemic circulation. However, multiple factors associated with organ donation and preservation may interfere with continuation of glomerular filtration during HMP.

Alongside deleterious processes such as thrombus formation, cessation of blood flow during kidney procurement may impact glomerulus permeability, which has been

demonstrated to be actively mediated by continuous endothelial sensing of fluid shear stress exerted by flowing blood(183). The sub-physiological perfusion pressures maintained during machine perfusion (e.g. 30 mmHg) are well below the >75mHg pressure thought to be required for renal function(62). Furthermore, the colloid used in clinically used preservation fluids (Hydroxyethyl starch, or HES) has a molecular weight 250kDa(184), which is far above the generally accepted molecular weight cut-off conductive to ultrafiltration (70 kDa)(185).

Together, these reports indicate that structures located on the other side of the glomerular filtration barrier may not benefit from perfusion, or from the oncotic protection offered by the presence of HES during HMP. As discussed in later Chapter 6, HES may not be the best colloid choice in preservation solutions, irrespective of whether or not it crosses the glomerulus. Regardless, glomerular damage is observed during organ storage(186,187) , which could potentiate the entry of undefined quantities of storage solutions into the downstream nephron.

In light of all of these observations, there is no clear consensus on the *ex vivo* post glomerular environment. It is unclear whether commonly used perfusion fluids filter through the glomerulus in the absence of damage given the low perfusion pressure, and if they do, whether the filtration barrier modifies the perfusate by restricting the entry of colloid into the proximal tubule lumen (Appendix 2).

In health, the glomerular ultrafiltrate is captured by a cup-like structure, the Bowman's capsule, which collates ultrafiltrate to before it flows into the proximal tubule. While metabolic waste, such as urea is passively isolated from the blood by glomerular filtration, so are essential serum components such as glucose, electrolytes and water. These must be consistently and actively reacquired in the face of fluctuating ultrafiltrate flow rates, and

this is the primary function of the proximal tubule, however it is unknown if this process is active during hypothermic storage.

1.7.3 The proximal tubule *in vivo* and *ex vivo*

In health, the proximal convoluted tubule (PCT), which is supplied by the Bowman's capsule is the primary site of Na+, HCO_3^-, albumin, water and glucose reabsorption in the kidney(188). Around 60% of water and salt is taken up by this structure(189) and these transport activities are highly reliant on an adequate supply of oxygen to meet the high aerobic metabolic requirements of proximal tubule cells(190). This reliance on oxygenation makes proximal tubule cells particularly sensitive to energy store depletion as a consequence of ischemia(135,191), with a linked but mechanistically separate secondary insult generated by depletion of intracellular antioxidants(192), presumably through interactions with reactive oxygen species (ROS).

We do not currently have the technology to determine the oxygen concentration within the *in vivo* renal cortex(193) , any kind of biopsy or incision will lead to oxygen entry into the tissue studied. Accordingly, it is unknown whether or not the metabolic support offered by conventional preservation practices is optimal for PCT function remaining under hypothermia, or even if selective reabsorption of glucose occurs.

Clinically used preservation fluids are not routinely subjected to active perfusate oxygenation. The acellularity of the glomerular ultrafiltrate means that the cells forming the nephron must either get their oxygen from the relatively little dissolved in the glomerular ultrafiltrate, or from closely associated blood vessels.

Paired with sub-physiological/ absent PCT perfusion during HMP, and the hypoxia enhancing effect of *ex vivo* oxygen shunting(194) described later, standard preservation practices may culminate in *ex vivo* proximal tubule environments which are incapable of

providing the oxygen required to support the metabolic processes remaining under hypothermic storage. This is reflective of the general uncertainty surrounding the oxygen requirements of the kidney during organ preservation.

1.7.4 Modulation of proximal tubule physiology by fluid flow.

In health, the various reabsorbative activates of the PCT are kept relatively constant despite fluctuations in the preceding GFR. This modulation of PCT activity is known as glomerular tubular balance (GTB)(195). There are two mechanisms through which GTB is maintained, i.e. modulation of tubule diameter and regulation of solute transporter expression.

Modulation of tubular diameter is a passive process. In the early PCT, the rate of fluid flow (volume/time) is equal to the GFR, although by the time the ultrafiltrate reaches the end of the proximal tubule, this has dropped to around 55%(196). However, the rate of flow (distance/time) through the PCT remains constant, evidenced by studies which also demonstrated that that diameter of the proximal tubule gradually decreases as it moves further downstream from the Bowman's capsule. This trend remains throughout simulations of increases and decreases in GFR and also in haemorrhage, although the overall tubule diameter increases in relation to increases in GFR, and decreases in relation to decreased GFR and blood loss(197).

Therefore, there is a consistent rate of flow across the proximal tubule. It is commonly reported that the physiological GFR of 115ml/min/1.73m^2 is associated with the induction of fluid shear stress on the *in vivo* proximal tubule monolayer in the order of magnitude of 1 dyne/cm^2(198–201), although this is an approximation of the early PCT as water reabsorption affects the viscosity of fluid and tubular dimensions downstream(202).

It is known that fluid flow across the vascular endothelium under hypothermic storage results in modulation of cellular phenotype(113). The key role fluid shear stress plays in regulating proximal tubule form and function *in vivo* may suggest a potential effective role during *ex vivo* storage.

Chapter 4 describes ShearFAST a development through which high throughput shear stress experiments may be easily executed *in vitro,* therefore a concise description of what fluid shear stress is and what modulates it is pertinent.

Fluid shear stress occurs when a liquid flow over a solid boundary. It is a force that acts parallel to the solid boundary in the direction of the supplied flow(203).

The fluid motion at the solid boundary is limited due to the no-slip condition(204), i.e. the adhesive interactions between fluid molecules and solid boundary are stronger than the cohesive interactions with other moving fluid particles.

If the adherent fluid molecules form a metaphorical anchor on the solid boundary, then cohesive interactions between fluid particles form a chain that attaches the anchor to the relatively fast-moving fluid at the fluid free surface. This results in the transfer of kinetic energy from the moving fluid particles into the shearing force that acts on the solid boundary.

Immediately above the adhered fluid molecules, fluid flow is slowed due to cohesion with the static fluid molecules. With laminar flow, layers of fluid can be imagined by their incrementally increasing flow rate up until the fluid free surface, i.e. the surface of the fluid that is in contact with the air(205).

The shear stress imparted by a flowing fluid is therefore modulated by factors which change the resistance between fluid layers, i.e. change its viscosity. Factors changing viscosity in Newtonian fluids include the interactive nature of components dissolved in the fluid and the thermal properties of the system(206). In fluid mechanics, fluid shear stress

is commonly quantified by the dyne/cm^2, with 1 dyne/cm^2 being the force required to move 1 gram 1 cm/s(203).

When the fluid has no free surface, such as within a cylindrical structure like the renal proximal tubule, the velocity profiles of the fluid are mirrored, resulting in the highest fluid flow rate in the centre of the tube (Figure 1.17).

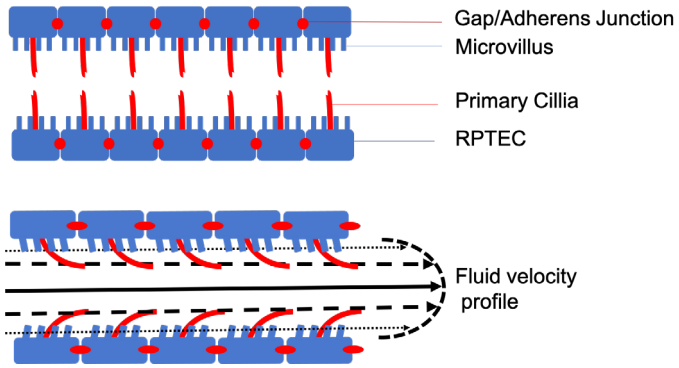

Figure 1.17. Illustration of the static (top) and perfused (bottom) proximal tubule.

The proximal tubule possesses at least three mechanosensors which are capable of detecting and responding to changes in flow, i.e. stretch receptors and FSS sensors such as the microvilli the and the primary cilia (Figure 1.17)(207). It is through these mechanosensors that membrane solute transporters phenotype is mediated, permitting sufficient reabsorption in the face of variable fluid volumes supplied by a varying GFR. For instance, sodium, and bicarbonate reabsorption, as well as the expression of their transporters (NHE3 and H+/ATPase respectively) have all been found to increase with increases in flow(208). The endocytic reabsorption of filtered albumin has also been found to be flow dependent(201).

An estimated 180g of glucose is absorbed the proximal tubule every day(148). This is mediated by low affinity/ high capacity sodium glucose (SGLT-2) transporters on the brush

border of the S1 and S2 segments of the proximal tubule, and residual glucose is later taken up by low affinity SGLT1 in the straight convoluted tubule(209). Using *in vitro* microfluidic devices, both SGL2 expression and glucose uptake was found to be upregulated in proximal tubule cells subjected to fluid shear stress(210).

SGL2 functions as a cotransporter for Na+ and it its action contributes significantly to oxygen consumption in the kidney(211). Together, these potentiate a transcriptional link between FSS experienced by the PCT and the fate of oxygen in the kidney.

With respect to the proximal tubule in isolation, fluid shear stress has been shown to play an important role as a regulator of cytoskeletal structure(198), retention of a healthy phenotype alongside downregulation of the fibrotic plasminogen receptor(212) , and of cell viability under physiological temperatures(213).

The integral role fluid flow plays in modulation of proximal tubule cell function and integrity described above suggests that there may be an optimal shear stress for the proximal tubule under hypothermic storage, and this is unlikely to be 0 dyne/cm^2, definitive of fluid stasis.

As stated previously, the extent to which the proximal tubule experiences fluid flow during *ex vivo* storage is unknown. It is therefore unclear what level of shear stress the *ex vivo* proximal tubule experiences, or whether or not the has any bearing on cellular function or integrity during or after HMP. Realising the optimised magnitude of FSS parameter experienced by different structures in the kidney during organ storage is an avenue which could conceivably lead to development of improved preservation conditions, however is relatively unexplored, perhaps due to the difficulty in isolating different renal structures and submitting them to defined degrees of FSS.

1.7.5 Renal oxygenation *in vivo* and *ex vivo*

Although blood carries oxygen in bound and dissolved forms, oxygen transport within the kidney does not necessarily follow the bloodstream. The renal cortex in particular relies heavily on adequate oxygenation to fuel ATP dependent reabsorbative activities (214,215), but the downstream medulla is characterized to be a largely hypoxic region, reliant on anaerobic metabolism(65). Despite this, the oxygen saturation of blood entering the renal artery and exiting the renal vein are very similar (216,217). This is indicative of arterial-venous oxygen shunting, a counter current mechanism reported to transfer up to 50% of the oxygen carried in the preglomerular arterioles to the blood flowing out of the kidney via the post glomerular venules(218).

Since the renal medulla is known to function under hypoxia, oxygen shunting has been proposed as an anti-oxidative process which may have evolved to limit ROS damage to the renal tissue caused by hyperoxia associated with the kidneys considerable receipt of cardiac output(218).

It is however unknown if oxygen shunting is maintained during organ preservation.

Progressive perfusate oxygen depletion is a well-evidenced consequence of the HMP storage of kidneys in circuits that do not include an oxygenator(219,220) and UWMPS does not possess a designated oxygen carrier. It is therefore unclear if oxygen delivery during standard HMP is sufficient to provide the oxygen required for any aerobic processes continuing under hypothermic storage.

Nonetheless, perfusate oxygen consumption during whole organ storage has been shown to be linked with improvements in glomerular filtration rate post-transplant(221) and has also been described as predictors of transplant outcomes(220), corroborated by other

studies which in improved oxygen availability during storage improved outcomes in models of auto transplantation(121).

These observations fuelled speculation into a therapeutic role of active perfusate oxygenation, which may be key in the combating the major insults the kidney in the transplantation process, which are the warm ischemic time during organ procurement, the cold ischemic preservation time and most significantly, the multifaceted insult incurred by ischemic reperfusion injury (IRI).

However, neither the oxygen requirements in the hypothermic organ, and whether or not oxygen shunting occurs during organ preservation is known. With the risk of increased oxidative stress linked with active oxygenation, the renal medulla in particular may be deleteriously affected by excessive oxygen. Indeed, perturbations in normal renal oxygenation may be significant contributors to the development of kidney disease(222). Incubation of proximal tubule cells in hypoxic UW results in reduced of cellular injury when compared to cells exposed atmospheric oxygen(223), implying dissolved oxygen tensions in storage solutions are an important parameter governing cellular pathology.

1.7.6 Chapter Summary:

To summarise, different organ preservation modalities affect the incidence and severity of delayed graft function. DGF is associated with increased likelihood of graft failure- and the return of the patient to costly and clinically unsustainable dialysis. These patients will remain on dialysis until death, unless a transplant is performed. However with each successive transplantation, future transplant outcomes are inferior due to accumulating immune sensitization(224).

Identification of more supportive organ preservation environments may further reduce the incidence of DGF and graft failure and if this is realized, patients can expect their

transplanted kidney to function better and for longer. This is desirable for the patient population awaiting kidneys, and also for the healthcare provider who could benefit from further enhancements to the cost effectiveness of transplantation over dialysis(36).

Additionally, development of more supportive organ storage environments for deceased donor organs may allow the preservation of kidneys for extended durations before they are rendered non-transplantable. Logistically, this could facilitate deceased donor international organ sharing schemes similar to existing schemes for living donors(225), which could increase the speed with which an immunologically matched kidney could be delivered to a patient(226).

A barrier impeding the refinement of organ storage protocols is the low throughput, high stakes nature of whole organ research. A tiered strategy, in which a novel cell line model capable of simulating hundreds of unique organ preservation environments in a single experiment directs whole organ research could expedite discovery of optimal preservation environments.

This thesis will focus largely on the proximal tubules and renal cortex during organ preservation, therefore in an in-depth account of renal physiology beyond the proximal tubule is beyond the scope of this thesis. However, the well characterised homoeostatic activities of the distal tubules, loop of Henle and the collecting ducts all been found to be regulated to some extent by fluid shear stress(227–230) or oxygen availability(231,232)

Proximal tubule cells possess key attributes which make them a suitable foundation upon which to build a cell line model of organ preservations. However due to the anatomy of the kidney and current preservation protocols, it is unknown if the *ex vivo* proximal tubule benefits from fluid flow, oncotic protection from colloid or metabolic support through delivery of metabolic substrates and oxygen.

1.7.7 Research hypothesis

Current pretransplant kidney preservation protocols are not yet optimised. Making as yet undefined changes to the extracellular environment of the hypothermicly stored kidney may result in indirect measures of benefit, which could translate to improved outcomes for the transplant recipient.

1.7.8 Statement of aims

Broadly speaking, this project has 3 aims.

The first is to develop a reproducible *in vitro* model of organ preservation. This model should permit high throughput generation of different oxygen environments (Chapter 3), levels of fluid shear stress (Chapter 4) and storage fluid formulations.

Using the tools developed as part of aim 1, the second aim of this work is to identify environmental stimuli which enhance cell survival or improve cellular metabolism after simulated storage (Chapter 6 and 7. After high-throughput screening of diverse environments, a 'lead target' modification will be selected for validation in the whole organ setting.

The final aim of this thesis is to determine whether the lead target modification identified *in vitro* can also confer metabolic, structural or physiological benefit to *ex vivo* kidneys after whole organ preservation. If such benefit is demonstrated, this thesis will seek to further optimise the beneficial modification.

2 Application of nuclear magnetic resonance spectroscopy

With the recognition that metabolism of the hypothermicly stored organ may play a key role in modulating patient outcome following kidney transplantation, it became apparent that advanced tools for quantifying metabolic changes was required. In this thesis, Nuclear Magnetic Resonance (NMR) spectroscopy is used to detect metabolic changes arising from modified organ storage protocols. This technology relies on manipulation of certain phenomena of atomic physics.

2.1 NMR and the atom

Conventional illustrations depict atoms as cores of positively charged protons and uncharged neutrons, orbited by shells of negatively charged electrons (Figure 2.1).

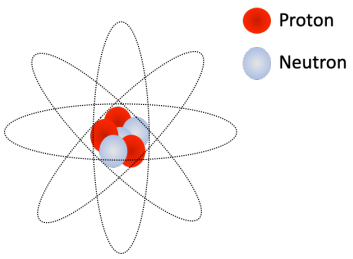

Figure 2.1. Conventional illustration of an atom

2.1.1 Nuclear Spin

All sub-atomic particles have an intrinsic property known as spin, an angular momentum which proceeds within the atom.

Particle spin can be illustrated in a macroscopic model as a sphere rotating around its axis. A detailed description of the quantum equations governing how variable spin states manifest is beyond the scope of this chapter. In general, the spin number (!) of a given element can be ascertained from its nuclear characteristics (Table 2).

Mass number	Neutron number	Atomic number	Spin number
odd	odd	even	Half integer
	even	odd	Half integer
even	odd	odd	Integer
	Even	even	0

Table 2. Nuclear characteristics and spin number

Hydrogen, having an odd mass number and atomic number (being composed of just a proton) has a half integer spin number (i.e. ½).

From the above table we can determine that, like hydrogen, both ^{13}C and ^{15}N have half integer spin, whereas the higher abundance isotopes ^{12}C has a spin number of 0 and ^{14}N has the spin number 1.

This thesis describes the use of ^{13}C and ^{15}N as metabolic tracers. These isotopes occur naturally, but at considerably lower abundance than their ^{12}C and ^{14}N counterparts i.e. at (1.07% and 0.37% respectively)(233). Like hydrogen, these isotopes have ½ integer spin, which as described later, makes them NMR detectable. The additional neutron within these elements also enables differentiation of isotopically labelled compounds from their non-labelled counterparts by mass spectrometry, an orthogonal method utilised later in this thesis.

The low natural abundance of ^{13}C and ^{15}N gives these isotopes great utility in the assessment of metabolism. When a biological system is exposed to metabolic substrates enriched with ^{13}C or ^{15}N, downstream detection of metabolic endpoints enriched with that isotope reflects *de novo* synthesis.

2.1.2 The magnetic moment and gyromagnetic ratio

Analogous to the observation that a moving charge (i.e. electrons) passing through a coil of wire creates an electromagnetic field, the combination of an angular momentum and net charge grants particles with both of these properties an additional intrinsic property, which is the existence of a magnetic moment (μ)

The magnetic moment (μ) experienced by a given particle may be calculated by:

$$\# = \frac{\%\&\hbar}{2)}$$

Equation 1 The magnetic moment(234)

Where $\%$ is the gyromagnetic ratio of that nucleus and $\hbar$ is the reduced Planck's constant, a multiplier (i.e. through which angular momentum is quantized). Since net nuclear charge is derived from the number of protons in that nucleus, which also defines the element, and the total mass of a nucleus is determined from the numbers of protons and neutrons- each element and isotope has a different gyromagnetic ratio, which is the ratio of the magnetic moment to its angular momentum.

The magnetic moment of spin half particles generates a nuclear dipole, an intrinsic nuclear feature manipulated by NMR experiment to enable detection of that nucleus.

Electrons, also spin half particles experience both an orbital magnetic moment generated by their procession around the atomic nucleus, and another magnetic moment generated by their intrinsic angular momentum. The importance of electron magnetic moments for NMR experiments is discussed later in the nuclear shielding effect.

2.1.3 The Boltzmann distribution

In practice, when we pipette sample into the NMR tube, there is no net magnetisation vector for the sample. The individual magnetic moments of its composite particles cancel each other out and as such net magnetisation is zero (Figure 2.2).

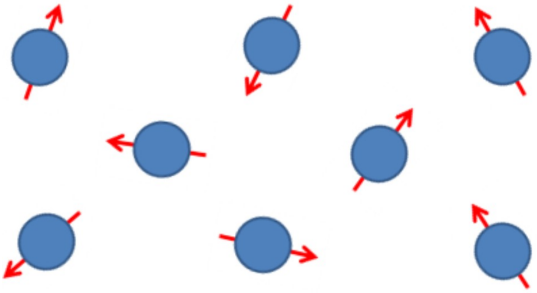

Figure 2.2. Unaligned spin 1/2 particles in the absence of a magnetic field

In an NMR experiment, the sample is placed in the lumen of a receiver coil, which is itself housed within a solenoid electromagnet (Figure 2.3). The solenoid magnet in this spectrometer generates uniform external magnetic field (B_0) with an upwards magnetisation vector.

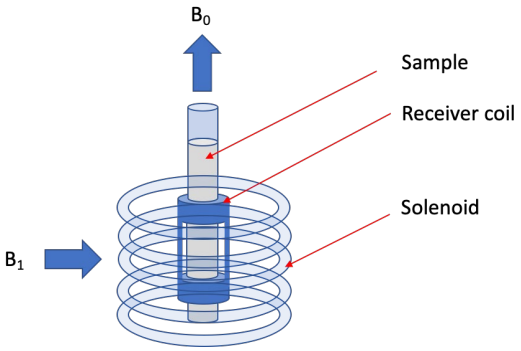

Figure 2.3. An NMR sample enclosed in a receiver coil and solenoid magnet.

In the presence of this external magnetic field, the nuclear dipole possessed by each spin ½ nucleus within that sample aligns parallel (i.e. α–state nuclei) or antiparallel with this

field (i.e. β-state nuclei) (Figure 2.4).

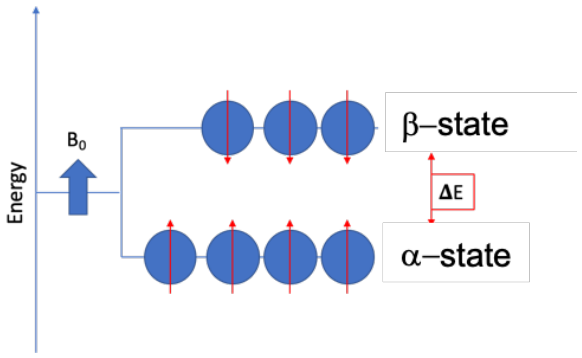

Figure 2.4. Different orientations of spin ½ nuclei under an external magnetic field.

There is a difference in energy levels possessed by nuclei in α and β state, with β state nuclei inherently possessing greater energy levels which enables them to oppose B_0. This is an important phenomenon, and is the primary reason NMR is considered an insensitive technique when compared to tools like mass spectrometry. It is only the small difference in nuclei between spin-states that contribute to the NMR signal.

The numbers of nuclei with magnetic moments aligned in the direction of the B_0 is described using the Boltzmann distribution.

$$\frac{+_{,}}{+_{-}} = \cdot^{\frac{/\Delta 1}{23}} = \cdot^{\frac{/456_7/9:}{23}}$$

Equation 2. The Boltzmann distribution(235)

Where the population difference between nuclei in α state (N_α) and β state (N_β) is calculated from the exponential of the difference in energy levels (which is Planck's constant (h) multiplied by γ, multiplied by B_0), divided the multiplication of Boltzmann's constant (k) and temperature in Kelvin (T). Boltzmann's constant describes the energy

imparted to a particle in joules at a given temperature (i.e. 1.3807×10^{-23} J/K) and Planck's constant describes the energy carried by a photon at a known frequency.

Therefore, at absolute zero (i.e. 0K), the energy imparted to the sample particles is zero. Under these circumstances, all of the particles would exist in the α–state, lacking the excitation energy required for transition to β-state.

Although advanced NMR techniques, such as dynamic nuclear polarisation NMR do use very low temperatures (e.g. 100 K), it is not currently possible to generate absolute zero temperatures. This generates a practical problem, ambient thermal energy, even at room temperature is sufficient to grant NMR active nuclei enough energy to align antiparallel to the external magnetic field. This results in a subdivision of the spin-half nuclei as defined using Boltzmann's equations.

The ambient sample temperature in our NMR experiments, which utilise a 14.1T 600 MHz spectrometer is actively controlled and set at 300K. The variable distribution of nuclear spin states can be therefore be determined based on characterisation of that particular nuclei's gyromagnetic ratio, which for the proton is 26.752×10^{7} rad/T^{-1} s^{-1} and for ^{13}C is 16.726×10^{7} rad/T^{-1} s^{-1} (236). If a sample contained 1 million protons in the α state, only 999396 would occupy the higher energy β- state leading to a net excess of 603 α-state nuclei which can be manipulated to derive the NMR signal. This small difference is in spin states is sufficient to confer a small net magnetisation vector to the NMR sample.

This is the reason proton NMR has a four-fold higher sensitivity than ^{13}C NMR, the lower gyromagnetic ration of ^{13}C under the same experimental conditions results in a net excess of 152 nuclei in α–state, a 4-fold decrease when compared to proton NMR.

2.1.4 Larmor Precession

Similar to a spinning gyroscope hung by a string, symbolising B_0, the angular momentum of these nuclei prevents them from aligning perfectly with the external magnetic field, instead forcing them to precess around B_0 (Figure 2.5). This rotation can be described by a sinewave.

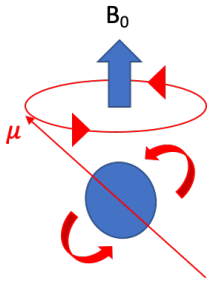

Figure 2.5. Nuclear precession around the external magnetic field

The frequency with which the nuclei precess around B_0 is known as the Larmor frequency, and is dependent on the strength of the magnetic field experienced by the nucleus and the individual atoms gyromagnetic ratio (Equation 2).

;=%<=

Equation 2. Larmor frequency (237,238)

2.2 The NMR Experiment

2.2.1 The pulse-acquire sequence

NMR experiments are controlled using pulse sequences which is illustrated in (Figure 2.6). The most basic experiment, a pulse-acquire sequence begins with a 90° pulse, a radio

frequency (RF) burst of controlled intensity and duration supplied in the x,y (or transverse) plane. The frequency and duration of this is optimised to result in a 90° rotation of the magnetisation vector from the z-axis into the transverse plane. Once transverse magnetisation has been created, the magnetisation vector will precess around the main axis of the external magnetic field (z-axis). This rotating magnetisation vector induces an electrical current in the receiver coil of the spectrometer. Because the RF pulse is transient, the nuclei relax back into equilibrium with the Boltzmann distribution, which releases the energy supplied to generate the α- to $\beta-$ state transition. The combination of cyclic rotation and gradual loss of transverse magnetisation results in free induction decay (FID) of the signal detected (D).

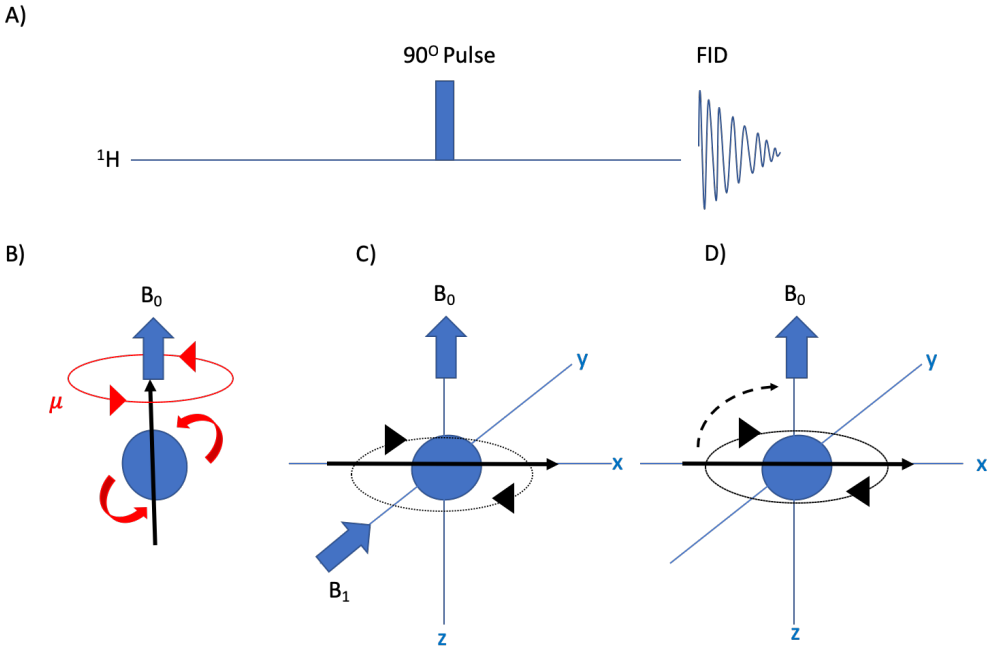

Figure 2.6. The NMR pulse-acquire sequence, and its effect on nuclear precession

When the sample is placed inside the NMR spectrometer, the magnetisation vectors align with the external magnetic field (B). A hard radio frequency pulse (A), with a defined power and variable duration results in a 90° rotation of the magnetisation onto the transverse plane where the nuclei begin to precess around B_0 (C). The nuclei relax back to equilibrium as defined using the Boltzmann distribution, which results in the decay of the signal detected (D). Detection of the precessing, relaxing nuclei results in the characteristic FID signal.

The FID acquired is then Fourier transformed to identify the underlying frequency within the decaying sine/cosine-waves.

In practice, the FID acquired in an experiment will be composed of all the different currents generated by all precessing nuclei. Some of these signals will be undesirable, such as the overwhelming contribution of water to total spectral intensity. Therefore, proton NMR pulse sequences contain multiple radio frequency pulse and period of relaxation in order to supress these signals. The most common NMR pulse sequence used in metabolomics is the NOESY-1D presat, which is illustrated in Figure 2.7.

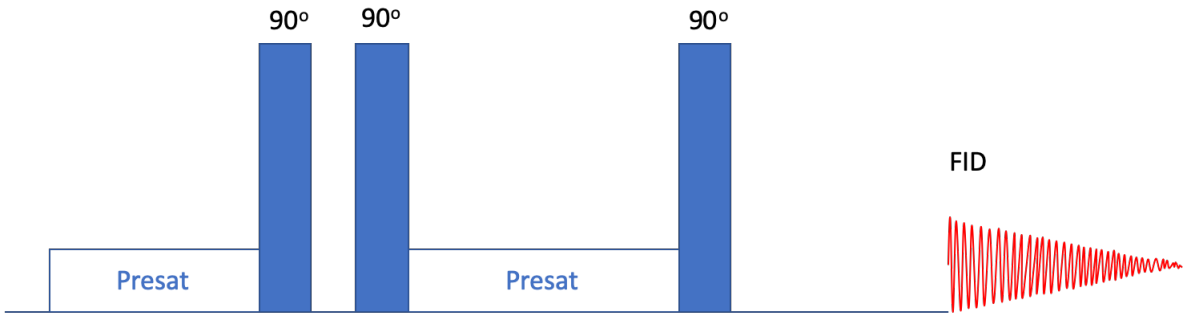

Figure 2.7. The NOESY Presaturation pulse sequence, adapted from(239).

The NOESY pulse sequence utilises a delay to allow for equilibration of sample magnetisation, and a continuous, low frequency RF pulse (i.e. the presat) is used to supress solvent signals. The successive 90° pulses excite solute protons and the intermediate period permits additional solvent suppression in our experiments(240).

2.2.2 Fourier Transformation and conversion to the ppm scale

Fourier transformation is used to resolve all the underlying frequencies which contribute to the acquired FID, i.e. it converts the time domain of the signal detected from decaying nuclear precession into a frequency spectrum.

However as described in Equation 2, the strength of the external magnetic field affects the frequency of Larmor-precession. Therefore, the frequencies resolved by Fourier transformation will also vary depending on the spectrometer used. NMR spectrometers are commonly described by the Larmor-precession they generate in protons, i.e. a 600 MHz spectrometer will result in a 600 MHz precession rate in bound hydrogen (or the proton will precess at a rate of 600,000,000 cycles per second).

To foster uniform reporting between different hardware, the frequencies reported are converted to convey chemical shift (>) (Equation 3) which is the frequency of Larmor precession (*v*) for a given nucleus relative to that of a supplied standard, such as 2,2-Dimethyl-2-silapentane-5-sulfonic acid (DSS) (v_{ref}).

$$>(@@A) = 10^{D}\frac{E - E_{GHI}}{E_{GHI}}$$

Equation 3. Standardisation of NMR signals from Hz to parts per million (ppm)(241)

2.2.3 The shielding effect of electrons

Through a process called shielding, the electrons (also spin half particles with a magnetic dipole) possessed by an atom influences the proportion of the external magnetic field experienced at the nucleus. Covalent bonds, formed by the sharing of electrons compose organic molecules. Therefore, within a given molecule, NMR sensitive nuclei with identical covalent interactions will experience the same level of shielding and therefore the same nuclear magnetic field. These nuclei will precess at the same frequency and will give rise to a single signal on the Fourier transformed spectrum.

Identical nuclei in different chemical environments, i.e. with non-identical covalent interactions will experience different degrees of the supplied magnetic field and undergo a

shift in frequency. This modulation of Larmor frequency by nuclear chemical environment is known as the chemical shift.

As shown in Figure 2.8, manifestation of chemical shift can be used to identify the presence of a compound.

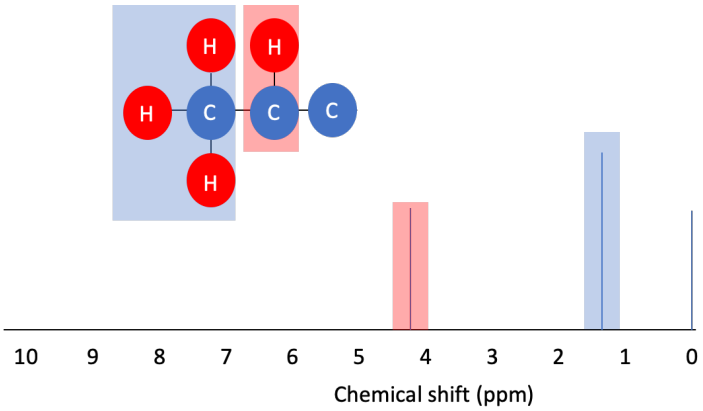

Figure 2.8. Two ^{1}H-NMR signals arising from the presence of lactate in a sample.

In this example, lactic acid may be detected following observation of peaks at two different chemical shifts, based on the two distinct chemical environments its protons exist in (i.e. the methyl group (blue) and the methine group (red).

2.2.4 Signal splitting and J-coupling

With the magnetic environment experienced by the nucleus modulating Larmor-frequency, an additional phenomenon is frequently observed in the Fourier transformed spectrum, which is the existence of signal splitting.

The resonant frequency of detected spin ½ nuclei is modulated to a small extent by spin state of neighbouring spin ½ nuclei connected by a chemical bond, all of which may exist in the α or β state. This splits the signal of the detected nuclei, with the number of split peaks a direct measure of the number of chemically equivalent spin ½ nuclei that are bound. By following the n+1 rule and using Pascals Triangle(242), the number of peaks and the ratio of signal intensities can be predicted (Figure 2.9).

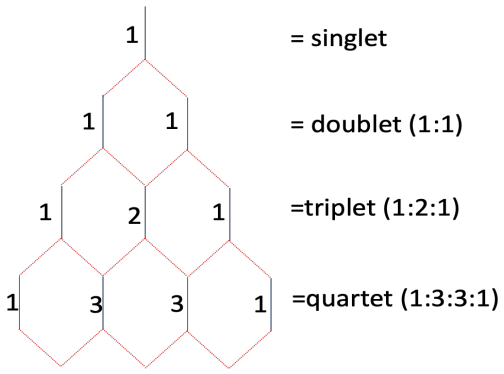

Figure 2.9. Pascals triangle and its prediction of split peak ratios

Signal splitting can be used to resolve chemical structure. We have deduced that each proton in the methyl group of lactates is chemically equivalent, and will give rise to a single peak. However, the proton in the methyl group may either be in the α or β state. This translates to two possible magnetic environments for each of proton in the methyl group. Since Larmor precession is modulated by magnetic environment, this splits the signal into 2 frequencies of approximately equal intensity (Figure 2.10).

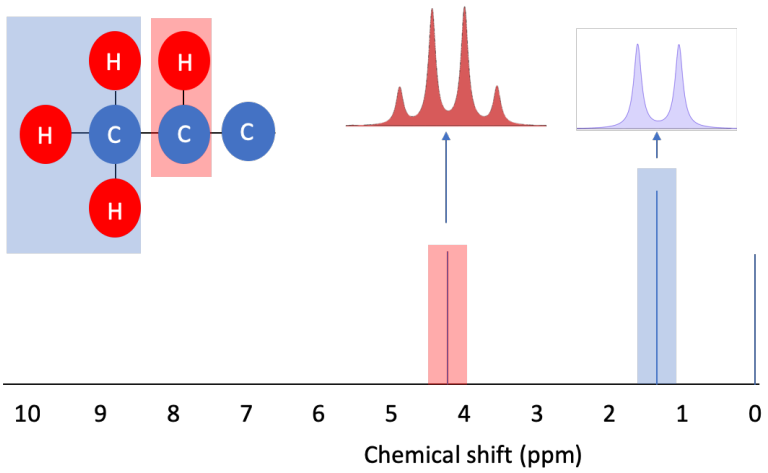

Figure. 2.10. Fine structure of the two lactate signals arising from J Coupling(243)

When the methyl group is studied (blue) the signal from each methyl group proton is split by that of the methine group proton (red), which may be in the α or β state. Using pascals triangle, the arising doublet has a ratio of 1:1 between split peaks. There are four possible alignments for the methyl group, i.e. all α, all β, 2α and1β, or 2β and 1α. Probability dictates a 37.5% chance of 2α and 1β, a 37.5% chance of 2β and 1α and a 12.5% chance of all nuclei being in α or β state. As such the methine group is split into a quartet, with relative intensities reflecting these probabilities (1:3:3:1).

NMR has the potential to be fully quantitative. This requires the use of a single standard compound such as DSS.

To quantify a given compound, the area under the curve of the reference compound signal is compared to the AUC of the signal of interest, while also considering how many protons contributed to the signal intensity.

Poor shimming (inhomogeneous magnetic fields) and inaccurate phase or baseline correction can deleteriously affect accurate quantification. To counteract these negative modulators, shimming was deemed acceptable at a linewidth of <1 Hz and phase and baseline correction was manually checked for each sample. Furthermore, the quantitative power of NMR relies on the nuclear spins of all molecules in the sample to be in near-equilibrium with $B_{0.}$ prior to deployment of a pulse sequence. To allow this, a sufficient relaxation time between transients must be present. In this thesis, the relaxation delay was set to $>5*T_{1.}$

To balance quantitate power with acceptable acquisition times, a relaxation time of 4 seconds, combined with 16 steady state scans was used. As this work focuses on NMR manipulation of small molecules, the incomplete T_1 relaxation will be similar for all molecules and quantification error is minimal.

2.3 Rationale for tracer studies in organ preservation research

While the ^{1}H-NMR experiments described above are invaluable for quantitative assessment of metabolic profiles in biological samples, this technique does not have the power to define the mechanisms governing any detected changes in metabolic profile (such as *de novo* metabolism, metabolite transport or cell lysis etc).

This is largely due to the targeting of protons as descriptors of molecular structure. Since ^{1}H is the dominant isotope of hydrogen in biological molecules- it is impossible to differentiate newly synthesised metabolites from those that were pre-existing in the biological system studied.

As stated previously, the carbon isotope most abundant in nature is ^{12}C, although around 1.07% of the carbon pool carries an extra neutron, i.e. ^{13}C. It follows that around 1% of carbon atoms composing the total pool of a given organic molecule in a sample

will have an extra neutron (i.e. will be ^{13}C rather than ^{12}C), Accordingly, the chance that natural label incorporation will lead to the inclusion of two carbon ^{13}C atoms in the same molecule will be around 1 in 10, 000 and the likelihood that a molecule contains three ^{13}C through natural label incorporation is atoms will be around 1in 1,000,000

The low natural abundance of ^{13}C indicates that if a biological system is exposed to nutrients artificially enriched with ^{13}C, one could chart ongoing metabolic processes by detecting which downstream metabolites are enriched in ^{13}C s above the level expected from natural label incorporation.

The extra neutron in each ^{13}C permits discrimination of ^{13}C enriched metabolites by their increased mass (using mass spectrometry) or by the resulting ½ integer nuclear spin through NMR spectroscopy.

1D ^{13}C NMR experiments may be used to detect ^{13}C labelled metabolites in a manner similar to proton NMR spectroscopy. However- due to the 4-fold smaller gyromagnetic ration of ^{13}C when compared to ^{1}H, there is a 32-fold decrease in sensitivity when measuring ^{13}C when compared to the ^{1}H nucleus (244).

NMR is considered an insensitive analysis compared to mass spectrometry. This insensitivity is likely to be compounded in this thesis due to the presumably lower label incorporation in downstream metabolites resulting from the hypothermic nature of the

organ storage environment, which is known to supress ongoing metabolic processes(173). Therefore, Heteronuclear **S**ingle **Q**uantum **C**oherence (HSQC) spectroscopy was utilised to overcome the inherent insensitivity of ^{13}C NMR.

2.3.1 Overview of the HSCQ experiment

The use of HSQC spectroscopy helps to overcome the limitation relating to low ^{13}C NMR sensitivity, by selective excitation of protons bound to ^{13}C, and transferring magnetisation to ^{13}C and back, thereby detecting proton magnetisation. In this manner, the enhanced detectability of protons by NMR in manipulated, and indirectly allows detection of bound ^{13}C nuclei (Figure 2.11). In practice, the HSQC pulse sequence is deployed multiple times per sample, with incrementally increasing delays (t1) changing the detected signal intensity. Recording the FIDs acquired allows construction of a sinewave between them (Figure 2.12), Fourier transformed can be applied across the FIDs collected, granting indirect assessment of ^{13}C chemical shift. Together, plotting the direct and indirect dimensions gives rise to the HSQC spectrum (Figure 2.13).

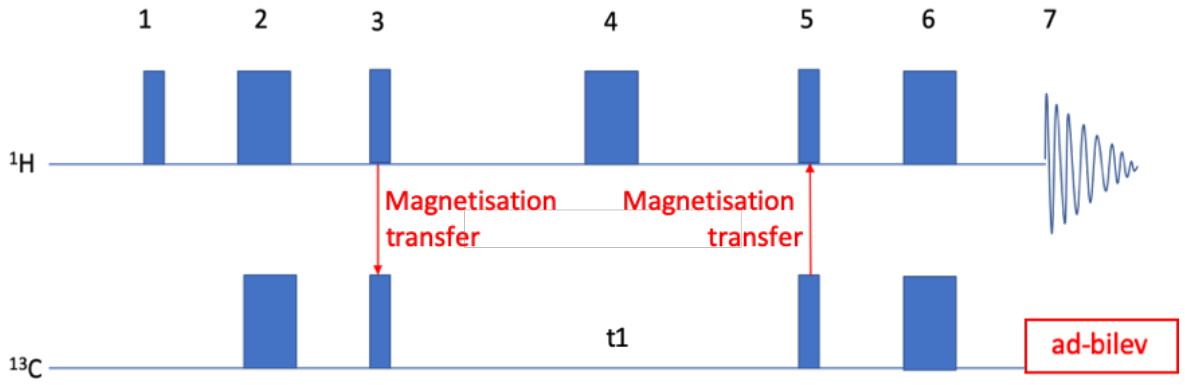

Figure 2.11. A breakdown of the HSQC pulse sequence.

The 1st 90° pulse on the proton channel (Point 1) results in transverse magnetisation, causing in phase (i.e. along the x-axis) magnetisation vectors. Transfer of magnetisation requires antiphase spin-spin coupling (i.e. one nucleus orientated along the x axis the other along the y axis(216) Following a delay enabling evolution of ^{1}H-^{13}C coupling constants, 180° pulses on both ^{1}H and ^{13}C channels (point 2) results in a refocussing of the chemical shift of both nuclei. The 90° pulses (point 3) transfers magnetisation from ^{1}H to ^{13}C. This sequence is known as the INEPT block, in which in insensitive nuclei (i.e. ^{13}C) are enhanced by polarisation transfer from connected protons. Following magnetisation transfer, the population difference in ^{13}C α and β state nuclei is now that which existed in the bound ^{1}H nuclei, ergo the reduced sensitivity of ^{13}C NMR caused by its relatively lower gyromagnetic ratio has been countered. The delay t1 is varied, while proton decoupling is applied (point 4) When magnetisation is transferred back to the protons using the by inverting the INEPT block, (i.e. the reverse INEPT block (Point 5), it is only ^{13}C bound protons that generate the FID obtained during spectral acquisition, as signals that would arise from precessing ^{13}C nuclei are decoupled using the adiabatic bilevel decoupling. This forces ^{13}C nuclei to rapidly switch between α and β state, such as the net spin is 0 and hence ^{13}C does not continue to contribute to the acquired proton directly, or indirectly through coupling(245).

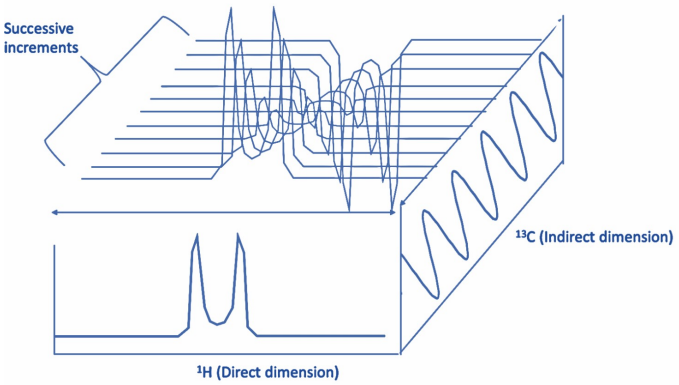

Figure 2.12.The dimensions of the HSQC spectrum

The direct dimension contains the Fourier transformed proton spectrum. The indirect dimension consist of the sine wave generated by incremental changes in t1 and resulting fluctuation in signal.

In the plotted HSQC spectrum, the proton dimension is plotted on the x axis which is informative of proton chemical shift. The indirect dimension is plotted on the y axis, and is formed from the fourier transformation of ^{13}C peak intensity at fixed timepoints (which varies because of variable T_1 delays periods employed(246). This has the effect of decluttering the peaks on the ^{1}H-spectrum as they are dispersed vertically along the y axis(247)

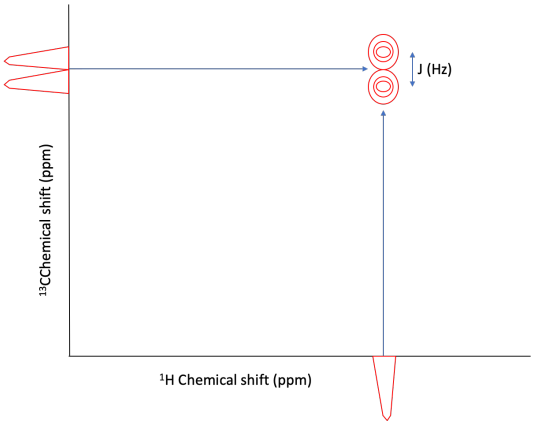

Figure 2.13. Overview of an HSQC plot for a single lactic acid signal

The third dimension of the HSQC spectrum is the Z-axis, which is a measure of spectral intensity. Similar to an ordinance survey map this is illustrated with contour rings to depict height While heteronuclear splitting (i.e. H-C) are decoupled, homonuclear splitting (^{13}C-^{13}C are left intact and appear in the indirect dimension (i.e. along the y-axis The magnitude of $1J^{13}C,^{13}C$ coupling provide additional information about the chemical environment of each ^{13}C nucleus in a molecule and can be used to resolve isotopic distribution of ^{13}C which is informative of the metabolic pathways that synthesised the molecule of interest(217).

2.3.2 Paired NMR and mass spectrometry analysis

Metabolic isotopologues are variations of the same metabolite, that have enrichment of a supplied label in different locations of that molecule. Determination of isotopologue structure of the molecule is an inference of the metabolic pathways that produced it(217), but this structure is not always discernible using a given analytical technique in isolation.

Considering lactic acid, which is composed of three carbons, there are different isotopic combinations which may make up the isotopologue pool. In the below example, 0 refers to a carbon that is ^{12}C, and 1 refers to a carbon that contains an extra neutron, i.e. is ^{13}C. For lactate, there are 8 possible combinations of ^{13}C (denoted '1') and ^{12}C (denoted 0) i.e. (000, 111, 011, 110, 100, 010, 001, 101) but these are not all discernible using HSQC or MID analysis independently (Figure 2.14). Mass spectrometry can provide quantitative analysis, and can determine the mass isotopic distribution of given metabolites. For example, lactate has 4 isotopomers (M0, M1, M2 or M3), referencing the numbers of carbons that are enriched above natural abundance. However, unlike liquid chromatography mass spectrometers, the mass spectrometry apparatus we have access to (i.e. a gas chromatography mass spectrometer (GCMS) is ill suited to the use of fragmentation patterns to determine positional labelling. This difficulty arises due to the requirement for derivatisation agents which are also fragmented along with the metabolite of interest. As such, in this work we could not differentiate between 011, 101 or 110 label incorporation using the mass spectrometry facilities available.

Due the INEPT sequence which uses the usage of the *I* nucleus as a vehicle for magnetization transfer, 2D ^{1}H-^{13}C NMR spectroscopic analysis is capable of determining the ^{13}C incorporation where the carbon of interest in linked to a proton. Analysis of carbon-carbon signal splitting of carbon 2 can be used to assess label incorporation in carbon 1. In this manner, multiplet analysis of the HSQC has greater topological resolution than MS, however the technique cannot differentiate between 001 and 101, as carbon 2 is unlabelled.

Furthermore, NMR has limitations in terms of measuring U-^{12}C abundance. Whether a proton is bound to ^{12}C or ^{13}C can be determined using 1D/2D ^{1}H NMR spectroscopy(248–

250), however this approach is limited to a small number of metabolites due to spectral overlap.

HSQC spectra are less congested however only contain signals of ^{13}C bound to a proton. Using the example of C(2) of lactate, it is not possible with HSQC spectroscopy to differentiate between an unlabelled molecule of lactate (000), which consists of ^{13}C natural abundance at C(2) and a molecule of lactate which has been labelled over and above natural abundance in position C(2) (010). Mass spectrometry however, can identify the M+2 presence in this isotopologue, rather than M+1 that would occur if the label incorporation was 001. By combining these analytical tools, it is possible to acquire a quantitative, model free assessment of isotopic distribution for a given metabolite (Figure 2.14).

This function is provided by MetaboLab, a software developed and maintained by Dr. Christian Ludwig(218) and reported in the paper *Combined Analysis of NMR and MS Spectra* (CANMS)(219). The power of NMR to resolve the position of ^{13}C nuclei within a molecule can depend on acquisition of spectra with high enough resolution to define split peaks. In appendix 1, a development is described which scales J in coupled ^{13}C nuclei, allowing their detection at lower resolution. This enables high throughput tracing of metabolism using NMR.

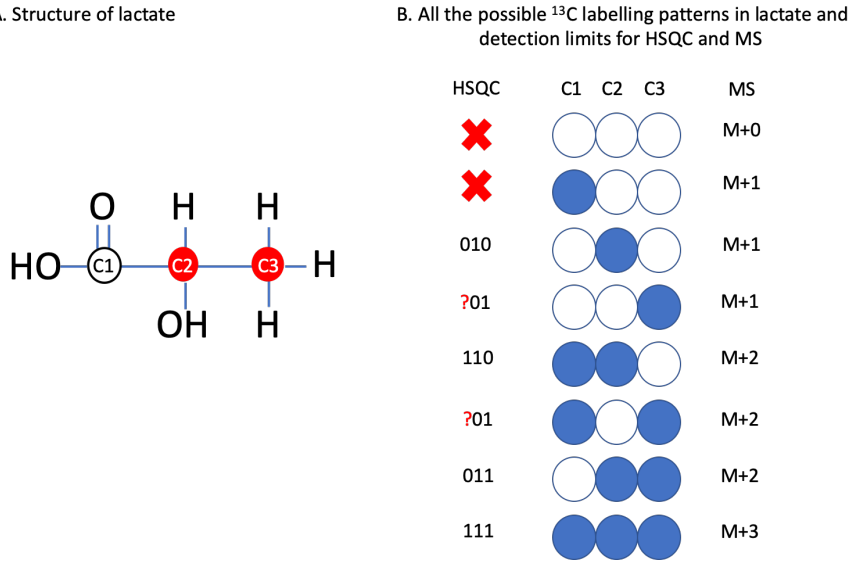

Figure 2.14. Different label resolution from HSQC and MID analysis

Lactate is three-carbon molecule (A), however only two of these carbons (i.e. carbons 2 and 3- coloured red) are bound to a proton. (B) Example of the different levels of resolution permitted by NMR and MS analysis. HSQC analysis can detect 110 labelling through analysis of carbon 2 signal splitting by J coupling with C1. NMR can detect 001 labelling, but cannot differentiate between this and 101 as C2 is not labelled. Paired analysis with MS, which can determine percentages of M1 and M2 resolves this uncertainty.

2.3.3 Chapter summary

In summary, the NMR spectrometer functions to orient the magnetic moment of specific nuclei in a uniform direction, and then manipulate that orientation so that the intrinsically unique precession rate of a given nucleus in a given chemical environment generates a current of measurable frequency. Through artificial introduction of nutrients composed of NMR active nuclei which are not commonly found in nature, NMR can be used to identify metabolites of these nutrients by their chemical shift, and also the location of the supplied NMR active nuclei in that molecule through analysis of peak splitting. This information is informative of the metabolic pathways through which the metabolite was produced(217), and is applied in this thesis to characterise modulation of cellular metabolism by different extracellular environments.

3 Methods and method development

This chapter details the general methods used throughout this thesis. Modifications or additions to these methods are charted in the relevant chapters.

3.1 *In vitro* methods

As alluded to in Chapter 1, current technical barriers prevent high throughput *in vitro* control over the level of fluid flow and oxygen availability. These two interacting stimuli are of interest in organ preservation research. Recognising the absence of suitable tools, the *in vitro* methods used throughout this thesis were conceived and developed by me during my PhD period. In this chapter, the development of novel hypoxia chamber filling circuits is described and validated. These allow high throughput control of *in vitro* oxygen environments in a manner compatible with the smartphone assisted fluid shear stress generation, which is described in Chapters 3 and 4.

3.1.1 Cell culture

The human renal proximal tubule epithelial cell line RPTEC/TERT1 (Evercyte GmbH, Austria) was sub-cultured in line with supplier specifications, with the exception of the usage of a custom media formulation.

In brief, cells were cultured in 75cm^2 tissue future flasks (Corning, UK, Cat: 430641U) until 90% confluent and split at 1:2 ratios following trypsinisation. The media used consisted of DMEM/Ham's F12 (1:1) media (supplemented with 1x Insulin transferrin selenium solution (Cat: I314600), 1% Penicillin Streptomycin (Cat: P0781), 36ng/ml Hydrocortisone (Cat:

H0888) and 40ng/ml Epithelial growth factor (Cat: SRP3027) (all procured from SigmaAldrich, UK).

For tracer studies, glucose and glutamine free DMEM/Hams F12 (1:1) (Zen-Bio, USA Cat: DMEMf12-NGG002) was supplemented as described above, with the addition of any combination of the following isotopically labelled substrates: 17.5mM isotopically enriched glucose [1,2-^{13}C] D-Glucose (Cat: 453188, SigmaAldrich), [U-^{13}C] glucose (Cambridge isotopes, UK, Cat: CLM-1396) and/or 2mM [U-^{13}C,U-^{15}N] L-Glutamine (SigmaAldrich, Cat: 607983). Exact media supplementation with isotopically labelled tracers is defined in the relevant chapters.

Cell counts and logging of the population doubling level was facilitated through smartphone applications developed during this PhD period (namely Autocount and PDL calculator respectively(249) (Figure 3.1). For all experiments, cells were seeded at a density of $4x10^4/cm^2$ at PDL ranging between 25.0 and 53.7, which is far below the 90 population doublings the RPTEC/TERT1 cell line is reported to maintain its phenotype(155). In all cases, experiments were performed when cells demonstrated dome formation and/or cobblestone morphology, which generally took between 7-10 days.

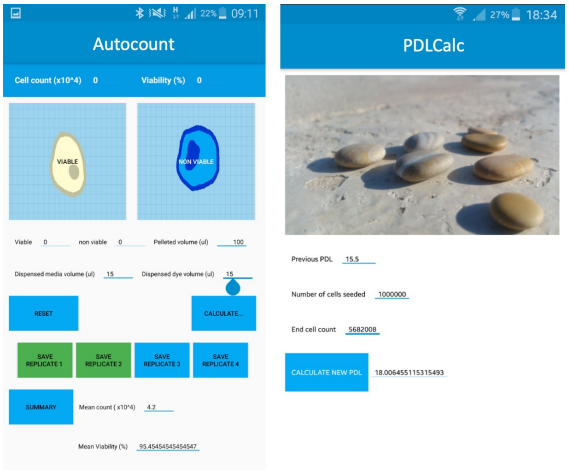

Figure 3.1. Cell culture apps developed during this PhD: *Autocount* and *PDLCalc*

Two smartphone tools developed during my PhD. Autocount expedites cell counts, replacing conventional manual counters and also automatically performs assessment of percentage viability and total cell counts. PDLCalc is a simple calculator that determines new population doubling level after a cell count has been performed.

3.1.2 ShearFAST assisted fluid shear stress experiments.

The use of cell rockers to generate defined degrees of FSS has been introduced in Chapter 1 and is discussed further in Chapter 4. Below is the method pertaining to how ShearFAST, a smartphone application developed during the course of this PhD was used to enable high throughput simulation of physiological degrees of fluid shear stress *in vitro*.

The ShearFAST application was installed on a smartphone (Samsung Galaxy Note 4). The smartphone was placed on the rocking platform of a cell rocker supplied by VWR (Cat: 444-0146) alongside a spirit level. The platform was set to a rotation of 0° using the spirit level (i.e. the platform was horizontal) and ShearFAST angle measures were zeroed at this rotation by pressing ‘Calibrate’ in the Angle tool menu.

Following this, the rocking platform was extended to its maximum rotation and the continuous measures of this angle were recorded by ShearFAST.

ShearFAST assessment of rocking frequency was performed after automatic calculation of mean maximal rocking angle. To perform rocking frequency assessment, the cell rocker

was switched on and allowed to rock freely for 10 seconds. ShearFAST recorded the changing angles and the time at which they changed, allowing in-app plotting of a sinewave. Using a built-in frequency modelling tool, the acquired sinewave was visually compared to overlaid sinewaves of the acquired intensity but user-defined frequency.

As shown in Chapter 4, ShearFAST analysis enables accurate quantification of rocking angle and speed. With these rocking parameters now known, the user selects the dimensions of their culture ware from a drop-down menu in the ShearFAST formula tool, and manually inputs the volume and viscosity of the solution they intend to use in each well. Using a built-in calculator, this determines the shear stress arising in the centre of the cultureware using a well-established mathematical model of shear stress induction using cell rockers(168).

3.1.2.1 Measurement of fluid viscosity

The rocking model requires knowledge of fluid viscosity in order to determine the shear stress imparted onto the cell monolayers. The viscosity of cell culture media has been reported to be equal to that of water (i.e. 0.001Pa.s)(168). However, the viscosity of preservation fluids at the clinically relevant range of 2-8°C has not been reported.

The viscosity of UWMPS (Organ Recovery Systems, USA) and an in-house variant of the UWMPS with the HES colloid replaced by 30g/L, 35kDa Polyethylene glycol (Sigma Aldrich, UK) was analysed on a Discovery Hybrid Systems Rheometer (40mm diameter, 4° cone and plate geometry). Fluid Rheology was ascertained utilising a shear ramp over a shear rate of 0.1-400 s^{-1}. Measurements were performed in triplicate and averaged to yield a measure of the viscosity of these two fluids (Figure 3.2).

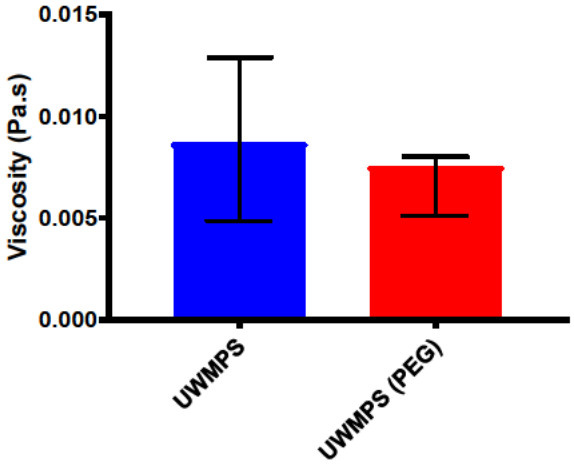

Figure 3.2. The viscosity of chilled preservation solutions

Comparing the viscosities of commercially available UWMPS (0.0087 Pa.s (range 0.0048-0.012 Pa.s) and an in-house variant (0.0075 Pa.s (range 0.0051-0.0080 Pa.s) which substitutes 30g/L of 35kDa Polyethylene glycol for the Hydroxyethyl Starch normally found in UWMPS.

Measurement of the storage fluid viscosity of was possible because of the expertise of Dr. Federico Alberini, who performed this analysis.

3.1.3 Measures of cellular viability, damage and metabolism

3.1.3.1 The Sulphorhodamine B assay

In this thesis, the SRB assay was performed by removing cellular supernatant and incubating the wells in 240μl/cm^2 media containing 4% Trichloroacetic acid. After this the Trichloroacetic acid was discarded and monolayers washed with deionised water. The plates were left to dry overnight, and then submerged in Sulphorhodamine dye in 1% acetic acid for 10 minutes at room temperature. Excess dye was collated for use in future experiments, and the monolayers washed four times with 1% acetic acid to remove non-bound dye. The plates were left to dry again, after which Tris (pH8.8) was added each well at volumes of 1.56μl/mm^2 of growth area. The retained dye was dissolved by shaking the

plate, and 50μl of this added to a 96 well plate for colorimetric detection. Absorbance was read at 510nm on a plate reader.

3.1.3.2 The Lactate dehydrogenase (LDH) assay

Assessment of supernatal LDH concentrations was performed using a commercially available kit (Cat MAK066, Sigma Aldrich, UK).

In brief, 50μl of sample was combined with 50μl of a reagent mixture containing a NAD and a propriety reagent that changes colour in the presence of NADH. The absorbance of light by each sample is modulated by colour changes which is deemed to be catalysed by the level of LDH in the sample provided. Therefore, higher levels of light absorbance are deemed to be reflective of increased concentrations of LDH in the sample. Quantification of LDH was performed using a standard curve and in line with the manufacturer instructions.

3.1.3.3 Extraction of cellular metabolites

For metabolic analysis, cell supernatant was removed and cell monolayers were washed in chilled 0.9% NaCl solution and scraped into methanol (-80°C). The suspension was collected and mixed with deionised water (4°C) and chloroform (-20°C) in a 1:1:1 ratio. The sample was vigorously agitated at 4°C for 10 minutes then centrifuged (1300g, 15 minutes, 4°C) to separate polar, non-polar and protein fractions. Polar fractions were dried using a SpeedVac concentrator (SPD1010), prior to preparation for NMR or MS analysis.

3.1.4 Control of *in vitro* oxygen tensions.

Two methods were used to control the oxygen available to the cultured cells. In cases where severe hypoxia was to be simulated under physiological temperatures, as in

Chapter 7, Whitley H35 hypoxia stations were used (Figure 1.12). These maintained physiological temperature (37°C) at oxygen concentrations of <0.3%.

However, hypoxia stations are incompatible with simultaneous instigation of hypothermia, and parallel assessment of multiple oxygen tensions, or simulation of fluid shear stress using a cell rocker. For these cases, a novel hypoxia chamber filling circuit was designed and utilised. Validation of this approach, and later whole organ oxygenation experiments required the deployment of fibre optic oxygen sensors.

3.1.5 Oxygen sensing *in vitro* and *ex vivo*

3.1.5.1 Needle type oxygen sensors

A needle type fibre optic oxygen sensor (Cat: 200000785, World precision instruments) was obtained and attached to an OxyMicro transmitter (Cat: OXY-MICRO-AOT, World Precision instruments, UK) calibrated as per the manufacturer's instructions. In brief, the 0% oxygen calibration control constituted of a vigorously mixed 1% sodium sulphite solution (Sigma Aldrich, UK) and the 100% oxygen control set as deionized water at 4 °C which had been left to equilibrate with the atmosphere overnight. The measurement software includes a temperature compensation, which was either measured manually or inferred from the ambient room temperature.

The 0% control was validated against nitrogen saturated waster, and the 100% control was validated against more samples of UWMPS and water that had been left to equilibrate with the ambient temperature. Data for the needle type sensors is reported as a relative oxygen concentration (ROC%), i.e. relative a 50% ROC would equal half the oxygen dissolved the 100% calibrator, which was chilled deionised water. These sensors were used in early iterations of a hypoxia chamber filling circuit (described later) and in the first series of whole organ experiments investigating the effects of perfusate oxygenation.

3.1.5.2 Flow-through oxygen sensing cells

Two pre-calibrated fibre optic transmitters (Cat: 300000007) with disposable flow-through cells (Cat: 200001613) and sensitive spots (Cat: 200000023) were obtained (all from PreSens Precision Sensing, Germany)

These allowed measurements of the oxygen content of the gas exiting hypoxia chambers in the cell line studies, and the level of dissolved oxygen in preservation fluid being passed through them in whole organ models of HMP. These function in a similar way to the needle type oxygen sensor, except the updated software automatically converts the ROC% to a standalone concentration. In this thesis, the Pascal (hPa and kPa) were selected as a units to allow for comparisons to the oxygen measurements for the group's clinical study ([13]Champion) which obtains readouts of HMP perfusate oxygen concentrations (kPa) using a blood gas analyser (Cobas b221, Roche Diagnostics Limited) (Figure 3.9).

3.1.5.3 Oxygen sensitive spot

A single *in vitro* experiment used an oxygen sensitive spot to determine real time rates of equilibration between the atmosphere within a hypoxia chamber during hyperopic filling and a sample stored within the chamber. This experiment was performed only once due to the damaging physical strain it exerted on fibreoptic cables required for sensor function.

3.2 Method Development

3.2.1 Controlling oxygen availability *in vitro* with custom hypoxia chamber filling circuits

Hypoxia chambers (Billups-Rothenberg, California) (Figure 1.13) are small, airtight units which are designed to be purged with nitrogen gas, thereby replacing the atmosphere within the chamber with 100% nitrogen. The manufacturers of the hypoxia chambers

utilised recommend that the chamber is purged with 100% nitrogen gas at a flow rate of 20L/min for 5 minutes in order to generate an anoxic environment(251).Throughout chamber filling, the supplied gas mixes with the atmosphere in the chamber and the increase in pressure results in expulsion of gas through the outflow port and incremental equilibrium of the gas mixture in the chamber with that of the supplied gas.

3.2.2 Generating hypoxic atmospheres

The oxygen concentration of the chamber outflow is measurable using a fibre optic oxygen sensor. When the hypoxia chamber filling circuit was first incepted, it utilised a needle type fibre optic oxygen sensor, which indirectly monitored the oxygen composition of the chamber outflow based on its capacity to deoxygenate a water reservoir distil from the chamber outflow (Figure 3.3).

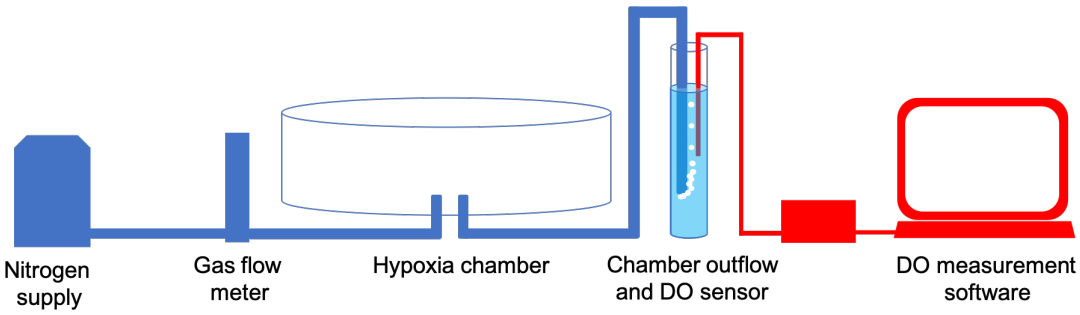

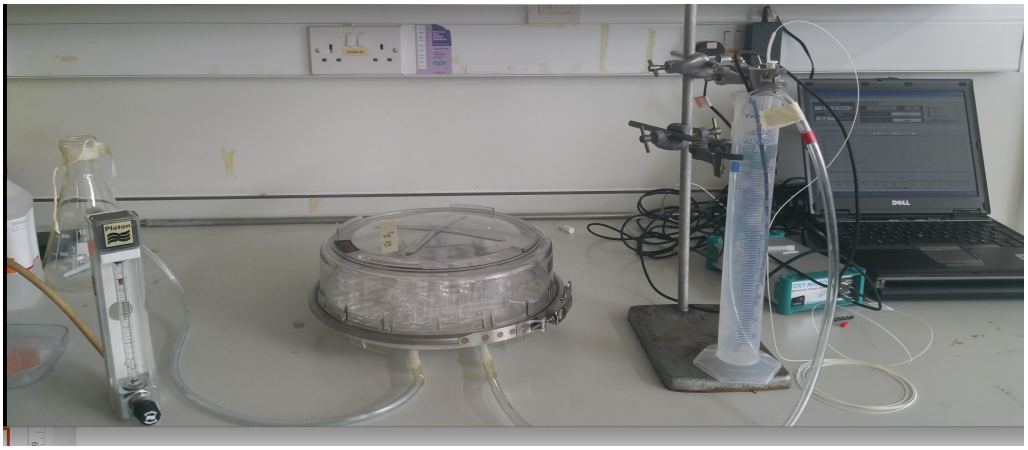

Figure 3.3. Hypoxia chamber filling circuit design 1.

Monitoring of the dissolved oxygen (DO) in the fluid reservoir, located downstream from the hypoxia chamber permits a time-delayed measure of the point at which atmosphere within the chamber is devoid of oxygen.

A nitrogen cylinder was set to supply 100% nitrogen at the maximum flowrate detectable by the flow meter utilised (i.e. 600ml/min) (Platon, France).

Continuous oxygen measurements of in the water reservoir were taken using a submerged needle type oxygen sensor.

Once the readings plateaued at 0%, it was assumed that addition of further nitrogen had no effect on the partial pressure of N_2 within the chamber and the oxygen had been completely removed, i.e. cells stored in that chamber would experience severe hypoxia/anoxia. As shown in Figure 3.4, the time taken for this to occur was between 0.5-1 hours of chamber filling.

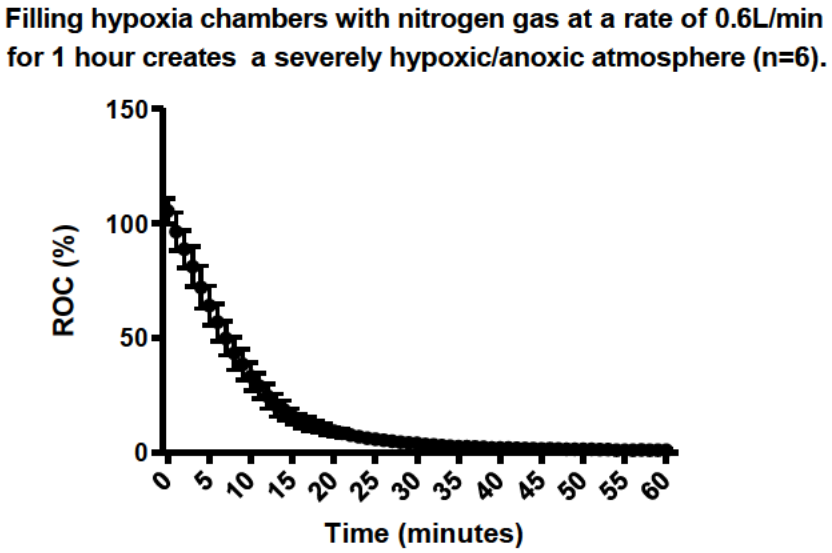

Figure 3.4. Monitoring chamber oxygen depletion in Hypoxia chamber filling circuit 1

Upon opening of the nitrogen supply, the oxygen concentration of the water in the measuring cylinder was around 100% that of the calibration control (i.e. Deionised water). Purging the chambers with 600ml/min of nitrogen gas resulted in removal of the dissolved oxygen within 40 minutes.

This set up is scalable, only requiring multiple chambers with their own flow meter arranged in a parallel circuit (Figure 3.5).

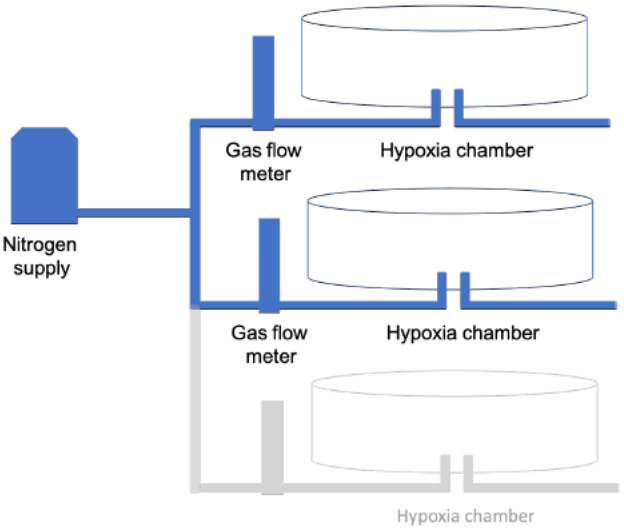

Figure 3.5. Filling of multiple chambers with a parallel circuit

As documented in Chapter 5, the capacity to generate identical chambers is useful as it allows simultaneous testing of the presence and absence of fluid shear stress using the ShearFAST assisted rocking model.

An experiment was set up to assess the sample oxygen content after extended hypothermic storage (i.e. 18 hours) in nitrogen filled hypoxia chambers, or left exposed to the atmosphere. As illustrated in Figure 3.6, the ROC of exposed plates was that of atmospheric oxygen, and with the exception of one poorly sealed chamber (ROC of 16%), the method above was found to be an effective means to generate anoxia *in vitro*, assuming the chambers remain sealed.

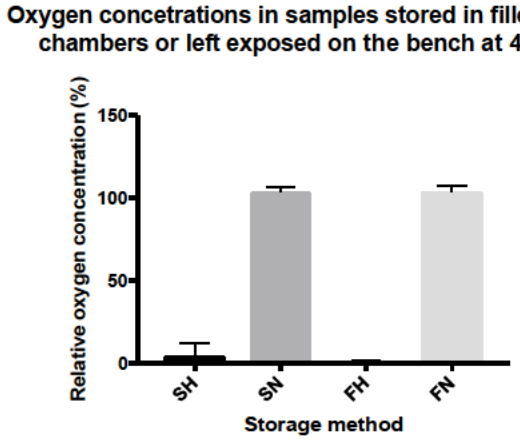

Figure 3.6. Validating simulation of hypoxic storage

The sealed hypoxia chambers (SH and FH) do retain the hypoxic condition generated during chamber filling for at least 18 hours. Poor sealing of one SH chamber (end point ROC of 16%) elevated mean endpoint ROC to 4%.

3.2.3 Programming of custom oxygen atmospheres

Chapter 6 shows that the porcine slaughterhouse model of HMP results in borderline anoxia of perfusate oxygen at around 8 hours of perfusion (Figure 6.5). Data from our clinical study ([13]Champion) may suggest clinical HMP does not confer this level of oxygen

depletion (Figure 8.5). Considering the current clinical interest in the role of perfusate oxygenation, it was apparent a means to subject cells cultured *in vitro* to user defined degrees of oxygen was required.

The first iteration of the modified circuit involved inclusion of an oxygen cylinder (Carbogen, 95% oxygen, 5% CO_2) and flow meter to the nitrogen line. By varying the flow rates of oxygen and nitrogen, the composition of the gas entering the hypoxia chamber became modifiable. Ergo, the resulting plateau in oxygen measurements when the chamber is filled became programable.

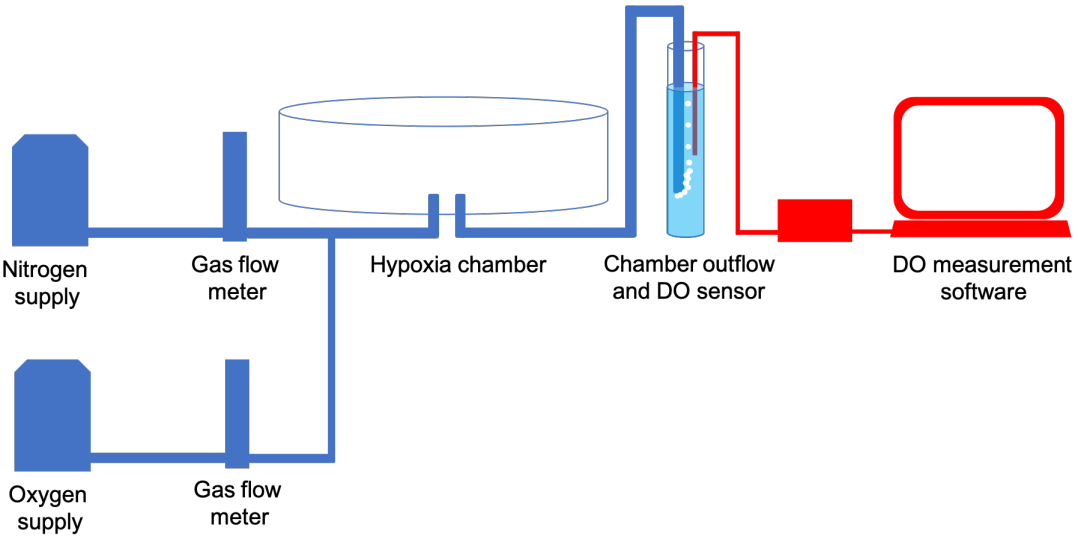

Figure 3.7. Hypoxia chamber filling circuit 2.

Inclusion of a parallel oxygen supply allows for a modification of the oxygen environment entering the chamber.

Using this circuit, it was found that flushing the chambers with 560ml/min 100% nitrogen and 40ml/min 95% oxygen was resulting in a ROC% of around 40% in the water reservoir (Figure 3.8).

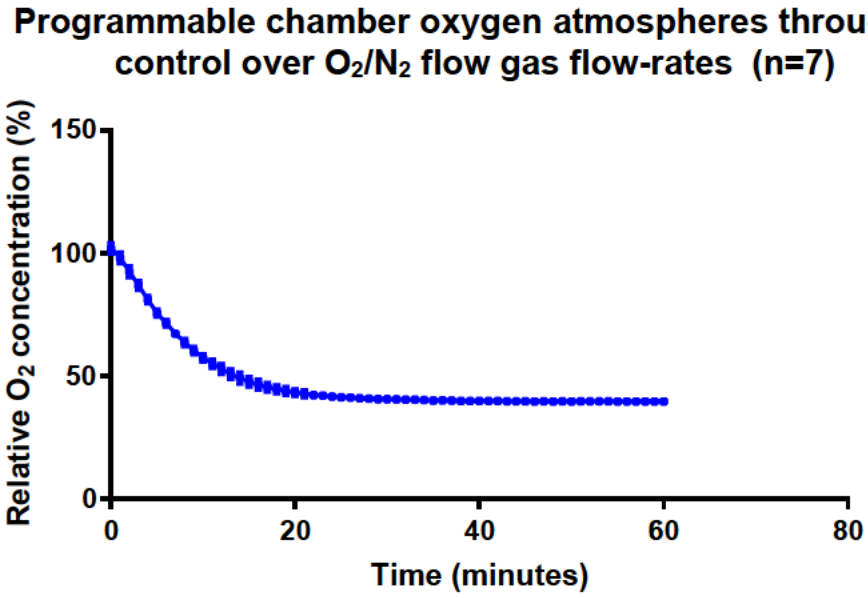

Figure 3.8. Endpoint chamber atmosphere modulated by inclusion of oxygen line

When the Oxygen flow rate was lowered to 560ml/min and oxygen added at a flow rate of 40ml/min, the chamber outflow plateaued at a ROC% of 40.53 ± 1.24% by 30 minutes of chamber filling. The endpoint ROC in the chamber atmosphere was 39.60 ± 1.03% at 1 hour.

To illustrate a time course of oxygen depletion, of 2ml of UW MPS was added to a 6 well plate and placed in the chamber. The chambers were filled with the gas blend depicted in Figure 3.9 and the chambers were opened either immediately after filling, or moved to a cold room and opened and at 1,2 and 18 hours after initiation of chamber filling. The needle type sensor was placed directly in the UWMPS fluid immediately after chamber after opening and temperature corrected oxygen measurements taken.

These are plotted in red in Figure 3.9 with the rate of oxygen depletion in kPa in human kidneys undergoing HMP detected by a blood gas analyser plotted in blue.

Absolute comparison of these two systems is ill advised as different method were used to assess oxygen concentration. However, if it is assumed that UWMPS used in the clinical and laboratory environments equilibrated to the same starting oxygen tension, there is the

potential for economical *in vitro* simulation of *ex vivo* oxygen depletion using the method described.

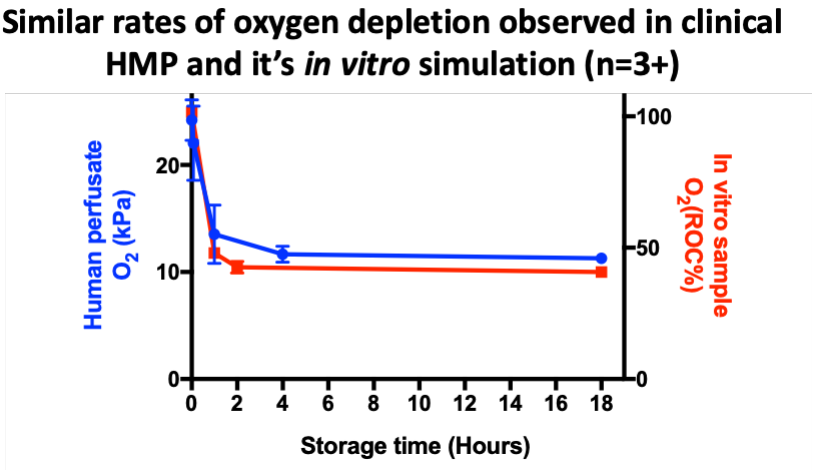

Figure 3.9. Fine control of sample oxygen availability using filling circuit 2.

During clinical HMP (blue), the starting perfusate oxygen concentration is 24.20 ± 1.90kPa (n=9). This falls to 13.53 ± 2.73kPa within 1 hour of perfusion (n=10) and appears to plateau at 11.29 ± 0.40kPA by 18 hours of perfusion (n=8). Therefore, the oxygen content of the circulating perfusate has fallen to 55.10% of its starting concentration by 1 hour of perfusion and plateaus at 46.65% by 18 hours or perfusion. At 1 hour since initiation of chamber filling the dissolved oxygen in UWMPS samples within the chamber was found to be 47.96 ± 1.71% of its starting concentration (n=3), and this fell to 40.73 ± 0.68% at 18 hours of cold storage (n=3).

3.2.3.1 Programming hyperoxia

Upon acquisition of flow through oxygen sensors, which negate the requirement for the water reservoir for needle type oxygen sensors, the filling circuit was modified again to allow for simultaneous monitoring of two chambers (Figure 3.10), or of chamber outflow and how this compares to the oxygen level of samples within the chamber (Figure 3.11 and Figure 3.12).

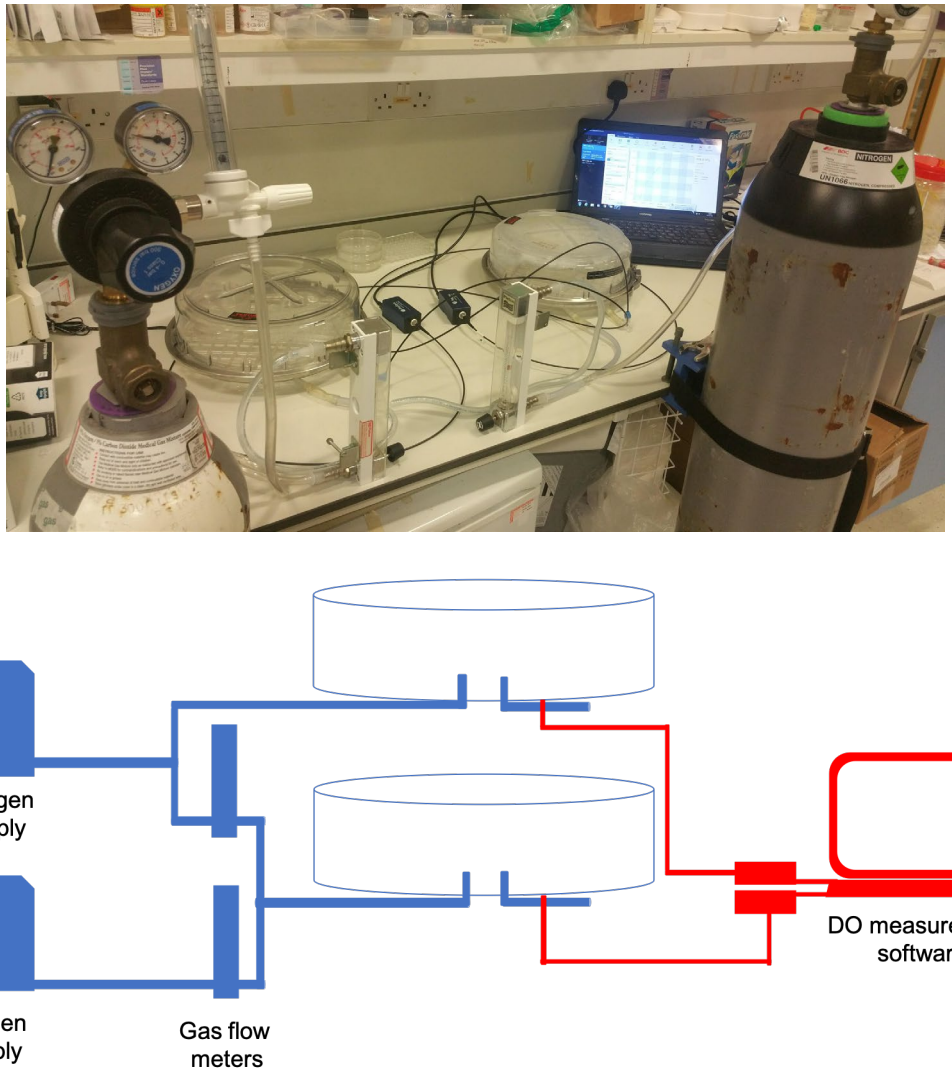

Figure 3.10. The final iteration of the hypoxia chamber filling circuit.

This set-up permits simultaneous generation of anoxia and hyperoxic chambers. An intermediate oxygen condition is generated by leaving plate outside of the chamber while filling which as described later, simulates continuous fluid aeration.

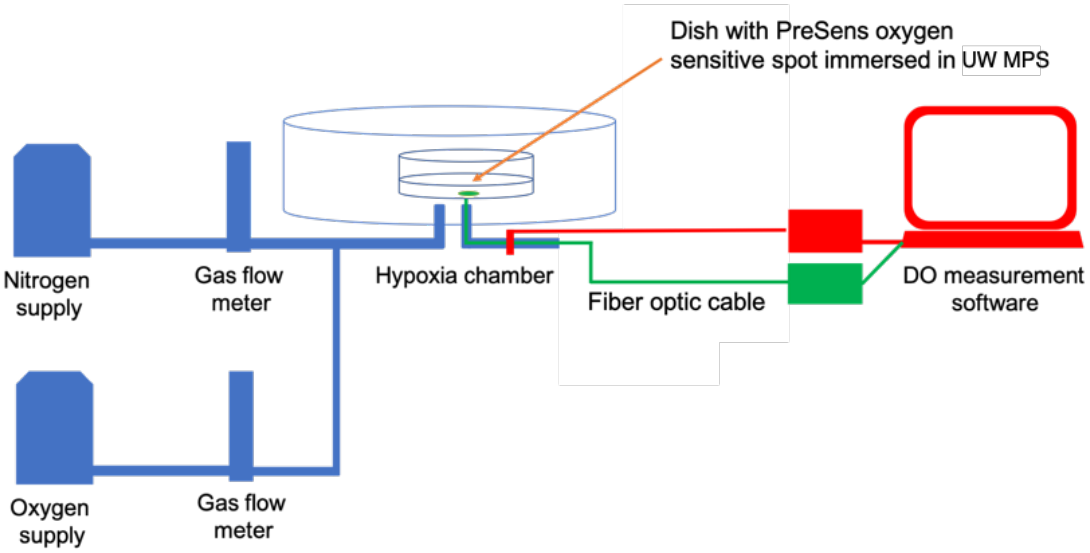

Figure 3.11. Monitoring of hypoxia chamber atmosphere and sample oxygenation.

Using this paired chamber circuit, three oxygen environments can be generated, i.e. hypoxia, atmospheric oxygen and some level of hyperoxia. Plates to be subjected to hypoxia were placed in hypoxia chambers and were flushed with 100% nitrogen. Plates to experience atmospheric oxygen were left exposed to the atmosphere and plates to experience hyperoxia were flushed with 360ml/min 95% oxygen and 240ml/min nitrogen). As shown in Figure 3.12, this generated an atmospheric oxygen concentration of 50 kPA within 30 minutes. In a single replicate investigating the coinciding sample oxygenation, an oxygen sensitive spot detected an end oxygen pressure in the fluid of pressure of 44kPa after 30 minutes of filling.

The sample oxygen measurements were not repeated due to the damaging level of torque exerted on the fibreoptic sensor to attain measurements on the dish bottom.

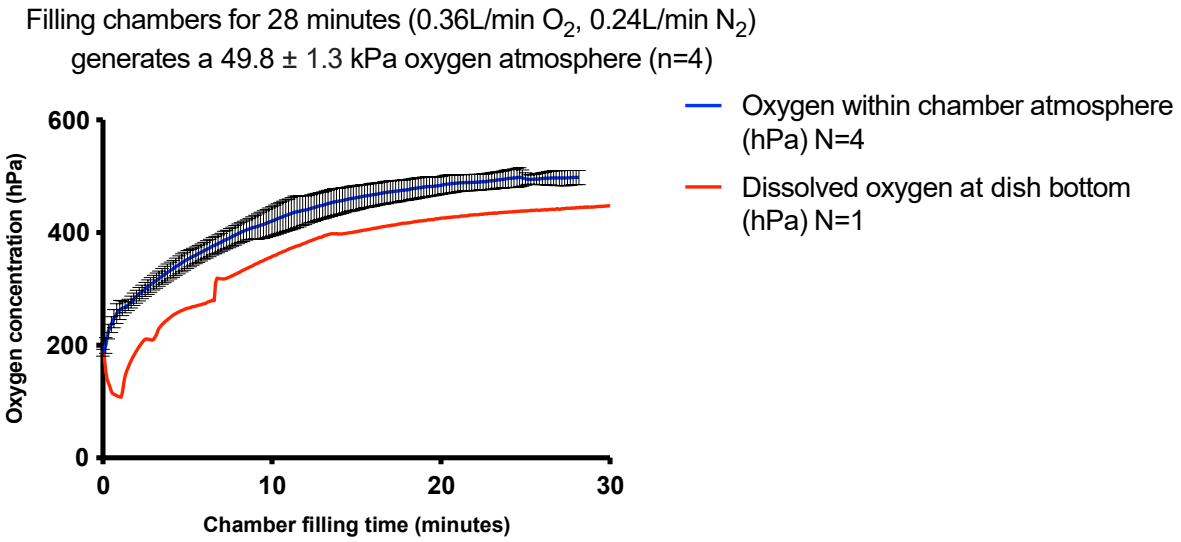

Figure 3.12. Measurement of chamber atmosphere and sample oxygenation

Immediately upon initiation of chamber filling, the oxygen concentration of the gas mixture exiting the gas outflow port was 186.78 ± 6.23hPa. By 30 minutes of chamber filling, the readings had plateaued at 497.99 ±12.76hPa. In a single replicate, the dissolved oxygen in a sample was assessed simultaneously. After an initial decrease in dissolved oxygen, the sample equilibrated with the new environment, plateauing at 447 hPa.

3.2.3.2 Manipulation of storage temperatures in the cell line model.

The three major organ preservation strategies of clinical interest are hypothermic (2-8°C), sub normothermic (i.e. 20°C) and normothermic (37°C). These temperatures may be simulated in multiwell plates by incubating the storage fluid to the temperature required prior to the experiment, and placing cell line experiment into the cold room (ambient temperature 4 °C), at room temperature (ambient temperature 19 °C) or in a warm room or standard cell culture incubator (ambient temperature 37 °C).

3.2.4 Concluding statement about the *in vitro* model

The advantage of these novel methods is that with sufficient hypoxia chambers and manpower, one can execute parallel experiments composed of any combination of storage fluid, duration, temperature, oxygen environment and mechanical fluid stress. As introduced in Chapter 1, these comprise all the variables believed to be pertinent to cellular response to organ preservation.

However, the capacity to perform these economical high throughput screens is futile if equally high throughput and economical analytical tools with which to assess the effects of different storage environments are not used.

3.3 *Ex vivo* methods

3.3.1 The paired whole organ model.

Pairs of porcine kidneys were routinely sourced from a local slaughterhouse (F.A. Gill, Wolverhampton, UK. Upon arrival, an operating theatre-like environment was set up (Figure 3.13).

Figure 3.13. Abattoir set up for procurement of kidneys from freshly sacrificed pigs

3.3.1.1 Animal Sacrifice

Male English White Pigs aged 22 ± 2 weeks and weighing 82.5 ±2.5kg were killed by electrical stunning followed by exsanguination. Kidneys were retrieved following a laparotomy, and warm ischemic time was strictly maintained to be no greater than 15 minutes (with the exception of two studies highlighted later, which had a controlled WIT of 30 minutes).

3.3.1.2 Kidney Acquisition

Immediately after acquisition, the kidneys were inspected for pathology or cuts that may impede perfusion, and in the absence of these were cannulated with a suitably sized T-connector (Figure 3.14) or with an O-ring if an aortic patch was present.

Figure 3.14. A porcine kidney attached to an 8mm T-connector using a surgical suture.

Kidneys were cold flushed with Soltran solution (Baxter, UK) to remove intravascular blood, inhibit metabolism and ATP depletion as per clinical practice.

Following flush, kidneys were bagged and placed in UW solution (Organ Recovery Systems, USA) for transport back to our laboratory. Variations to the flush protocol used, for example when including compounds for later metabolic tracing are described in the relevant chapters.

3.3.2 Hypothermic machine perfusion.

Our industrial partner, Organ Recovery Systems donated two LifePort® Kidney transporters (1.0) to our group for use in research.

After a controlled 2 hours of static storage while slaughterhouse kidneys were transported back to our laboratory, the kidneys were removed from SCS and attached to the LifePort® Kidney Transporter via their renal artery. Kidneys were perfused with UWMPS at a pressure of 30 mmHg and at a temperature ranging between 2-8 °C.

3.3.2.1 Sampling during HMP

The HMP setup permits acquisition of several different data types, i.e. digital readouts, and perfusate or tissue analytes.

Assessment of perfusion parameters; i.e. temperature, flow rate and resistance are provided by a digital readout on the LifePort® devices.

Perfusate, sampled from the dedicated sampling port permits non-invasive assessment of analytes present in the fluid compartment, such as biomarkers, extracellular metabolites and levels of dissolved oxygen.

Tissue sampling potentiates assessment of metabolic phenotype, and was performed by laterally bisecting the kidney at experimental endpoint (Figure 3.15), isolating cortical and medullary tissues of interest and snap freezing them in liquid nitrogen, followed by immediate storage at -80°C.

Tissue sampling was generally restricted to experimental endpoint since biopsy of tissue during perfusion will affect perfusion profile as perfusate exudes from the biopsy site. Changes from this protocol are highlighted where relevant.

Figure 3.15. A bisected porcine kidney after HMP.

The tissues sampled routinely, i.e. the outer cortex and inner medulla are identified.

In light of proposed changes in clinical practice(252), where a 5mm cortical punch biopsy will be obtained from all pretransplant kidneys(253), a single experiment is described where we assess the utility of a serial biopsy in determination of ATP kinetics during HMP.

3.3.3 Tissue homogenisation

Fragments of frozen cortical and medullary tissue were retrieved from storage at -80°C and immediately placed in a Cryocup grinder (BioSpec products, USA) which had been chilled with liquid nitrogen. The tissue samples were kept in LN_2 and were pulverised to a fine powder.

3.3.3.1 Tissue extraction

Following pulverisation, 0.5g of pulverised tissue was added to a 7ml CK28 homogenisation tube (Stretton Scientific, UK) which also contained 5.1ml HPLC grade methanol (Sigma, UK).

The samples were sealed and subjected to 8 homogenisation cycles (5000RPM, 15 seconds) using a Precellys 24 homogeniser (Bertin instruments, France) with cooling on dry ice between each run. As the lowest homogenisation setting possible on this device, this limited sample heating during the process of homogenisation.

The sample was then mixed with 5.1ml HPLC grade chloroform (SigmaAldrich, UK))and 4.65ml ultrapure water and mixed vigorously at 4 °C for 10 minutes. The samples were then centrifuged (1300g, 15 minutes, at 4 °C), resulting in separation of polar metabolites in the upper aqueous phase from non-polar metabolites in the lower chloroform layer and protein which was trapped on the meniscus of the chloroform. For each sample, 8ml of Polar phases were aspirated and dried using a Speedvac concentrator as with the cell extraction.

3.3.3.2 Perfusate LDH analysis

Perfusate samples aspirated from the LifePort® sampling port were snap frozen in liquid nitrogen. Upon thawing, LDH quantification processed much as with the cell culture supernatant samples, with 50μl of perfusate added in to each well of a 96 well plate, as per manufacturer instructions.

3.4 General methods

3.4.1 Metabolic analysis using NMR

3.4.1.1 Preparation of cell and tissue extracts.

Using cycles of vortexing and centrifugation, extracted material located in separated aliquots was collated and was resuspended in D_20 containing 0.1M phosphate buffer, 2mM imidazole and 0.5mM DSS. For analysis using a 1.7mm cryoprobe, the extracts were resuspended in 45µl NMR buffer and 35µl of this was added to a 1.7mm NMR tube. For samples run using a 5mm cryoprobe, 660µl of buffer was used to resuspend the samples and 600µl of this added to the tubes.

3.4.1.2 Neat perfusates

Neat perfusates were mixed with concentrated NMR buffer in ratios such that the final concentration of the resulting fluid was as that used in the cell and tissue extracts, i.e. 0.1M phosphate buffer, 2mM imidazole and 0.5mM DSS. Neat perfusates were exclusively ran in 5mm tubes, and as such the final volume of buffer and sample was 600µl

3.4.2 NMR experimental parameters

3.4.2.1 ^{1}H-1D NMR Spectra

The NOESY-1D presat pulse sequence (Figure 2.7) was used to identify and quantify the metabolites within samples.

In all cases, sample temperature was set to 300K. For non-extracted samples such as perfusates, the proton signal from water was supressed by the NOSEY Presat sequence. For extracted samples the use of deuterium-oxide (D_2O) as the sole solvent reduced the requirement for water suppression, however this was still performed to supress residual

water signals. As non-exchangeable protons were used exclusively in this work, the impact of chemical exchange effects (i.e. exchange of protons for deuterium and generation of water) on analytical accuracy should be negligible.

Data was acquired using a Bruker Avance III 600 MHz spectrometer equipped with an inverse cryoprobe. Proton spectral width was set to 12 ppm. The spectrometer was manually tuned, matched and shimmed to the first sample, and then automatically tuned, matched and shimmed to successive samples. Line width was deemed acceptable at <1Hz.

In total, 32768 data points with a relaxation time of 4 seconds and 128 transients were acquired for each sample. The FID was subjected to zero filling (131072 data points) and a 0.5Hz line broadening.

Conversion of the acquired FID to Bruker format, Fourier transformed NMR spectra, as well as spectral processing operations such as manual phase and baseline correction was performed using MetaboLab software(254). Baselines points were corrected using a spline function Each sample referenced to 0 ppm using the to the chemical shift of the internal DSS standard.

3.4.3 Metabolite identification and quantification

Chenomx software v8.3 (Chenomx Inc, Canada) was used for metabolite identification and quantification. For each spectrum, the chemical shift axis was aligned so that 0 ppm fell directly under the detected DSS peak, and the area under the curve of that DSS peak was used to define peak area which translates to the known buffer DSS concentration of 0.5mM. By comparing the signals detected in the Fourier transformed spectrum with the possible library peak profiles for each metabolite at their known proton chemical shifts, the metabolites composing the sample were identified. Each isolated proton in a given

molecule gives rise to a peak in the NOESY spectrum, therefore a metabolite identification and quantification was performed using characteristics peak at the same chemical shift for each experiment. These are tabulated in Table 3.

Signals were quantified using the established relationship between DSS Area under the curve (AUC) and its known molarity (Figure 3.16).

Metabolite	Chemical shift utilised (ppm)	Metabolite	Chemical shift utilised (ppm)
Acetate	1.91	Glucose	3.52, 5.2
Adenine	8.2	Glutamate	2.34
Alanine	1.47, 3.78	Glutathione	2.97
Citrate	2.67	Glycine	3.54
Formate	8.44	Lactate	1.32, 4.1
Fumarate	6.51		
Gluconate	4.03 ,4.13, 3.66		

Table 3. Chemical shift references used for metabolite quantification

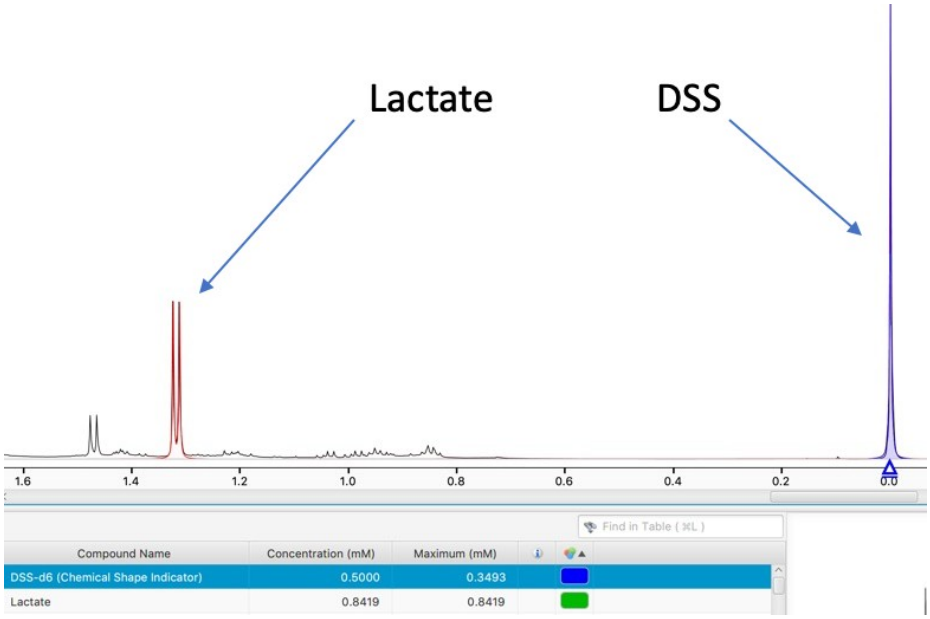

Figure 3.16. Example metabolite quantification using Chenomx (Lactate)

After data prepossessing, the Fourier transformed spectrum is uploaded into Chenomx Software. The characteristic peak of DSS is the calibrator used to define 0ppm, and the area under the curve of this signal is used to determine the relationship between measured signal intensity and the known concentration of DSS. This relationship is then applied to other metabolites to determine their concentration.

3.4.4 Tracer analysis

3.4.5 HSQC analysis

The pulse sequence used was a standard Bruker echo/anti-echo 2D HSQC (hsqcetgpsp.2) with a modification allowing scaling of $^{13}C,^{13}C$ J-coupling based splittings in the spectrum (249) The spectral width for proton dimension was set to 7.812kHz (12 ppm) and ^{13}C dimension was set to 24,155kHz (160 ppm). 512 complex data points were acquired in the ^{1}H dimension. A total of 25% out of 2048 complex data points (512 complex data points), employing non-uniform sampling was used to sample the ^{13}C dimension to reduce acquisition time to 1 hour. The $^{13}C,^{13}C$ J coupling based splittings were 4-fold enhanced (249,255).

Each successive increment of the ^{1}H-^{13}C utilised 2 transients. Construction of the 2D HSQC spectrum was performed using NMRpipe and MDDNMR software(256–258). Spectra were zero filled to 1024 data points in the proton dimension and 16384 real data points were reconstructed in the ^{13}C dimension, after which multiplet analysis and isotopologue analysis were performed using MetaboLab(218).

3.4.5.1 Referencing the 2D plot

MetaboLab contains a library the x,y coordinates (generated through established proton and ^{13}C linked proton chemical shifts) for numerous metabolites of interest. To identify the signals on the spectrum, the spectrum must be aligned using a reference compound.

Lactate was selected as its methyl group NMR signal is easily discernible (Figure 3.17) and as the glycolytic endpoint, is the metabolite most rapidly produced from glucose during hypothermic machine perfusion.

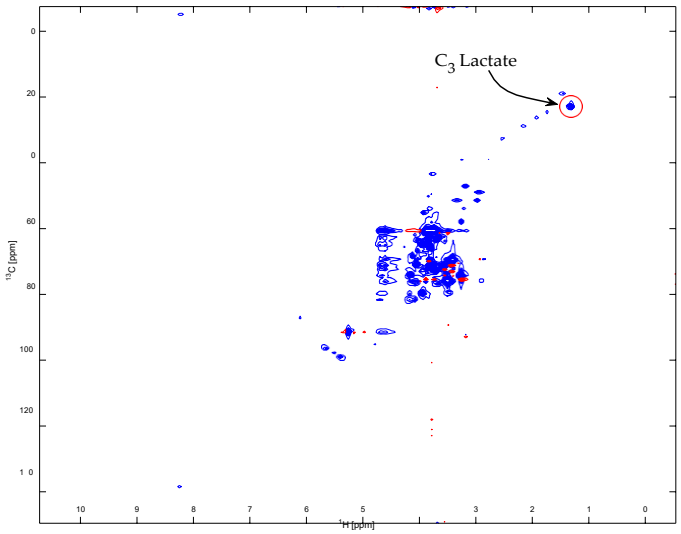

Figure 3.17. Referencing the HSQC spectrum to a library signal (carbon 3 of lactate)

The chemical shift of lactate (carbon 3), and its attached proton signal is used to replot the generated HSQC spectrum. Once referenced, the other peaks detected can be identified using a built- in library.

3.4.5.2 Multiplet analysis

MetaboLab contains a database of the coupling constants (Hz) between the carbon of interest and those adjacent to it if they happen to be labelled. By cycling through these spin systems, which manifest as different degrees of signal splitting (ppm) the operator determines the ^{13}C status of adjacent carbon atoms (Figure 3.18). By comparing signal intensities to the small peak in the very middle of the signal, which represents single ^{13}C labelling at the position of the respective carbon nucleus, a measure of the percentage contribution of the detected spin systems is established.

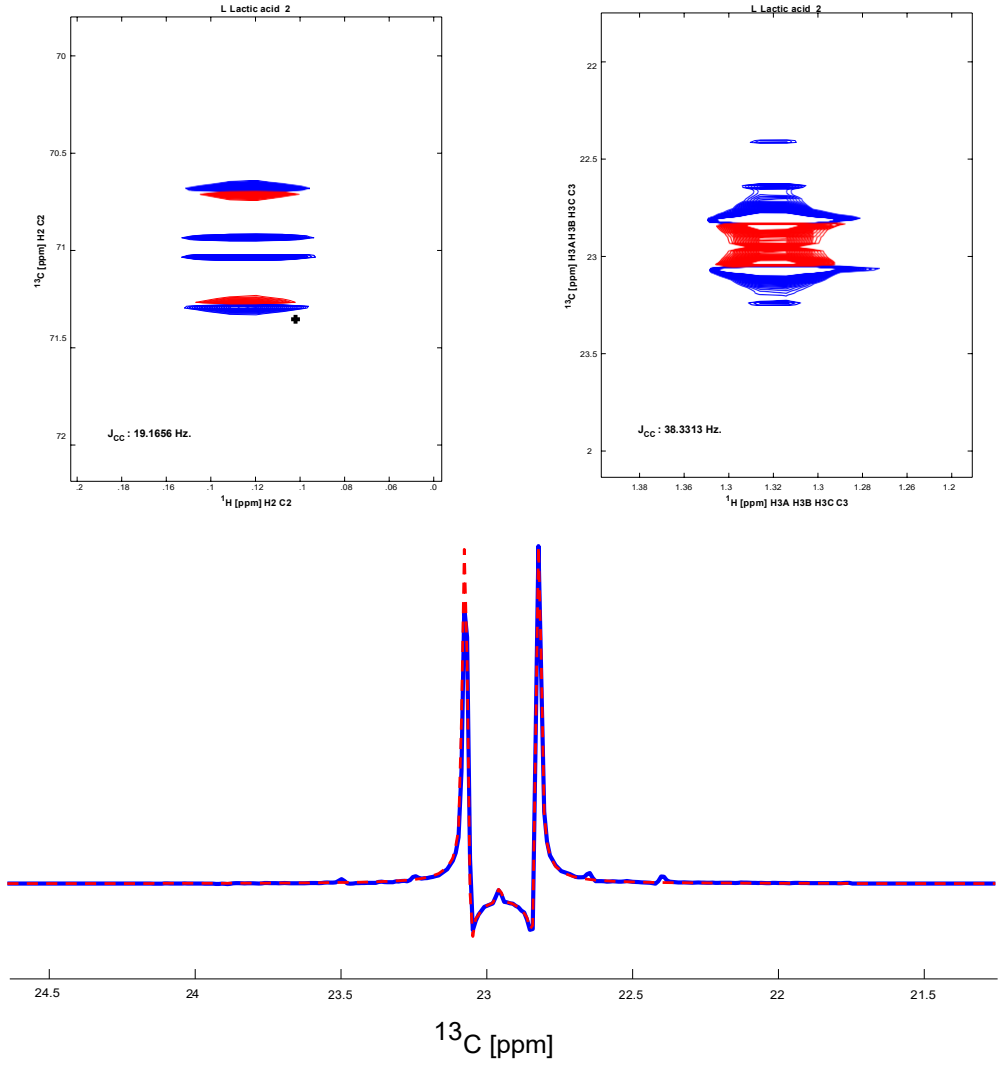

Figure 3.18. The split structure of lactate (C_3) observed during multiplet analysis. Blue denotes the acquired spectra and red the simulation used to define isotopic distribution.

3.4.5.3 Isotopologue analysis

The isotopologue analysis tool collates the multiplet information from all the carbons submitted for a given molecule. The relative intensity of each peak to the middle signal, which (is assumed to represent the unlabelled carbon) is used to calculate the relative contribution of each isotopologue to the total metabolite pool (Figure 3.19).

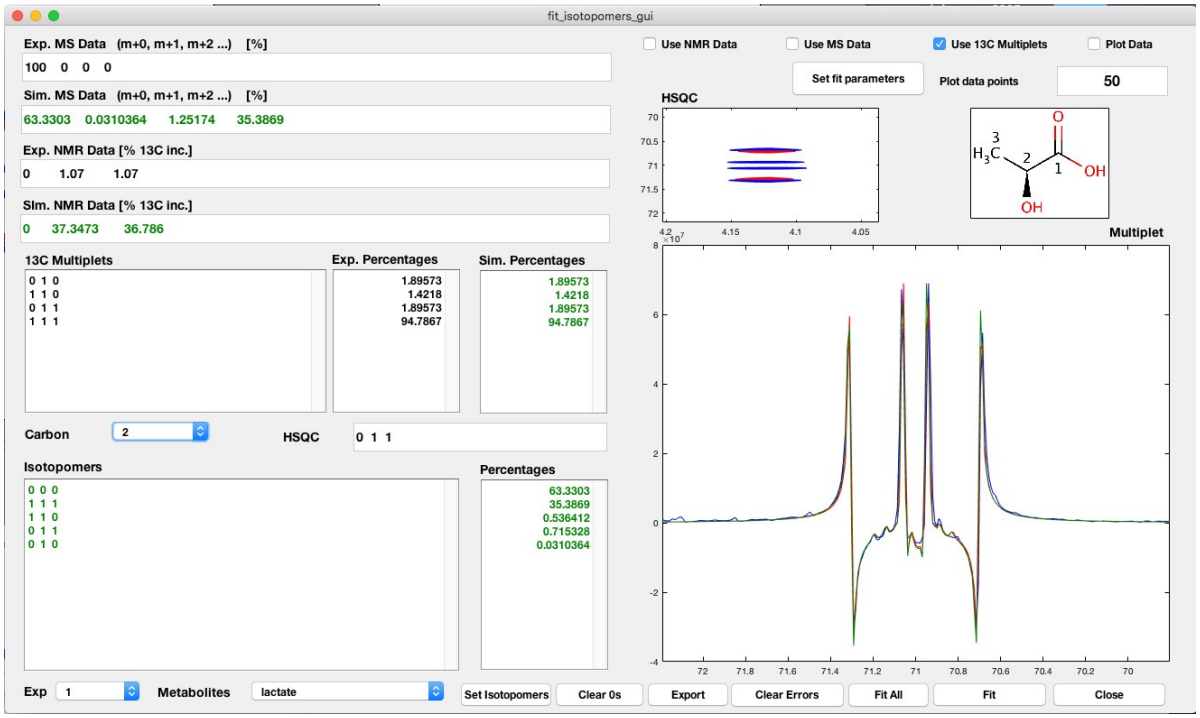

Figure 3.19. Isotopologue analysis

Herein, the data acquired during multiplet analysis and the possible isotopomers set by the operator are used to determine relative contributions of all defined spin systems. There is an input area for mass spectrometry data, which can be used to overcome the limitation of the INEPT sequence, which is carbons are undetectable if they do not possess a bound proton.

3.4.6 Mass spectrometry

Dried extracts were suspended in 40µl of 2% methoxyamine Hydrochloric acid in pyridine (Sigma-Aldrich, UK) and incubated at 60°C for an hour. After this the sample was mixed 60µl of derivatization agent, composed of N-tertbutyldimethylsilyl-N-methyltrifluoroacetamide and 1% tertbutyldimethyl-chlorosilane. Samples were incubated again as before and centrifuged at 13,000 RPM for 5 minutes.

The supernatant, containing derivatized metabolites was added to a chromatography vial and added to an automated GCMS worklist. Samples were run on an Agilent 7890B GC containing a polydimethylsiloxane column (Agilent UK, Stockport).

The Mass spectrometer was tuned to a full width at half maximum peak width of 0.6 atomic mass units (Mass range 50-650 m/z using a PFTBA tuning fluid.

Samples were injected using split mode (1:10) with the helium carrier gas flow rate set to 1ml/min and heated with the oven which had to a ceiling temperature of 320 degrees.

Metabolite Detection was performed using scan mode (50-650 m/z) with 3±1 scans/second at a transfer line temperature of 280°C and a solvent delay of 6.5 minutes.

The software MetaboliteDetector(259) was used to convert raw mass isotopic distributions into natural abundance corrected characterisations of isotopic profile for each metabolite detected.

Dr. Alpesh Thakkar provided all mass spectrometry expertise used in this thesis, ranging from resuspension of dried extracts through to reporting of results.

3.4.7 Colorimetric ATP assay.

A commercially available kit (MAK190) was used to assess cellular ATP content in cell monolayers and later tissue extracts where HPLC was unavailable.

For cell monolayers at experimental endpoint, cell monolayers were scraped intro 2ml ATP assay buffer, aliquoted into 2ml Eppendorf tubes and snap frozen in liquid nitrogen. When ready for analysis, the lids of the tubes were opened and the samples were boiled for 15 minutes on a preheated block to denature enzymes and limit ATP depletion(260).

Boiling water was also used to for colorimetric detection of ATP in tissue samples, this protocol was adapted from previous reports ATP stabilisation of in tissue(261) and Royale

Jelly(262) . Frozen tissue was powdered in a Cryocup Grinder (Stretton Scientific, UK) and 0.5g of this was submerged in a 15ml falcon tube (Corning, UK) followed by 3ml boiling ATP buffer. Samples were agitated and added to a glass beaker on a rolling boil to maintain temperature for 15 minutes. After this, the samples were briefly centrifuged to pellet detritus and 50μl of the supernatant was used for ATP quantification as before.

3.5 Statistical analysis

This thesis documents charts development of an *in vitro* screening tool and *ex vivo* validation model to expedite discovery of optimal kidney preservation environments. Given conceptual similarity with approaches for drug discovery, in all cases, statistics were performed following the guidelines advised in the British journal of Pharmacology(263). Experiments to be tested for statistical significance were composed of a minimum of 5 biological replicates, which where possible (e.g. in the *in vitro* data) were each calculated from the mean of the technical replicates ran per replicate.

Any studies affected by missing values that did not meet the 5 biological replicate minimum are clearly identified, and are included for descriptive purposes but were not assessed for statistical significance.

Although the Shapiro Wilks is a preferable normality test, non-normality was assumed for all studies(229). The *in vitro* model has the potential to grant sufficient biological replicates (e.g. n>30) for meaningful assessment of normality, However the tool was used for the broad screening of diverse environments in this thesis, and this ‘wide net’ paired with time constraints limited the number of biological replicates that could be performed.

Non-normality was assumed for the *ex vivo* studies given the low throughput associated while whole organ research.

3.5.1 *In vitro* statistics

As all cells in each experimental condition were seeded in parallel, a paired model was assumed for the *in vitro* studies(265).

When biological replicates were analysed on different days, the data in each replicate was normalised to a control value within each biological replicate(263). When biological replicates were analysed in a single assay, the raw data did not require normalisation and the assay values were used. Differences were detected using the Wilcoxon matched-pairs signed rank test(266–268), and deemed significant at $p<0.05$). Departures from this analysis, and the justification for it is documented where relevant. In all cases where statistical analysis was employed, data are plotted and tabulated as median and range.

3.5.2 *Ex vivo* statistics

The unpaired, non-parametric Mann Whitney U test was applied for the majority of the whole organ experiments utilising HMP, with differences deemed significant at $p<0.05$. This was due to observed differences in flow rate observed between paired kidneys during perfusion (Appendix 5). For a few *ex vivo* experiments, where pairing could be reasonably established, the Wilcoxon matched-pairs signed rank test was used instead. This is justified where appropriate. In all cases where statistical analysis was employed, data are plotted and tabulated as median and range.

4 ShearFAST: an *in vitro* toolset for high throughput, inexpensive fluid shear stress experiments.

The following article describes the experimental validation of a ShearFAST, a smartphone application which I created.

ShearFAST measures the rocking parameters on a standard laboratory cell rocker, and uses these measurements to calculate the shear stress arising in standard cell culture dishes using a well-established mathematical model(168).

I conceived, developed and optimised the smartphone application. I wrote the attached paper and performed or directed all analysis. The attached manuscript has been submitted for publication, and a preprint has been deposited online:

Smith TB, Nunzio AM De, Patel K, Munford H, Alam T, Powell O, et al. ShearFAST: a user-friendly *in vitro* toolset for high throughput, inexpensive fluid shear stress experiments. bioRxiv. 2020 Feb 2;2020.01.31.929513.

The ShearFAST application will be made freely available for research purposes, along with the raw data used to validate its measurements.

4.1.1 Manuscript

Title:

ShearFAST: a user-friendly *in vitro* toolset for high throughput, inexpensive fluid shear stress experiments.

Authors:

Thomas Brendan Smith[1]*, Alessandro Marco De Nunzio[4], Kamlesh Patel[1,2], Haydn Munford[1], Tabeer Alam[1], Ohema Powell[1], Nicola Heneghan[3,4], Andrew Ready[2], Jay Nath[2], Christian Ludwig[1]

Affiliations:

[1] Institute of Metabolism and Systems Research, University of Birmingham, England

[2]Department of Renal Surgery, Queen Elizabeth Hospital Birmingham, England

[3]Centre of Precision Rehabilitation for Spinal Pain (CPR Spine), School of Sport, Exercise and Rehabilitation Sciences, University of Birmingham, England

[4]LUNEX International University of Health, Exercise and Sports, Differdange, Luxembourg

***Corresponding author details:**

Name: Thomas Brendan Smith

Email: [redacted]

Author involvement is detailed below. No external entity was involved in the writing of this paper.

Conception, design and coding of the software: TS
Conception and design of the study: TS
Acquisition of data: TS, AMDN, NH, HM, TA, OP
Analysis and interpretation of data: TS, AMDN, KP, HM, TA, OP, NH, AR, JN, CL
Drafting the article: TS
Critical revision of article for intellectual content: TS, AMDN, KP, HM, TA, OP, NH, AR, JN, CL
Final approval of version to be submitted: TS, AMDN, KP, TA, HM, OP, NH, AR, JN, CL

Abstract

Fluid shear stress is a key modulator of cellular physiology *in vitro* and *in vivo*, but its effects are under-investigated due to requirements for complicated induction methods.

Herein we report the validation of ShearFAST; a smartphone application that measures the rocking profile on a standard laboratory cell rocker and calculates the resulting shear stress arising in tissue culture plates.

ShearFAST measured rocking profiles were validated against a graphical analysis and also against measures reported by an 8-camera motion tracking system.

ShearFAST angle assessments correlated well with both analyses ($r \geq 0.99$, $p \leq 0.001$) with no significant differences in pitch detected across the range of rocking angles tested.

Rocking frequency assessment by ShearFAST also correlated well when compared to the two independent validatory techniques ($r \geq 0.99$, $p \leq 0.0001$), with excellent reproducibility between ShearFAST and video analysis (mean frequency measurement difference of 0.006 ± 0.005Hz) and motion capture analysis (mean frequency measurement difference of 0.008 ± 0.012Hz)

These data make the ShearFAST assisted cell rocker model make it an attractive approach for economical, high throughput fluid shear stress experiments.

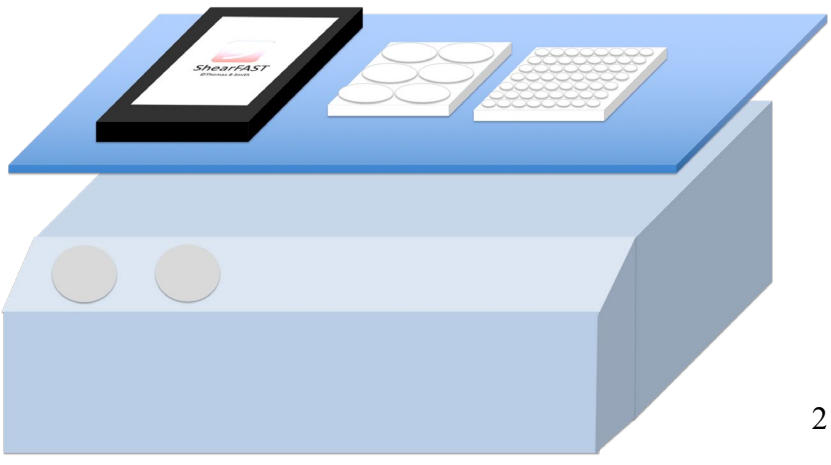

A cell rocker based method for the delivery of defined degrees of FSS has been described (34) and is utilised in several reports (4,35–39) . This approach uses a mathematical model to calculate the resulting fluid shear stress when the rocking parameters (i.e. angle and speed), fluid parameters (i.e. volume and viscosity) and plate dimensions are known.

Many cell rockers possess with a means to adjust rocking angle or speed; however our experience has demonstrated that when even when rocking profile is modifiable, the setting selected may either be incompatible with the model, lack the resolution required or be grossly inaccurate (Figure 6).

Difficulties in delivering the mathematical and analytical accuracy required for the proper execution of cell rocker FSS models may help explain the underutilisation of this otherwise accessible tool in in biomedical research.

Fortunately, the technology to address these problems is currently in place in laboratories throughout the world. Competition between major smartphone manufacturers has led to the ubiquitous presence of handheld devices capable of assessing spatial orientation (40) and performing complex mathematical operations. Since the cell rocker-based approach does not require additional equipment other than the tissue culture dish itself, using smartphones to measure rocking profiles is a simple intuitive step that enables greater experimentation with FSS in cell line studies.

This paper describes the validation of ShearFAST (Shear **F**ormula, **A**ngle, **S**peed **T**oolset), a novel smartphone-based application which enables rapid characterisation of the rocking profile set on a standard laboratory cell rocker, and integrates its findings into the well-established mathematical model of cell rocker based FSS induction.

Methods

ShearFAST

ShearFAST is composed of three individual tools; The formula tool, which calculates the characteristic shear stress when experimental parameters are known, the angle tool which measures the maximal rocking angle set on the cell rocker and the speed tool which measures whole cycle rocking frequency.

Validation of the ShearFAST Formula tool

The formula tool calculates the characteristic fluid shear stress when the volume of fluid, dish diameter, cycle time, fluid volume and viscosity are known. The results of the formula tool (Figure 4) were validated against the example data from the original publication.

Validation of the ShearFAST angle tool

A graphical analysis method involved capturing side-on photos of the cell rocker, and measurement of the cell rocker platform angle with respect to 0° using ImageJ (41) (Figure 1). A second validation utilised an Infrared Optolectronic 8-camera System (BTS Bioengineering, Milan, Italy) from now on referred to as motion capture analysis (Figure 2).

The 2.2 Megapixel infrared cameras resolution (2048x1088 px, BTS DX 6000 model) tracked the 3D motion of retroreflective markers placed on the rocking platform (1.2 cm in diameter) with a precision of 0.1 mm (see https://www.btsbioengineering.com/products/smart-dx-motion-capture/).

Image J angle analysis

A camera was placed aligned so it could capture a side on view of the cell rocker platform. A smartphone with ShearFAST installed on it was placed on the rocker and the angle tool calibrated to 0° with the aid of a physical spirit level.

An image was taken of the rocker during calibration to allow for later correction of any slight rotation of the camera (Figure1A)

Following calibration, the rocker angle is considered to be 0° as per the spirit level measurements, therefore any apparent rotation of the rocking platform was assumed to be due to a slight camera rotation. The degree required to rotate the image so the platform is perfectly horizontal was determined and applied to the rest of the images after being deemed a suitable approach tested on a second, rotated calibration image (Figure 1B).

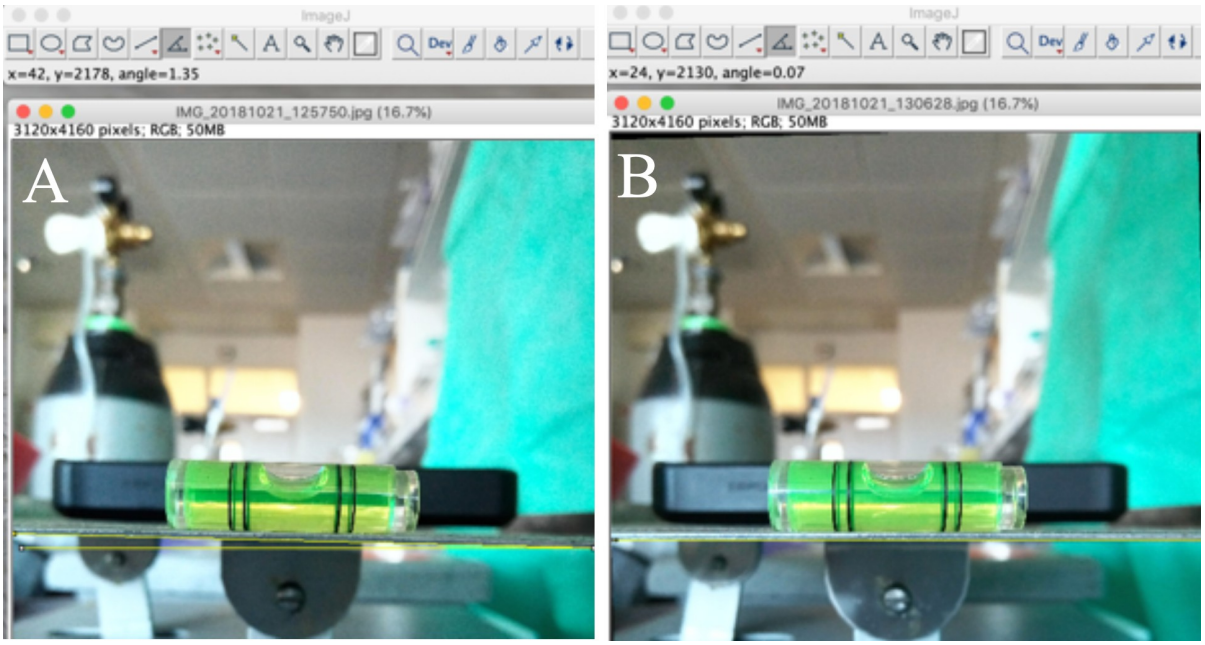

Figure 1. ShearFAST calibration using a spirit level. The leveled platform (A) was used to determine the angle by which the camera capturing the photo was itself offset (B), allowing compensation during ImageJ platform angle analysis.

After calibration, the cell rocker was set to a series of smartphone detected angles, with screenshots taken of the mean angle detected alongside side view images of the cell rocker. The angles set on the cell rocker images were assessed using the same method, and compared to the measurements obtained using the ShearFAST angle tool.

In a typical cell culture experiment using 35mm plates and 1.5ml media, the authors of the original model recommend avoidance of rocking angle above 10.2° to prevent exposure of the adherent cells to atmosphere. Therefore, 7 angles below this were assessed using the ShearFAST angle tool (Table S1).

Motion capture analysis

To perform motion capture analysis, the cell rocker was placed at the focal point of an 8-camera motion tracking system. Motion capture retroreflective markers were placed on the rocker (Figure 2A), alongside the smartphone housing the ShearFAST and a physical spirit level. The application was calibrated to 0º as before, then the maximal platform rocking angle adjusted to 12 angles falling between 0-10° using the smartphone application (Table S2).

The platform was then set rocking, and mean angle measurements were determined using the SMART ANALYZER software (BTS Bioengineering, version: 1.10.469.0) throughout the rocking period (Figure2B)

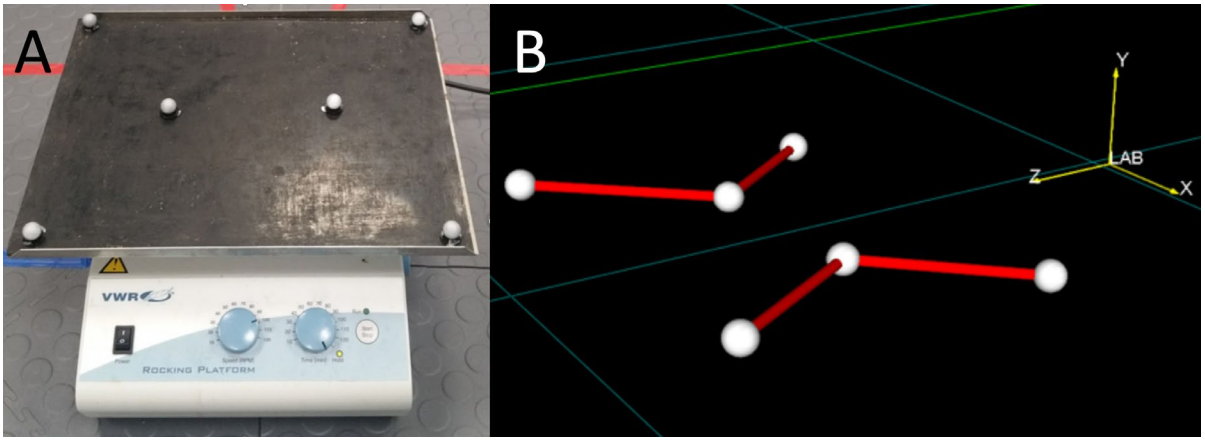

Figure 2. (A) A VWR cell rocker (Cat: 444-0146) which allows manual manipulation of rocking angle and RPM. Six tracking balls were attached to permit detection of rocking angle and cycle frequency. (B) The changes in the geometric position of each tracking ball (i.e. *x,y,z* coordinates) was determined using the 8 camera BTS motion tracking system.

Validation of the Speed tool.

Video Frequency analysis

The smartphone was placed on cell rocker, which was set to rock at speeds ranging between 30 and 110 rotations per minute (RPM) using dials on the rocker. Using ShearFAST, the acquired waveform was compared to modelled waveforms of user defined frequency until the acquired data was overlaid, granting rapid determination of rocking frequency.

A video was taken of each rocking experiment during ShearFAST data acquisition. The videos were observed alongside a stopwatch with millisecond resolution. A screencast of both video and stopwatch was recorded, and the timepoints at which the cell rocker reached its maximal rocking angle was determined over the course of the video (Figure 3).

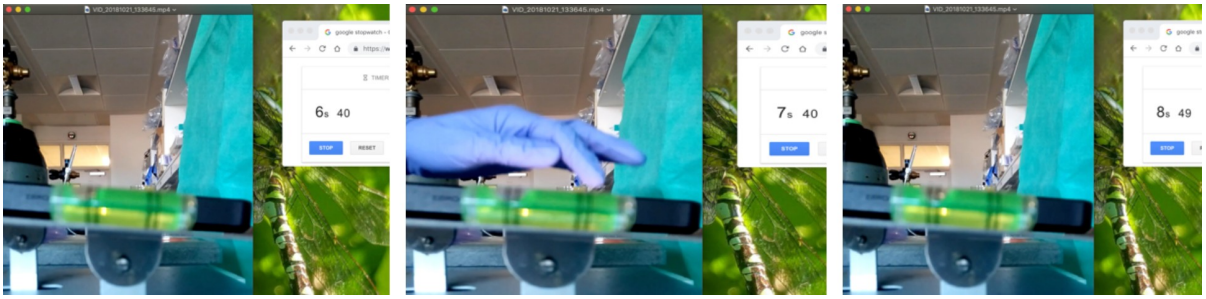

Figure 3. Measurement of cycle time using video analysis. The images show consecutive timepoints at which the rocking platform reached its maximum rocking angle, which were recorded.

At least three timepoints were collected for each rocking speed, subtraction of each timepoint from its preceding timepoint granted the assessment of the mean time taken to complete one full rocking cycle. These were averaged (*T)*, permitting calculation of cycle frequency (*Hz*) using Equation 1. The data is reported in Table 1, and correlations between the measurement methods reported in Figure 7.

$$!" = \frac{1000}{\& ()}$$

Equation 1: conversion of mean cycle time to rocking frequency simulations and frequency measured during video analysis

Motion capture Frequency analysis

Motion capture frequency analysis granted an assessment of the accuracy and reproducibility of the smartphone frequency measurements. Using the ShearFAST, the rocking frequency was set to 1Hz for three measures, and 0.65Hz for four other measures and compared to the motion capture results (Table 2).

Statistical analysis

Correlations between ShearFAST measurements of rocking angle or frequency and those detected by the other analysis were identified by the Spearman R test. Linear regression was used to determine if the slope generated by ShearFAST measurements of rocking pitch or frequency differed from those detected by the other analysis.

Results

Validation of the Formula tool

The formula tool calculates the characteristic fluid shear stress reported in when the volume of fluid, dish diameter, cycle speed, fluid volume and viscosity are known (Figure 4). The FSS calculated by the ShearFAST formula tool was validated against the example data from the original publication's supplementary data (34)

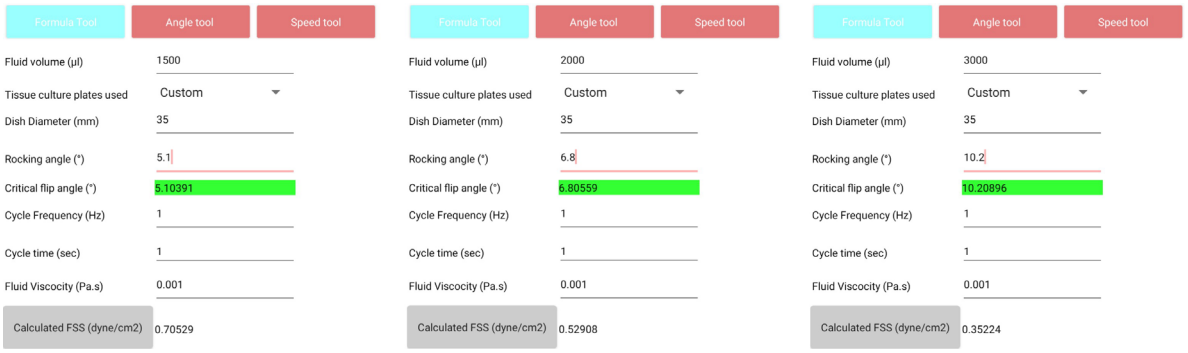

Figure 4. ShearFAST formula tool reproduces the example data reported in the supplementary data of the original publication original publication

Validation of the Angle tool

ImageJ angle analysis

ImageJ angle analysis demonstrated a close association with the smartphone application measurements ($r=1.0$, $p \leq 0.0004$) (5A). The smartphone measurements were around 0.25° higher than those of the graphical analysis (Table S1), but no difference in slope was found between angle measurement methods ($p>0.84$).

Motion capture angle analysis

On average, ShearFAST angle measures and those attained by motion capture analysis varied by 0.54 ± 0.16° however this difference was not found to be significant (p>0.32) (Table S2). Angle measures between the two angle assessment methods were found to be correlated (R=0.99, p ≤0.0001) (Figure 5B).

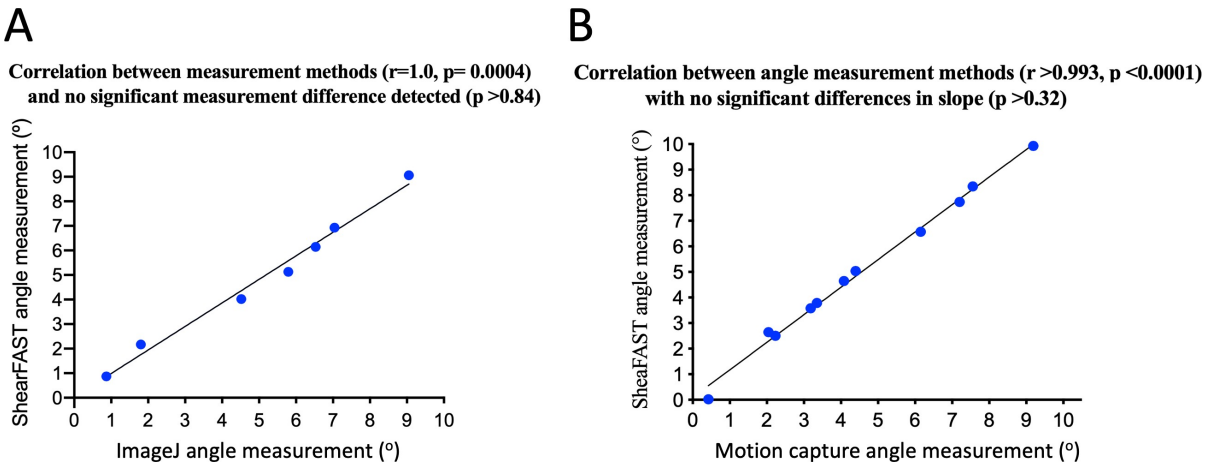

Figure 5. Correlation between pitch measurements detected using ShearFAST and Pitch measurements detected using ImageJ(A) and motion capture analysis (B)

Video frequency analysis

Video analysis of rocker cycle frequency corroborates the frequency assessment by the smartphone application (Table 1) and (Figure 6), with strong association between measurement techniques (r≥0.99, p≤0.0001) and no significant difference detected between the two measurement techniques (p=0.9219) (Figure 7).

Rocker speed (RPM)	ShearFAST detected frequency (Hz)	Mean cycle time (ms)	Standard deviation cycle time (ms)	Calculated mean frequency (Hz)	Difference in measurement (Hz)	Mean difference (Hz)
110	0.990	1003.333	41.833	0.997	0.007	0.006±0.005
100	0.915	1077.778	131.128	0.928	0.013	
90	0.835	1206.000	23.022	0.829	0.006	
80	0.760	1326.667	70.356	0.754	0.006	
70	0.680	1481.111	40.756	0.675	0.005	
60	0.590	1695.714	151.751	0.590	0	
50	0.480	2066.667	96.885	0.484	0.004	
40	0.385	2596.667	41.633	0.385	0	
30	0.290	3600.000	105.357	0.278	0.012	

Table 1. The rocking frequency detected by ShearFAST at different rocking speeds.

Figure 6. ShearFAST measured rocking frequencies at rocker defined rocking speeds (RPM). Illustrating the value of the ShearFAST approach; when manually selecting the rocking speed 60RPM (i.e. 1Hz) the resulting profile was visibly slower. ShearFAST determined a rocking speed of 0.59Hz which was corroborated by later video analysis (Table 1).

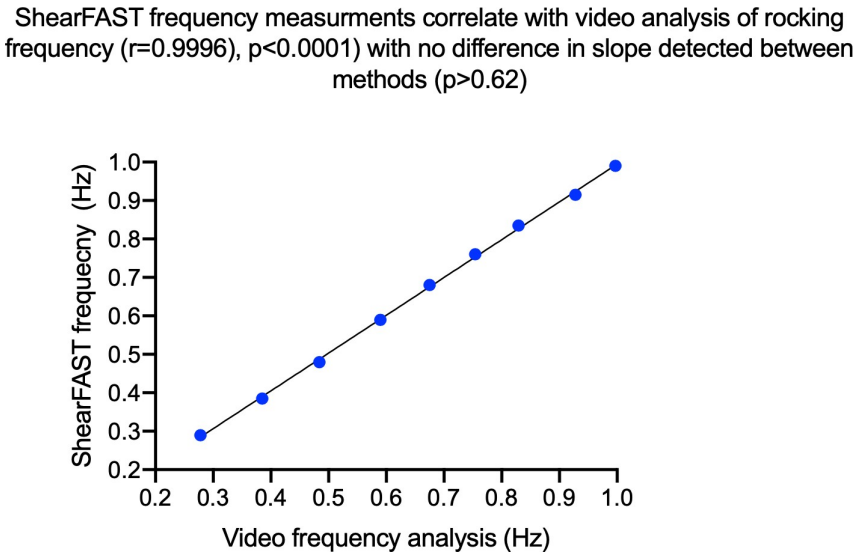

Figure 7. Correlation between ShearFAST frequency measurement and video frequency measurement.

Motion capture frequency analysis

This analysis revealed a small average difference in frequency assessment of 0.007 ± 0.012Hz between measures (Table 2).

ShearFAST determined frequency (Hz)	Motion capture frequency (Hz)	Difference (Hz)	Mean Difference (Hz)
1.0	1.035	0.035	0.007 ± 0.012
1.0	0.995	0.005	
1.0	0.995	0.005	
1.0	1.0	0.0	
0.65	0.645	0.005	
0.65	0.655	0.005	
0.65	0.65	0.0	
0.65	0.65	0.0	

Table 2. Reproducible frequency assessment by ShearFAST and motion capture analysis

Discussion

Within cell line research there is a drive to more accurately simulate physiological environments through the utilization of parallel plate flow chambers, microfluidics and organ-on-a-chip devices. These allow continuous instigation of fluid flow, however arguably diminish the versatility of the cell line approach.

The fixed growth area available to adherent cells cultured in such devices alongside the requirements for sperate perfusion circuits restricts both the type and number of the downstream analysis that can be performed.

The cell rocker model was proposed in 2010 (34) , and has been utilised to demonstrate important effects of FSS in diverse cell lineages and areas of medical research; (4,35–39) .

However, the complexity of the model, including its requirements for mathematical and technical accuracy may be a factor limiting its correct implementation.

ShearFAST provides a user-friendly experience with which to perform high throughput and scalable cell rocker induced cell line experiments in conventional laboratory cultureware.

We demonstrate that the speed tool interface is an effective, intuitive and very efficient means for the determination of whole cycle rocking frequency. ShearFAST measures of rocking frequency correlated strongly with those derived from the real time video analysis, with very small, insignificant and ineffectual differences observed when compared to the video and motion capture analysis (i.e. 0.006Hz and 0.007Hz respectively).

We also found the angle tool measures platform pitch with acceptable degrees of accuracy. No differences in slope were detected by between ShearFAST measured angles and motion capture analysis or graphical analysis.

Consider a hypothetical experiment in which 1.5ml of cell culture media is added to a 35mm dish and rocked at 1Hz. On average, the mean imprecision between the ShearFAST angle tool and the techniques used to validate it were found to be 0.54° for the motion capture analysis and 0.29° for the ImageJ analysis. Assuming perfect accuracy by the validatory methods and an angle overestimation by ShearFAST, these mean degrees of imprecision

would result in a characteristic shear stress generation of 0.63 dyne/cm^2 and 0.66 dyne/cm^2 respectively, rather than the mathematically calculated 0.7 dyne/cm^2 resulting from the conditions in the described hypothetical experiment.

Since, as modelled in the original rocker publication, FSS induced during seesaw rocking varies with both cycle time and dish location, these insignificant differences detected in pitch measurements are offset by the potential of ShearFAST to foster simple, reproduceable and high throughput FSS experiments.

The ShearFAST FSS induction method is compatible with high throughput apparatus to control additional extracellular environments, such as oxygen availability using hypoxia chambers. We performed the example screen under fluid anoxia using a nitrogen purged hypoxia chamber, thus we can be confident the protective effect of FSS observed did not stem from improved oxygen delivery to the submerged monolayers.

Cultured proximal tubule cells have been shown to respond dynamically to fluid shear stress, changing both their phenotype (44) , reabsorbative activities (1) as well as the 3D actin structure of their cytoskeleton (45) .

We found the mean differences in cellular viability caused by generation of fluid flux to be small (i.e. instigation of 1 dyne/cm^2 resulted in a 7% improvement in viability when compared to cells stored under fluid stasis).

This emphasizes the value of the ShearFAST assisted cell rocker model. Unlike alternative methods of FSS induction, it is simple and economical to perform large numbers of technical or biological replicates using the multiwell plate format. Through this advantage, the effects of biological variation between experiments may be silenced, leading to enhanced detection of small changes conferred by fluid movement in the extracellular environment.

Additionally, ShearFAST permits the generation of different degrees of FSS in the same experiment. The volume of fluid used is a variable governing the FSS generated under the same rocking profile. When paired with static parallel plates containing the same volumes of fluid, this phenomenon may be manipulated within ShearFAST to perform a ‘dose response’ of FSS induction.

Conclusions

ShearFAST is a useful tool which facilitates the rapid execution of fluid shear stress experiments using a cell rocker. The mobile format of the software permits instant user acquisition through established smartphone application providers, while the user interface provides an intuitive means with which to accurately measure the rocking profile on a standard laboratory cell rocker. The costless execution of ShearFAST assisted cell are particularly useful for proof of concept studies, and is applicable for research involving adherent cell lines.

Acknowledgements:

The authors would like to thank Kalliopy Tabry for her invaluable contributions to this work.

This work was supported by a generous grant from University Hospital Birmingham Charities.

Conflict of Interest:

The authors declare no conflicts of interest.

References

1. Raghavan V, Rbaibi Y, Pastor-Soler NM, Carattino MD, Weisz OA. Shear stress-dependent regulation of apical endocytosis in renal proximal tubule cells mediated by primary cilia. Proc Natl Acad Sci U S A [Internet]. 2014 Jun 10 [cited 2016 Apr 27];111(23):8506–11. Available from: http://www.pubmedcentral.nih.gov/articlerender.fcgi?artid=4060694&tool=pmcentrez&rendertype=abstract
2. Miravète M, Klein J, Besse-Patin A, Gonzalez J, Pecher C, Bascands J-L, et al. Renal tubular fluid shear stress promotes endothelial cell activation [Internet]. Vol. 407, Biochemical and Biophysical Research Communications. 2011 [cited 2017 Jun 23]. Available from: http://www.sciencedirect.com/science/article/pii/S0006291X1100516X
3. Gong X, Yang W, Wang L, Duncan RL, Pan J. Prostaglandin E2 modulates F-actin stress fiber in FSS-stimulated MC3T3-E1 cells in a PKA-dependent manner. Acta Biochim Biophys Sin (Shanghai) [Internet]. 2014 Jan [cited 2019 May 5];46(1):40–7. Available from: http://www.ncbi.nlm.nih.gov/pubmed/24296051
4. Michael Delaine-Smith R, Javaheri B, Helen Edwards J, Vazquez M, Rumney RMH. Preclinical models for in vitro mechanical loading of bone-derived cells. Bonekey Rep [Internet]. 2015 [cited 2019 May 5];4:728. Available from: http://www.ncbi.nlm.nih.gov/pubmed/26331007
5. Cha B, Geng X, Mahamud MR, Fu J, Mukherjee A, Kim Y, et al. Mechanotransduction activates canonical Wnt/β-catenin signaling to promote lymphatic vascular patterning and the development of lymphatic and lymphovenous valves. Genes Dev [Internet]. 2016 Jun 15 [cited 2017 Jul 20];30(12):1454–69. Available from: http://www.ncbi.nlm.nih.gov/pubmed/27313318
6. Wahle A, Lopez JJ, Olszewski ME, Vigmostad SC, Chandran KB, Rossen JD, et al. Plaque development, vessel curvature, and wall shear stress in coronary arteries assessed by X-ray angiography and intravascular ultrasound. Med Image Anal [Internet]. 2006 Aug [cited 2016 May 19];10(4):615–31. Available from: http://www.pubmedcentral.nih.gov/articlerender.fcgi?artid=2590653&tool=pmcentrez&rendertype=abstract
7. Maschmeyer I, Lorenz AK, Schimek K, Hasenberg T, Ramme AP, Hübner J, et al. A four-organ-chip for interconnected long-term co-culture of human intestine, liver, skin and kidney equivalents. Lab Chip [Internet]. 2015 Jun 21 [cited 2016 Mar 14];15(12):2688–99. Available from: http://www.ncbi.nlm.nih.gov/pubmed/25996126
8. Barnes JM, Nauseef JT, Henry MD. Resistance to Fluid Shear Stress Is a Conserved Biophysical Property of Malignant Cells. Olson MF, editor. PLoS One [Internet]. 2012 Dec 3 [cited 2019 May 5];7(12):e50973. Available from: https://dx.plos.org/10.1371/journal.pone.0050973
9. Heo K-S, Fujiwara K, Abe J. Shear stress and atherosclerosis. Mol Cells [Internet]. 2014 Jun [cited 2019 May 5];37(6):435–40. Available from: http://www.ncbi.nlm.nih.gov/pubmed/24781409
10. Tang X, Jin J, Huang S, Xin Y, Tan Y. Blood Shear Stress Selects Metastasis-Initiating Cells with Metastatic Advantages. Biophys J [Internet]. 2018 Feb 2 [cited 2019 May 5];114(3):325a. Available from: https://linkinghub.elsevier.com/retrieve/pii/S0006349517330540
11. Huang Q, Hu X, He W, Zhao Y, Hao S, Wu Q, et al. Fluid shear stress and tumor metastasis. Am J Cancer Res [Internet]. 2018 [cited 2019 May 5];8(5):763–77. Available from: http://www.ncbi.nlm.nih.gov/pubmed/29888101
12. Molladavoodi S, Robichaud M, Wulff D, Gorbet M. Corneal epithelial cells exposed to shear stress show altered cytoskeleton and migratory behaviour. PLoS One [Internet]. 2017 [cited 2019 May 5];12(6):e0178981. Available from: http://www.ncbi.nlm.nih.gov/pubmed/28662184
13. Garcia-Polite F, Martorell J, Del Rey-Puech P, Melgar-Lesmes P, O'Brien CC, Roquer J, et al. Pulsatility and high shear stress deteriorate barrier phenotype in brain

microvascular endothelium. J Cereb Blood Flow Metab [Internet]. 2017 Jul 4 [cited 2019 May 5];37(7):2614–25. Available from: http://journals.sagepub.com/doi/10.1177/0271678X16672482

14. Saxer T, Zumbuehl A, Müller B. The use of shear stress for targeted drug delivery. Cardiovasc Res [Internet]. 2013 Jul 15 [cited 2019 May 5];99(2):328–33. Available from: https://academic.oup.com/cardiovascres/article-lookup/doi/10.1093/cvr/cvt102
15. Houston P, White BP, Campbell CJ, Braddock M. Delivery and Expression of Fluid Shear Stress-Inducible Promoters to the Vessel Wall: Applications for Cardiovascular Gene Therapy. Hum Gene Ther [Internet]. 1999 Dec 10 [cited 2019 May 5];10(18):3031–44. Available from: http://www.ncbi.nlm.nih.gov/pubmed/10609662
16. Sato Y, Tsukada K, Hatakeyama K. Role of shear stress and immune responses in liver regeneration after a partial hepatectomy. Surg Today [Internet]. 1999 Jan [cited 2019 May 5];29(1):1–9. Available from: http://www.ncbi.nlm.nih.gov/pubmed/9934824
17. Tian S, Bai Y, Yang L, Wang X, Wu Y, Jia J, et al. Shear Stress Inhibits Apoptosis of Ischemic Brain Microvascular Endothelial Cells. Int J Mol Sci [Internet]. 2013 Jan 11 [cited 2019 May 5];14(1):1412–27. Available from: http://www.mdpi.com/1422-0067/14/1/1412
18. Thury A, van Langenhove G, Carlier SG, Albertal M, Kozuma K, Regar E, et al. High shear stress after successful balloon angioplasty is associated with restenosis and target lesion revascularization. Am Heart J [Internet]. 2002 Jul [cited 2019 May 5];144(1):136–43. Available from: http://www.ncbi.nlm.nih.gov/pubmed/12094200
19. Moers C, Pirenne J, Paul A, Ploeg RJ. Machine perfusion or cold storage in deceased-donor kidney transplantation. N Engl J Med [Internet]. 2012 Feb 23 [cited 2015 Nov 3];366(8):770–1. Available from: http://www.ncbi.nlm.nih.gov/pubmed/22356343
20. Moers C, Smits JM, Maathuis M-HJ, Treckmann J, van Gelder F, Napieralski BP, et al. Machine Perfusion or Cold Storage in Deceased-Donor Kidney Transplantation. N Engl J Med [Internet]. 2009 Jan [cited 2016 Sep 3];360(1):7–19. Available from: http://www.nejm.org/doi/abs/10.1056/NEJMoa0802289
21. Kox J, Moers C, Monbaliu D, Strelniece A, Treckmann J, Jochmans I, et al. The Benefits of Hypothermic Machine Preservation and Short Cold Ischemia Times in Deceased Donor Kidneys. Transplantation [Internet]. 2018 Aug [cited 2019 May 5];102(8):1344–50. Available from: http://www.ncbi.nlm.nih.gov/pubmed/29570164
22. Patel K, Smith TB, Neil DAH, Thakker A, Tsuchiya Y, Higgs EB, et al. The Effects of Oxygenation on Ex Vivo Kidneys Undergoing Hypothermic Machine Perfusion. Transplantation [Internet]. 2019 Feb [cited 2019 Mar 3];103(2):314–22. Available from: http://www.ncbi.nlm.nih.gov/pubmed/30461718
23. Jochmans I, Moers C, Smits JM, Leuvenink HGD, Treckmann J, Paul A, et al. The Prognostic Value of Renal Resistance During Hypothermic Machine Perfusion of Deceased Donor Kidneys. Am J Transplant [Internet]. 2011 Oct [cited 2019 May 5];11(10):2214–20. Available from: http://www.ncbi.nlm.nih.gov/pubmed/21834917
24. Lo Faro ML, Akhtar MZ, Boffa C, Ploeg R. Should Pulsatile Preservation Be the Gold Standard in Kidney Transplantation? Curr Transplant Reports [Internet]. 2015 Jun 15 [cited 2019 May 5];2(2):105–12. Available from: http://link.springer.com/10.1007/s40472-015-0063-8
25. Patel SK, Pankewycz OG, Nader ND, Zachariah M, Kohli R, Laftavi MR. Prognostic Utility of Hypothermic Machine Perfusion in Deceased Donor Renal Transplantation. Transplant Proc [Internet]. 2012 Sep [cited 2019 May 5];44(7):2207–12. Available from: http://www.ncbi.nlm.nih.gov/pubmed/22974956
26. Wan C, Wang C, Liu T, Wang H, Yang Z. Experimental study on the cryopreservation of LLC-PK1 epithelial cells with hypoxic UW solution. J Huazhong Univ Sci Technolog Med Sci [Internet]. 2007 Aug [cited 2016 Aug 26];27(4):426–8. Available from: http://www.ncbi.nlm.nih.gov/pubmed/17828502
27. Dutheil D, Rioja-Pastor I, Tallineau C, Goujon J-M, Hauet T, Mauco G, et al. Protective Effect of PEG 35 000 Da on Renal Cells: Paradoxical Activation of JNK

Signaling Pathway During Cold Storage. Am J Transplant [Internet]. 2006 Jul [cited 2015 Sep 30];6(7):1529–40. Available from: http://doi.wiley.com/10.1111/j.1600-6143.2006.01343.x

28. Neuhaus W, Schick MA, Bruno RR, Schneiker B, Förster CY, Roewer N, et al. The effects of colloid solutions on renal proximal tubular cells in vitro. Anesth Analg [Internet]. 2012 Feb [cited 2016 Aug 4];114(2):371–4. Available from: http://www.ncbi.nlm.nih.gov/pubmed/22025492
29. Sung JH, Kam C, Shuler ML. A microfluidic device for a pharmacokinetic-pharmacodynamic (PK-PD) model on a chip. Lab Chip [Internet]. 2010 Feb 21 [cited 2016 Apr 14];10(4):446–55. Available from: http://www.ncbi.nlm.nih.gov/pubmed/20126684
30. Frohlich EM, Zhang X, Charest JL. The use of controlled surface topography and flow-induced shear stress to influence renal epithelial cell function. Integr Biol (Camb) [Internet]. 2012 Jan 1 [cited 2016 Apr 14];4(1):75–83. Available from: http://pubs.rsc.org/en/Content/ArticleHTML/2012/IB/C1IB00096A
31. Spruell C, Baker AB. Analysis of a high-throughput cone-and-plate apparatus for the application of defined spatiotemporal flow to cultured cells. Biotechnol Bioeng [Internet]. 2013 Jun [cited 2016 Aug 24];110(6):1782–93. Available from: http://www.ncbi.nlm.nih.gov/pubmed/23280552
32. Esch MB, Mahler GJ, Stokol T, Shuler ML. Body-on-a-chip simulation with gastrointestinal tract and liver tissues suggests that ingested nanoparticles have the potential to cause liver injury. Lab Chip [Internet]. 2014 Aug 21 [cited 2016 Mar 22];14(16):3081–92. Available from: http://www.pubmedcentral.nih.gov/articlerender.fcgi?artid=4144667&tool=pmcentrez&rendertype=abstract
33. Kotsis F, Nitschke R, Boehlke C, Bashkurov M, Walz G, Kuehn EW. Ciliary calcium signaling is modulated by kidney injury molecule-1 (Kim1). Pflügers Arch Eur J Physiol [Internet]. 2007 Mar [cited 2016 Aug 3];453(6):819–29. Available from: http://www.ncbi.nlm.nih.gov/pubmed/17205356
34. Zhou X, Liu D, You L, Wang L. Quantifying fluid shear stress in a rocking culture dish. J Biomech [Internet]. 2010 May 28 [cited 2016 Apr 26];43(8):1598–602. Available from: http://www.pubmedcentral.nih.gov/articlerender.fcgi?artid=2866761&tool=pmcentrez&rendertype=abstract
35. Chen JC, Chua M, Bellon RB, Jacobs CR. Epigenetic changes during mechanically induced osteogenic lineage commitment. J Biomech Eng [Internet]. 2015 Feb 1 [cited 2019 May 5];137(2):020902. Available from: http://www.ncbi.nlm.nih.gov/pubmed/25581684
36. Srinivasan PP, Parajuli A, Price C, Wang L, Duncan RL, Kirn-Safran CB. Inhibition of T-Type Voltage Sensitive Calcium Channel Reduces Load-Induced OA in Mice and Suppresses the Catabolic Effect of Bone Mechanical Stress on Chondrocytes. PLoS One [Internet]. 2015 [cited 2019 May 5];10(5):e0127290. Available from: http://www.ncbi.nlm.nih.gov/pubmed/26011709
37. Oliazadeh N, Gorman KF, Eveleigh R, Bourque G, Moreau A. Identification of Elongated Primary Cilia with Impaired Mechanotransduction in Idiopathic Scoliosis Patients. Sci Rep [Internet]. 2017 [cited 2019 May 5];7:44260. Available from: http://www.ncbi.nlm.nih.gov/pubmed/28290481
38. Hyler AR, Baudoin NC, Brown MS, Stremler MA, Cimini D, Davalos R V, et al. Fluid shear stress impacts ovarian cancer cell viability, subcellular organization, and promotes genomic instability. PLoS One [Internet]. 2018 [cited 2019 May 5];13(3):e0194170. Available from: http://www.ncbi.nlm.nih.gov/pubmed/29566010
39. Wang W, Sarazin BA, Kornilowicz G, Lynch ME. Mechanically-Loaded Breast Cancer Cells Modify Osteocyte Mechanosensitivity by Secreting Factors That Increase Osteocyte Dendrite Formation and Downstream Resorption. Front Endocrinol (Lausanne) [Internet]. 2018 [cited 2019 May 5];9:352. Available from:

http://www.ncbi.nlm.nih.gov/pubmed/30034365

40. Li M, Xu S, Mazilu D, Turkbey B, Wood BJ. Smartglasses/smartphone needle guidance AR system for transperineal prostate procedure. In: Fei B, Linte CA, editors. Medical Imaging 2019: Image-Guided Procedures, Robotic Interventions, and Modeling [Internet]. SPIE; 2019 [cited 2019 May 5]. p. 34. Available from: https://www.spiedigitallibrary.org/conference-proceedings-of-spie/10951/2512250/Smartglassessmartphone-needle-guidance-AR-system-for-transperineal-prostate-procedure/10.1117/12.2512250.full
41. Rueden CT, Schindelin J, Hiner MC, DeZonia BE, Walter AE, Arena ET, et al. ImageJ2: ImageJ for the next generation of scientific image data. BMC Bioinformatics [Internet]. 2017 Dec 29 [cited 2019 Jul 17];18(1):529. Available from: http://www.ncbi.nlm.nih.gov/pubmed/29187165
42. Aschauer L, Gruber LN, Pfaller W, Limonciel A, Athersuch TJ, Cavill R, et al. Delineation of the key aspects in the regulation of epithelial monolayer formation. Mol Cell Biol [Internet]. 2013 Jul [cited 2015 Nov 10];33(13):2535–50. Available from: http://www.pubmedcentral.nih.gov/articlerender.fcgi?artid=3700122&tool=pmcentrez&rendertype=abstract
43. Vichai V, Kirtikara K. Sulforhodamine B colorimetric assay for cytotoxicity screening. Nat Protoc [Internet]. 2006 Aug 17 [cited 2017 Oct 20];1(3):1112–6. Available from: http://www.nature.com/doifinder/10.1038/nprot.2006.179
44. Timsit M-O, Adams WJ, Laguna-Fernandez A, Ichimura T, Bonventre J V, García-Cardeña G, et al. Flow is critical for maintaining a protective phenotype in renal proximal tubular cells. Am J Transplant [Internet]. 2013 Jun [cited 2016 Aug 9];13(6):1617–8. Available from: http://www.ncbi.nlm.nih.gov/pubmed/23617882
45. Duan Y, Gotoh N, Yan Q, Du Z, Weinstein AM, Wang T, et al. Shear-induced reorganization of renal proximal tubule cell actin cytoskeleton and apical junctional complexes. Proc Natl Acad Sci U S A [Internet]. 2008 Aug 12 [cited 2016 May 17];105(32):11418–23. Available from: http://www.pnas.org/content/105/32/11418.long

5 Isolating mechanisms of benefit in models of HMP and SCS

The attached manuscript was published in Cryobiology in 2017.

Nath, J., **Smith, T. B**., Patel, K., Ebbs, S. R., Hollis, A., Tennant, D. A., Ludwig, C, Ready, A. R. (2017). Metabolic differences between cold stored and machine perfused porcine kidneys: A 1H NMR based study. *Cryobiology*, *74*, 115–120. https://doi.org/10.1016/j.cryobiol.2016.11.006

As second author, I contributed significantly to this publication, performing all whole organ experiments, metabolic assays and data analysis on the tissue and fluid samples obtained. I made significant contributions to the writing and editing of this paper, up until the application of the systems approach described within which addressed in following commentary.

5.1 Comparing metabolic differences between HMP and SCS stored kidneys

5.1.1 Introduction

Assessment of pre-transplant HMP perfusate by ^{1}H-NMR has identified a potential link between metabolism during organ storage and functional outcome(109,110). However surprisingly, whether metabolic difference contribute to the benefit of HMP over SCS had not been established.

The inclusion of glucose in UWMPS may confer metabolic support to the HMP stored kidney, and the notable absence of any metabolic substrates in UW may suggest a key role of the provision of metabolic support in the search for an optimised organ storage protocol. This warrants assessment of the metabolic differences between HMP and SCS stored kidneys.

The attached manuscript details characterisation of absolute metabolic differences observed in a whole organ model of HMP and SCS.

This chapter begins with incorporation of the published manuscript, followed by a critical discussion of its findings. The contribution of cell line models follows in Chapter 6, which details the *in vitro* consequences of the simulation of isolated environmental parameters intrinsic to each storage modality.

Cryobiology 74 (2017) 115e120

Contents lists available at ScienceDirect

Cryobiology

journal homepage: www.elsevier.com/locate/ycryo

Metabolic differences between cold stored and machine perfused porcine kidneys: A ^{1}H NMR based study

Jay Nath [a, b, *], Tom B. Smith [b], Kamlesh Patel [a, b], Sam R. Ebbs [b], Alex Hollis [b], Daniel A. Tennant [b], Christian Ludwig [b, 1], Andrew R. Ready [a, 1]

[a] Department of Renal Surgery, University Hospitals Birmingham, Birmingham, UK
[b] Institute of Metabolism and Systems Research (IMSR), College of Medical and Dental Sciences, University of Birmingham, Birmingham, UK

articleinfo

Article history:
Received 11 July 2016
Received in revised form
18 October 2016
Accepted 21 November 2016
Available online 3 December 2016

Keywords:
Hypothermic machine perfusion
Kidney
Transplantation
Metabolism
NMR
Organ preservation

abstract

Hypothermic machine perfusion (HMP) and static cold storage (SCS) are the two methods used to preserve deceased donor kidneys prior to transplant This study seeks to characterise the metabolic profile of HMP and SCS porcine kidneys in a cardiac death donor model

Twenty kidneys were cold flushed and stored for two hours following retrieval Paired kidneys then underwent 24 h of HMP or SCS or served as time zero controls Metabolite quantification in both storage fluid and kidney tissue was performed using one dimensional ^{1}H NMR spectroscopy For each metabolite, the net gain for each storage modality was determined by comparing the total amount in each closed system (i e total amount in storage fluid and kidney combined) compared with controls

26 metabolites were included for analysis Total system metabolite quantities following HMP or SCS were greater for 14 compared with controls (all $p < 0.05$) In addition to metabolic differences with control kidneys, the net metabolic gain during HMP was greater than SCS for 8 metabolites (all $p < 0.05$) These included metabolites related to central metabolism (lactate, glutamate, aspartate, fumarate and acetate)

The metabolic environments of both perfusion fluid and the kidney tissue are strikingly different between SCS and HMP systems in this animal model The total amount of central metabolites such as lactate and glutamate observed in the HMP kidney system suggests a greater degree of *de novo* metabolic activity than in the SCS system Maintenance of central metabolic pathways may contribute to the clinical benefits of HMP

1. Introduction

Hypothermic Machine Perfusion (HMP) and Static Cold Storage (SCS) are the two methods of kidney preservation that are used widely in clinical practice during the time period between organ retrieval and implantation [16]. A key concept for both preservation modalities is that cellular metabolism, and therefore cellular metabolic requirements, are minimised in these hypothermic conditions and the rate of metabolism reported to be about 5e8% at temperatures below 4 °C [29] with a similar decrease in oxygen requirement [1].

The superiority of HMP over SCS is well documented [4,17,22,23,27] but the mechanisms by which this occurs are not clear. Improvement in flow dynamics, with fall in the intra-renal resistance is likely to be one factor but the additional metabolic support derived from the circulation of nutrient-containing perfusion fluid may also help preserve organ function and have a beneficial effect [7,30].

Metabolomic analyses of preservation fluid during HMP using 1D-^{1}H NMR (One-dimensional proton nuclear magnetic resonance) spectroscopy, by groups including our own, have demonstrated this to be reproducible and highly specific for metabolite identification and quantification [2,10,24]. However, surprisingly, to our knowledge there are no studies that have sought to compare the metabolomic profiles, or metabolome, of HMP and SCS kidneys.

Porcine kidneys are widely used in transplantation studies owing to their similar physiological and anatomical properties to human organs [9,11]. In addition, the metabolic profiles during

* Corresponding author Department of Renal Surgery, University Hospitals Birmingham, Birmingham, UK
[1] Authors contributed equally to this manuscript

http://dx doi org/10 1016/j cryobiol 2016 11 006
0011-2240/

periods of HMP for porcine and human kidneys are comparable [24], with a correlation between metabolite profiles during storage and post transplant outcome [2]. For HMP preserved human kidneys, the metabolic profile from perfusates of immediate graft function kidneys differs from those with delayed function [10] and reinforces the concept that significant metabolism occurs during HMP and that metabolism reflects functional outcome.

The aims of this study were twofold. Firstly, to determine the distribution of metabolites between the two different compartments (fluid and tissue) during the organ preservation period. Secondly, to determine the total amount of each metabolite within HMP and SCS kidneys systems after 24 h of organ storage and through comparison with control kidneys, the metabolic changes that occur.

2. Methods

2.1. Animal research

Abattoir/slaughterhouse pig kidneys (F.A. Gill, Wolverhampton, UK) were used and no animals were sacrificed solely for the purposes of this study, negating any need for ethical board approval. Experiments were performed on 22e26 week old male 'bacon weight' pigs, weighing 80e85 kg. All experiments were performed following the principles of laboratory animal care according to NIH standards. Animals were sacrificed by electrical stunning and exsanguination. Initial organ preservation was performed following organ retrieval and occurred within 14 min of death, replicating deceased cardiac death (DCD) donor conditions. Kidneys were cold flushed (4 °C) with 1 L SPS-1 (UW) solution at a pressure of 100 mm Hg. Organs were then stored at 4 °C in SPS-1 for 2 h to replicate the clinical period of organ transportation.

2.2. Experimental groups

Paired kidneys were randomly allocated to receive either HMP or SCS for 24 h. HMP kidneys were perfused with 1 L of KPS-1 using the LifePort Kidney Transporter 1.0 (Organ Recovery Systems, Chicago, IL). (Perfusion pressure 30 mm Hg). SCS Kidneys were submerged in 1 L of fresh chilled SPS-1 solution with a surrounding ice bath. Preservation fluid was sampled for each kidney at baseline and 2, 4, 8, 12, 18, and 24 h. After 24 h, organs were rapidly dissected and tissue samples (1 cm^3 sections) flash frozen and stored (−80 °C). All experiments were performed in a cold room (4 °C) to ensure consistency.

2.3. Control kidneys

To ascertain metabolism during SCS or HMP storage conditions, baseline values prior to storage conditions were needed (time 0). Large volume tissue sampling precludes effective organ perfusion and therefore 'Control kidneys' were used to establish baseline metabolite levels. These were (n = 6) flushed and cold transported in identical fashion to experimental kidneys and tissue samples obtained as described above (i.e. not subjected to 24 hr of SCS or HMP).

2.4. Sample processing and metabolite quantification

NMR samples were prepared from storage fluid by mixing 150 μL of 400 mM (pH 7.0) phosphate buffer containing 2 mM DSS (4,4-dimethyl-4-silapentane-1-sulfonic acid) and 8 mM imidazole with 390 μL of each fluid sample and 60 μL of deuterium oxide (D_2O) to reach a final phosphate buffer concentration of 100 mM and a final DSS concentration of 500 μM. After mixing, the 600 μL samples were pipetted into 5 mm NMR tubes, sonicated and centrifuged. Technical replicates of samples (x3) were prepared for each timepoint.

For cell extract studies, 500 mg of renal cortex was manually cryohomogenised in liquid nitrogen. 5.1 ml of both methanol (−80 °C) and chloroform was added to the powdered tissue and samples diluted with 4.65 ml of dH_20 at 4 °C. Samples were centrifuged to separate into polar and non-polar layers and 1.5 ml of the upper polar layer was dispensed into a cryovial and dried. Three technical replicates were performed for each tissue sample. Dried polar residue was then dissolved in 390 μL of dH_20 and 210 μL of buffer solution as described above.

The protocol used for ^{1}H NMR analysis has been described previously [10,24]. Briefly, this entailed processing on a Bruker AVII 500 MHz spectrometer, acquisition of one dimensional spectra and then metabolite identification and quantification using Matlab based 'Metabolab' software [18] and Chenomx 8.1 (ChenomxInc) software respectively. Metabolites were deemed to be present if they exhibited non-ambiguous spectral patterns or their presence deemed biologically plausible and confirmed on ultra performance liquid chromatography mass spectrometry. Any metabolites that were present in different concentrations in the SCS and HMP fluid (e.g. glucose, gluconate, mannitol, adenine, adenosine etc.) were excluded from comparative analysis. Metabolite quantifications were corrected to allow for sample dilution with sample buffer. When determining concentrations of metabolites using Chenomx, the researchers were blind to the storage group. Quantification of the total amount of metabolite in the storage fluid, tissue and total system was calculated based upon the weight of the kidney at time of sample acquisition and final volume of storage fluid.

2.5. Statistical analysis

For each timepoint, three results were obtained (technical replicates) and the median value used. For comparison of SCS and HMP conditions, analysis was performed using Wilcoxon paired signed rank test (two tailed) as one kidney from each pair was subjected to each condition and normality was not consistent on prior analysis. When comparing SCS or HMP with control kidneys, Mann-Whitney u test (two tailed) was used, as these were non-paired samples. Data were reported as median concentrations and interquartile (IQ) range. All analysis was performed using GraphPad Prism version 6.00 for Mac OS X, GraphPad Software, La Jolla California USA, with $p < 0.05$ deemed to be indicative of statistical significance.

3. Results

Metabolic optimisation of cadaveric kidneys is a potential target to improve the function of kidneys for transplantation. This study seeks to establish the degree of metabolism, if any, that occurs in the two widely used methods of kidney organ storage prior to transplantation (HMP and SCS).

The total quantity of each metabolite after 24 h of either HMP or SCS was calculated using ^{1}H NMR methods and compared with control organs to determine the net metabolic change during each storage method.

We found evidence of metabolite production for both storage modalities with 14 metabolites present in significantly greater quantities in the HMP or SCS system compared with controls (all $p < 0.05$) (Table 1) (Fig. 1, Fig 1(Suppl)). There were significantly more metabolites with a net increase in the HMP system (13/14) compared with the SCS system (7/14) ($p = 0.033$).

Eight of the metabolites were significantly elevated in the HMP system compared with both the control and SCS systems (all $p < 0.05$), indicating a greater degree of metabolite production.

Table 1
Total amount of metabolite present in each of the storage modalities at time zero (controls) or after 24 h of preservation (SCS or HMP) Data reported as Median (Interquartile Range), unless stated otherwise Statistical test: J Mann-Whitney u test (two tailed) #Wilcoxon paired signed rank test (two tailed) *Significant at p < 0 05

	Storage Modality			p-Values		
	Control System (mmol)	SCS System (mmol)	HMP System (mmol)	Control vs SCS J	Control vs HMP J	SCS vs HMP #
Glutamate	1 54 (1 12e1 84)	1 38 (1 11e1 66)	3 97 (3 69e4 71)	0 731	0 002*	0 031*
Myoinositol	1 18 (1 16e1 19)	1 29 (1 01e1 52)	2 16 (1 85e2 41)	0 731	0 002*	0 031*
Lactate	1 11 (0 976e1 23)	1 38 (1e1 75)	2 13 (1 67e2 71)	0 138	0 002*	0 031*
Hypoxanthine	0 454 (0 356e0 515)	0 710 (0 641e0 762)	1 05 (0 909e1 17)	0 001*	0 002*	0 156
Formate	0 442 (0 274e0 638)	0 643 (0 589e0 779)	0 842 (0 750e0 943)	0 101	0 004*	0 031*
Acetate	0 210 (0 206e0 212)	0 296 (0 253e0 301)	0 552 (0 494e0 654)	0 234	0 041*	0 031*
Alanine	0 302 (0 243e0 360)	0 486 (0 339e0 499)	0 501 (0 368e0 558)	0 035*	0 015*	0 313
Succinate	0 283 (0 267e0 297)	0 462 (0 312e0 52)	0 434 (0 307e0 541)	0 001*	0 015*	0 844
Inosine	0 588 (0 561e0 628)	1 08 (0 885e1 12)	0 185 (0 146e0 233)	0 001*	0 002*	0 031*
Aspartate	0 114 (0 104e0 118)	0 107 (0 0879e0 11)	0 165 (0 140e0 215)	0 234	0 041*	0 031*
Leucine	0 0476 (0 0441e0 0517)	0 0667 (0 0513e0 0820)	0 0693 (0 0495e0 0773)	0 014*	0 026*	0 688
Niacinamide	0 0196 (0 0181e0 0207)	0 0289 (0 0243e0 0319)	0 0490 (0 0420e0 0557)	0 001*	0 002*	0 031*
Tyrosine	0 0262 (0 0217e0 0302)	0 0434 (0 0339e0 0462)	0 0387 (0 0332e0 0431)	0 001*	0 013*	0 438
Fumarate	0 00412 (0 00339e0 00418)	0 00308 (0 00145e0 00348)	0 0133 (0 0077e0 0212)	0 064	0 002*	0 031*

These included lactate, glutamate, aspartate, fumarate, acetate, myo-inisitol, niacinamide and formate (Fig. 1).

Despite the additional 24 h of organ preservation, albeit in static conditions, the amount of lactate in the SCS system was comparable to controls (1.37 vs 1.11 mmol p¼0.138). However the amount in the HMP system (2.13 mmol) was almost twice the amount of either controls or SCS systems (p 0.002 and p¼0.031). However, despite greater amounts overall, the amount present in the HMP tissue (0.76 mmol) was actually lower than SCS tissue (1.14 mmol) or control tissue (1.11 mmol) (p 0.031 and p¼0.002 respectively), reflective of lower intracellular concentrations for HMP kidneys.

The distribution of metabolites between the extracellular storage fluid and tissue samples for both storage conditions are detailed in Table 2. As expected, there were greater quantities of metabolites in the circulating HMP fluid compared with the static conditions of SCS at most time-points. After 24 h, the total amount of metabolite in the perfusate for the HMP kidneys was significantly greater than the SCS group for (21/26, 80.8%) of metabolites. Whilst concentrations rose most rapidly in the first 2 h of perfusion and therefore may be in part due a metabolite washout phenomenon, there was an increase in most metabolites over sequential timepoints as would be expected with on-going production (Fig. 2aec).

Reduced glutathione is a constituent of both KPS-1 (used in HMP) and SPS-1 (used in SCS) fluids at equal concentrations. Whilst this remained at stable in the SCS environment, the glutathione was clearly consumed by the HMP group and after 8 h concentrations were 17.6 fold higher in the SCS fluid (1.60 mM vs. 0.091 mM, p 0.001) (Fig. 2d). Despite apparent organ uptake of reduced glutathione, there was no evidence of this in the tissue samples from either group.

4. Discussion

The aim of this study was to determine any metabolic differences between the two clinically used methods of organ storage in this animal model.

Whilst the calculation of the total amount of metabolite within the system does rely on several assumptions (complete metabolite extraction from tissue and metabolite homogeneity within tissue), we felt this was imperative to draw meaningful comparison between groups and enables the calculation of net metabolite production/consumption in these two closed systems (HMP and SCS).

Although the storage fluid used in each experimental group differs (most notably absence of glucose in the SCS fluid) and therefore caution should be exercised in attributing any differences merely to the parameters of storage (i.e. HMP or SCS), this study was designed to assess metabolism during the two clinically used organ preservation techniques, not merely the storage modality in isolation.

This study clearly demonstrates the presence of major central metabolites such as lactate, glutamate, fumarate, aspartate and acetate at greater levels in the HMP system compared with both controls and SCS (Fig. 1). This strongly suggests that these metabolites are being produced during HMP. Furthermore, the accumulation of these metabolites into the circulating perfusion fluid demonstrates effective homeostatic mechanisms are active to prevent over accumulation within the local cellular environment.

The list of metabolites reported in this study is not exhaustive and is a limitation of this study. Some interesting substrates (eg glucose) were excluded as this is only present in one of the storage fluids (KPS-1). For others the 1D ^{1}H NMR spectral pattern is either ambiguous or can be hidden under more domineering peaks from other compounds.

The increased total lactate in the HMP system is likely to reflect increased glycolysis in the HMP model. Although new glycolytic activity of the glucose within the HMP fluid is one likely contributor, this is unlikely to the singular cause. This is supported by evidence that the HMP fluid glucose concentrations did not decrease during the study period and replicates findings from previous human studies [10]. However conversion of a proportion of perfusion fluid glucose into lactate through glycolytic pathways has been corroborated by work demonstrating activity of these pathways using ^{13}C labelled glucose tracers [25].

The net gain of glutamate, fumarate, aspartate and acetate during HMP is also intriguing. Whilst identification of responsible metabolic pathways is difficult to ascribe solely with ^{1}H NMR studies, one explanation could be increased oxygen dependent tricarboxylic acid (TCA) cycle activity. Although uniform upregulation of TCA intermediates would support this theory, as discussed, many are not easily identifiable using ^{1}H NMR methods [6] and are rarely found in equipoise even *in vivo* [14]. Several (^{13}C) NMR studies have reported glutamate as a valid marker of TCA activity [3,5,20].

For some metabolites, the total system amounts for HMP and SCS kidneys were comparable to the controls, suggesting that either *de novo* production does not occur during the 24 h preservation or that consumption mirrors production (Table 1 *supplementary*). However, for metabolites with similar total amounts, the compartment in which they were located varied per metabolite. Some metabolites were entirely contained within the HMP kidney

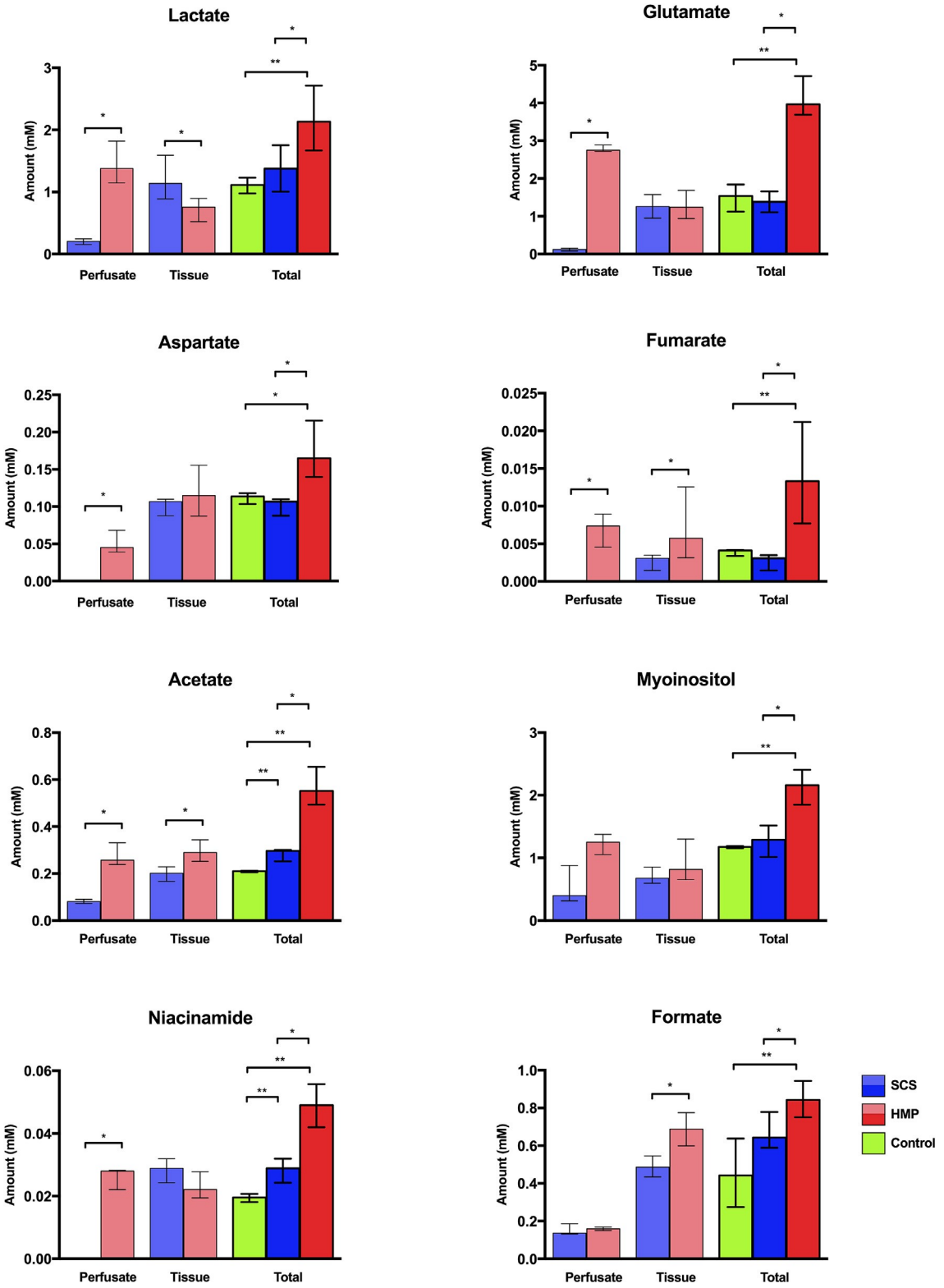

Fig. 1. Metabolites significantly elevated in the HMP system compared with both SCS and control kidneys Metabolite levels represent total amounts (mmol) in the storage fluid, kidney tissue and entire system for porcine kidneys after 24 hr of HMP or SCS or time zero controls Highly significant (**p < 0 01) and significant (*p < 0 05) differences between HMP system versus both controls and SCS kidneys

tissue (e.g. ADP, AMP, NADP) and presumably in the intracellular compartment. Other metabolites were evident in both the tissue and storage fluid but at higher concentrations in the HMP fluid. These discrepancies in metabolite location further highlight that cellular transport processes are active in this environment but that movement of metabolites into the extracellular fluid is not

Table 2
Metabolites present in tissue and storage fluid in HMP or SCS kidney systems at 24 h Data reported as Median (Interquartile Range), unless stated otherwise Statistical test: #Wilcoxon paired signed rank test (two tailed) *Significant at p < 0 05

	Storage	Total storage fluid amount (mmol)	p-value#	Total kidney tissue amount (mmol)	p-Value#
Glutamate	SCS	0 0812 (0 125e0 155)	0 0312*	0 952 (1 26e1 58)	0 6875
	HMP	2 72 (2 75e2 89)		0 94 (1 24e1 68)	
Myoinositol	SCS	0 316 (0 399e0 879)	0 0625	0 596 (0 676e0 853)	0 5625
	HMP	1 05 (1 25e1 38)		0 653 (0 816e1 3)	
Lactate	SCS	0 153 (0 205e0 245)	0 0312*	0 89 (1 14e1 59)	0 0312*
	HMP	1 15 (1 38e1 82)		0 521 (0 755e0 895)	
Hypoxanthine	SCS	0 294 (0 328e0 404)	0 0312*	0 289 (0 407e0 424)	0 0625
	HMP	0 705 (0 781e0 867)		0 189 (0 258e0 31)	
Formate	SCS	0 132 (0 136e0 186)	0 4375	0 434 (0 486e0 545)	0 0312*
	HMP	0 151 (0 16e0 169)		0 688 (0 599e0 774)	
Acetate	SCS	0 073 (0 0808e0 0912)	0 0312*	0 167 (0 201e0 229)	0 0312*
	HMP	0 239 (0 257e0 331)		0 252 (0 289e0 344)	
Alanine	SCS	0 0465 (0 0643e0 0815)	0 0312*	0 303 (0 415e0 435)	0 0312*
	HMP	0 253 (0 306e0 358)		0 116 (0 187e0 207)	
Succinate	SCS	0 0104 (0 0155e0 0184)	0 0312*	0 298 (0 446e0 498)	0 0312*
	HMP	0 104 (0 131e0 208)		0 203 (0 294e0 347)	
Inosine	SCS	0 703 (0 852e0 961)	0 0312*	0 145 (0 182e0 201)	0 0312*
	HMP	0 0877 (0 108e0 128)		0 058 (0 0723e0 109)	
Aspartate	SCS	e	0 0312*	0 0879 (0 107e0 11)	0 3125
	HMP	0 039 (0 0452e0 0682)		0 0874 (0 115e0 155)	
Leucine	SCS	0 00442 (0 00506e0 00761)	0 0312*	0 0486 (0 0591e0 0775)	0 0312*
	HMP	0 0285 (0 038e0 0468)		0 0222 (0 0304e0 0318)	
Niacinamide	SCS	e	0 0312*	0 0243 (0 0289e0 0319)	0 0938
	HMP	0 0221 (0 028e0 0282)		0 0194 (0 0221e0 0278)	
Tyrosine	SCS	0 00336 (0 0071e0 00843)	0 0312*	0 0306 (0 0371e0 0391)	0 0312*
	HMP	0 0197 (0 0228e0 0276)		0 0112 (0 0143e0 0171)	
Fumarate	SCS	e	0 0312*	0 00145 (0 00308e0 00348)	0 0312*
	HMP	0 00456 (0 00737e0 00895)		0 00314 (0 00574e0 0126)	

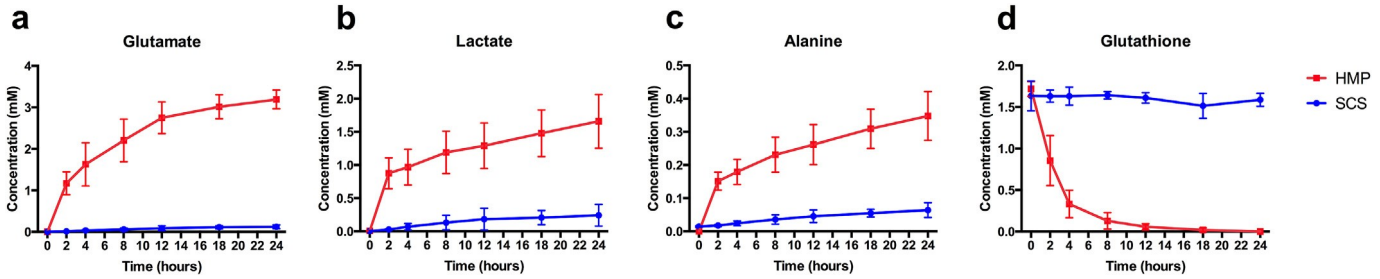

Fig. 2. Concentration of metabolites in the storage fluid of SCS and HMP kidneys over 24 h time period for four example metabolites Values plotted as median (interquartile range)

indiscriminate.

Reduced glutathione is a constituent of the preservation fluid KPS-1 and is thought to play a role in the removal of Reactive Oxygen Species (ROS) generated during metabolism [19] In contrast to the SCS kidney, there is a rapid decrease in the concentration of glutathione in the preservation fluid of HMP stored kidneys and is about 5% of the SCS values after 8 h (Fig. 2d.). The rate of glutathione depletion observed in this study is similar to a previously reported animal model [28] and is likely to reflect cellular uptake of this protective antioxidant. Interestingly, glutathione concentration remained relatively constant in the SCS kidney group. This further reinforces the concept that HMP exerts its beneficial effects, at least in part, by providing access to the cellular components of the kidney during perfusion. Absence of reduced glutathione in tissue demonstrates that not only is this protective antioxidant readily absorbed by the kidney during perfusion but that even after a few hours it is not longer available in the reduced state.

Although the number of organs in each experimental group is small (n ℅), it is comparable to other porcine kidney transplant reports [8,12,15,21,26,30]. To improve validity, samples were processed in triplicate at each timepoint and over 250 NMR spectra were analysed. One strength of this study is that the kidneys stored by HMP or SCS were paired, i.e. from the same pig, thus minimising any metabolic differences arising from polymorphism in cellular mediators of porcine metabolism. Although this approach does not provide functional outcome information for the preserved organ, previous studies have demonstrated good function for otherwise healthy porcine organs stored by either SCS or HMP for similar time periods [2,8,13,15,21,26].

This study demonstrates that in a porcine model, the distribution and amounts of metabolites vary significantly with the storage method (HMP or SCS). The net gain of many central metabolites during HMP conditions further supports the notion that significant metabolism occurs during HMP and this may contribute to the beneficial role of machine perfusion.

Funding

This work was funded through grants from University Hospitals Birmingham Charities and Organ Recovery Systems.

Conflict of interest

As detailed in the funding section, the research was in-part

funded by a grant from Organ Recovery Systems, manufacturers of the LifePort Kidney Transporter used to create conditions of HMP in the laboratory. We do not have any further conflicts of interest to declare.

Acknowledgements

This work was funded through grants from University Hospitals Birmingham Charities (16-5-751) and Organ Recovery Systems.

Appendix A. Supplementary data

Supplementary data related to this article can be found at http://dx.doi.org/10.1016/j.cryobiol.2016.11.006.

References

[1] F O Belzer, J H Southard, Organ preservation and transplantation, Prog Clin Biol Res 224 (1986) 291e303
[2] D Bon, C Billault, R Thuillier, W Hebrard, N Boildieu, O Celhay, J Irani, F Seguin, T Hauet, Analysis of perfusates during hypothermic machine perfusion by NMR spectroscopy: a potential tool for predicting kidney graft outcome, Transplantation 97 (2014) 810e816
[3] S C Burgess, E E Babcock, F M Jeffrey, A D Sherry, C R Malloy, NMR indirect detection of glutamate to measure citric acid cycle flux in the isolated perfused mouse heart, FEBS Lett 505 (2001) 163e167
[4] R M Cannon, G N Brock, R N Garrison, J W Smith, M R Marvin, G A Franklin, To pump or not to pump: a comparison of machine perfusion vs cold storage for deceased donor kidney transplantation, J Am Coll Surg 216 (2013) 625e633 discussion 633e4
[5] E M Chance, S H Seeholzer, K Kobayashi, J R Williamson, Mathematical analysis of isotope labeling in the citric acid cycle with applications to 13C NMR studies in perfused rat hearts, J Biol Chem 258 (1983) 13785e13794
[6] J C Chatham, S J Blackband, Nuclear magnetic resonance spectroscopy and imaging in animal research, ILAR J 42 (2001) 189e208
[7] B J Fuller, C Y Lee, Hypothermic perfusion preservation: the future of organ preservation revisited? Cryobiology 54 (2007) 129e145
[8] A Gallinat, A Paul, P Efferz, B Luer, G Kaiser, J Wohlschlaeger, J Treckmann, T Minor, Hypothermic reconditioning of porcine kidney grafts by short-term preimplantation machine perfusion, Transplantation 93 (2012) 787e793
[9] S Giraud, F Favreau, N Chatauret, R Thuillier, S Maiga, T Hauet, Contribution of large pig for renal ischemia-reperfusion and transplantation studies: the preclinical model, J Biomed Biotechnol 2011 (2011) 532127
[10] A J Guy, J Nath, M Cobbold, C Ludwig, D A Tennant, N G Inston, A R Ready, Metabolomic analysis of perfusate during hypothermic machine perfusion of human cadaveric kidneys, Transplantation 99 (2015) 754e759
[11] J P Hannon, C A Bossone, C E Wade, Normal physiological values for conscious pigs used in biomedical-research, Laboratory Animal Sci 40 (1990) 293e298
[12] S A Hosgood, M Patel, M L Nicholson, The conditioning effect of ex vivo normothermic perfusion in an experimental kidney model, J Surg Res 182 (2013) 153e160
[13] I Jochmans, E Lerut, V Heedfeld, T Wylin, J Pirenne, D Monbaliu, Reproducible model for kidney autotransplantation in pigs, Transpl Proc 41 (2009) 3417e3421
[14] H A Krebs, Rate control of the tricarboxylic acid cycle, Adv Enzyme Regul 8 (1970) 335e353
[15] G La Manna, D Conte, M L Cappuccilli, B Nardo, F D'Addio, L Puviani, G Comai, F Bianchi, R Bertelli, N Lanci, G Donati, M P Scolari, A Faenza, S Stefoni, An in vivo autotransplant model of renal preservation: cold storage versus machine perfusion in the prevention of ischemia/reperfusion injury, Artif Organs 33 (2009) 565e570
[16] C Y Lee, M J Mangino, Preservation methods for kidney and liver, Organogenesis 5 (2009) 105e112
[17] S A Lodhi, K E Lamb, I Uddin, H U Meier-Kriesche, Pulsatile pump decreases risk of delayed graft function in kidneys donated after cardiac death, Am J Transpl 12 (2012) 2774e2780
[18] C Ludwig, U L Gunther, MetaboLabeadvanced NMR data processing and analysis for metabolomics, BMC Bioinforma 12 (2011) 366
[19] R J Mailloux, S L McBride, M E Harper, Unearthing the secrets of mitochondrial ROS and glutathione in bioenergetics, Trends Biochem Sci 38 (2013) 592e602
[20] C R Malloy, A D Sherry, F M Jeffrey, Analysis of tricarboxylic acid cycle of the heart using 13C isotope isomers, Am J Physiol 259 (1990) H987eH995
[21] T Minor, A Paul, P Efferz, J Wohlschlaeger, U Rauen, A Gallinat, Kidney transplantation after oxygenated machine perfusion preservation with Custodiol-N solution, Transpl Int 28 (2015) 1102e1108
[22] C Moers, J M Smits, M H Maathuis, J Treckmann, F van Gelder, B P Napieralski, M van Kasterop-Kutz, J J van der Heide, J P Squifflet, E van Heurn, G R Kirste, A Rahmel, H G Leuvenink, A Paul, J Pirenne, R J Ploeg, Machine perfusion or cold storage in deceased-donor kidney transplantation, N Engl J Med 360 (2009) 7e19
[23] C Moers, J Pirenne, A Paul, R J Ploeg, G Machine Preservation, Trial Study, Machine perfusion or cold storage in deceased-donor kidney transplantation, N Engl J Med 366 (2012) 770e771
[24] J Nath, A Guy, T B Smith, M Cobbold, N G Inston, J Hodson, D A Tennant, C Ludwig, A R Ready, Metabolomic perfusate analysis during kidney machine perfusion: the pig provides an appropriate model for human studies, PLoS One 9 (2014) e114818
[25] J Nath, T Smith, A Hollis, S Ebbs, S W Canbilen, D A Tennant, A R Ready, C Ludwig, (13)C glucose labelling studies using 2D NMR are a useful tool for determining ex vivo whole organ metabolism during hypothermic machine perfusion of kidneys, Transpl Res 5 (2016) 7
[26] M L Nicholson, S A Hosgood, M S Metcalfe, J R Waller, N R Brook, A comparison of renal preservation by cold storage and machine perfusion using a porcine autotransplant model, Transplantation 78 (2004) 333e337
[27] J M O'Callaghan, R D Morgan, S R Knight, P J Morris, Systematic review and meta-analysis of hypothermic machine perfusion versus static cold storage of kidney allografts on transplant outcomes, Br J Surg 100 (2013) 991e1001
[28] K Ormstad, T Lastbom, S Orrenius, Evidence for different localization of glutathione oxidase and gamma-glutamyltransferase activities during extracellular glutathione metabolism in isolated perfused rat kidney, Biochim Biophys Acta 700 (1982) 148e153
[29] J H Southard, F O Belzer, Organ preservation, Annu Rev Med 46 (1995) 235e247
[30] M J Taylor, S C Baicu, Current state of hypothermic machine perfusion preservation of organs: the clinical perspective, Cryobiology 60 (2010) S20eS35

5.2 Manuscript commentary.

5.2.1 Lactate and the hypothermicly stored kidney

This paper successfully characterises differences in the metabolic profile of cortical metabolites in kidneys stored by SCS or HMP.

Findings of particular interest include the observation that when compared to HMP, cortical levels of lactate are significantly elevated in SCS kidneys when compared to those stored by HMP. Other differences reported in tissue metabolic profiles included succinate, acetate, fumarate and formate. While intriguing, these metabolites are identifiable only as a single peak on the ^{1}H NMR spectrum and their assignment is subjective. Since ^{1}H NMR was the only analysis performed in this study, no conclusions were drawn from their detection to retain objectivity. Future studies could resolve the identity of these metabolites by spiking the samples with defined concentrations of the suspected metabolites and determining whether the peaks increasing in intensity matches that of the single detected peaks.

Metabolites were identified when there were either multiple signals (i.e. peaks at different chemical shifts) that matched library profiles of a given metabolite, or the J coupling at a single chemical shift permitted confident characterisation of the metabolite. A good example of this is lactate, which has a doublet structure at 1.3ppm that can be used to identify the metabolite.

Lactate has been described as being ‘at the cross roads’ of metabolism and inflammation(269), with tissue accumulation linked with inferior transplant outcomes through processes such as increased anaerobic metabolism and tissue acidification(270).

However, an alternative explanation for cortical lactate accumulation could stem from the central role the kidney plays in lactate uptake and metabolism(271). The higher levels of lactate in SCS kidneys could infer enhanced uptake of this nutrient, however the absence of flow intrinsic to SCS makes this explanation seem unlikely. The missing piece in this puzzle is the evidence suggesting that cortical lactate in SCS is increased because of cortical glucose metabolism.

In any case, elevated lactate concentrations after preservation or during reperfusion are repeatedly associated with the development of DGF in the literature (272).

With SCS being linked to increased likelihood of DGF development(94,273) preventing intracellular accumulation of lactate may be a potential metabolic mechanism through which HMP, which affords limited tissue reoxygenation exerts a protective effect. The mechanism through which HMP affords reduced tissue lactate accumulation over SCS, despite intuitively greater glucose delivery is yet to be established.

5.2.2 Limitations of this study

The whole organ model is an invaluable simulation of renal physiology during organ preservation, but is subject to several limitations that may impact the conclusions drawn in the manuscript.

Namely, ‘cortical’ metabolites detected in the whole organ study will include extracellular metabolites trapped within the vasculature and tubulature during snap freezing.

While the perfusate within HMP kidneys is continually flushed into the bathing fluid, the absence of fluid flow in SCS kidneys limits the extra-renal release of intraluminal metabolites to that permitted by diffusion. The presence of flow in HMP may result in metabolite washout, while its absence must result in some degree of intraluminal metabolite accumulation in SCS.

A systems approach was designed in an effort to account for this, in which the total concentration for a given metabolite was calculated from the contribution of tissue profile (corrected by whole kidney weight) and storage fluid profile (corrected for by residual perfusate volume).

For the metabolites known to be produced *de novo* during HMP (i.e. alanine, lactate and glutamate(235), metabolic profiling of perfusate grants a good reflection of cortical metabolic profile (Figure 8.4). However, this does not mean the system approach can be applied to the entire kidney in SCS. Although several metabolites were found to differ between storage modalities using the systems approach, the validity of the results gleaned using this method as a whole are subject to several key assumptions.

5.3 Assumptions of the systems approach

5.3.1 Assumption 1-SCS fluid is representative of intraluminal fluid.

The first assumption on which the systems approach depends is that the fluid bathing the SCS stored kidney is reflective of the metabolic profile of the intraluminal or even extra cellular environment, i.e. that diffusion under static storage is sufficient to result in equilibration between the two fluid extra renal and intrarenal fluid compartments.

A simple experiment was designed to test this, in which 3 pairs of porcine kidneys were acquired submitted to 6 hours HMP or SCS, with the slight modification that the preservation fluids were modified to contain 0.3% trypan blue dye, used routinely in cell culture laboratories as an indicator of cell viability.

As shown in Figure 5.1, diffusion during SCS does not appear to appear to result in any tangible equilibration of intravascular and bathing fluid compartments, with the total

absence of any visible colouration in any SCS stored tissues, contrasting with consistently blue medullary and cortical colouration under HMP.

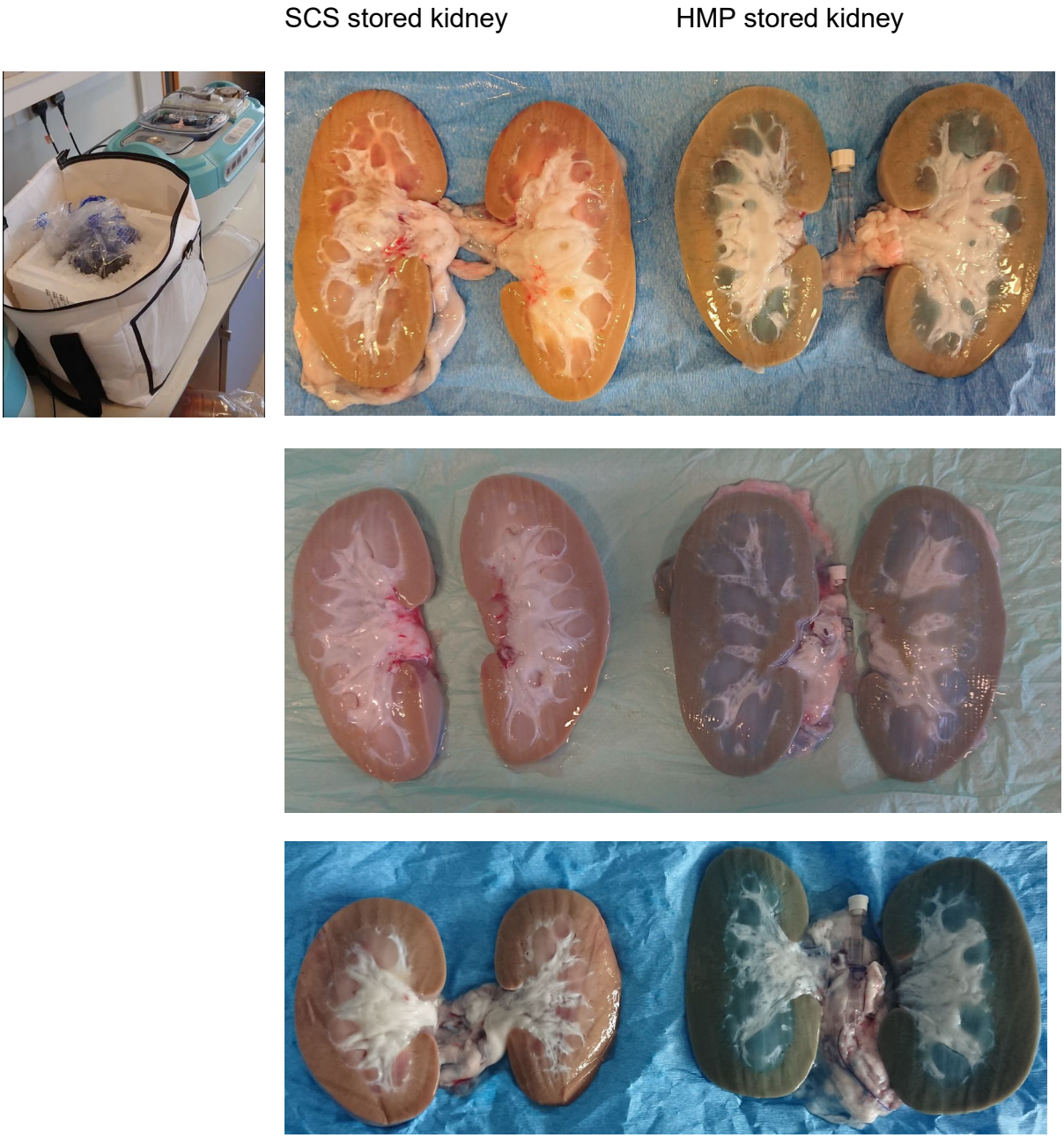

Figure 5.1 Different staining of HMP and SCS kidneys using trypan blue

Discolouration of renal tissues by 0.3% trypan blue dye during Static Cold Storage and Hypothermic machine perfusion. SCS kidneys were left remarkably unaffected by the dye, whereas HMP kidneys were consistently stained blue, particularly in the renal medulla but also consistently in the cortex.

This observation has stark implications on the efficacy of static preservation fluids as a whole, which do not permeate the SCS stored kidney to any great extent.

Additionally, in terms of the findings from the attached manuscript, if diffusion of luminal fluid components into the kidney is restricted as Figure 5.1 would suggest, then the reverse is intuitively true. Sampling the fluid surrounding the static kidneys is unlikely to give a quantitative analysis of fluid stored within the kidney.

This does help explain surprising findings from the whole organ manuscript, in which fluid glutathione was not found to be depleted under static storage, and that fluid concentrations of lactate and alanine where higher in the HMP fluid despite being at markedly higher concentrations in the samples tissue after SCS. In Figure 8.4, it is shown that HMP perfusate is a good indicator of cortical metabolic profile. Tissue concentrations of hypoxanthine were not found to be significantly higher in SCS, despite the fact that UW contains allopurinol, a xanthine oxidase inhibitor and also is not subject to the metabolic washout experienced by HMP stored kidneys. These observations point to either ineffectual action of allopurinol under hypothermia, or restricted access of allopurinol into the intracellular space, supporting the SCS-no flow speculation.

5.3.2 Assumption 2- Tissue weight reflect the same biomass between HMP and SCS samples

A second assumption of the systems approach is that the wet weight of the HMP and SCS tissues is composed of equal ratios between fluid and tissue compartments. Though a consistent weight of tissue (wet weight of 0.5g) was extracted, the known vasodilatory effect of HMP (Chapter 1) may indicate that greater volumes of perfusate were snap frozen *in situ* within the tissue than occurred in the SCS kidneys. Conversely, the vasospasm

which occurs during kidney preservation in UW(103) indicates the weight measured contains less fluid and a greater cellular contribution to that half gram of frozen tissue .

Metabolite quantification may therefore be affected by differences in vessel luminal diameter between the two modalities.

5.3.3 Assumption 3- The metabolic profile of the tissue sampled is reflective of the whole organ

Since the kidney tissue profile was multiplied by the weight of the kidney, a third assumption of the systems approach is that the metabolic processes within the tissue profiled (i.e. the cortex) is representative of the whole kidney.

The renal cortex maintains higher oxygen pressures than the medulla to fulfil the aerobic demands of the significant transport activities occurring in this tissue(65)

In Chapter 8 it is shown have shown that this holds true during hypothermic preservation, with oxygen supplementation during HMP resulting in significant elevation in indicators of TCA cycle and electron transport chain activity in cortical, but not medullary tissues(274).

It is unknown if all renal tissues under standard HMP or SCS have a similar metabolic profile, this should be validated prior to deployment of the systems approach.

6 *In vitro* dissection and modification of HMP and SCS environments

6.1.1 Introduction

The data presented in Chapter 5 shows a clear accumulation of lactate and alanine within the renal cortex during SCS storage. These metabolic differences may be related to the apparent benefit of HMP over SCS.

A criticism of that work is that it did not seek to identify the mechanisms causing the different metabolic profiles, or evidence whether these changes were beneficial or deleterious. While linking the metabolic profiles detected with indicators of damage was not the purpose of the attached manuscript, this is an undeniably important consideration if the data are to be used to optimise organ preservation.

However, the low throughput, paired whole organ model is limited in its capacity to achieve this. Using the whole organ model, it is unclear whether or not metabolic differences detected between HMP and SCS stored tissue arise through different metabolic processes, or are a consequence of coincidental environmental differences, such as the absence of fluid circulation in SCS.

If there is a beneficial modulation of metabolism caused by HMP, it is unclear which aspects of HMP (i.e. differences in fluid composition (Table 1), oxygen availability (Figure 6.3) or the physical existence of perfusion are responsible and are therefore grounds for optimisation.

Cell line models have an advantage in that the uniform growth area ensures a consistent biomass per sample, and this biomass is easily isolated from the bathing fluid.

The combination of the ShearFAST assisted cell rocker model described in Chapter 4 and the hypoxia chamber filling circuits described in Chapter 3 permit *in vitro* dissection of complex HMP and SCS preservation environments (Figure 6.2). Therefore, assessment of the isolated impacts of preservation fluid, flow dynamics and oxygen availability becomes more easily accessible.

Another finding from Chapter 6, which has also been reported elsewhere(275) was that in HMP, the level of glutathione in the circulating perfusate becomes rapidly depleted. Enhanced antioxidant supplementation may therefore be beneficial during HMP. The cell model is well suited to investigate the effects of different preservation environments and to screen the *in vitro* benefits of enhanced antioxidant supplementation. The following three *in vitro* studies are described in this section:

6.1.2 Study 1: Identification of environmental stimuli governing cellular viability and metabolism

When used together, the *in vitro* methods described in Chapters 3 and 4 permit dissection of complex organ storage environments (Figure 6.2), allowing definition of their isolated and combined effects. This required prior characterisation of the level of hypoxia prevalent during organ preservation, which is the first experiment described. This study complements the findings of the whole organ study experiments in Chapter 5 by illuminating differences in cellular damage or metabolic profile arising *in vitro* from differences in preservation fluid composition, oxygen availability or fluid flow.

6.1.3 Study 2: Assessing fluid metabolites for their potential as biomarkers *in vitro*

^{1}H-NMR analysis of HMP perfusates has been proposed as a useful screening tool for the assessment of kidney quality pre-implantation, with the observation of higher alanine and

glutamate concentrations a predictor of inferior transplant outcomes(275). Similar work from our own group has highlighted increased glucose uptake as a potential predictor for the development of DGF(109).

Study 2 investigates whether when removed from confounding factors such as retention of fluid in the organ, ^{1}H-NMR profiling of the storage fluid from each well bathing the cells used in study 1 yields any correlation with the measures of cell damage used for the monolayer in that same well. This studies aim is therefore to establish whether a metabolic biomarker of cell damage can be established *in vitro*, which is independent from differences in fluid flow dynamics between kidneys.

6.1.4 Study 3: Screening the merits of increased antioxidant provision *in vitro*

Inspired by the observation that HMP results in the rapid and total depletion of intracellular glutathione(276), this study sought to establish whether enhanced fluid glutathione supplementation resulted in reduced cellular damage *in vitro*.

Speculated in Chapter 1, and noted in personal communications with key figures in organ preservation research (Appendix 2), is the query surround whether or not HES crosses the glomerulus and enters the proximal tubule lumen during HMP. Therefore, the structures downstream from the glomerulus may be left without colloidal protection, resulting in cellular damage.

Polyethylene glycol (35kDa) (PEG 35kDa) is an colloid with antioxidant properties(277). PEG (35kDa) also has a molecular weight compatible below the generally accepted molecular weight cut-off for glomerular filtration (70kDa). Importantly, PEG (35kDa) has been shown to exert a beneficial effect in *in vitro* models of static storage(130) where as HES has been shown to confer injury *in vitro*(278) and potentially in the whole kidney(279)

Parallel to the *in vitro* study investigating the effect of glutathione supplementation, a modified variant of UWMPS, containing 30g/L polyethylene glycol (35kDa) instead of HES was assessed for its protective potential.

The ultimate aim of these three studies was to identify preservation modifications that lead to *in vitro* benefit, and provide *in vitro* evidence in the definition of a metabolic biomarkers relevant to organ preservation. These insights would be used to direct further whole organ experiments later in the chapter.

6.2 Methods

6.2.1 Study 1: Identification of environmental stimuli governing cellular viability and metabolism

6.2.1.1 Defining oxygen depletion during the HMP of porcine kidneys.

Chapter 3 details the development of a hypoxia chamber filling circuit with which the researcher can programme defined degrees of fluid oxygenation *in vitro*. In order to indicate the level of hypoxia pertinent to the porcine DCD model, 6 pairs of porcine kidneys were procured and perfused by standard HMP for 18 hours, but using perfusion circuits which had been modified to incorporate a flow through oxygen sensor (Figure 6.1). This allowed rapid continuous sampling of perfusate oxygen levels. Oxygen readings were taken every 5 minutes during the first hour of perfusion, every 10 minutes between 1 and 2 hours and then extending to every 30 minutes-1 hour as perfusion proceeded. The different timepoints were selected to preserve sensor integrity, as these have a finite number of readings before they are depleted.

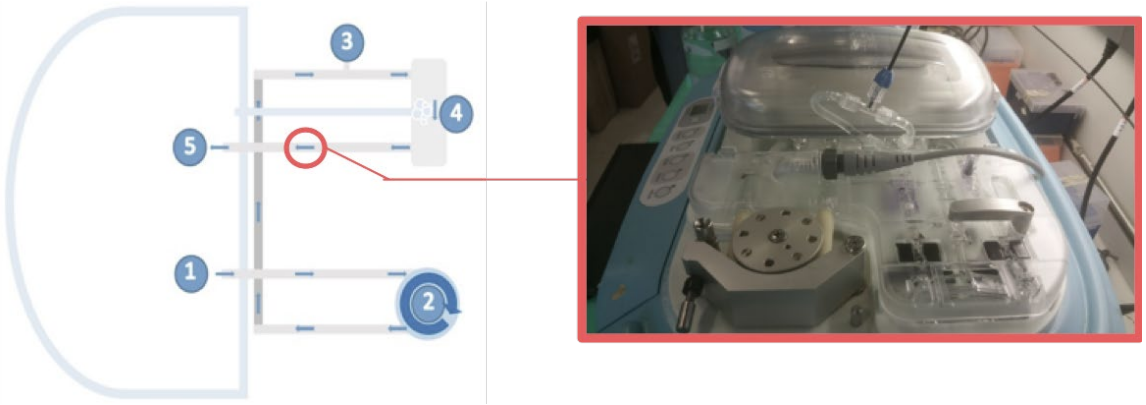

Figure 6.1. Installation of a flow-through O_2 sensor in the standard LifePort® circuit.

An incision was made in the tubing leading from the LifePort® cassette to the renal artery and an extended section of sterile tubing allowed placement of the flow-through oxygen sensor.

For a single kidney, the oxygen levels within circulating perfusate within the arterial inflow limb and within the venous effluent were measured using a needle type oxygen sensor, giving a single indication of oxygen consumption throughout the standard HMP preservation period (Figure 6.3). Perfusate oxygenation was assessed every 2 hours using the needle type-sensor.

6.2.1.2 The effect of preservation fluid on intracellular metabolic profile after hypoxic storage.

Metabolic changes were found to exist between HMP and SCS stored kidneys. The following *in vitro* simulation was designed to determine whether these could be explained differences in the preservation fluid itself, when all other environmental factors were equal. RPTEC/TERT1, grown to confluence in in 10cm dishes were submerged in 240µl/cm^2 UW or UWMPS (n=5). Both sets were placed in the same hypoxia chamber to potential differences in environment, outside of fluid composition. The chamber was purged with nitrogen at 0.6L/min to generate the near total anoxia observed by 8 hours HMP in the

porcine model (Figure 6.3). The sealed chamber was moved to a cold room to instigate 24-hour hypothermic storage. Following this, the metabolic profiles of extracted cells was assessed by ^{1}H-NMR (Figure 6.4).

6.2.1.3 Fluid effects on cellular viability and LDH release in different environments

RPTEC/TERT1, cultured in 48 well plates were washed and submerged in 240µl/cm^2 UW, UWMPS or cell culture media. One plate was placed in a standard cell culture incubator and the other in a sealed hypoxia chamber, which was then purged as before with nitrogen gas to generate severely hypoxia/ anoxia. After 24-hour storage, the plates were retrieved. The supernatants were harvested for assessment of LDH release and the monolayers used for SRB analysis of cellular viability. In this experiment the media stored cells in both environments were used as the controls, i.e. the measures reported for UW and UWMPS stored cells are percentages of the SRB or LDH absorbance values observed from cells stored in media

This experiment is included for illustrative purposes, after being abandoned upon realisation that UW does not appear to permeate the cold-stored kidney (Figure 5.1). As such data are presented as relative measures ± standard deviation, and no statistical assessment was performed given the small number of biological replicates.

6.2.1.4 In vitro simulation of the physical extremes of HMP and SCS storage.

RPTEC/TERT1, collated from a single pool of cells was cultured in four 48 well plates (Greiner BioOne, Germany, Cat:677102).

Upon reaching confluence, the media was discarded and ~123.5µl of chilled UWMPS (mean viscosity of 0.00857 Pa.s, (Figure 3.2) was added to each well (n=6) in each plate

(n=4). Using a paired nitrogen filling circuit (Figure 3.5) and an N_2 gas flow of 0.6L/min, two hypoxia chambers, each containing a single plate were simultaneously purged of oxygen. Meanwhile, otherwise identical plates were left exposed to the atmosphere during chamber filling. After filling, all plates were moved to a cold room to maintain 18-hour hypothermia.

Within both hypoxic and atmospheric oxygen groups, half of the plates were submitted to FSS in the region of 1 dyne/cm^2 using the ShearFAST assisted cell rocker method described in Chapter 4, and the remaining half stored statically on the benchtop.

In this manner four different preservation environments were instigated (i.e. stasis with hypoxia (SH), static under atmospheric oxygen (SN), fluid shear stress under hypoxia (FH) and fluid shear stress under atmospheric oxygen (FN) (Figure 6.2). This experiment was repeated 9 times.

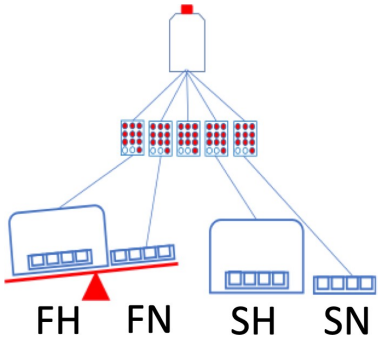

Figure 6.2. Illustration of the generation of 4 separate preservation environments

Key: (FH) fluid shear stress under hypoxia, (FN) fluid shear stress under atmospheric oxygen, (SH) Static storage under hypoxia and (SN) static storage under atmospheric oxygen. A cold room was used to maintain hypothermia in the chilled preservation fluid.

After 18 hours of hypothermic storage, the isolated and combined effects of relevant HMP parameters were assessed using the SRB assay.

To foster comparisons between experiments, the data in each individual technical replicate was converted to a percentage of the average absorbance exhibited by a control group run with each experiment(263) . The control group selected was static storage under atmospheric oxygen (SN). The rationale for this was that such an environment could not be generated in clinical organ preservation and also, was the most simple and consistent condition to reproduce between biological replicates. In four of these replicates, the LDH activity in the bathing fluid was also assessed (n=5).

Whether or not the SRB and LDH assays are both necessary components of the high throughput model, (i.e. if they provide equivocal data) was examined through a correlation analysis using Spearman's R test (Figure 6.8).

6.2.1.5 Effect of varying the level of shear stress on of cell viability

RPTEC/TERT1 were cultured in 96 well plates and divided into 2 groups, plates that would experience different degrees of FSS (n=5) and plates that would be left statically. Each plate was incubated in UWMPS, the volume of which varied by column on each plate. Column 1 received 20µl, and each successive column received an additional 5µl up to a final volume of 50µl. The FSS plates were rocked as before, with the increasing fluid volumes resulting in generation of ever decreasing levels of FSS as determined using the ShearFAST assisted rocking mode. This is illustrated in Figure 6.9.

Static plates served as a control with which to gauge the independent effect of varying fluid volume. Monolayer integrity after 18-hour storage under these conditions was assessed using the SRB assay. Whether slopes differed significantly between experimental conditions was assessed using regression analysis (GraphPad Prism 8, Mac OSX) with significance determined when $p<0.05$.

6.2.2 Study 2: Assessing fluid metabolites for their potential as biomarkers *in vitro*

For each well in the above experiment, the normalised SRB (n=162) and LDH data (n=94) was assessed for its correlation to normalised (i.e. % of SN control) fluid metabolite signals attained using ^{1}H-NMR (Figure 6.10 and 6.11 respectively).

Spearman's R test was used to determine the correlation coefficient between variables, with significant correlations determined at with $p<0.05$.

6.2.3 Study 3: Screening the merits of increased antioxidant provision *in vitro*

With the correlation between lactate and LDH suggestive of membrane insult through anaerobic metabolism (Figure 6.11) the relative benefits of increased antioxidant delivery were assessed.

RPTEC/TERT1 were cultured in 48 well plates (Greiner- BioOne Ltd, Germany, Cat:677102) and incubated in one of four UWMPS variants (Factory UWMPS, In-house MPS containing 30g/L PEG 35kDa instead of HES, or in-house UW MPS without colloid. Plates were stored under hypoxia or atmospheric oxygen, and cellular pathology after 18-hour hypothermic preservation inferred using the LDH assay (Figure 6.12). In a separate *in vitro* experiment, the effect of increasing fluid glutathione concentrations to 10mM after 18 our storage under hypoxia was assessed by the SRB and LDH assays, with results reported relative to a UW control. (Figure 6.13). The effect of this glutathione supplementation strategy was later validated using the *ex vivo* porcine model.

Whole organ experiments, in which one kidney from each pair received UWMPS, or UWMPS containing 10mM glutathione were performed by Dr. Charlotte Turnbull (Appendix 4). This provided perfusate samples for LDH analysis.

6.3 Results

6.3.1 Study 1: Identification of environmental stimuli governing cellular viability and metabolism

6.3.1.1 Oxygen depletion during HMP of porcine kidneys

At initiation of perfusion, the oxygen contained in the preservation fluid was found to be around 242.73 hPa (range 220.26-271.46 hPa.), By 45 minutes, this had fallen to 147.87 hPa (range 78.93—181.64 hPa) and by 2 hours the perfusate oxygen had fallen to 42.54 hPa, range 12.52-79.91 hPa). The oxygen levels plateaued at around 6 hours both circuits had less than 20 hPa oxygen remaining.

(Figure 6.3A). Continuous monitoring of the oxygen dissolved in fluid immediately prior to its entry into the kidney revealed that by 6-10 hours of perfusion the dissolved oxygen had been effectively depleted.

Analysis of the fluid exuding from the renal vein revealed that at initiation of HMP, i.e. after 2-hour CIT in SCS the fluid exuding from the renal vein has an oxygen concentration around 10 times lower less than that being delivered at the renal artery (Figure 6.3B). Within an hour of perfusion, the had become became anoxic.

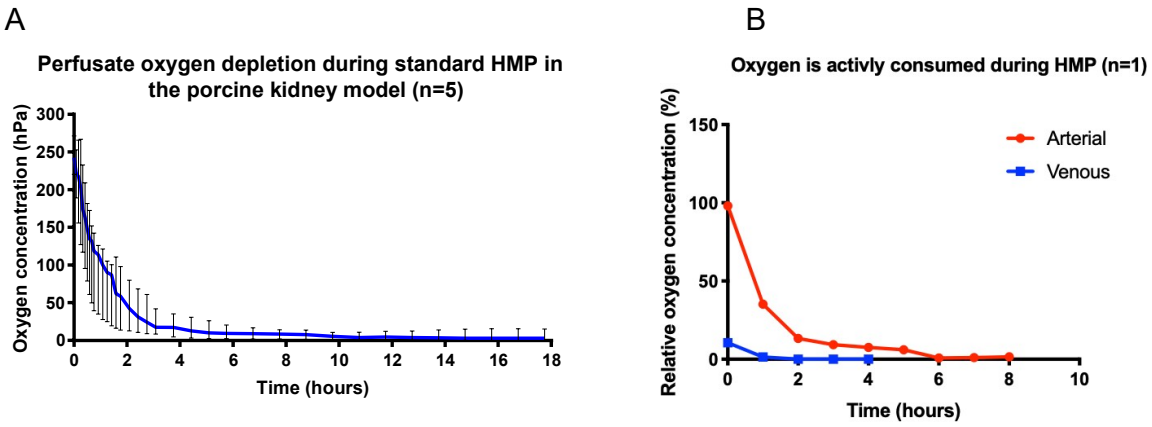

Figure 6.3. Perfusate oxygen depletion during HMP of porcine kidneys as assessed using an inline oxygen sensor (A) and a needle type oxygen sensor (B)

6.3.2 Cellular effects of isolated HMP and SCS parameters

6.3.2.1 Effect of fluid composition on cellular metabolic profile

After 18 hours of hypothermic, anoxic storage in either UW or UW MPS, cells were extracted and metabolic profiles were assessed by ^{1}H NMR (Figure 6.4).

^{1}H-NMR analysis revealed total depletion of intracellular glucose stores in UW stored cells, compared to maintenance of median intracellular glucose concentrations of 8.29 mM (range 7.21-13.36 mM) in UWMPS. Lactate was also elevated in UW stored extracts with a concentration of 2.35mM (range 1.54-2.83 mM) vs 1.18 mM (range 0.66-1.64 mM) in UWMPS). However, these differences did not attain statistical significance (p 0.0625 for both metabolites).

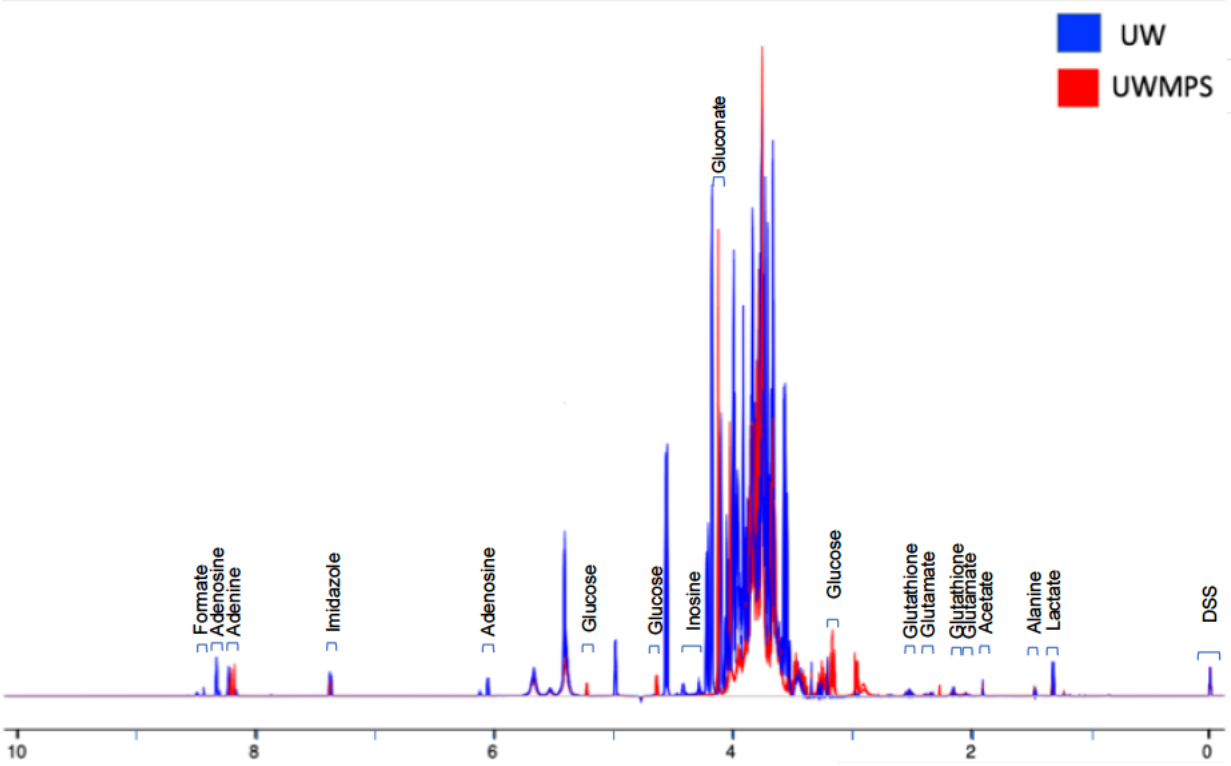

Figure 6.4. Metabolic differences in cell monolayers stored in UW or UWMPS.

6.3.2.2 Effect of fluid composition on cellular viability and LDH release in different environments

As shown in Figure 6.5, fluid selection plays a visible role in maintenance of the cell monolayer under normothermic storage, with use of UW resulting in visible cell death.

The control environment (i.e. storing in cell culture media) predictably displayed the greatest viability over the UW and UW MPS (52.56 %, range 44.31-53.50% and 77.71%, range 72.49-80.94% respectively) (A). UWMPS was observed to better protect the cells than UW in this environment. These differences in cell viability were complemented by the LDH data, with the media control exhibiting the lowest LDH release (C), followed by storage in UWMPS, followed by storage in UW (1882.67%, range 1110.91-4397.57% and 2741.16%, range 1465-4770.84% respectively).

Hypothermic storage of cells in UWMPS resulted in a marginally higher mean absorbance than storage in UW or media (B). These differences were very slight (i.e. ~5%) and were mostly complemented by the LDH data, in which storage of cells in UW exhibited the higher LDH release than storage of cells in UWMPS (D), Interestingly, cell culture media was observed to result in the lowest LDH release at all temperatures and oxygen environments (C and D).

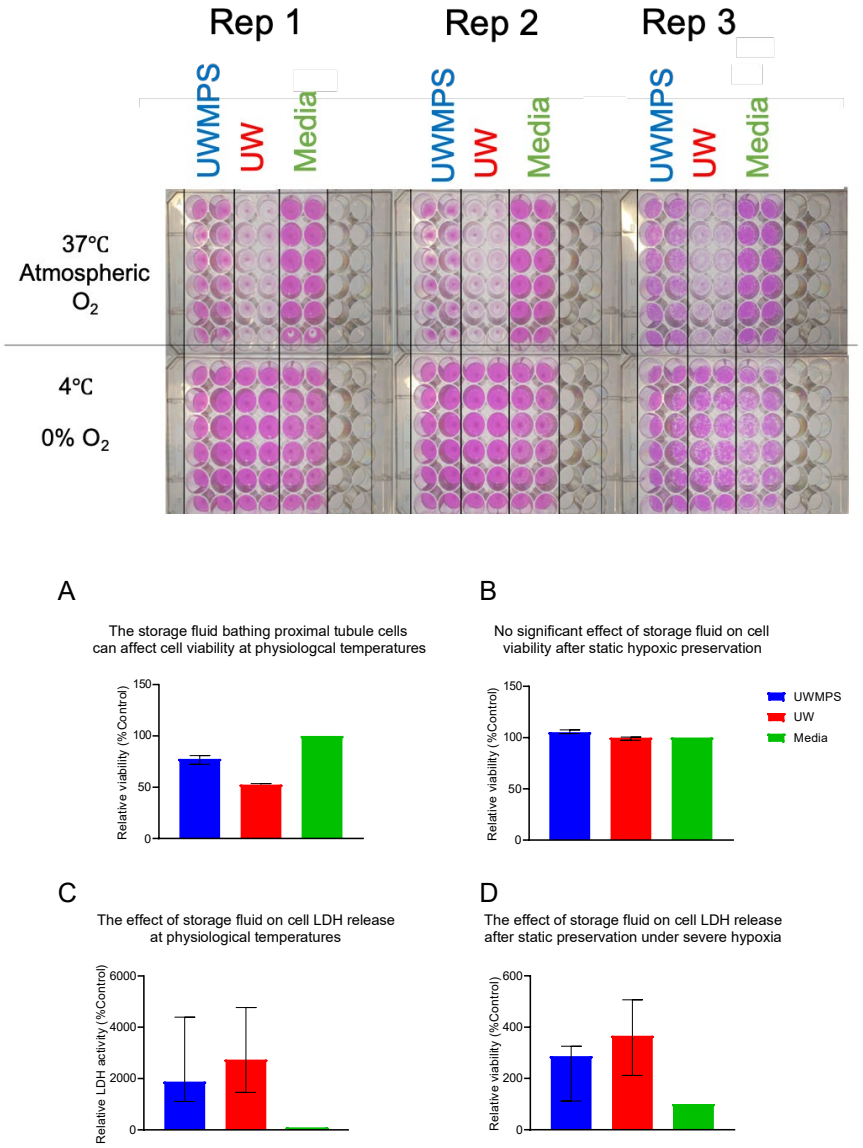

Figure 6.5. Screening the effect of preservation fluid and temperature on cell damage as assessed through the SRB (A and B) and LDH assays (C and D).

6.3.2.3 *Effect of Fluid shear stress and oxygen availability on cellular viability after hypothermic storage*

The physical presence of perfusion may be a factor contributing to the benefit of HMP over SCS. However, whether this benefit is driven by mechanical stresses across the cell membranes, fluid mixing, or through tissue reoxygenation is unclear.

Using the novel *in vitro* model, each possible combination of fluid flow profile and oxygen availability was created and the stimuli modulating cell viability in the 4-way comparison was assessed using the SRB assay (Figure 6.6).

Static storage under hypoxia was found to cause the greatest insult to RPTEC/TERT1, with a viability 93.26% (range, 77.34-99.45%) that of the atmospheric control ($P<0.004$). Additionally, generation of 1 dyne/cm^2 shear stress exerted a protective effect under hypoxic storage, with an increase in viability (median 97.14%, range 88.31-105.88%) compared to cells stored under fluid stasis ($p<0.04$) However, the combined effect of atmospheric oxygen and 1 dyne/cm^2 shear stress did not translate to any change in cellular viability compared to the control condition static atmospheric storage.

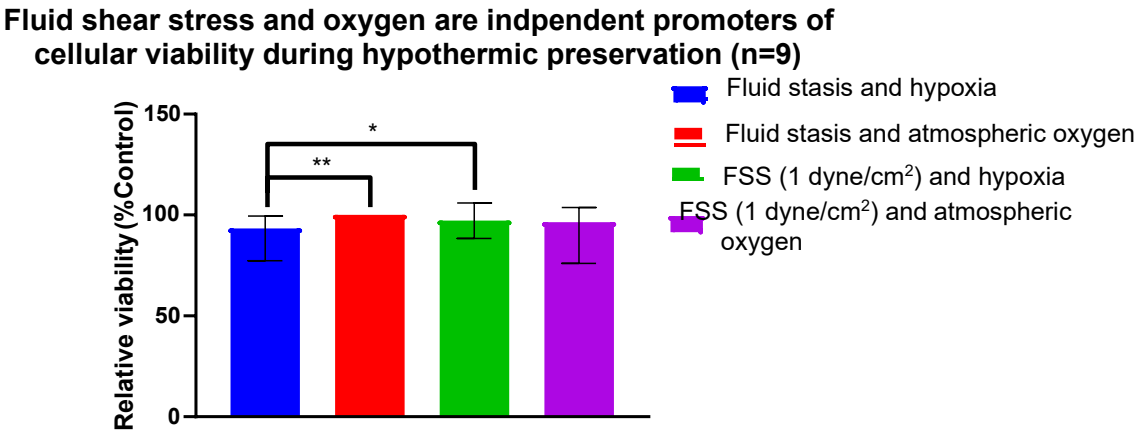

Figure 6.6. The effect of physical environment on cellular viability. In each replicate, the data from each condition was normalised to the replicate control value (i.e. fluid stasis with atmospheric oxygen) at the experimental endpoint.

Preliminary data suggests elevation of *in vitro* oxygen tensions to atmospheric oxygen or generation of shear stress does not appear to change the level of LDH release by hypothermicly stored proximal tubule cells (Figure 5.7).

When compared to static cells under atmospheric oxygen, generation of hypoxia or shear stress did not appear to radically alter LDH release (Relative levels of 65.94%, range 47.71-163.42% and 81.22%, range 63.47-144.29% respectively. Combined, these stimuli resulted in a mean elevation in relative LDH (169%, range 86.74-185.32%) The effect of oxygenation on LDH activity is more thoroughly examined in Chapter 8 onwards.

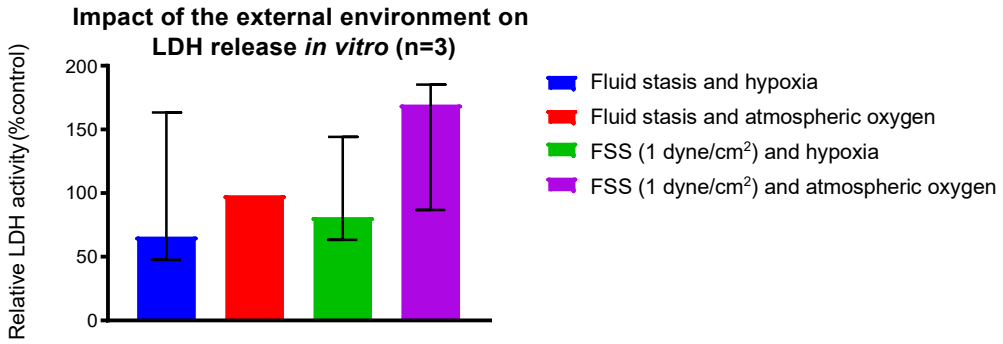

Figure 6.7. The effect of the extracellular environment on LDH release *in vitro*

6.3.2.4 *Correlating relative cell viability with relative LDH release*

A disadvantage of using the SRB assay to indicate viability is the loss of cell monolayer, which could be used for other purposes. To access whether or not the LDH assay could be used as a surrogate, a correlation analysis between the measures reported by the SRB and LDH assays was performed (Figure 6.8)

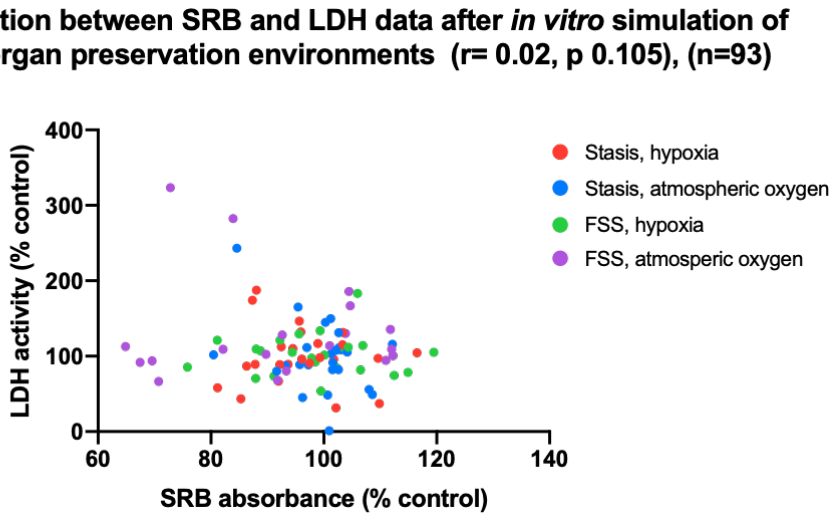

Figure 6.8. Assessment of correlation between relative cell viability and LDH activity

The relative viability of 93 well across the four preservation conditions was assessed by the SRB assay was assessed for correlation with the relative LDH activity reported in the fluid bathing the same monolayers No correlations were observed between the SRB and LDH data results in any condition or when the results of each environment were pooled.

6.3.2.5 *Does FSS magnitude affect proximal tubule cell viability in vitro?*

We have demonstrated that the presence of 1 dyne/cm^2 exerts a protective effect on hypothermicly stored proximal tubule cells. To determine whether varying the level of FSS affect cell viability, a 'dose/response of FSS induction was performed, and is detailed in Figure 6.9. In cells stored statically and subjected to varying degrees of shear stress, the act of increasing fluid volume appeared to decrease cell viability, although the difference

was not found to be significant (p=0.06) Across the range of shear stresses tested, generation of FSS yielded evidence of a protective effect when compared to cells stored statically. The slope of both curves was found to differ significantly following linear regression analysis (p 0.0064).

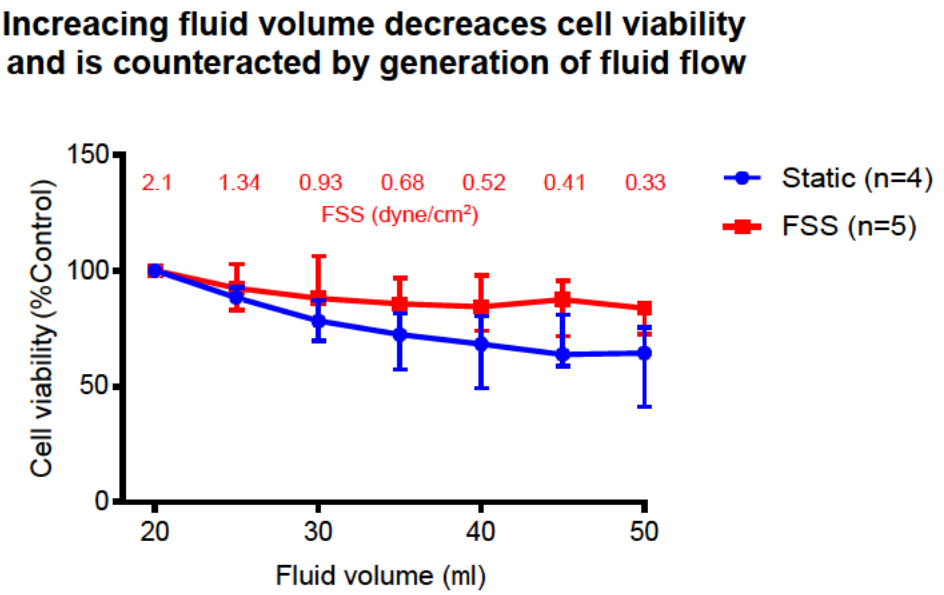

Figure 6.9. Protective effect of FSS over a range of fluid volumes. Cell Viability across different fluid volumes is reported as percentage of the control volume (i.e. 20 μl) in static or rocked plates.

6.3.3 Study 2: Assessing fluid metabolites for their potential as biomarkers *in vitro*

Correlation analysis revealed that fluid profile is linked with measures of cellular viability using the SRB assay (Figure 6.100), and indicators of membrane pathology using the LDH assay (Figure 6.12). Relationships between particular metabolites are described below

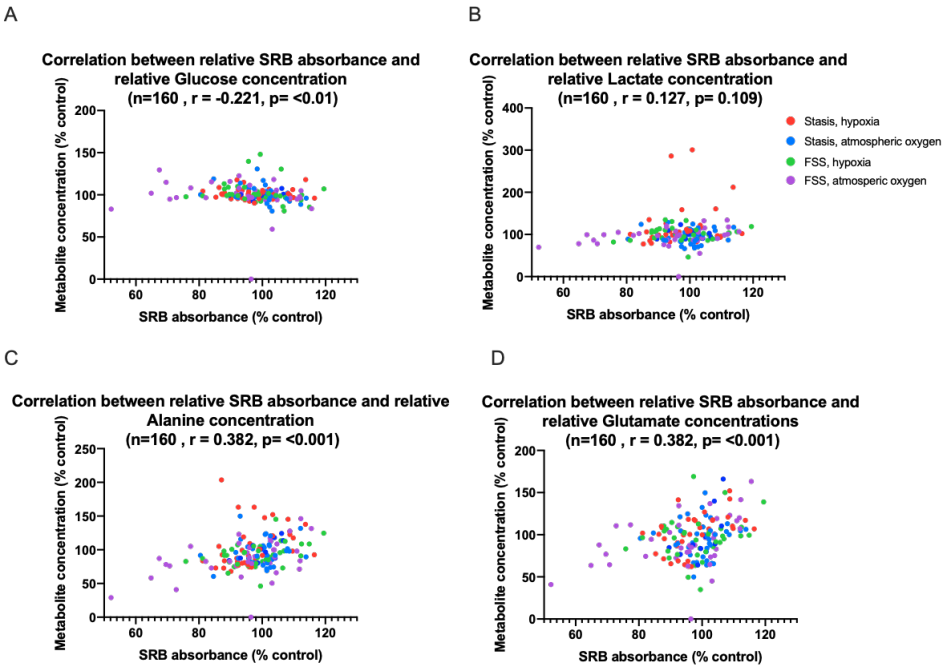

Figure 6.10. Correlations between the relative cell viability and fluid metabolic profile

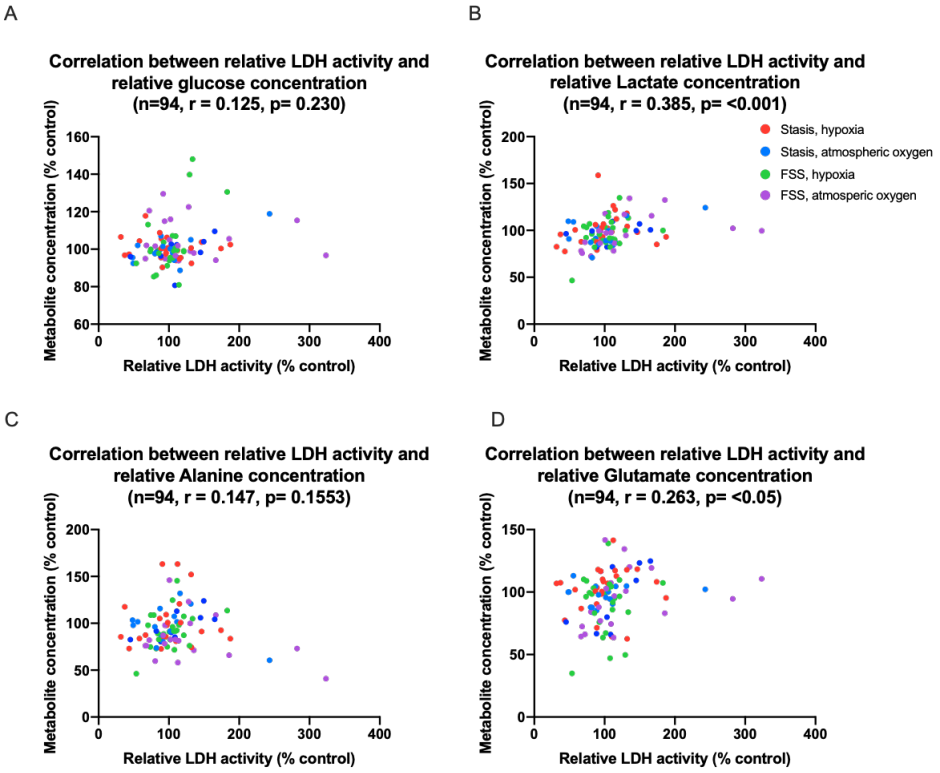

Figure 6.11. Correlation analysis between fluid LDH and metabolic profile

6.3.3.1 Glucose

A slight inverse relationship between SRB absorbance and fluid glucose levels were noted (Figure 6.10A). No significant correlation was observed when the four environmental conditions were assessed independently, and LDH release was not found be linked to perfusate glucose levels when assessed collectively or by individual storage condition (Figure 6.11A).

6.3.3.2 Lactate

Cell viability at the end of the preservation time was not found to be linked to lactate production for the majority of conditions or when all data was collated and assessed (Figure 6.10B). However, lactate levels were found to be linked to percentage viability under the FSS with atmospheric oxygen environment (r=0.387, p 0.0179)

Additionally, in when all conditions were examined together, fluid lactate release was found to be linked to LDH release R=0.385, p=0.001) (Figure 6.11B). This observation did not retain significance when the storage conditions were assessed in isolation.

6.3.3.3 Alanine

Alanine release was found to be linked to cell viability under all conditions combined (r=0.382, p= <0.001) (Figure 6.10C). This trend remained when all conditions were assessed in isolation, i.e. under static hypoxic storage (r=0.43, p=<0.007), under static storage with atmospheric oxygen (r=0.33, p=0.042), under fluid shear stress and hypoxia (r= 0.43, p= 0.073) and under FSS with atmospheric oxygen(r=0.46, p= 0.0057). Alanine release was not found to be related to LDH release when the storage conditions were tested individual as a collated group (Figure 6.11C).

6.3.3.4 Glutamate

Glutamate release was found to be linked to cell viability under when all conditions were examined together (r= 0.385, p=<0.001). This relationship remained in isolated environments such as static hypoxic storage (r=0.51, p= 0.0012) static storage with atmospheric oxygen (r=0.33, p=0.042), and under FSS with atmospheric oxygen (r=0.45, p= 0.0049) (Figure 6.10D). When assessed all storage conditions were assessed together, fluid glutamate levels were found to be correlated with fluid LDH concentrations (r=0.263, p=<0.05) (Figure 6.11D). This observation did not retain significance when the storage conditions were assessed in isolation.

6.3.4 Study 3: Screening the merits of increased antioxidant provision *in vitro*

Colloid selection demonstrated a potent effect on LDH release (Figure 6.12). Hypoxic storage of RPTEC/TERT1 in UWMPS resulted in lower LDH release (6.50 mU/ml, range 5.83-7.48 mU/ml) than storage in PEG UWMPS (11.51 mU/ml, range 10.31-12.31 mU/ml (p=0.032) and colloid free UWMPS (14.20 mU/ml, range 11.47-15.25 mU/ml) p=0.0312). Under atmospheric oxygen, cells stored in UWMPS, PEG UWMPS and Colloid-free UWMPS exhibited LDH activity of 6.91 mU/ml (range 5.87-7.46), 10.25 mU/ml (range 9.57-11.44) and 13.07 mU/ml (range 11.42-15.54 mU/ml) respectively.

Similar differences were detected under atmospheric storage as under hypoxic storage, with UW MPS storage having lower LDH release than storage in PEG UWMPS (p=0.0313), which itself conferred lower LDH release than colloid free UWMPS (p 0.0313). When compared to the most protective solution (UWMPS), Colloid free UWMPS resulted in the highest level of LDH release in both oxygen environments (p=0.0313 under hypoxia and atmospheric oxygen). No difference in LDH release between hypoxic and atmospheric

environments was detected following RPTEC/TERT1 storage in UWMPS (p=0.6991), UWMPS (PEG) (p=0.0625) or colloid free UWMPS (p=0.6875).

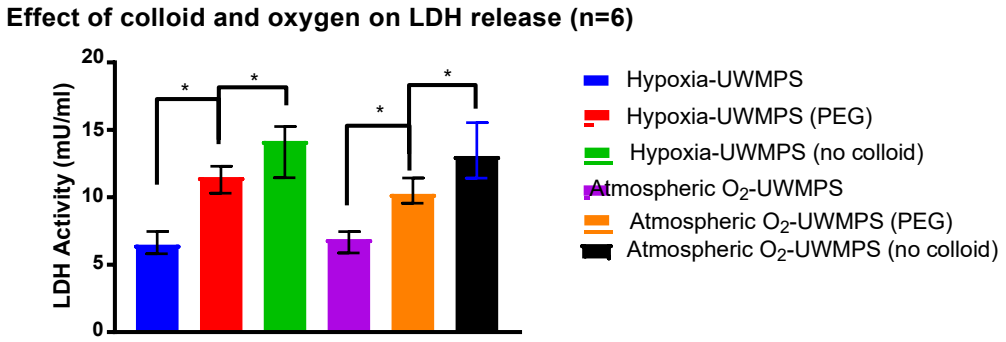

Figure 6.12. The effect of colloid on release of LDH in different oxygen environments.

6.3.4.1 Effect of increased glutathione on indicators of cellular damage.

Glutathione supplementation of UWMPS was found to increase LDH activity to 125.07% that of the UW control (range 112.46 to 147.73%), a significant increase over that seen in UWMPS (97.53%, range 90.43-105.86%) (p=0.0313). Glutathione supplementation was also observed to improve cell viability compared to standard UWMPS (relative viability of 110.06% that of the UW control (range 79.06-118.76%) and 88.18% that of the UW control (range 82.87-107.76%) respectively (p=.313) (Figure 6.13).

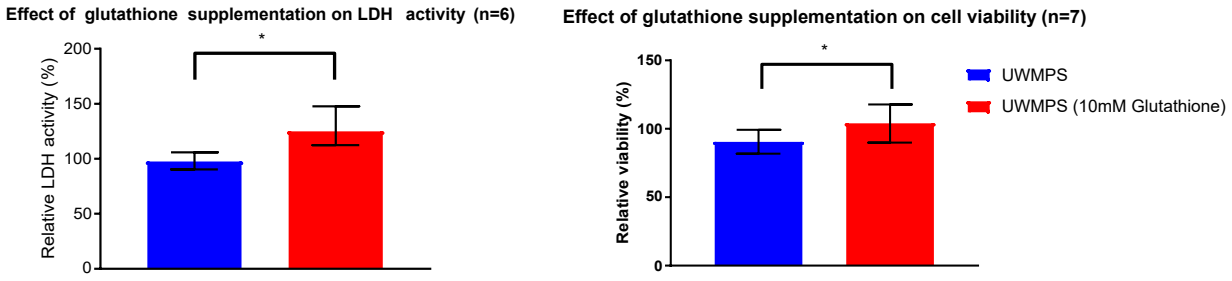

Figure 6.13 Effect of glutathione supplementation on cellular damage *in vitro*

6.3.5 Whole organ assessment of key *in vitro* findings

6.3.5.1 Cortical glucose concentration stores after 2 hours of SCS, and 24 hours of HMP or SCS.

In light of *in vitro* findings indicating proximal tubule glucose concentrations are not maintained by incubation in UW, but are by UWMPS, spectra acquired from cortical biopsies in the whole organ HMP vs SCS study were re-analysed to include glucose quantification.

In line with the *in vitro* study, kidneys submitted to SCS were found to have a greater than 6-fold decrease in cortical glucose concentrations than those stored by HMP (Figure 6.14). SCS storage results in marked cortical glucose depletion, when compared to HMP stored kidneys (i.e. 0.10 mM, range 0.07-0.12 mM and 0.63 mM, range 0.62-0.66 mM respectively). This difference reached statistical significance (p=0.013).

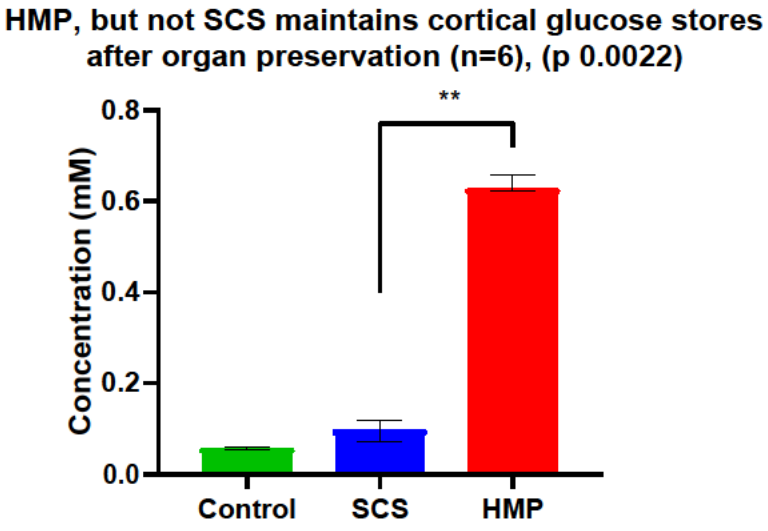

Figure 6.14. Cortical glucose levels after 24-hour HMP, or 2 and 24-hour SCS

Cortical glutathione concentrations after HMP and SCS storage of kidneys

The *in vitro* observation that intracellular glutathione appeared to be elevated in UW stored cells was not using observed again using the *ex vivo* model. After 24 hours, cortical glutathione levels in SCS kidneys (0.04mM, range 0.04-0.05 mM) were not found to be different from those in HMP stored kidneys (0.03 mM, range 0.02-0.06mM (p=0.309) (Figure 6.15)

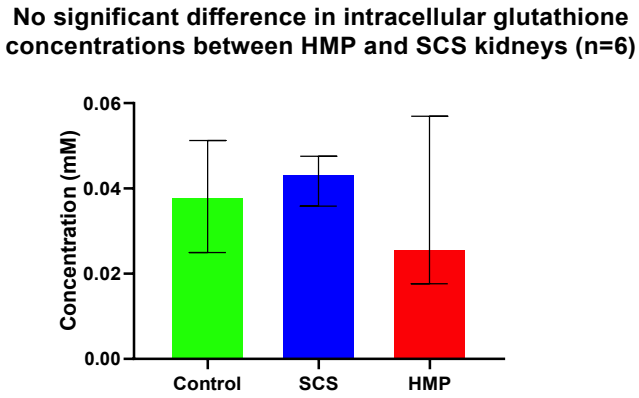

Figure 6.15.Cortical glutathione in kidneys after 24 hours HMP or SCS

LDH release from HMP kidneys following enhanced glutathione supplementation

When assessed using the whole organ model, perfusate glutathione supplementation did not lead to a significant difference in LDH release when compared to kidneys perfused using the standard UWMPS formulation. Endpoint LDH activity was found to be 15.44 ±3.96 IU/ml in standard UWMPS vs 11.70 ± 5.95 IU/ml following glutathione supplementation. This difference did not attain significance (p= 0.3095).

However, a consistent and continuous decrease in LDH release was tangible in the glutathione supplemented kidneys (Figure 6.16).

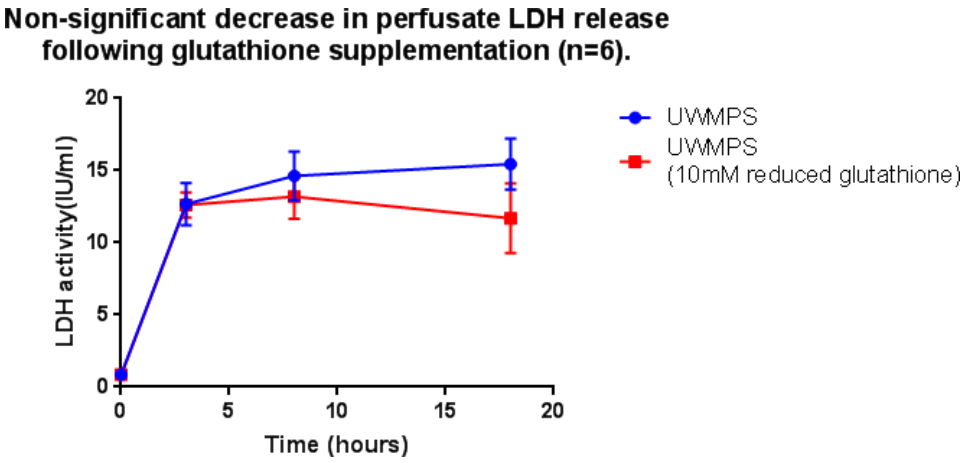

Figure 6.16. Reduction in perfusate LDH by glutathione supplementation *ex vivo*.

6.4 Discussion

6.4.1 Study 1: Identification of environmental stimuli governing cellular viability and metabolism

6.4.1.1 The effect of storage fluid on cell viability

DGF may be indicated by reduced urine production, caused by impaired movement of fluid through the nephron(280). The clear damage experienced by RPTEC/TERT1 stored in UW under normothermia (Figure 6.5) indicates that UW is not the optimal preservation solution to be trapped within the proximal tubule after transplantation, as could conceivably occur in the DGF kidney if UW enters the tubule lumen.

Although further data indicated that proximal tubule cells stored in UW also results in increased LDH release in all environments, the experiment was abandoned at midpoint. The reason for this is illustrated in Figure 5.1, which depicts the areas of HMP and SCS kidney which are in contact with the supplied preservation fluid.

While blue colouration was macroscopically visible in tissues in the HMP stored kidney, the SCS kidney was consistently and completely unaffected by the inclusion of dye in the bathing fluid. Continuous perfusion can be expected to generate a greater influx of dye in to the renal tissue. However, the absence of any colouration observed under SCS does make it questionable whether the components of UW permeate the cold-stored kidney. As illustrated in the attached manuscript, the fact that glutathione levels in UW remain unchanged over a 24-hour cold ischemic time further supports the notion that there really isn't any significant exchange between the intra and extra renal fluid compartments in SCS. Therefore, assessments made of proximal tubule cell viability after immersion in UW may not translate to the *ex vivo* environment, and as such the experiment was discontinued.

However, as a metabolically inert fluid, UW still serves as a useful control against which to gauge the metabolic effects of glucose supplementation in UWMPS (Figure 6.4).

Active perfusion appears to be required to ensure kidneys benefit from the therapeutic reagents added to the preservation fluid, however as discussed in Chapter 1, whether the whole of the kidney benefits from perfusion under HMP is also unclear.

While blue colouration was consistently visible in the renal cortex after perfusate supplementation with trypan blue dye (Figure 5.1), there was consistently greater colouration in the renal medulla. The different staining could indicate significant regions of the cortex are not being perfused. Dye must follow fluid flow, and mechanistically this imbalance in perfusion may arise through pre glomerular blood shunting by the porcine kidney(281), or through impairment of glomerular filtration.

6.4.1.2 The effect of storage fluid on proximal tubule cell metabolism

Hypoxic storage of proximal tubule cells in UW appeared to result in intracellular glucose depletion and lactate accumulation when compared to cells stored in UW MPS (Figure

6.4). Although these differences narrowly missed attaining statistical analysis using the Wilcoxon signed rank test, this is likely a reflection of the low sample number, which was utilised for all screening experiments to enable coverage of the broadest range of environmental stimuli. When the cell line model was treated as unpaired and submitted for Mann Whitney U analysis, these differences became significant.

Assessment of fluid metabolic profile was not attempted, the rationale for this was that in the SCS stored kidney, UW does not appear to permeate the tissue. Therefore, metabolic differences in caused by UW components are unlikely to reflect the clinical scenario. Furthermore, the metabolic profile of HMP perfusate in the clinical setting will be modulated by many different cell types within the kidney. Therefore, this simple *in vitro* screen focused on the metabolic effects on proximal tubule cells themselves.

However, this is a limitation, and does occlude full understanding of the processes occurring *in vitro*. Future work could use metabolic tracer analysis and fluid/cell extract analysis to more closely investigate metabolic flux in the *in vitro* system and address this limitation.

Nonetheless, this cell line experiment achieved its purpose in directing whole organ research. The stark difference in intracellular glucose concentrations between UW and UWMPS (i.e. the total absence of glucose in UW stored cells vs equilibrium with fluid glucose concentration in UW MPS stored cells (Figure 6.4) did lead to a fruitful second assessment of the whole organ data. Cortical glucose concentrations were also found to be significantly elevated in HMP stored porcine kidneys in the *ex vivo* model (Figure 6.14). These data infer that that SCS storage is incapable of preventing glucose depletion to the extent offered by HMP during extended hypothermic storage. A low glucose/lactate ratio has been observed in biopsies from DGF kidneys(272), and this may signify glycolytic

exhaustion, a mediator of the cold ischemic injury generated through ATP depletion(140), introduced in Chapter 1.

Improved metabolic support offered by UWMPS has been proposed as modulator of the benefit of HMP over SCS. Mechanistically, this may manifest as increased concentrations of tissue glucose to serve as a metabolic substrate upon reperfusion.

6.4.1.3 Oxygen dependent effects

6.4.1.4 Effects of hypoxia on cell viability

In SCS storage, the cold-stored porcine kidney rapidly becomes severely hypoxic, with fluid exiting the renal vein immediately after initiation of HMP having dissolved oxygen concentrations around 10% that of the fluid entering the renal artery (Figure 6.3B)

Initiation of HMP affords a time limited respite from hypoxia, the circulation of perfusate in equilibrium with the atmosphere allows for some degree of tissue reoxygenation, until that too becomes oxygen depleted. The data presented in (Figure 6.3A) demonstrates that within 4 hours of HMP using the porcine model, the oxygen content of UWMPS falls from 24.7kPa to 1.6kPa and goes on to plateau at around 0.7kPa over the 18 hour preservation time. This is a clear indication that oxygen dependent processes are ongoing during the HMP storage of porcine kidneys, and also that these processes and are not sufficiently supported by passive oxygen diffusion for extended preservation periods.

When simulated *in vitro*, this magnitude of hypoxia, which extends for the majority of the preservation period results in the lowest proximal cellular viability of all environments tested using the SRB assay (Figure 6.6).

The high aerobic requirement of proximal tubule cells are well established(67), and it appears that severe hypoxia exerts a detrimental effect on their viability during storage. The inclusion of atmospheric oxygen was largely beneficial, resulting in a consistent and

significant increase in viability (Figure 6.6). It follows that the depletion of oxygen observed in the whole organ perfusion model manifests as progressive development of the hypoxic environment, which is pathological to proximal tubule cells *in vitro.* This may be an *in vitro* reflection of the mechanism governing the deleterious effect of extended cold ischemic times, and the potential therapeutic benefit offered through active oxygen perfusate supplementation(121,125,274).

Atmospheric oxygen exerted a positive effect on cell viability when assessed using the SRB assay, however a deleterious effect of atmospheric oxygen on hypothermicly stored proximal tubule cells has been reported previously(282). The impacts of fluid oxygenation on LDH release *in vitro* is more thoroughly investigated in Chapter 7, however suffice to say that that LDH release *in vitro* does not appear to mediated to a great extent by changes in oxygen concentration in the experiments described in this chapter (Figure 6.7 and Figure 6.12). In any case, while increases in LDH activity may suggest membrane damage as well as the occurrence of cell death(171), the signal derived using the SRB assay is directly proportional to the number of cells that have died and lysed or detached from the plastic of the culture dish. Therefore, the SRB results are more informative of the environments that protect cells from death during preservation, whereas the LDH assay may be regarded a non-specific assessment of injury. An indication that these assays are reporting sperate phenomena is visible in the absence of a clear correlation between SRB and LDH data (Figure 6.8). It follows that the LDH data may indicate membrane deterioration that does not progress to cell death during the preservation period.

6.4.1.5 Fluid flow modulated effects

6.4.1.6 The effect of fluid flow on cell viability

Under atmospheric oxygen, generation of FSS was found to exert a beneficial effect on cell viability. Varying the fluid volume in both static and FSS plates was required to control the level of FSS generated, and independently, this also affected the viability of the stored cells, with increasing volumes of fluid being linked to inferior measures of viability in statically stored cells (Figure 6.9).

An explanation for the protective effect of increased viability associated with FSS generation may not be through FSS itself, but through continuous mixing of the fluid. An oxygen gradient exists in cell culture media, with respiring cells causing oxygen depletion in fluid close to them(283). Continuous rocking disrupts this gradient, enabling enhanced mixing of dissolved oxygen and therefore offering protection from hypoxia, which as demonstrated in statically stored cells, is deleterious to monolayer integrity (Figure 6.6). This supports the growing notion that modulation of oxygen availability may be a primary therapeutic intervention in organ preservation optimisation.

However, disruption of oxygen gradients cannot account for the consistent improvement in cell viability caused when cells stored in hypoxia chambers are rocked (Figure 6.6). The consistent and near absolute hypoxia generated infers an alternative mechanism must be active. This may be related to the generation of 1 dyne/cm^2 shear stress, or could be through mixing effects on nutrient delivery and waste dilution. In any case, fluid flow exerted a beneficial effect under hypoxia and atmospheric oxygen- supporting the notion that the presence of fluid flow is an independent driving force behind the apparent benefit of HMP over SCS. Modulation of perfusion pressure to generate fluid optimal perfusion parameters may be an avenue for organ storage optimisation, and the ShearFAST

assisted rocking model can be used to provide *in vitro* evidence of the optimal degrees of shear stress for defined cell types in the hypothermicly stored organ.

6.4.2 Study 2: Assessing fluid metabolites for their potential as biomarkers *in vitro*

Metabolic profiling during HMP has been proposed as a tool for monitoring organ quality (109,275). Unlike the whole organ model, the cellular and fluid compartments of *in vitro* models are easily separated This, with the capacity to generate large numbers of replicates makes the cell line model a useful tool in linking supernatal metabolic profiles with indicators of cellular damage.

A previous study by our group demonstrated that human kidneys that take up more glucose from the perfusate during HMP go on to have a higher likelihood of DGF development(109). An opposite relationship was determined *in vitro*, with increases in cell viability inferred from the SRB assay being linked with decreases in glucose absorption. Although proximal tubule cells undergo a glycolytic switch and use glucose to fuel repair after injury(153) the absence of any correlation between LDH activity and glucose reabsorption does not support increased cellular damage as explanation for increased glucose uptake *in vitro.* The slight negative correlation detected may simply indicate that increased numbers of cells surviving preservation have greater capacity to absorb a greater fraction of the glucose available in the preservation fluid.

Fluid lactate levels appear to be a good indication of membrane damage during hypothermic preservation, with significant correlations between the LDH activity and lactate levels (Figure 6.11B) that were not correlated to the number of cells remaining in the well when assessed with SRB assay (Figure 6.10B).

Rising lactate release with LDH may be an indicator of ongoing oxidative stress, which damages membranes through lipid peroxidation(284). Even with the presence of fluid flow, the glutathione present in UWMPS does not appear to be sufficient to meet the antioxidant requirements of the hypothermicly stored porcine kidney (Figure 6.16). Therefore, a potential modification to fluid composition could be perfusate supplementation with more antioxidants. Indeed, work from our group demonstrates that increasing perfusate levels of glutathione to 10mM in the porcine model reduced release of lactate when compared to standard HMP (Appendix 4).

Supernatal alanine and glutamate were both found to increase with increases in cell viability, indicating that the presence of this metabolite into the fluid is largely dependent on the number of cells in contact with the fluid (Figure 6.10).

Glutamate release was also found to be linked to LDH release (Figure 6.11), indicating that detection of glutamate in perfusate may not infer metabolic modulation or improved flow rates, but increased membrane damage. In the previous section, an association between enhanced fluid glutamate concentrations and LDH release was noted. This conflicts with the cell viability data, which also showed an association between fluid glutamate and increased cell viability. A potential mechanism for this disparity is discussed in the following section, however, this simple analysis offered by the accessible cell line model illustrates the great difficulty associated with the determination of meaningful inferences from standard metabolic analysis. Tissue and fluid metabolites may differ in concentration due to increases in membrane damage, changes in the number of cells in contact with fluid, or through modulation of metabolism

The exception is fluid lactate, which stays largely consistent across different degrees of cell viability in rises in tandem with LDH. These data suggest that total perfusate lactate levels may have potential as a metabolic biomarker, at least *in vitro*.

6.4.3 Study 3: Screening the merits of increased antioxidant provision *in vitro*

In the attached manuscript we observed total depletion of perfusate glutathione levels within 18 hours of perfusion (276), and in Figure 6.15, it is shown that there is no evidence of glutathione accumulation in cortical tissue after 24 hours of HMP. Together, these indicate the glutathione present in UWMPS may be insufficient to provide antioxidative support for extended CIT. This warranted assessment of the merits of perfusate glutathione supplementation.

Glutathione supplementation *in vitro* yielded surprising results, with storage of proximal tubule cells in glutathione supplemented UWMPS displaying significant increases in LDH release when compared to those stored in standard UWMPS.

Proximal tubule cells express γ–glutamyltransferase (GGT) on their brush border, an enzyme involved in the cleavage of glutathione into constituents glycine and glutamate(285). Importantly, the action of this enzyme has pro-oxidative effects in renal ischemia(286). This could explain the apparent correlation between fluid glutamate concentrations and LDH release observed previously. In Appendix 4 it is noted that glutathione supplementation in whole organs results in increased perfusate presence of both glycine and glutamate, the break-down products of glutathione by GGT (287).

It was therefore important to ascertain whether the glutathione supplementation *ex vivo* was deleterious and conferred a similar increase in perfusate LDH levels as to what was observed *in vitro*.

It was found that glutathione supplementation results in a non-significant decrease in LDH release, when compared standard HMP of porcine kidneys. This may indicate that the deleterious *in vitro* effect inferred from the LDH data did either not occur in the whole organ

model, or was masked by a largely beneficial effect of glutathione supplementation on systemic LDH release *ex vivo*.

Glutathione depletion during HMP warrants some form of additional antioxidant supplementation. However, this does not have to be with glutathione. Polyethylene glycol could confer enhanced oncotic and antioxidant protection to proximal tubule cells during hypothermic preservation (130), and its lower molecular weight, combined with the resulting decrease in fluid viscosity at PEG 35kkA concentrations of 30g/L (Figure 3.2) may make it more likely to enter the proximal tubules than HES.

6.5 Conclusion

Porcine kidneys stored by HMP or SCS rapidly become hypoxic during hypothermic preservation (Figure 6.3), with both displaying demonstrating considerable degrees of anaerobic metabolism, evidenced by lactate release into the perfusate in HMP and tissue accumulation in SCS(276).

While modification of perfusate and generation of fluid flow have the potential to modulate cell viability *in vitro* (Figure 6.5, Figure 6.12, and Figure 6.13), the most potent protective environmental stimulus was avoidance of hypoxia by maintaining equilibrium with atmospheric oxygen. This generated a ˜10% improvement in cell viability (Figure 6.6) and has potential to counteract the largely anaerobic phenotype in whole organ preservation (235), which may be a key contributor to poor transplant outcomes(272,288).

The following chapter uses the described *in vitro* model to define the environmental stimuli that generate or maintain the anaerobic environment in the period between donation and transplantation, and whether oxygen supplementation during simulated storage can be used to confer a more favourable aerobic metabolic phenotype.

7 Metabolic changes in proximal tubule cells submitted to *in vitro* simulations of kidney donation and preservation.

7.1 Introduction

The fate of intracellular glucose in the period between kidney donation and reperfusion is of clinical interest. It has been reported that increased glucose uptake during HMP may be associated with inferior patient outcomes, notably in the likelihood of DGF development(109). Additionally, in Chapter 6, it was determined that a key metabolic difference between HMP and SCS stored kidneys is that SCS stored kidneys, known to be associated with inferior transplant outcomes(89) have reduced glucose stores (Figure 6.14) and have greater intracellular lactate concentrations(276). This could suggest that the level of ongoing anaerobic metabolism during kidney preservation is an important mediator of post-transplant outcomes, an assertion reinforced by observation that increased renal production of lactate during reperfusion is a consistent feature in patients with inferior with post-transplant outcomes(272). Therefore, minimising or reversing the glycolytic phenotype in hypothermicly stored kidneys could confer post-transplant benefits. This chapter seeks to provide *in vitro* indications of the environmental stimuli, encountered between donor death and the end of organ preservation that are capable of modulating normal proximal tubule cell metabolism. This understanding could facilitate introduction of modifications that foster a more beneficial metabolic phenotype

Some environmental factors mediating ongoing metabolism are already well documented, for example the ischemic periods intrinsic to organ donation are known to confer an anaerobic phenotype (86,289), however other stimuli; such as high glucose concentrations(290) or the absence or excess of fluid shear stress (291,292) may also be implicated.

We have previously concluded that metabolism ongoing during HMP is predominantly glycolytic(235) and throughout preservation, the HMP stored kidney utilises significant proportions of the oxygen available to it (Figure 6.3), an inference of ongoing aerobic metabolism for a limited duration.

This limited reoxygenation may be beneficial, Chapter 6 indicates that equilibrium of UWMPS with atmospheric oxygen leads to enhanced survival of stored proximal tubule cells (Figure 6.6). However, whether this level of oxygenation drives restoration of aerobic metabolism in hypothermic proximal tubule cells has not been characterised. Hypothermia in isolation may not directly cause an anaerobic switch(293) but is known to reduce metabolic enzyme efficacy (in line with the thermal performance curve(294) which may balance ongoing ATP depletion with the environmental oxygen available(295). Optimisation of aerobic metabolism under hypothermia may therefore be possible.

Using *in vitro* methods developed in Chapters 3 and 4, this chapter seeks to determine the metabolic effects of modifying the extracellular environments and close in on beneficial modifications that can be trialled in the whole organ setting.

Within, five experiments are described.

The first experiment has the purpose of validating that under normal culture-RPTEC/TERT1 use glucose as a carbon source for TCA cycle metabolism. Although glucose reabsorption is well characterized to be a primary function of this segment, dated publication state that only 1% of the glucose that absorbed is used by the cell to fuel

ongoing metabolism(296). Other reports stipulate lactate, glutamine or fatty acids are in fact the primary metabolic substrate used by the *in vivo* PCT(159). Validating that cultured cells are capable of aerobic glucose metabolism, and that the analytical tools used (i.e. GCMS) can accurately and precisely measure mass isotopic distribution is a pretext for the rest of this chapter. This also serves as a measure of metabolic maturation of the cell line, proliferating cells are characterised to have a glycolytic phenotype- where as a mature RPTEC/TERT1 monolayer has been demonstrated utilise more oxidative metabolism(153).

The second experiment will determine whether simulation of known induces of an anaerobic switch (i.e. a warm ischemic insult) drives evidence of an anaerobic switch *in vitro*. This will validate that the results derived from the cell line model used can reflect current understanding in this field.

The third experiment in this chapter seeks to determine how falling temperature affects proximal tubule metabolism of glucose, and also, whether the metabolic suppression generated during cold ischemia can instead be delivered pharmacologically. It is thought that the deployment of complex IV inhibitors, such as thiosulphate or hydrogen sulphide under normothermia or sub-normothermia may provide hypothermia like metabolic suppression without the simultaneous cold induced cellular injury(297).

A recent study demonstrated that hydrogen sulphide resulted in marked reductions in oxygen utilisation during normothermic machine perfusion, as well as maintenance of ATP stores(298).

The last experiments of this chapter focus on the role of shear stress in metabolic modulation during hypothermic preservation, and to a greater extent, the potential of oxygen supplementation to drive desirable metabolic changes *in vitro.*

7.2 Methods

Five experiments are described which aim to resolve key metabolic questions about the proximal tubule during preservation. Routinely, cells were cultured as described in Chapter 3 and left to mature prior to introduction of metabolic tracers (assessed by the presence of dome formation and /or cobblestone morphology, which generally took between 7-10 days. At the experimental endpoint, monolayers were prepared for metabolic analysis using mass spectrometry, also as described in Chapter 3.

7.2.1 Study 1: Assessing RPTEC/TERT1 metabolism of glucose under standard culture

Confluent RPTEC/TERT1 cells in T75 flasks (n=18) were labelled for 24 hours in 18ml media supplemented with 17.5mM [U-^{13}C] glucose.

Since the main purpose of this experiment was to indicate whether glucose serves as carbon source, this 18 hour labelling time was selected to ensure TCA cycle intermediates had sufficient time for label incorporation.

After this, flasks were divided into 3 sets of 6 and cultured for a further 6 hours in media containing 17.5mM [1,2 ^{13}C] Glucose, 17.5mM ^{12}C glucose or 17.5mM [U^{13}C] glucose (Cambridge isotopes, UK). This step was to determine if changes in the glucose label led to predictable differences in the analysis returned in the later mass spectrometry. As discussed later- this second labelling time was included as a validation of the analytical approach used . After the six-hour labelling time with different glucose ^{13}C incorporation, the monolayers were prepared for metabolic analysis. As the only difference between groups were the position of ^{13}C labelling in the supplied glucose, this experiment is purely qualitative and statistical assessment is not applicable.

7.2.2 Study 2: The effect of warm ischemia on RPTEC/TERT1 glucose metabolism

In this experiment, 12 T75 Flasks, were each seeded with RPTEC/TERT1 from 12 separate frozen stocks of cells. Flasks were labelled for four hours with 18ml [U-^{13}C] glucose and [U-^{13}C], [^{15}N] glutamine. Monolayers were washed with 0.9% saline solution and then either re-cultured in more tracer media (n=5) for four hours to permit ongoing isotopic labelling continued or alternatively incubated in 18ml mineral oil (Sigma Aldrich Merck, UK) to simulate proximal tubule nutritional inadequacy during warm ischemia (n=6), as described elsewhere(299). The mineral oil plates experienced a 0.3% oxygen atmosphere using a hypoxia station (Figure 1.12), whereas those subjected to standard culture experienced atmospheric oxygen. After a 4 hour isotopic labelling time, monolayers were prepared for metabolic analysis as per Chapter 3. Differences in mass isotopic distribution were determined using an unpaired analysis (the Mann Whitney U test). Since cells were not cultured in parallel from the same source vial a paired analysis was not used.

The metabolic analysis in this study was limited to lactate and pyruvate. Labelled glutamine was originally included for a series of ongoing NMR method development studies- but of course these confound biological interpretation of the metabolic pathways resulting in modulation of TCA cycle metabolite MID. Therefore, this simple screen focused exclusively on the effect of simulated warm ischemia on two glycolytic metabolites, i.e. lactate and pyruvate, and as such is unlikely to be affected by the use of the labelled glutamine label (^{13}C or ^{15}N).

7.2.3 Study 3: Quantifying thermal and pharmacological inhibition of metabolism.

RPTEC/TERT1 was seeded in 12 150cm^2 tissue culture dishes and cultured until confluence. The plates were divided into 4 sets of 3, with 3 plates to be subjected to hypothermic storage, 6 plates to be stored at room temperature and 3 plates to be stored at 37° C. Three of the plates stored at room temperature were used to screen the effects of hydrogen sulphide on metabolism, described later.

Prior to experimental start, the supernatant was discarded and each plate was washed twice with 0.9% NaCl solution which had been incubated to the plates designated experimental temperature. After this, 36ml of clinical grade UW MPS containing 10mM [U-^{13}C] Glucose (Organ Recovery Systems, USA), also at the plates designated temperature was added to each dish.

Hypothermic experiments were moved to a cold room, plates simulating sub normothermic storage were kept at room temperature and plates simulating physiological temperatures were stored in a standard cell culture incubator.

7.2.3.1 Determination of sodium hydrogen sulphide concentration required to protect RPTEC/TERT1 during sub-normothermic storage

This experiment sought to define a dose of sodium hydrogen sulphide which resulted in improved cellular viability at room temperature.

RPTEC/TERT1, cultured in 96 well plates (n=6) were subjected to storage in UW MPS at room temperature. The protective effect of 12 different concentrations of sodium hydrogen sulphide (NaHS) (Alfa Azar), ranging between 0-0.2mM were assessed after 18 hour storage by the SRB assay (Figure 7.3) The absorbance in each dose was normalised to

the 0mM control on each plate and differences between control and different NaHS concentrations assessed using the Wilcoxon signed rank test.

7.2.3.2 Effect of NaHS on de novo metabolism during subnormothermic storage

This experiment was run parallel to the temperature study. Of the 6 plates to be kept at room temperature, three were supplemented with 0.1mM Sodium Hydrogen Sulphide (NaHS) (Alfa Azar) and stored in a fume cupboard at room temperature. This concentration of NaHS was selected based on the protective effect observed at NaHS concentrations between 0.06 and 0.2mM (Figure 7.3).

The remaining three-room temperature plates were stored on the bench top. All storage experiments at all temperatures were performed for 18 hours, after which monolayers were harvested and prepared for MID analysis as described in Chapter 3. This comparison is shown in Tables 4 and 5.

7.2.4 Study 4: Effect of fluid flow on proximal tubule cell metabolism

RPTEC/TERT1, cultured in 12 15cm dishes were washed and submerged in 9.8ml of chilled in house UW MPS. A cell rocker (VWR 444-0146) was moved to a cold room and rocked at rocker settings of an estimated 5° and at an estimated 60RPM. The remaining 6 plates were placed on the bench next to the rocker. In this manner, all plates experienced hypothermia and atmospheric oxygen, but only half experienced fluid flow. Since this experiment predated the inception of ShearFAST, accuracy of rocking angle and cycle frequency cannot be assumed, and as such this experiment functions more as a proof of concept investigating the potential of fluid flow to modulate proximal tubule cell metabolism during hypothermic storage.

7.2.5 Study 5: The effect of oxygen availability on proximal tubule metabolism.

RPTEC/TERT 1 was grown to confluence in nine 10cm dishes (Corning, UK), washed with 0.9% NaCl and then submerged in 16ml of chilled UWMPS (Organ recovery systems, USA) containing 10mM [U-^{13}C] glucose.

Using the hypoxia chamber filling circuit described in Chapter 3, three oxygen environments a were generated (i.e. severe hypoxia/anoxia, atmospheric oxygen and hyperoxic oxygen with pressures of~50kPa (Figure 3.12). Plates were divided into three groups and placed in their respective hypoxia chambers for filling. After filling for 30 minutes, the plates were moved to a cold room which maintained hypothermia throughout an 18 hour storage time. This was performed 6 times, giving 6 biological replicates.

After experimental endpoint, the chambers were opened and plates were prepared for metabolic analysis using Mass spectrometry, and biochemical ATP analysis using the method described in Chapter 3. Differences were detected using the Mann Whitney U test.

A prior experiment, comparing the effects of hypoxic storage against that of storage under atmospheric oxygen was conducted din a similar fashion, with the exception that 75cm^2, flasks were used instead of 10 cm^2 dishes and with the results analysed by HSQC alone.

7.3 Results

7.3.1 Study 1: Assessing RPTEC/TERT1 metabolism of glucose under standard culture

This experiment sought to determine whether mature RPTEC/TERT1 monolayers use glucose as a carbon source for TCA cycle metabolism.

Routine culture of RPTEC/TERT1 with different glucose tracers yielded diverse ^{13}C labelling patters in central metabolites. There was discernible ^{13}C enrichment in TCA cycle associated metabolites (alpha-ketoglutarate, fumarate, malate, succinate), most abundantly with M+2 label incorporation.

Notably, when [U-^{13}C] enriched glucose was switched for ^{12}C glucose, there was very limited labelled contributions in all metabolites after 6-hour culture,

Metabolites associated with glycolysis and the TCA cycle were found to be ^{13}C enriched following RPTEC/TERT1 culture with different glucose isotopologues. Also, usage of [1,2-^{13}C] labelled glucose yielded an M+2 contribution of lactate and pyruvate roughly half of the M+3 contribution when [U-^{13}C] glucose was used i.e. 17.58%, range 13.90-22.94% and 13.46%, range 12.53-17.83% vs 45.24%, range 37.34-50.0% and 33.82%, range 27.86-36.06% respectively. (Figure 7.1).

This is an indirect validation of the analytical accuracy afforded by the GCMS set up used. Glucose, a 6 carbon molecule may be metabolised to two 3 carbon molecules (i.e. lactate or pyruvate). When [U-^{13}C] is the sole glucose source, the six labelled carbon generates two 3 carbon molecules in which all of the composite carbons are labelled. However, when [1,2-^{13}C] glucose is used, only one of the two 3 carbon metabolites will possess label, and that metabolite will be a M+2 mass isotopomer. Therefore, use of [1,2-^{13}C] glucose should yield roughly half the mass isotopic contribution of lactate and pyruvate when compared to use of fully labelled glucose, which is what was observed.

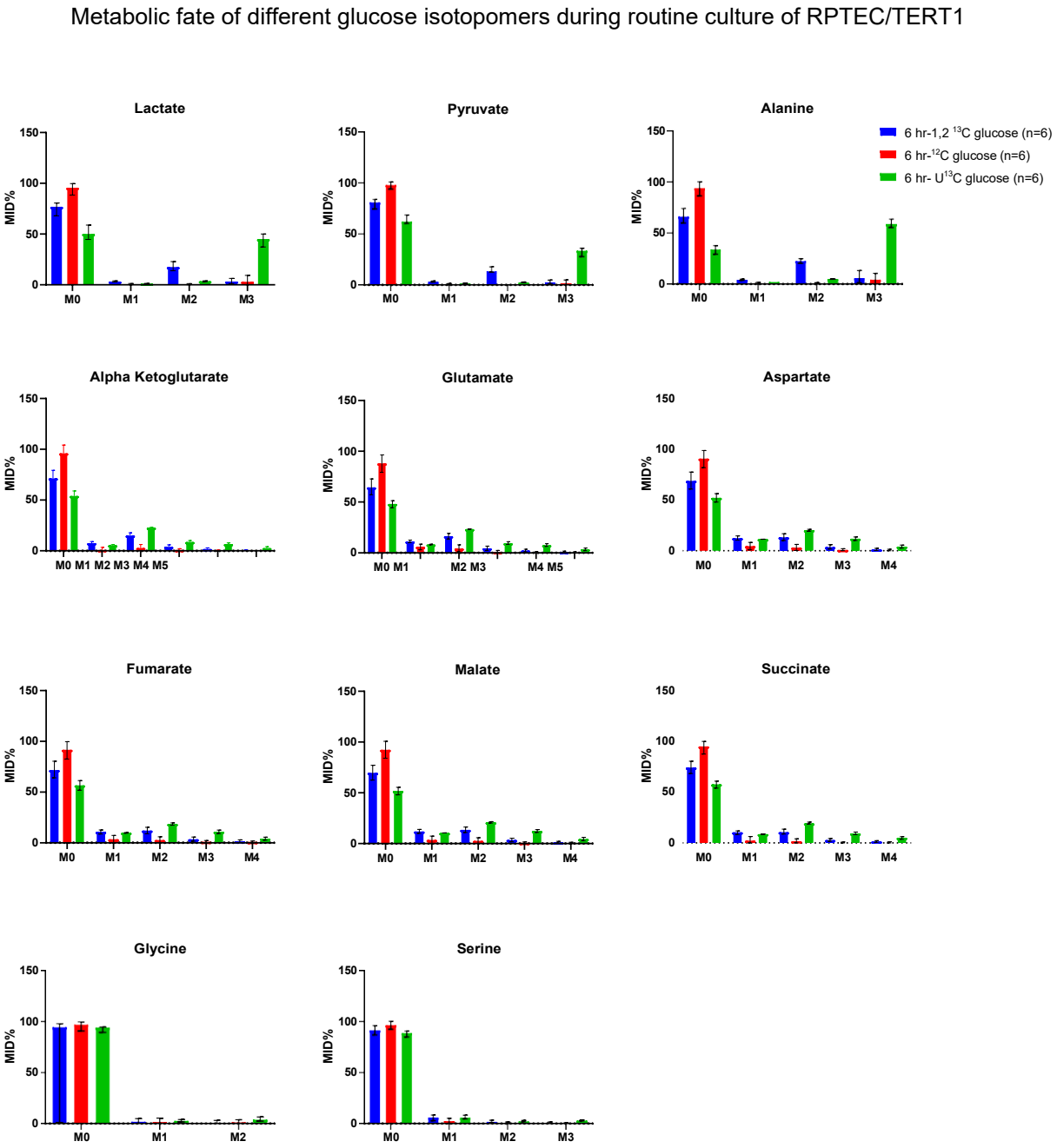

Figure 7.1. RPTEC/TERT1 metabolises glucose under standard culture

7.3.2 Study 2: The effect of warm ischemia on RPTEC/TERT1 glucose metabolism

This experiment sought to determine whether or not a known stimulus of an anaerobic switch (i.e. warm ischemia) gave rise to evidence of an anaerobic switch when it was simulated *in vitro.*

The combination of nutrient deprivation with hypoxia was found to invoke a multitude of changes to the percentage contribution of different isotopomers within each metabolite (Figure 7.2). M0 lactate contribution was not found to differ between standard culture and warm ischemia (56.12%, range 32.54-62.21% and 36.19%, range 30.93-48.44% respectively), (p 0.1255). M1 lactate contributions differed significantly between standard culture and those exposed to simulated warm ischemia (1.41%, range 0.99-1.49% vs 3.95, range 2.79-4.51% respectively) p=(0.035). This trend was mirrored in M2 lactate contributions (3.23%, range 2.56-4.75% under standard culture and 7.14%, range 5.67-7.95% under warm ischemia)(p=0.0043). However, the different M3 contributions to the total lactate pool did not achieve statistical significance (p=0.662).

M0 Pyruvate contributions were increased by generation of warm ischemia when compared to standard culture (78.26%, range 68.05-94.52% vs 36.11%, range 28.49-66.88% respectively) (p 0.0043). Production of M3 Pyruvate was reduced by warm ischemia (contribution of 18.71%, range 5.85-25.01%) when compared to standard culture (contribution of 58.56%, range 30.30-66.21%) (p 0.0043).

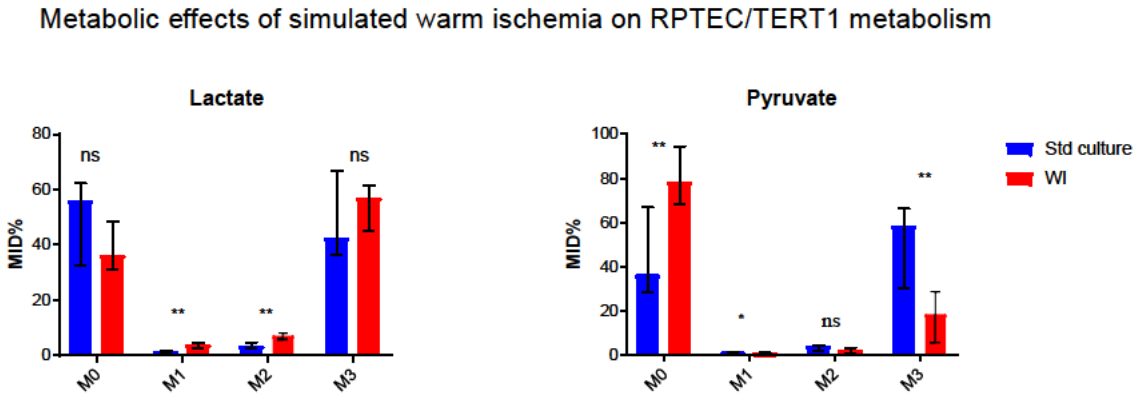

Figure 7.2. Simulated warm ischemia(WI) generates an anaerobic shift in RPTEC/TERT1

7.3.3 Study 3: Quantifying thermal and pharmacological inhibition of metabolism

This experiment sought to determine whether reductions in temperature inhibited ongoing metabolism i*n vitro*, and also whether the level of metabolic suppression at 4 °C could be generated pharmacologically at room temperature using hydrogen sulphide.

7.3.3.1 Determination of a therapeutic dose of hydrogen sulphide at room temperature

This experiment sought to define a therapeutic dose of sodium hydrogen sulphide at room temperature.

Although there was the suggestion of trendline improvement in mean viability with lower concentrations, between 66- 200μM NaHS was found to foster significant protection of cultured proximal tubule cells stored in aerated UWMPS at room temperature. UWMPS supplementation with NaHS improves cell viability at 200μM (107.83%, range 104.39-131.82%) vs control (100%, range 100-100%) (p=0.031) (Figure 7.3).

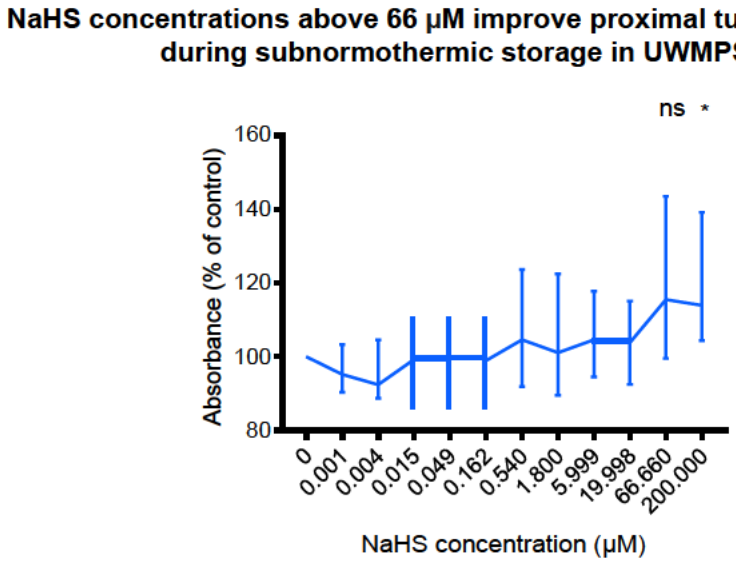

Figure 7.3. NaHS in region of 0.06-0.2mM protects cultured cells at room temperature

7.3.3.2 Metabolic effects of NaHS supplementation at the determined therapeutic dose

As indicated in Tables 4 and 5, and in the summary shown in Figure 7.5, hypothermic storage was unparalleled in its capacity to supress ^{13}C enrichment for all metabolites detected.

7.3.3.3 Glycolytic metabolism

The contribution of M0 lactate and pyruvate to their respective isotopomer pools was found to be greater after storage at 4 °C (median contribution of 79.85% and 80.07% respectively) than at 37°C (median contributions of 54.11% and 40.88% respectively). This coincided with net decreases in the contributions of each M3 isotopomer by hypothermic storage, with the pyruvate M3 isotopic contribution at 19.76 % at 4°C, rising to 52.44% at 37°C and lactate M3 contributions rising from 18.05% at 4 °C to 39.91% at 37°C. (Table 2). Storage at room temperature appeared to supress production of these

metabolites to a lesser extent than hypothermic storage, but to a greater extent compared to normothermic storage. Administration of hydrogen sulphide (NaHS) did not appear to foster a considerable change in the M0 or M3 contributions in pyruvate and lactate when compared to untreated cells stored at room temperature.

The effect of temperature and hydrogen sulphide on pyruvate MID%

Temperature	4℃	19℃	19℃ +NaHS	37℃
M0 (%)	80.07 (77.15-81.00)	44.93 (42.77-63.32)	51.40 (45.27-61.59)	40.88 (32.67-45.74)
M1 (%)	0.54 (0.49-0.56)	1.60 (0.95-1.66)	0.94 (0.816-1.11)	2.93 (2.91-3.07)
M2 (%)	0.50 (0.33-0.60)	2.16 (1.39-2.17)	1.69(1.18-1.95)	4.59 (3.75-5.43)
M3 (%)	19.76 (19.20-22.54)	52.05 (35.11-54.64)	46.85 (37.73-52.41)	52.44 (49.05-59.54)

The effect of temperature and hydrogen sulphide on lactate MID%

Temperature	4℃	19℃	19℃ +NaHS	37℃
M0 (%)	79.85 (78.26-81.58)	42.44 (40.70-49.35)	41.93(35.81-54.43)	54.11 (43.08-59.71)
M1 (%)	0.68 (0.59-0.71)	1.56 (1.40-1.62)	1.08 (0.82-1.17)	1.84 (1.68-2.33)
M2 (%)	1.43 (1.31-1.48)	3.34 (3.02-3.47)	3.25 (2.59-3.59)	4.177 (3.65-4.96)
M3 (%)	18.05(16.55-19.62)	52.71 (46.15-54.17)	53.63 (42.17-59.27)	39.91 (35.03-49.64)

Table 4. Modulation of anaerobic metabolism by temperature and hydrogen sulphide. Data reported as median with range (%)

Label incorporation into citrate, malate, fumarate and succinate, and also into indicators of TCA cycle progression (aspartate and glutamate) was found be lowest following hypothermic storage, followed by storage at room temperature. Supplementation of UWMPS with 0.1mM sodium-hydrogen sulphide did not grant the expected reduction in ^{13}C label incorporation , Conversely, the relative contributions of the above metabolites was almost universally elevated over that found at room temperature. These differences are tabulated in Table 5 and an overview of the temperature dependent changes in de ne novo metabolism are plotted below for added clarity (Figure 7.4).

The effect of temperature and hydrogen sulphide on citrate MID%

Temperature	4°C	19°C	19°C+NaHS	37°C
M0 (%)	73.58 (72.44-76.00)	68.21 (68.19-69.75)	56.53 (50.31-57.12)	56.83 (53.63-57.21)
M1 (%)	18.85 (18.76-18.88)	20.49 (20.31-20.64)	20.37 (19.98-20.53)	21.44 (21.38-21.63)
M2 (%)	5.74 (4.30-6.33)	7.11 (6.68-7.43)	13.16 (13.13-15.20)	11.84 (11.55-12.95)
M3 (%)	1.73 (0.99-2.14)	2.68 (2.25-2.80)	6.39 (6.23-9.07)	7.25 (7.10-8.30)
M4 (%)	0.38 (0.12-0.50)	0.94 (0.61-0.95)	2.53 (2.46-4.44)	2.16 (2.12-2.69)
M5 (%)	0.13 (0.13-0.23)	0.29 (0.18-0.35)	0.99 (0.66-1.29)	0.44 (0.40-0.64)
M6 (%)	-0.53 (-0.63-0.39)	0.07 (0.05-0.08)	0.20 (0.04-0.24)	0.13 (0.12-0.15)

The effect of temperature and hydrogen sulphide on succinate MID%

Temperature	4°C	19°C	19°C+NaHS	37°C
M0 (%)	95.24 (94.22-95.29)	89.04 (88.41-92.28)	90.33 (88.42-91.94)	89.80 (87.92-90.94)
M1 (%)	2.57 (2.03-2.74)	5.23(4.18-6.13)	4.28 (3.49-5.58)	5.28 (4.73-5.75)
M2 (%)	2.34(1.83-2.66)	3.97 (2.82-4.31)	3.65 (2.94-4.03)	4.33 (3.76-5.22)
M3 (%)	0.21 (0.12-0.25)	1.27 (0.60-1.35)	1.41(1.31-1.73)	0.48 (0.45-0.85)
M4 (%)	0.27 (0.21-0.27)	0.34 (0.24-0.34)	0.54 (0.49-0.56)	0.24 (0.23-0.46)

The effect of temperature and hydrogen sulphide on aspartate MID%

Temperature	4°C	19°C	19°C+NaHS	37°C
M0 (%)	96.21 (95.83-97.22)	86.97 (86.73-89.29)	53.39 (44.32-64.01)	74.28 (71.27, 74.55)
M1 (%)	1.18 (1.01-1.25)	5.87 (5.03-6.01)	10.72 (9.30-10.91)	10.23 (10.20-11.09)
M2 (%)	1.84 (1.39-2.09)	4.65 (3.77-4.73)	9.10 (7.92-9.13)	8.70 (8.57-9.73)
M3 (%)	0.68 (0.35-0.82)	2.00 (1.55-2.06)	21.42 (12.73-31.81)	6.16 (6.02-7.03)
M4 (%)	0.03 (0.02-0.04)	0.19 (0.13-0.25)	1.48 (1.13-1.78)	0.38 (0.36-0.52)

The effect of temperature and hydrogen sulphide on malate MID%

Temperature	4°C	19°C	19°C+NaHS	37°C
M0 (%)	95.38 (94.79-97.14)	84.02 (82.35-87.88)	71.61(70.02-72.23)	73.85 (69.88-74.03)
M1 (%)	1.67 (1.04-1.78)	7.33 (5.63-8.07)	13.37 (12.93-14.05)	10.36 (10.27-11.67)
M2 (%)	2.98 (1.84-3.35)	6.54 (5.04-6.97)	11.03 (10.63-11.70)	8.95 (8.88-10.49)
M3 (%)	0.18 (0.14-0.32)	2.03(1.43-2.46)	3.85 (3.72-4.66)	6.56 (6.54-7.53)
M4 (%)	-0.06(-0.09-0.05)	0.18 (0.09-0.29)	0.52 (0.51-0.62)	0.35 (0.32-0.49)

The effect of temperature and hydrogen sulphide on fumarate MID%

Temperature	4°C	19°C	19°C+NaHS	37°C
M0 (%)	97.21 (96.61-98.57)	86.50 (85.81-90.41)	83.43 (83.03-88.23)	77.65(74.85-79.35)
M1 (%)	1.07 (0.59-1.43)	6.4 (4.57-6.81)	8.05 (6.40-8.14)	9.02 (8.32-9.62)
M2 (%)	1.95 (1.10-2.20)	5.47 (4.00-5.48)	6.17 (4.70-6.50)	7.59 (7.07-8.76)
M3 (%)	0.22(0.09-0.24)	1.64 (1.11-1.93)	2.21 (1.78-2.39)	5.56 (5.07-6.46)
M4 (%)	-0.51 (-0.54--0.40)	0.14 (0.05-0.20)	0.32 (0.11-0.33)	0.26(0.26-0.41)

The effect of temperature and hydrogen sulphide on glutamate MID%

Temperature	4°C	19°C	19°C+NaHS	37°C
M0 (%)	94.86 (94.16-95.48)	85.27 (84.03-88.02)	75.08 (74.82-78.60)	73.84 (70.61-74.94)
M1 (%)	2.01 (1.93-2.07)	6.24 (5.44-6.50)	9.54 (8.19-9.79)	10.81 (10.33-11.62)
M2 (%)	3.04 (2.46-3.54)	6.67 (5.40-6.95)	11.28 (9.29-11.32)	11.09 (10.65-12.57)
M3 (%)	0.10 (0.01-0.16)	1.25 (0.84-1.69)	2.76 (2.63-2.76)	3.51 (3.35-4.11)
M4 (%)	0.04 (0.02-0.06)	0.46 (0.23-0.67)	1.10 (1.064-1.11)	0.55 (0.54-0.78)
M5 (%)	0.004 (0.002-0.005)	0.09 (0.05-0.15)	0.24 (0.23-0.24)	0.17 (0.17-0.28)

Table 5. Modulation of TCA cycle progression by temperature and hydrogen sulphide,

In all cases, generation of hypothermia resulted in stark reduction the level of ongoing metabolism, with M+0 contributions at 4°C appearing considerably greater than those observed at any other temperature, with or without hydrogen sulphide. When compared to sub normothermic temperatures, (i.e. 19°C), hydrogen sulphide supplementation at 0.1mM conferred increases in label incorporation in TCA cycle metabolites citrate, malate, succinate, fumarate, and in TCA cycle associated metabolites glutamate and aspartate (Fig 7.4)

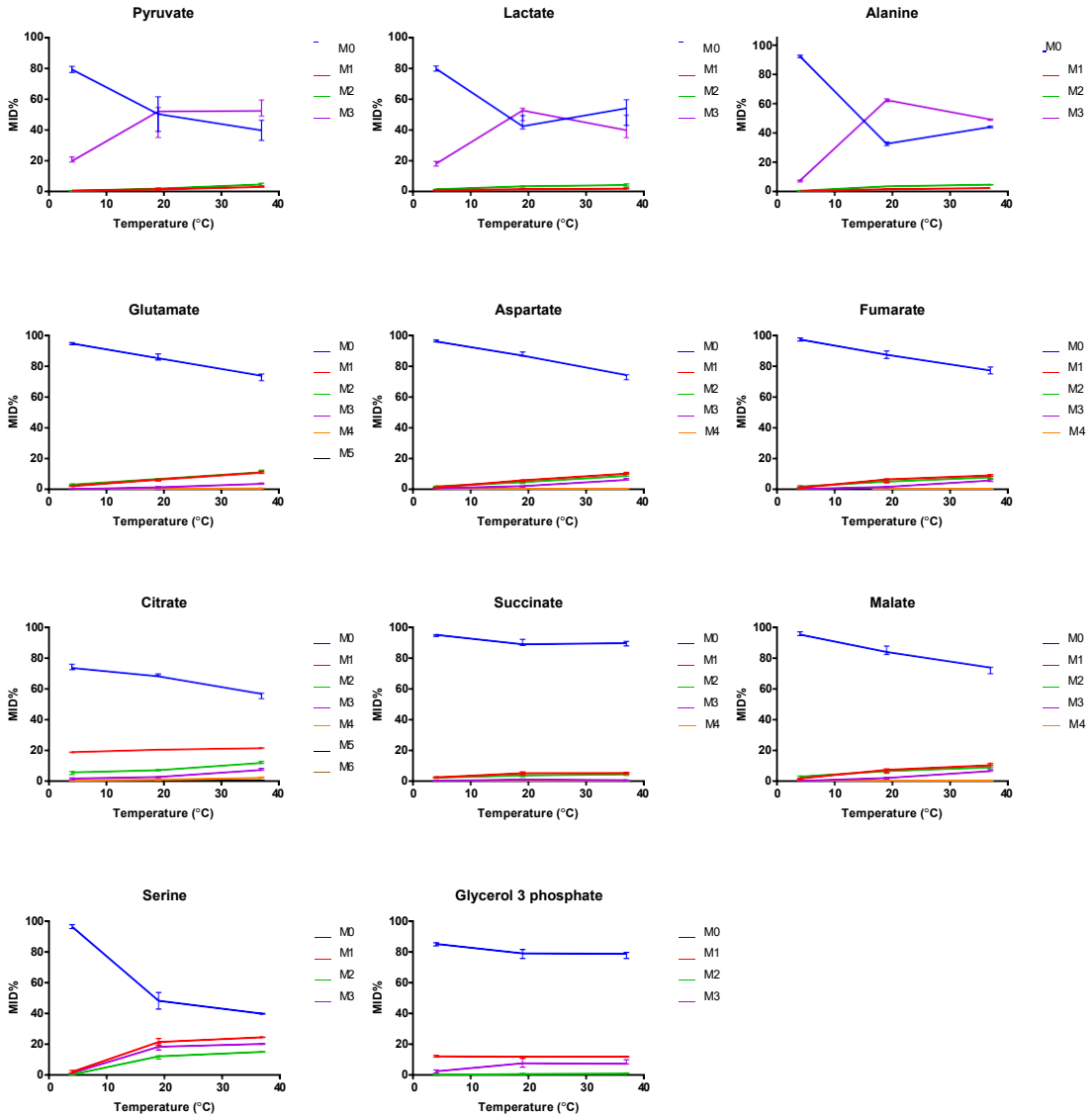

Figure 7.4. Modulation of mass isotopic distribution by temperature

7.3.3.4 Effect of storage temperature, NaHS supplementation on LDH release.

LDH release appeared to decrease with temperature. Notably, release seemed equal between hypothermic and sub normothermic temperatures- and the hydrogen sulphide supplementation did not appear to affect LDH release (Figure 7.5).

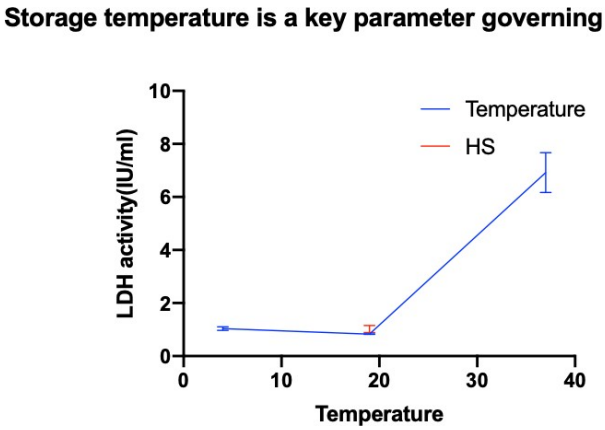

Figure 7.5. Effect of storage temperature and NaHS supplementation on LDH release

7.3.4 Study 4: Effect of fluid flow on proximal tubule cell metabolism

Shear stress has been described as a stimulus for an anaerobic switch, this experiment sought to screen if rapid fluid flux across a cell monolayer could mediate ongoing metabolism.

For the vast majority of metabolites, generation of fluid flow exerted no tangible modulation on MID. An exception is lactate, which experienced a mean increase in the M3 contribution of under fluid flow (23.37%, range 0.00-27.72%) when compared to static storage (10.42%, range 7.04-23.37%), However, this difference did not reach statistical significance (p=0.0873) (Figure 7.6).

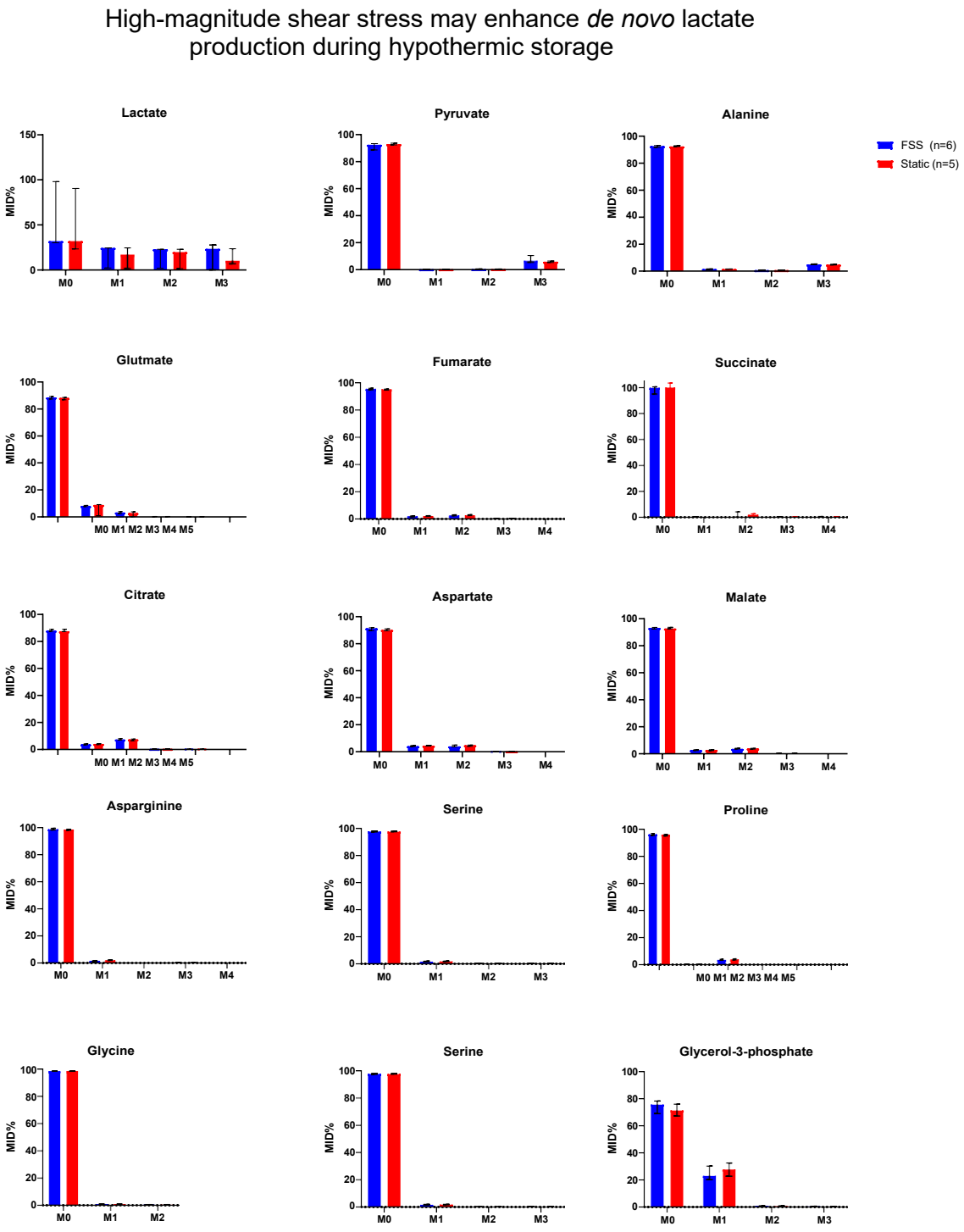

Figure 7.6. No effect of FSS on metabolic profile during hypothermic preservation

7.3.5 Study 5: The effect of oxygen availability on proximal tubule metabolism

This final experiment sought to define whether submission of proximal tubule cells to continuous atmospheric oxygen, or hyperoxic oxygen tensions had any effect on ongoing metabolic processes during simulated preservation.

Submission of RPTEC/TERT1 to severely hypoxic environments or atmospheric oxygen revealed no difference in the ^{13}C incorporation when assessed using the isotopologue analysis provided by MetaboLab (Figure 7.7).

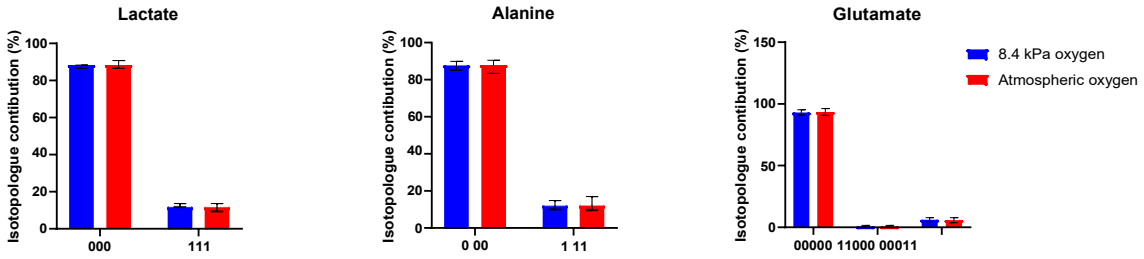

Figure 7.7. Effect of atmospheric oxygen and oxygen depletion on metabolic profile

When the whole study was repeated, and more sensitive analytical tools used, the same observation was apparent, there was no difference in the mass isotopic distribution of detected metabolites under extremes of oxygenation (Figure 7.8) observed in the porcine HMP (Figure 6.3).

However, generation of hyperoxia (i.e.~40-50kPa) resulted in an increase in the label incorporation of lactic acid, and an increase in M+2 contributions of glutamate and aspartate when compared to the lower oxygen tensions (Figure 7.8).

Oxygen environments including and below atmospheric oxygen exerted no obvious effect on the contribution of M+3 lactate (Hypoxia = 13.44%, range 9.16-14.15%) (Atmospheric

oxygen = 12.68%, range 9.19-17.78%). Generation of hyperoxia did increase M+3 lactic acid contributions, elevating them to 19.64%, range 17.83-22.64% which was significantly greater than aeration of the monolayer (p=0.0022). The median M+2 contributions of glutamate were (9.34% (range 7.64-11.198) under hypoxia, 12.47 10.25% (range 8.15-11.86%) under atmospheric oxygen and 12.74% (range 10.71-14.92%) under hyperoxia. Generation of Hyperoxia resulted higher M+2 glutamate concentrations than Atmospheric oxygen (p=0.0317) and hypoxia (p=0.0159). The contribution of M+2 Aspartate was also found to be elevated under hyperoxia when compared to hypoxia i.e. 9.63%, (range 7.55-12.78%) vs 7.31%, (range 5.65-7.74%) respectively (p=0.0317).

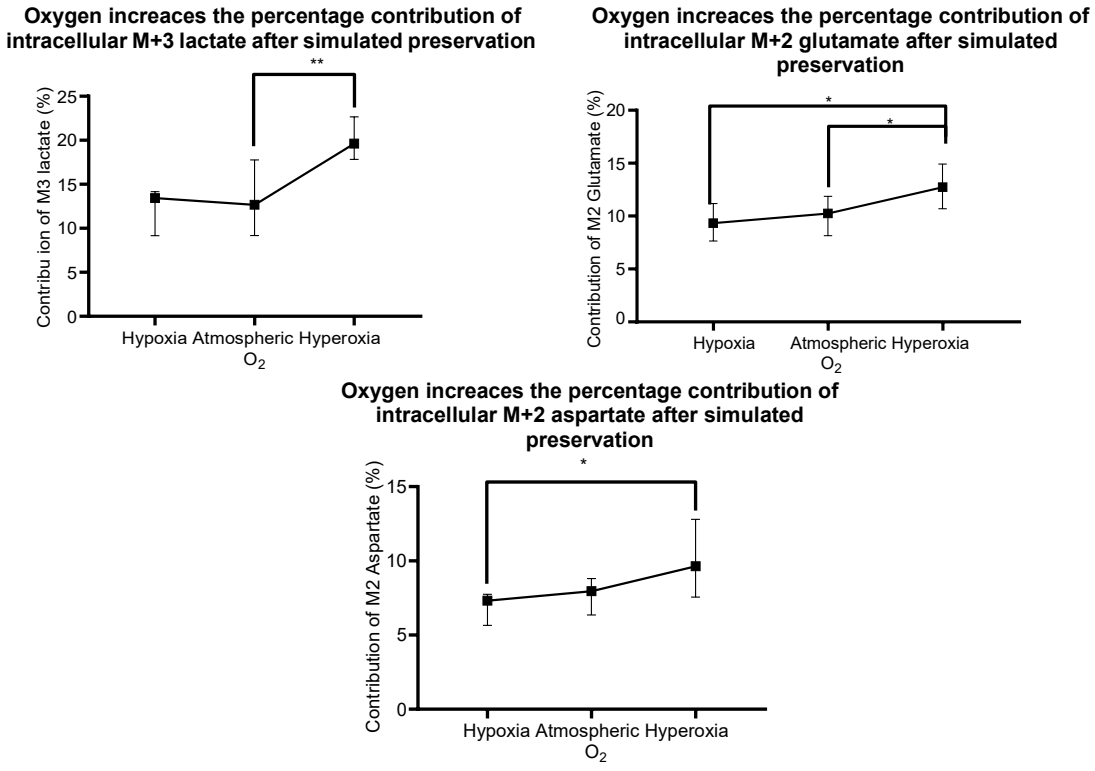

Figure 7.8. Oxygen modulates RPTEC/TERT1 metabolism during hypothermic storage

These metabolic observations coincided with apparent increases in intracellular ATP concentrations with elevations in oxygen, however this did not attain significance (Figure

7.9) Compared to the hypoxic control, which defined 100%, RPTEC/TERT1 exposed to atmospheric oxygen had median relative ATP concentrations of 121.31% (range 66.19-125.63%) and cells stored under hyperoxic conditions had endpoint relative ATP concentrations of 123.78% (range 42.63-201.35)%. The ATP concentrations were not found to differ significantly between different environments (hypoxia vs hyperoxia p=0.2188 and hypoxia vs atmospheric O2 p=0.8750).

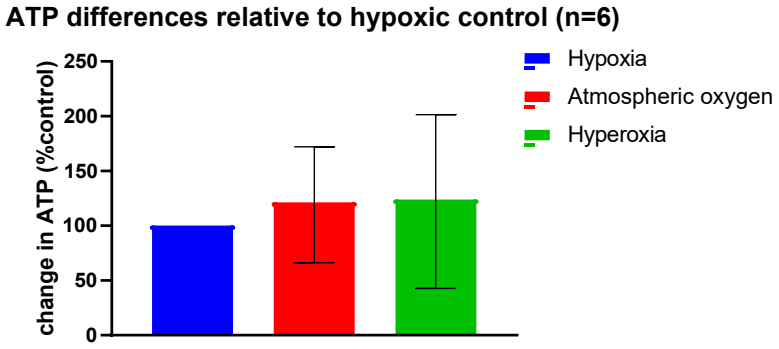

Figure 7.9. Trendline increases in cellular ATP with increases in oxygen availability.

No obvious relationship between oxygen environment and LDH release were observed (Figure 7.10).

When compared to the atmospheric control, the mean relative LDH release under hyperoxia was 118.73% (range 66.70-139.08%). Under hyperoxia, the relative LDH release was 118.38% (range 68.82-152.00%). No significant differences in LDH release were detected between oxygen environments.

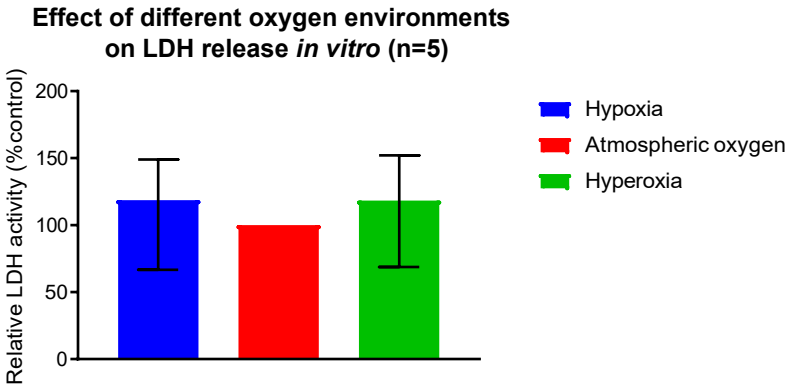

Figure 7.10. The effect of oxygen environment on LDH release *in vitro*

7.4 Discussion

7.4.1 Study 1: Assessing RPTEC/TERT1 metabolism of glucose under standard culture

The data presented herein grants unequivocal evidence that under standard cell culture and in all environments simulated, RPTEC/TERT1 absorb and metabolise glucose from the supplied fluid. The magnitude of glucose utilization *in vitro* is considerably more than the 'little to none', (302) or 1% described to occur *in vivo* (157,303,304). Whether this reflects the *in vivo* scenario is scope for future study.

During routine culture, there is evidence of both glycolytic and aerobic metabolism of glucose, inferred from M3 lactate and pyruvate respectively (Figure 7.1). The latter is reinforced by diverse labelling in downstream TCA cycle intermediates such as alpha-ketoglutarate, malate, succinate and fumarate and indirect indicators of TCA cycle activity such as aspartate and glutamate. Confidence in the accuracy of these results is provided by the routine observation of roughly half the label incorporation when [1,2-^{13}C] glucose was used instead of [U-^{13}C] glucose. Following glycolysis, the glucose hexamer is split into

two three carbon molecules which may be either lactate or pyruvate depending on the metabolic pathways currently active in the system.

With ^{13}C enrichment through the supplied [1,2-^{13}C] glucose, only half of the glycolytic endpoints would possess label, and would have a mass profile of M2, which is exactly what was observed (Figure 7.1).

Interestingly, 6-hour culture in media containing standard glucose was sufficient to render ^{13}C label almost undetectable in all metabolites, indicating the rapid and near complete turnover of metabolites under standard culture within 6 hours. In the whole organ research setting, particularly with tracer-based perfusion experiments with clinical inference gleaned following auto transplantation, this may suggest a finite timeframe through with metabolic analysis of tissue can yield meaningful results.

7.4.2 Study 2: The effect of warm ischemia on RPTEC/TERT1 glucose metabolism

The combination of oxygen and nutrient deprivation, characteristic of warm ischemia exerted the most potent modulation of ongoing cellular metabolism of all stimuli assessed. Similar to the preceding glucose isotope tracer experiment, standard culture of RPTEC/TERT1 in [U-^{13}C] glucose resulted in considerable M+3 isotopomer contributions to the total lactate pool i.e. (44.9% and 49.4% respectively. While simulated warm ischemia did not significantly affect the M3 lactate contribution, M+3 pyruvate production was found be significantly reduced to 17%, compared to the 51.2% isotopic contribution observed under standard culture ($p=0.004$) (Figure 7.2).

It is possible that this is the primary factor directing the initiation of the glycolytic phenotype observed in hypothermicly preserved kidneys (235).

7.4.3 Study 3: Quantifying thermal and pharmacological inhibition of metabolism

Reducing the ambient temperature consistently resulted in a decrease in label incorporation in the majority of the metabolites, which can be visually observed by increasing M+0 (i.e. unlabelled) contributions of each metabolite (Figure 7.4).

If the goal is to reduce lactate production given its associated deleterious connotations described in the introduction of this chapter (e.g. seemingly inferior patient outcomes based on an anaerobic phenotype at reperfusion (272), it appears that hypothermia (4°C) is the optimal preservation temperature with which to achieve this. Although NaHS concentrations between 66-200μM were found to protect cultured proximal tubule cells under atmospheric oxygen, this does not appear to be due to suppression of metabolism (Table 5.).

Hydrogen sulphide is described as competitive inhibitor of oxidative metabolism, which diminishes oxygen consumption while preserving intracellular ATP and mitochondrial membrane potential(298). However, at high levels, hydrogen sulphide can function as an electron donor(300).

As expected, the addition of hydrogen sulphide exerted minimal influence on label incorporation in anaerobic metabolites, indicating that it cannot be used lower lactate production. However, addition of 0.1mM NaHS hydrogen sulphide had pronounced effect on the production of TCA cycle intermediates, in most cases elevating production of each mass isotopomer above the level recorded at the room temperature comparator. This suggests that 0.1mM NaHS enhances TCA cycle activity in proximal tubule cells, without the corresponding desirable inhibition of anaerobic metabolism. Interestingly, this reinforces the assumption that oxygen supplementation during preservation is beneficial due to support of aerobic metabolism, since in this experiment supplying an additional

electron donor (i.e. hydrogen sulphide) also yielded a beneficial effect on cellular survival (Figure 7.3). It is unlikely that this protective effect was derived from the pH changes. Although hydrogen sulphide is a strong base, the concentration added was small (0.1mm) and the fluid bathing the cells was (UWMPS) contains 25mM phosphate and a 10mM HEPES which together confer a potent pH buffering capacity(301). Investigating the optimal pH for proximal tubule cell protection is however very interesting certainly scope for further work.

Hypothermic preservation also reduced the level of LDH release, when compared to storage of cells at physiological temperatures. This is likely a reflection that UW MPS is poor at supporting cells under physiological temperatures. No obvious difference in LDH release was observed between hypothermic and sub normothermic storage temperatures, indicating that at least in terms of preserving membrane integrity in UWMPS, sub normothermic storage and hypothermic storage are relatively equal *in vitro.* Addition of 0.1mM NaHS did not increase LDH release when compared to untreated cells at room temperature Figure 7.5, indicating the toxicity associated with cellular exposure to 1mM hydrogen sulphide (302) did not manifest as membrane damage in this proof of concept experiment.

7.4.4 Study 4: Effect of fluid flow on proximal tubule cell metabolism

Unlike what has been reported under physiological temperatures, the presence and absence of fluid shear stress did not appear to cause a difference in *de novo* metabolic profile, with the possible exception of M+3 lactate, which narrowly avoided significant difference (Mean FSS MID% 0.24, Mean Static MID% 0.12, p= 0.0873) (Figure 7.6).

However, this experiment does assess the effect of low-level fluid shear stress, which exerted a protective effect on cell viability in Chapter 6.

This early experiment into the effect of FSS on *de novo* cellular metabolism during simulated storage predated the creation of ShearFAST, and its execution demonstrates the utility for such a tool in FSS research. In this experiment, the effect of FSS on cell metabolism was investigated, inspired by the rocking model publication(168), but without a validated method to measure rocking parameters.

The rocker speed set (60RPM) would intuitively suggest a rocking speed of 1 Hz, which was utilised in the paper reporting the rocking method(168). As described in Chapter 4, the actual rocking speed when this speed is set on this rocker was found to be 0.59Hz using ShearFAST.

Regardless, the low volume of UWMPS used, relative to the 152 cm^2 growth area on a 150mm dish would result in a characteristic FSS of around 32 dyne/cm^2 which is far greater than the 1 dyne/cm^2 proposed to be physiology relevant. This study retains utility, because it demonstrates potentially deleterious effect of uncontrolled FSS on proximal tubule metabolism during simulated storage. Subjugation of the proximal tubules to high flow could conceivably occur following the glomerular damage observed in Hypothermic kidney preservation (186,187) . Further work is required to determine if the perceived benefit of low-level FSS (Figure 6.9 and Figure 6.6) has a metabolic component.

7.4.5 Study 5: The effect of oxygen availability on proximal tubule metabolism

No modulatory effect of lactate levels fluid oxygenation was observed between cells stored under severe hypoxia or under atmospheric oxygen (Figure 7.7 and Figure 7.8).

These are the two extremes in oxygen availability observed in the porcine whole organ model (Figure 6.3) and are likely to cover a greater range of oxygen environment that exists in the HMP storage pretransplant human kidneys (Figure 8.5).

Based on this information, one could surmise that oxygen levels above atmospheric oxygen may be required if one hopes to meditate lactate production and/or restore aerobic metabolism during *ex vivo* storage.

In vitro instigation of supraphysiological levels of fluid oxygen (40-50kPa) (Figure 3.12) resulted in increased contributions of M+3 Lactate, and M+2 Aspartate and Glutamate to their respective metabolite pools (Figure 7.8).

Glutamate and aspartate labelling are indirect readouts the TCA cycle activity, and with trendline increases in ATP concentrations with increases in oxygen availability (Figure 7.9), it does appear that oxygen environments above that permitted by continuous aeration of preservation fluid are required to exert some restoration of aerobic metabolism *in vitro*. However, the detected increase in lactate production under hyperoxia was a surprising observation with no clear explanation. However, as discussed in later chapters, oxygen supplementation during hypothermic storage may generate enhanced oxidative stress to stored cells. ROS can modulate enzymes involved in glucose metabolism, and in response- glycolytic intermediates are driven into the pentose phosphate cycle as a protective response to regenerate NADPH, an essential factor for reduction of oxidised glutathione and consequently, bolstering of cellular antioxidant potential (303).. Upregulation of lactate production under high oxygen has been observed in critically ill patients, and it is speculated this glycolytic shift, along with a demonstrated upregulation of Pentose phosphate pathway genes serves to facilitate improved antioxidative support through NADPH regeneration(304).

Understanding the mechanism behind hyperoxia stimulated increases in lactate production is scope for further work. In any case, these data support the hypothesis that proximal tubule energy state and metabolism can be augmented by exposure to high levels of oxygen.

7.5 Conclusions

Brief periods of warm ischemia are sufficient to drive a pronounced anaerobic shift in glucose metabolism, and hypothermia is required to suppress lactate production caused by this shift. Super-physiological FSS experienced by the proximal tubule may be a continuous stimulus for anaerobic metabolism even under atmospheric oxygen, however elevating the storage fluid concentration of dissolved oxygen above atmospheric levels is a potential route to metabolic optimisation of renal tissue and improved ATP generation.

8 Metabolic and physiological effects of oxygen supplementation during whole organ perfusion.

This chapter includes a manuscript in which the metabolic and physiological effects of continuous oxygen supplementation as delivered in current clinical trials are compared to kidneys receiving continuous perfusate aeration. This article was published in a special edition of *Transplantation in February 2019,* i.e. *Tissue Regeneration and Repair.*

*Patel K, ***Smith TB**, Neil DAH, Thakker A, Tsuchiya Y, Higgs EB, et al. The Effects of Oxygenation on *Ex vivo* Kidneys Undergoing Hypothermic Machine Perfusion. Transplantation [Internet]. 2019 Feb 103(2):314–22.

As first author, I was responsible for experimental design, execution sampling and analysis, I wrote the article, and played a key role in all stages of its preparation and submission.

This chapter is composed of a brief introduction to the paper, followed by the inclusion of the published manuscript and a critical review of the paper.

8.1 Manuscript overview

The role of perfusate oxygen during HMP is at the forefront of organ preservation research, with multiple clinical trials assessing both short and long term transplant outcomes following continuous perfusate oxygenation (123,305).

Oxygenated hypothermic machine perfusion may exert a protective influence through multiple mechanisms, including improvements to blood flow rate post reperfusion (306) and GFR as assessed by creatinine clearance(121).

A central rational behind the deployment of oxygenated machine perfusion is its potential to redirect the residual metabolic processes occurring under hypothermia. ATP depletion is a presiding pathological aetiology in both cold and warm ischemia which if alleviated may lead to therapeutic benefit (140,307–309)Perfusate oxygenation has the potential to mitigate the progressive hypoxia observed during HMP, and potentially support the regeneration of ATP through the electron transport chain.

In the previous chapter, it was observed that exposure of hypothermicly stored proximal tubule cells to hyperoxic atmospheres resulted in *de novo* synthesis of M+2 glutamate.

M+2 Glutamate can be an indicator of TCA cycle activity, if that isotopologue is [1,2-^{13}C] glutamate, which signifies conversion from alpha ketoglerate and multiple passages of the TCA cycle, or [4,5-^{13}C] glutamate which signifies a single passage the of TCA cycle (310,311).

Building on the data from the *in vitro* model, the main purpose of this article was to use advanced metabolic analyses to determine whether or not oxygen supplementation during whole organ HMP results in unequivocal restoration of aerobic metabolism.

A secondary objective was to submit the paired kidney to continuous perfusate aeration. This was to determine if the high level of oxygen delivered by continuous oxygenation was

required in order to achieve the beneficial metabolic effect, or if in fact it just generated an unnecessary risk of oxidative insult.

The Effects of Oxygenation on Ex Vivo Kidneys Undergoing Hypothermic Machine Perfusion

Kamlesh Patel,[1,2] Thomas B. Smith,[1] Desley A.H. Neil, PhD, FRCPath,[3] Alpesh Thakker, PhD,[1] Yugo Tsuchiya, PhD,[3] Ellen B. Higgs,[5] Nikolas J. Hodges, PhD,[5] Andrew R. Ready, FRCS, MD,[2] Jay Nath, FRCS, PhD,[1,2] and Christian Ludwig, PhD[1]

Background. Supplemental oxygenation of the standard hypothermic machine perfusion (HMP) circuit has the potential to invoke favorable changes in metabolism, optimizing cadaveric organs before transplantation. Methods. Eight pairs of porcine kidneys underwent 18 hours of either oxygenated (HMP/O_2) or aerated (HMP/Air) HMP in a paired donation after circulatory death model of transplantation. Circulating perfusion fluid was supplemented with the metabolic tracer universally labeled glucose. Perfusate, end-point renal cortex, and medulla samples underwent metabolomic analysis using 1-dimension and 2-dimension nuclear magnetic resonance experiments in addition to gas chromatography-mass spectrometry. Analysis of ^{13}C-labeled metabolic products was combined with adenosine nucleotide levels and differences in tissue architecture. Results. Metabolomic analysis revealed significantly higher concentrations of universally labeled lactate in the cortex of HMP/Air versus HMP/O_2 kidneys (0.056 mM vs 0.026 mM, $P < 0.05$). Conversely, newly synthesized [4,5-^{13}C] glutamate concentrations were higher in the cortex of HMP/O_2 kidneys inferring relative increases in tricarboxylic acid cycle activity versus HMP/Air kidneys (0.013 mmol/L vs 0.003 mmol/L, $P < 0.05$). This was associated with greater amounts of adenoside triphosphate in the cortex HMP/O_2 versus HMP/Air kidneys (19.8 mmol/mg protein vs 2.8 mmol/mg protein, $P < 0.05$). Improved flow dynamics and favorable ultrastructural features were also observed in HMP/O_2 kidneys. There were no differences in thiobarbituric acid reactive substances and reduced glutathione levels, tissue markers of oxidative stress, between groups. Conclusions. The supplementation of perfusion fluid with high-concentration oxygen (95%) results in a greater degree of aerobic metabolism versus aeration (21%) in the nonphysiological environment of HMP, with reciprocal changes in adenoside triphosphate levels.

(*Transplantation* 2019;103: 314–322)

Hypothermic machine perfusion (HMP) of kidneys has been widely used as a modality of organ preservation in clinical practice for over a decade. Hypothermic machine perfusion involves the recirculation of chilled perfusion fluid at subphysiological pressures through the renal vasculature of the ex vivo kidney in the hours before transplantation.

The benefits of HMP have been reported for all subtypes of cadaveric kidneys including improved short-term outcomes[1,2] and graft survival[3,4] compared with static cold storage. The proposed mechanisms by which HMP exerts benefit include decreased vasospasm,[5] the protection of vascular endothelium,[6] the washout of toxic metabolites and supplementation of metabolism[7,8] with the potential for the metabolic profile of the ex vivo kidney to predict early graft function.[9]

Oxygenation of circulating perfusate during HMP has recently been revisited as a means of optimizing cadaveric kidneys before transplantation. Previous human and animal studies have used a variety of methodologies yielding inconsistent but promising results in terms of functional outcomes.[10] Porcine autotransplant studies have shown functional benefits when the HMP circuit is modified to include oxygenation in a

Received 28 June 2018. Revision received 20 September 2018.

Accepted 13 October 2018.

[1] *Institute of Metabolism and Systems Research, College of Medical and Dental Sciences, University of Birmingham, Birmingham, United Kingdom.*

[2] *Department of Renal Surgery, University Hospitals Birmingham, Birmingham, United Kingdom.*

[3] *Department of Histopathology, University Hospitals Birmingham, Birmingham, United Kingdom.*

[4] *Department of Structural and Molecular Biology, University College London, London, United Kingdom.*

[5] *School of Biosciences, University of Birmingham, Birmingham, United Kingdom.*

K.P., T.B.S., J.N., and C.L. contributed equally to this work.

Several authors (K.P., J.N., T.S., C.L., and A.R.) have ongoing research in part funded by Organ Recovery Systems. The other authors declare no conflicts of interest.

This work was funded through grants from University Hospitals Birmingham Charities, The Kidney Patient Association and Organ Recovery Systems.

J.N., A.R., and C.L. designed research. J.N., K.P., T.S., and C.L. performed research. K.P., T.S., J.N., C.L., A.T., D.N., Y.T., E.H., N.H., and Y.T. analyzed data. C.L. contributed new analytical tools relating to NMR spectral analyses. K.P. and T.S. wrote the article. All authors reviewed the article before submission.

Correspondence: Kamlesh Patel, Department of Renal Surgery, Queen Elizabeth Hospital Birmingham, University Hospitals Birmingham NHS Foundation Trust Mindelsohn Way, Edgbaston, Birmingham, B15 2GW, United Kingdom.

Supplemental digital content (SDC) is available for this article. Direct URL citations appear in the printed text, and links to the digital files are provided in the HTML text of this article on the journal's Web site (www.transplantjournal.com).

ISSN: 0041-1337/19/10302-0314

DOI: 10.1097/TP.0000000000002542

donation after circulatory death (DCD) model of transplantation,[11] but the same did not hold true for a donation after brainstem death model.[12]

KPS-1 (Organ Recovery Systems, Itasca, IL), the kidney perfusion solution commonly used in clinical practice, is a hypertonic, acellular fluid with no designated oxygen carrier. Any oxygenation of perfusion fluid is a result of passive diffusion from the air contained within the perfusion fluid reservoir. Supplemental oxygenation during HMP may be an effective way to alter metabolic pathway activity, with the presumption that oxygenation encourages aerobic metabolism and therefore replenishes cellular adenoside triphosphate (ATP) stores.[13] In addition to potential functional benefits after reperfusion, increased ATP stores prevent detrimental processes such as cellular swelling, apoptosis and necrosis.

Despite these proposed benefits of oxygenation, damage due to reactive oxygen species (ROS), responsible for many consequences of ischemia reperfusion injury (IRI) is a potential drawback.[14] Any potential metabolic benefits of organ oxygenation must, therefore, be tempered against the potentially deleterious effects of ROS injury, and it would seem rational that oxygen delivery should occur at the lowest therapeutic concentration possible to achieve such benefits. In conditions of oxidative stress leading to typical changes, such as oxidative DNA modifications[15,16] and lipid peroxidation,[17] levels of reduced glutathione (GSH) are depleted. Thiobarbituric acid reactive substances (TBARS) provide a sensitive assay for lipid peroxidation.[18]

Metabolic tracer studies using perfusion fluid supplemented with universally labeled ^{13}C glucose ([U-^{13}C] glucose) have been used to accurately demonstrate de novo metabolism within biological systems, including the ex vivo HMP kidney.[19] In conjunction with adenosine nucleotide analysis, the concentration and isotopic labeling patterns of central metabolites enable description of aerobic/anaerobic pathway activity in addition to their metabolic sequelae.

The aims of this study are to compare the metabolic consequences, changes in perfusion dynamics, damage secondary to oxidative stress, and histological changes between perfusate oxygenation with atmospheric oxygen (21%) and high concentration oxygen (95%).

MATERIALS AND METHODS

Retrieval of Organs

Experiments were performed on 8 pairs of porcine kidneys (n = 16). Porcine organs were procured from 22- to 26-week-old male English white pigs weighing 80 to 85 kg from a local abattoir (F.A. Gill, Wolverhampton, UK) in a previously described controlled model of DCD.[20]

Our model, similar to other well-reported controlled DCD models in pigs,[21] was designed to simulate a Maastricht category III donor.[22] Animals were sacrificed by electrical stunning and exsanguination before in situ warm ischemia for 15 minutes, during which time, laparotomy and bilateral nephrectomy were performed. After retrieval, all kidneys were checked for damage and suitability for the study. To permit fair comparison, pairs of kidneys were only included if both kidneys were supplied by a single artery at the point of origin from the abdominal aorta. Kidneys were initially flushed with 1 L of Soltran solution (Baxter Healthcare) at 4°C at a pressure of 120 mm Hg, supplemented with 0.93 g [U-^{13}C] labeled glucose (5 mM) at 4°C and 5000 iU heparin to remove any residual blood products and enable rapid cooling.

The purpose of adding ^{13}C-enriched glucose to the cold flush solution was to increase initial availability of glucose for generation of downstream labeled metabolic substrates later during HMP. Organs were then stored in static conditions (1 L Soltran with 1% PenStrep) for 2 hours before commencing HMP. All experiments were performed following the principles of laboratory animal care according to the National Institutes of Health standards. No animal was slaughtered solely for the purpose of experimentation.

Hypothermic Machine Perfusion

Machine perfusion was initiated using the LifePort Kidney Transporter 1.0 (Organ Recovery Systems) at a pressure of 30 mm Hg. Kidneys were perfused with 1 L KPS-1 (Organ Recovery Systems) supplemented with 0.93 g [U-^{13}C] glucose (5 mM) giving a total glucose concentration of 15 mM. Single arterial anatomy permitted cannulation with a 5 mm T-connector to attach to the LifePort.

The standard LifePort perfusion circuit was modified (Figure 1) to incorporate a pediatric membrane oxygenator (Hilite 800 LT series hollow fiber oxygenator; Medos, Medizintechnik, AG). One kidney from each pair was randomly allocated to either the oxygenated or aerated perfusion group with contralateral organ allocated to the other perfusion group. In the oxygenated perfusion group (HMP/O_2) in which 95% O_2, 5% CO_2 (Carbogen, BOC Medical) was passed through the oxygenator via a flow valve at 0.1 L/min. In the aerated perfusion fluid (HMP/Air) group, sterile filtered room air (assumed 21% oxygen) was delivered at the same rate (0.1 L/min).

During perfusion, the dissolved oxygen concentration in the fluid entering the kidney via the in-flow limb was measured using an oxygen sensor (Oxygen Microsensor NTH-PSt1; Presens GmbH, Germany) paired with a microfiber optic oxygen transmitter (Microx TX3; Presens GmbH). Before experiments, this was calibrated using the oxygen-carrying capacity of deionized water at 4°C (100%, maximum) and vigorously agitated 1% sodium sulphite solution (0%, minimum). The negative control was validated against deionized, nitrogenated water at room temperature. The mean concentration of oxygen in the inflow limb of the HMP/O_2 circuit

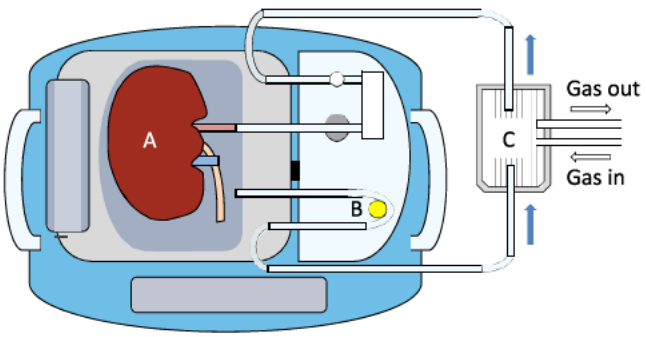

FIGURE 1. Schematic diagram of a modified LifePort circuit which includes a pediatric membrane oxygenator. Perfusate is drawn from the fluid reservoir containing the kidney (A) into the perfusion circuit via a peristaltic pump (B) and pushed through a pediatric membrane oxygenator (C). The oxygenator allows for the gas supplied (either atmospheric air or 95% oxygen) to be dissolved in the fluid before it passes through a bubble chamber and into the kidney (A) via the cannulated renal artery.

was 68.7 kPa, whereas mean oxygen concentration in the inflow limb of the HMP/Air circuit was 21.0 kPa.

Kidneys were perfused for 18 hours. Perfusate samples (2 mL) were frozen immediately after retrieval via the sampling port of the LifePort cassette at multiple timepoints (0, 1, 6, 12, 18 hours) with perfusion parameters also reported at these times. At the end of the perfusion period, kidneys were laterally bisected with cortex and medulla samples snap frozen in liquid nitrogen before storage at −80°C for metabolic analysis. Wedges of renal cortex and medulla and pieces of renal artery were immersion fixed in 10% formalin for histology and samples of cortex (2 × 2 × 5 mm) were immersion fixed in glutaraldehyde in phosphate buffer for electron microscopy.

Sample Processing

Perfusate and tissue sample extraction was performed as previously described.[19] Perfusate samples for 1-dimension (1D) ^{1}H nuclear magnetic resonance (NMR), 2-dimension (2D) ^{1}H,^{13}C HSQC NMR, and gas chromatography–mass spectrometry (GC-MS) analysis were taken from the upper layer of a biphasic solution containing polar metabolites, and formed from a vigorously mixed solution of equal amounts of neat perfusate, high-performance liquid chromatography (HPLC) grade methanol (−80°C), and HPLC grade chloroform (−20°C). Polar extracts were dried at 35°C in a vacuum drier.

Frozen cortex and medulla samples were powdered using a Cryo-cup grinder (Biospec Products). From this, 0.5 g was suspended in methanol (−80°C) and homogenized in Precellys homogenization tubes using a Precellys 24 Dual homogenizer (Bertin Technologies, Montigny-le-Bretonneux, France) at low speeds in short intervals (5000 RPM for 8 × 10 s) to prevent samples from heating. Cholorform (−20°C) and deionized water were then added and the resultant solution mixed vigorously before sampling from the upper layer containing polar metabolites. Samples were then dried at 35°C overnight in a vacuum drier.

Nuclear Magnetic Resonance Spectroscopy

For NMR analysis, dried perfusate and tissue extracts were suspended in 100-mM phosphate buffer, containing 0.5-mM dry sealing system, 2-mM imidazole, and 10% D_2O.

Both 1D ^{1}H and 2D ^{1}H, ^{13}C heteronuclear single quantum coherence (HSQC) NMR, spectra were acquired using a 600-MHz Bruker Avance III NMR spectrometer in 5-mm NMR tubes. All 1D ^{1}H NMR spectra were processed within the MetaboLab software package version 1.0.0.1.[23] After this, 0.5 Hz line broadening was applied with zero-filling the data up to 131072 real data points before Fourier transformation. The resulting spectra were referenced using dry sealing system and manually phase corrected. Subsequently, the spectral baseline was corrected using MetaboLab's spline baseline correction before the spectra were exported to Bruker format for metabolites to be quantified using Chenomx 8.2 (Chenomx INC, Edmonton, AB, Canada).

For 2D ^{1}H,^{13}C HSQC NMR, the ^{13}C dimension was acquired with a spectral width of 160 ppm using 25% of 8192 data points using a nonuniform sampling scheme. The nonuniformly sampled spectra were reconstructed with compressed sensing using the MDDNMR and NMRPipe software.[24-26] All spectra were processed without baseline correction to avoid complications in the multiple-analysis procedure. MetaboLab was used to combine data from 2D ^{1}H,^{13}C HSQC NMR and GC-MS using a previously described model free approach[27] to give more accurate isotopomer distributions for key metabolites of interest.

Gas Chromatography-mass Spectrometry

The dried polar extract was dissolved in 2% methoxyamine HCl in pyridine (Sigma-Aldrich, Dorset, UK) followed by incubation at 60°C and subsequently 60 μL N-tertbutyldimethylsilyl-N-methyltrifluoroacetamide with 1% (w/v) tertbutyldimethyl-chlorosilane (Sigma-Aldrich, Dorset, UK) derivatization reagent was added.

GC/MS was performed using an Agilent 7890B Series GC/MSD gas chromatograph with a polydimethylsiloxane GC column coupled, with a mass spectrometer (Agilent Technologies UK Limited, Stockport, UK).

For determination of the mass isotopomer distributions, spectra were corrected for natural isotope abundance. Data processing from raw spectra to mass isotopomer distribution correction and determination was performed using MetaboliteDetector software.[28]

HPLC: Adenosine Nucleotide Analysis

Concentrations of adenosine monophosphate (AMP), adenosine diphosphate (ADP), and ATP were determined using HLPC analysis of extracted kidney cortex and medulla samples from the oxygenated and aerated experiments. Adenine nucleotides were extracted from frozen powdered tissue with ice-cold 0.35 M perchloric acid and analyzed by ion-pair reverse phase HPLC as described elsewhere.[29]

Biochemical Assays: Markers of Oxidative Stress

The GSH assay, as originally described by Hissin and Hilf,[30] was performed on samples of renal cortex to provide an indication of oxidative stress. Quantification of cortical malonaldehyde (MDA) was performed using TBARS assay. Assay results for GSH and TBARS were normalized to protein content as per the Bradford assay.[31] Full assay protocols can be seen in the Supplemental Materials and Methods (SDC, http://links.lww.com/TP/B660).

Light Microscopy

Wedges of renal cortex and medulla from 3 pairs of HMP/O_2 and HMP/Air kidneys and renal arteries were fixed in formalin and processed to a paraffin block. After this, 4-μm sections of renal cortex and medulla were stained with hematoxylin and eosin and periodic acid Schiff, whereas renal artery sections underwent staining with hematoxylin and eosin alone.

Photomicrographs of 10 random glomeruli (40× magnification), 10 random areas containing predominantly tubules (5 subcapsular and 5 midcortex at 20× magnification) and 5 transverse sections of intraparenchymal arteries (20× magnification) were assessed. Image J 1.05i software (National Institutes of Health, Bethesda, MD) was used for morphometric assessment.

Images were assessed for evidence of injury using glomerular shrinkage, interstitial edema, and perivascular edema as indicators of damage. The extent of injury of extraparenchymal renal arteries was semiquantitatively graded. Further information on grading of injury can be seen in Supplemental Materials and Methods (SDC, http://links.lww.com/TP/B660).

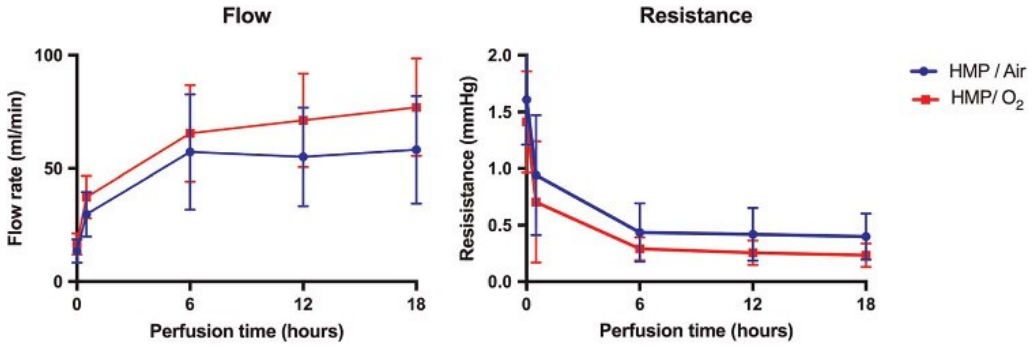

FIGURE 2. Perfusion parameters for oxygenated hypothermic machine perfusion (HMP/O_2) and aerated hypothermic machine perfusion (HMP/Air) porcine kidneys.

Electron Microscopy

Standard protocols of the Electron Microscopy Laboratory, University Hospitals Birmingham, Birmingham, UK, were followed. For electron microscopy (EM), biopsies (3 × 3 × 5 mm) of renal cortex were fixed in 2.5% glutaraldehyde in 0.1 M phosphate buffer, pH 7.4 then postfixed in osmium tetroxide and en-bloc stained with uranyl acetate before being processed by standard techniques to an epon araldite block. Thick sections were stained with toluidine blue and ultrathin sections stained with lead citrate and examined by a Joel JEM1200-EX 11 electron microscope.

Random photomicrographs were taken of glomeruli, tubules, and arteries/arterioles at 680× to include mesangial areas and glomerular capillary loops. Of the total mitochondria present, the percentage of glomeruli of normal morphology, condensed, and containing flocculent densities were determined for each kidney. Both the pathologist and technician who acquired and analyzed images with light and electron microscopy were blinded to the kidney allocation groups.

Statistical Analysis

Statistical analysis was performed using GraphPad Prism version 6.00 for Mac OS X (GraphPad Software, La Jolla, CA). Analyses were deemed to be statistically significant when P is less than 0.05. HMP/O_2 and HMP/Air groups were compared using Mann-Whitney U test.

RESULTS

Preliminary Studies

Using previously described methodology, a porcine kidney was perfused using a standard unmodified LifePort circuit[8] which does not provide oxygenation or aeration of perfusate. After 2 hours of storage in static conditions, oxygen levels in the in-flow limb dropped by over 90% in 2 hours from an initial PaO_2 of 20.58 to 1.77 kPa, whereas the venous effluent declined from 2.15 kPa, approximately 10% of that in the in-flow limb at T0, to absolute anoxia within 80 minutes.

Perfusion Parameters

Mean resistance readings were lower, and therefore flow readings higher, for all timepoints in HMP/O_2 kidneys. However, the difference did not reach statistical significance at 6, 12, or 18 hours (P values 0.063, 0.278, 0.063, respectively) (Figure 2).

1D ^{1}H-NMR: Quantification of Metabolites Concentrations

1D ^{1}H-NMR analysis was used to determine the concentration of unlabeled metabolites within the circulating perfusate at 6, 12, and 18 hours (Table S1, SDC, http://links.lww.com/TP/B660). The concentrations of unlabeled metabolites in renal cortex and medulla (Table S2, SDC, http://links.lww.com/TP/B660) were also determined. No significant differences were observed between circulating metabolites in the perfusate of HMP/O_2 compared with HMP/Air kidneys.

2D NMR and GC-MS Analysis: Isotopomer Distributions for ^{13}C-labeled Metabolites

Using 2D NMR, isotopomer combinations were determined for the metabolites alanine, glutamate, and lactate in the perfusion fluid and tissues of both HMP/O_2 and HMP/Air kidneys, indicating de novo metabolism (Table 1). For these metabolites, 2D NMR data were combined with GC-MS data to determine isotopomer distributions in Table 1.

TABLE 1.

Isotopomer distributions for isolated labeled metabolites in the perfusate and tissue of HMP/O_2 and HMP/Air porcine kidneys

	Isotopomer		HMP/O_2, %	HMP/Air, %	P
Lactate[a]	+3	Perfusate	5.43	9.85	0.0078[b]
		Cortex	6.36	8.73	0.0078[b]
		Medulla	13.80	15.70	0.0312[b]
Alanine[a]	+3	Perfusate	4.05	8.54	0.0078[b]
		Cortex	6.07	8.09	0.0078[b]
		Medulla	6.78	8.39	0.0312[b]
Citrate	+2	Perfusate	0.00	0.00	>0.9999
		Cortex	0.48	0.33	0.6250
		Medulla	0.00	0.36	0.2500
Glutamate[a]	+2	Perfusate	1.80	0.27	0.1250
		Cortex	1.60	0.50	0.0312[b]
		Medulla	3.13	0.40	0.0312[b]
Succinate	+2	Perfusate	1.01	0.26	0.2500
		Cortex	1.46	0.41	0.0156[b]
		Medulla	2.54	0.36	0.0312[b]
Malate	+2	Perfusate	0.38	0.34	0.6250
		Cortex	1.09	0.87	0.4688
		Medulla	2.80	0.00	0.0312*

[a] Combined NMR/MS analysis used to calculate isotopomer distributions.
*P < 0.05.
HMP/Air, aerated hypothermic machine perfusion; HMP/O_2, oxygenated hypothermic machine perfusion.

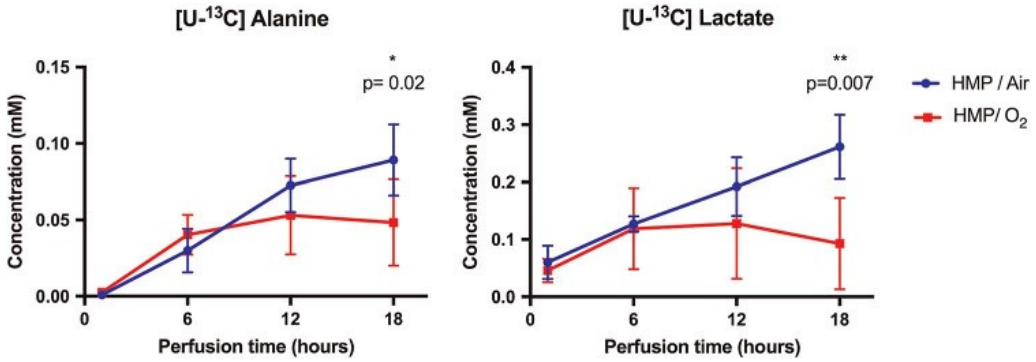

FIGURE 3. Absolute concentrations of universally labeled 13C ([U-13C]) alanine and [U-^{13}C] lactate in circulating perfusate. * 0.01 < *P* < 0.05, ** 0.001 < *P* <0.01, *** *P*< 0.001.

Absolute Quantification of Labeled Metabolites

Using a combination of 1D, 2D NMR and GC-MS, concentrations of [U-^{13}C] alanine and [U-^{13}C] lactate were quantified for extracted perfusate samples at each timepoint (Figure 3). Labeled isotopomers of glutamate were absent in early perfusate samples, thus continuous data is not reported for glutamate. Absolute concentrations of [U-^{13}C] alanine, [U-^{13}C] lactate and [4,5-^{13}C] glutamate were determined for endpoint perfusate, cortex, and medulla samples (Figure 4).

Microscopy: Light Microscopy and Electron Microscopy

Glomeruli

Glomeruli were shrunken but otherwise appeared normal on light microscopy in both groups. There was significantly more shrinkage of glomeruli in the HMP/Air 52% (range, 40-70) versus HMP/O_2 67% (range, 47-83) (*P* < 0.001). There was no ultrastructural difference between the 2 groups; epithelial and endothelial cells appeared condensed with preservation of podocyte foot processes and an intact endothelial lining with retained fenestrations.

Tubules and Interstitium

Changes consistent with acute tubular injury were present up to a similar extent in both HMP/O_2 and HMP/Air kidneys on light microscopy. Ultrastructural changes include edema/separation between the basolateral infoldings, focal areas of denuded basement membranes, and moderate numbers of exfoliated epithelial cells within the lumen. The brush border was largely intact.

Abnormal mitochondrial morphology consisted of either condensed mitochondria or mitochondria containing flocculent densities, an indication of irreversible injury. Examples are

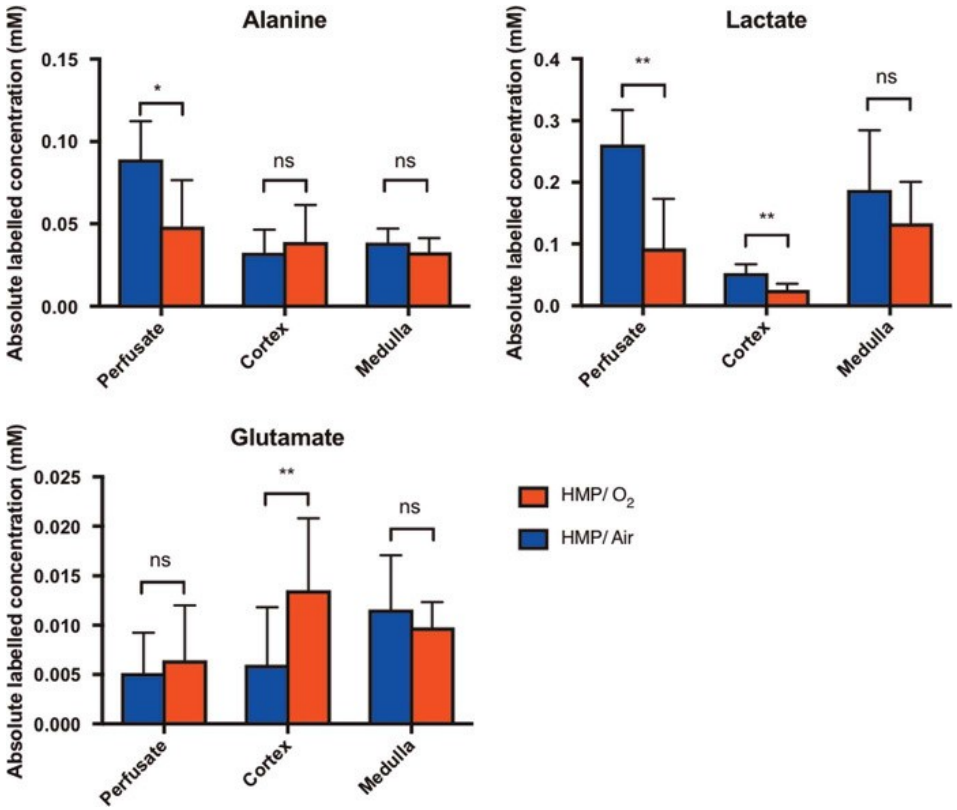

FIGURE 4. Absolute concentrations of universally labeled 13C ([U-13C]) alanine, [U-^{13}C] lactate and [4,5-^{13}C] glutamate determined using 1-dimensional ^{1}H nuclear magnetic resonance, 2-dimensional heteronuclear single quantum coherence nuclear magnetic resonance, and gas chromatorgraphy-mass spectometry data. * 0.01 < *P* < 0.05, ** 0.001 < *P* < 0.01, *** *P* < 0.001. HMP/O_2, oxygenated hypothermic machine perfusion; HMP/Air, aerated hypothermic machine perfusion.

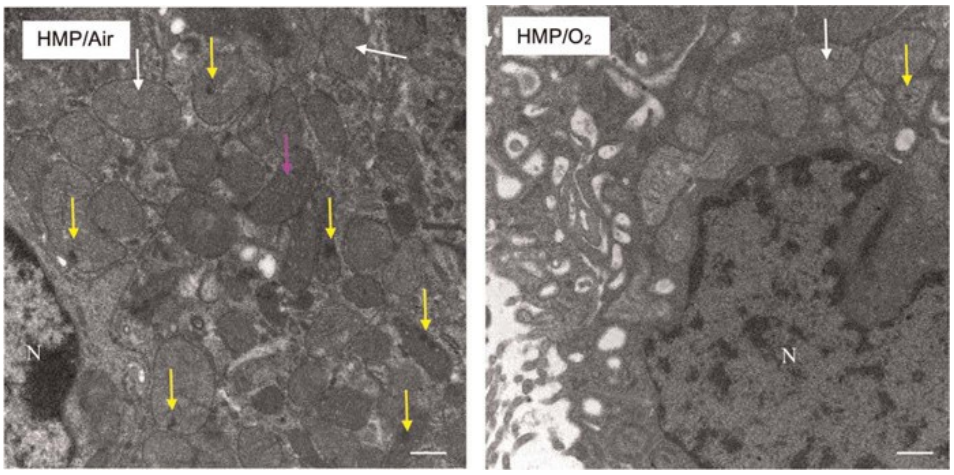

FIGURE 5. Electron micrographs of a tubular epithelial cell from A, aerated hypothermic machine perfusion (HMP/Air) and B, oxygenated hypothermic machine perfusion (HMP/O_2). The mitochondria within the HMP/Air group have a mixture of appearances: normal (white arrow), condensed (purple arrow) and contain multiple flocculent densities (yellow arrow). The mitochondria in the HMP/O_2 group are of normal appearance (white arrow) with a rare flocculent density (yellow arrow). Part of the nucleus (N) is apparent in both. Original magnification ✕ 18 500; bar, 500 nm.

shown in Figure 5. Swelling of mitochondria was not observed. There was evidence of increased injury in HMP/Air kidneys with 29% (24-61%) of mitochondria displaying normal morphology compared with 72% (49-78%) of HMP/O_2 kidneys (P = 0.200). The percentage of mitochondria containing flocculent densities was similar in both groups; 16% (14-23%) HMP/Air versus 20% (13-28%) HMP/O_2. Interstitial edema was similar in both groups with a median of 17 (11-34) pixels in HMP/O_2 compared with 20 (13-24) pixels in HMP/Air group (P = 0.184).

Arteries

Although endothelium was intact in intraparenchymal renal arteries and arterioles, there was at least moderate denudation of the extraparenchymal renal arteries in both groups. Patchy medial edema was seen between medial smooth muscle cells in both groups. Periarterial edema was similar in both groups with a median of 26% (13-66%) HMP/O_2 versus 34% (20-88%) HMP/Air (P = 0.211).

HPLC: Adenosine Nucleotide Analysis

Tissues samples from 4 pairs of porcine kidneys underwent analysis by HPLC. ATP levels in the cortex of HMP/O_2 kidneys were over sevenfold greater than for HMP/Air kidneys (mean, 19.8 mmol/mg protein vs 2.8 mmol/mg protein, P = 0.029). AMP levels were higher in both the cortex and medulla of HMP/O_2 versus HMP/Air kidneys although the results did not reach statistical significance, whereas ADP levels were significantly higher in the cortex of HMP/O_2 kidneys (Table S3 SDC, http://links.lww.com/TP/B660; Figure 6).

TBARS: MDA Quantification

Hypothermic machine perfusion/O_2 had slightly lower levels of MDA content but this was nonsignificant (7.26 ± 0.99 nmol/mg protein vs 8.07 ± 0.61 nmol/mg protein, P = 0.486).

GSH: Tissue GSH Concentrations

There was no significant difference in mean GSH concentration in the cortex of HMP/Air and HMP/O_2 groups at the end of the perfusion period (7.22 ± 0.72 nmol/mg protein vs 7.80 ± 0.96 nmol/mg protein, P = 0.200).

DISCUSSION

Supplemental oxygenation during the HMP of kidneys invokes a multitude of changes which have scope to improve outcomes after transplantation. Our results show pronounced metabolic differences between HMP/O_2 and HMP/Air kidneys in addition to significant consequences for tissue architecture, mitochondrial morphology, and cellular ATP levels.

The Role of Oxygenation in Supporting Metabolism

Cessation of blood supply during organ retrieval is the start of a period of hypoxia leading to a depletion in cellular ATP stores and a resultant switch to anaerobic metabolism,[32] reflected in the build-up of the products of glycolysis, such as lactate and alanine in both tissue and perfusate.[8] Hypothermia during this period, whether in static conditions or

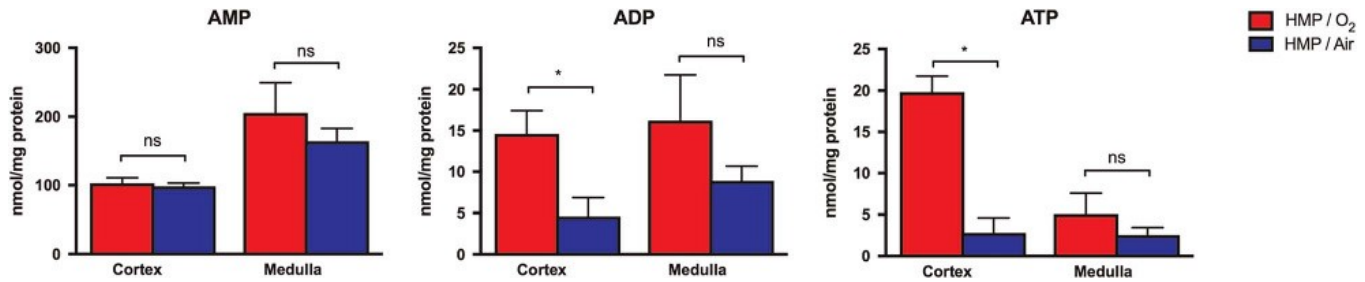

FIGURE 6. Adenoside monophosphate (AMP), adenoside diphosphate (ADP), adenoside triphophate (ATP), and overall energy levels in the cortex and medulla of oxygenated hypothermic machine perfusion (HMP/O_2) and aerated hypothermic machine perfusion (HMP/Air) kidneys. * 0.01 < P < 0.05.

HMP, leads to a reduction in metabolism[33] and consequentially, a decrease in oxygen requirement.[34]

Historically, this decrease in oxygen requirement has led to the acceptance that the hypoxic environment of a standard HMP circuit is adequate to meet the oxygen demands of ex vivo kidneys. Our results show that oxygenation promotes aerobic metabolism, as reflected in significantly higher concentrations of [4,5-^{13}C] glutamate in the cortex of HMP/O_2 kidneys versus HMP/Air kidneys. The reciprocal outcome is a decrease in de novo glycolytic activity in HMP/O_2 kidneys which is reflected in lower cortical concentrations of universally labeled alanine and lactate compared with HMP/Air kidneys.

We have previously observed small (<0.5%) proportions of [4,5-^{13}C] glutamate during standard HMP in the cortex of porcine kidneys after a 24-hour period.[19] However, the percentage of [4,5-^{13}C] glutamate observed in the cortex of both HMP/Air and HMP/O_2 conditions was higher, even with a reduced perfusion period and a lower concentration of [U-^{13}C]-labeled glucose, indicating that both conditions promote tricarboxylic acid (TCA) cycle activity compared with standard HMP.

Within the perfusate, changes in the absolute concentration of [U-^{13}C] alanine and [U-^{13}C] lactate mirrored a potential metabolic switch after several hours of HMP/O_2, resulting in a reduction in the production of glycolytic endpoints. This was in contrast to HMP/Air kidneys where a steady rate of production of [U-^{13}C] alanine and [U-^{13}C] lactate was observed.

Significantly higher proportions of labeled TCA cycle intermediates, in addition to [4,5-^{13}C] glutamate, an indication of TCA cycle activity, were observed in the cortex of HMP/O_2 kidneys compared with HMP/Air kidneys. Our results show oxygenation during HMP promotes TCA cycle activity, with ATP regeneration seen within cells as a result. In comparison, perfusate aeration seems to result in a metabolic phenotype, dependent on glycolytic pathway activity to produce ATP (Figure 7). Other studies have also observed an increase in tissue ATP levels as a result of oxygenated HMP. In a small study using a porcine model of HMP, high levels of dissolved oxygen (100 kPa) using a membrane oxygenator increased tissue ATP resynthesis as detected by ^{13}P NMR spectroscopy.[13] Similarly, enzymatic analysis of tissue samples showed significantly higher levels of ATP after oxygenated machine perfusion compared to cold storage.[35] The relative increase in ATP levels in HMP/O_2 within the renal cortex is likely to be of benefit to graft function posttransplantation.

In contrast to the changes seen in the renal cortex, no significant changes in metabolic profile (Figure 4) or adenosine nucleotide levels (Figure 6) were observed in the medulla of HMP/O_2 and HMP/Air kidneys. This may reflect reduced perfusion of the medulla due to shunting of cortical blood flow seen in normal physiological conditions, with reduced medullary perfusion likely exaggerated in conditions of HMP, resulting in anaerobic metabolism.[36-38] Thus, the usual preponderance toward anaerobic metabolism is likely to be unaffected by oxygenated perfusion fluid if perfusion of the medulla is poor.

Changes in Perfusion Parameters

The effects of oxygenation are not limited to metabolism within the parenchyma. As a result of flow-related shear stress during nonmodified HMP, vascular endothelium may be protected by modulation of Kruppel-like factor 2 and subsequent upregulation of endothelial nitric oxide synthase signaling pathways,[39] even as a result of short durations of HMP.[6]

The observation of improved flow dynamics in HMP/O_2 kidneys did not reach statistical significance. This was likely a limitation of sample size as such improvement in renal flow dynamics has previously been observed during oxygenated HMP in other studies.[12,40] This may occur secondary to upregulation of endothelial nitric oxide synthase pathways, an oxygen-dependent process,[41] leading to increased renal artery nitric oxide–dependent vasodilation. Renal artery nitric oxide–dependent vasodilation is associated with improved early microcortical circulation after reperfusion of HMP kidneys[39] which may play a role in the prevention of

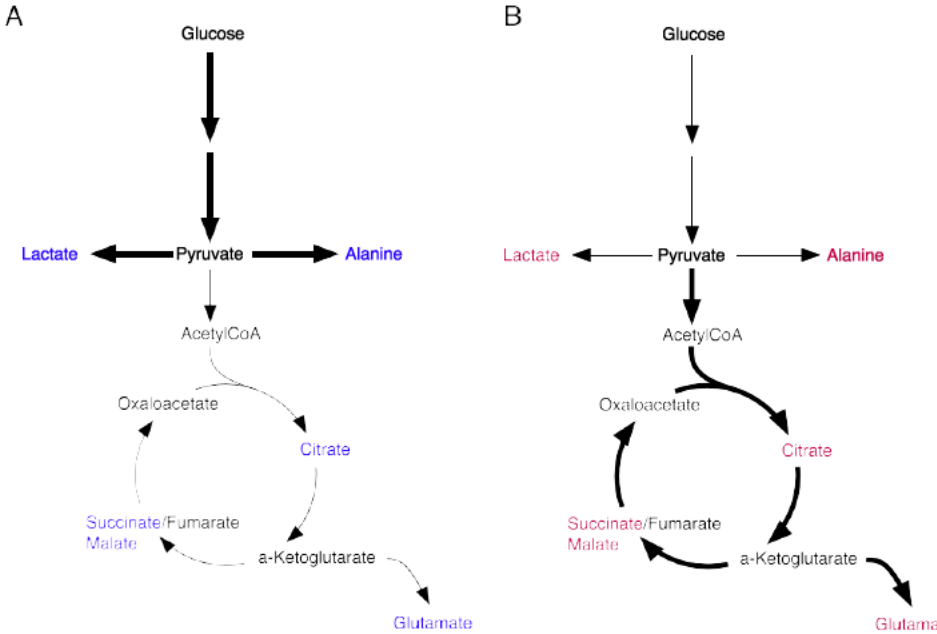

FIGURE 7. Differences in isotopic labeling patterns in the cortex of aerated hypothermic machine perfusion (HMP/Air) (blue) and oxygenated hypothermic machine perfusion (HMP/O_2) (red) kidneys. Thick black arrows indicate upregulated pathways interpreted from metabolite isotopomer combinations and metabolite concentrations indicating de novo activity.

delayed graft function. However, an alternative mechanism may be vasodilatation secondary to dissolved CO_2,a constituent of carbogen.

Given notable changes in metabolic profile between HMP/O_2 and HMP/Air kidneys in addition to a sevenfold increase in ATP levels in the renal cortex, small differences in flow are unlikely to be the sole determinant of the observed changes between the 2 groups. The localized use of the vasodilator papaverine has been explored in the setting of live donor nephrectomy with favorable clinical effect.[42] With HMP lending itself to delivery of drugs throughout the ex vivo kidney, such vasodilator administration in an unmodified HMP circuit would determine the extent to which flow effects alone promote beneficial changes in hypoxic conditions.

Structural Changes as a Result of Oxygenation

The benefits of oxygenation are reflected in the histology seen on light microscopy and electron microscopy. The increased shrinkage of glomeruli within the HMP/Air group indicates acute changes due which are likely due to lower perfusion pressures, in keeping with worse perfusion characteristics detected in this group. This diminished flow, together with the lower oxygen content of the perfusate produces relative ischemia evidenced by the increased injury to the tubules in this group with a higher percentage of morphologically abnormal mitochondria. However, the degree of change is still compatible with tubular epithelial cell recovery with well less than half the mitochondria containing flocculent densities, suggesting avoidance of irreversible cell injury.[43] Chromatin condensation of nuclei was seen in both groups and is a sign of reversible cell injury.[44] This degree of injury would suggest that, despite the cells being able to recover, the time to recovery may be increased, resulting in prolonged delayed or poor graft function.

Changes in mitochondrial architecture have been noted as a result of IRI during renal transplantation process.[45] Yet despite recent interest, no study has assessed the changes in mitochondrial morphology using EM in kidneys undergoing oxygenated HMP. Mitochondrial changes have been studied during HMP of hearts. Preserved architecture of mitochondria during oxygenated HMP of hearts has been observed with damage in those organs in static storage manifesting as mitochondrial flattening.[46]

Metabolic pathway activity central to aerobic metabolism, namely TCA activity cycle and oxidative phosphorylation, occur within mitochondria. Hence preservation of mitochondrial architecture may facilitate such aerobic metabolism contributing to higher levels of ATP in HMP/O_2 kidneys.

Harmful Effects of Oxygenation

Our results showed equivalence of damage due to ROS in both experimental conditions, suggesting that delivery of high concentrations of O_2 via perfusate during HMP is nondetrimental. However, conclusions drawn from such results may be limited due to both sample size and timing of IRI; our model does not take into account injury as a consequence of reperfusion.

Functional Outcomes

To date, 2 autotransplantation porcine studies have shown short-term functional benefits of perfusate oxygenation compared with a nonoxygenated control, both for prolonged periods (>20 hours) using DCD models.[11,47]

Potential functional benefits of the changes we have demonstrated are yet to be explored in the clinical setting. Clinical trials are currently under way investigating the use of oxygenation in HMP of kidneys in differing scenarios. The POMP trial seeks to compare outcomes of oxygenated HMP kidneys compared with static cold storage in high-risk donor organs, whereas the COMPARE trial is assessing the value of oxygenated versus nonoxygenated HMP.[48] We await the results of these trials to ascertain whether the differences we have observed translate into clinical benefit.

Limitations

While describing the metabolic profile and tissue adenine nucleotide levels of HMP/O_2 and HMP/Air kidneys, our preclinical large animal perfusion model used slaughterhouse kidneys with limitations inherent to such models.

Conclusions drawn from histology and HPLC data were limited due to sample size because not all pairs of kidneys underwent analysis. The significant differences noted between HMP/O_2 and HMP/Air kidneys should be reproduced in further research.

Oxygenation of the HMP/O_2 circuit was provided using a membrane oxygenator resulting in concentrations in the "arterial limb" of the circuit of 68.7 kPa. Arguably, such high concentrations are not required to supplement metabolism during hypothermia. Carbogen, used in the HMP/O_2 arm of the study, contains supraphysiological (5%) levels of carbon dioxide. When dissolved in the solution, it is likely to have resulted in a lower pH, changing the acid-base balance of interstitial fluid. However, KPS-1 contains pH buffers, such as HEPES which counteracts this acidity.

CONCLUSIONS

With increasing numbers of transplants from high-risk donors being performed to address organ shortage,[49] strategies to optimize donor organs have the potential to improve outcomes and increase utilization of such marginal organs. Oxygenation of circulating perfusion fluid during HMP is 1 potential method of optimization with a multitude of beneficial sequelae demonstrated by evidence of aerobic respiration using tracer-based metabolism, regeneration of ATP stores and improved perfusion characteristics with reciprocal histological changes in the absence of demonstrable damage secondary to oxidative stress.

ACKNOWLEDGMENTS

The authors would like to thank Sefa Canbilen, Samuel Ebbs, Alex Hollis, William Ries and Charlotte Turnbull for their contributions to this work.

REFERENCES

1. O'Callaghan JM, Morgan RD, Knight SR, et al. Systematic review and meta-analysis of hypothermic machine perfusion versus static cold storage of kidney allografts on transplant outcomes. *Br J Surg*. 2013;100:991–1001.
2. Patel K, Nath J, Hodson J, et al. Outcomes of donation after circulatory death kidneys undergoing hypothermic machine perfusion following static cold storage: a UK population-based cohort study. *Am J Transplant*. 2018;18:1408–1414.
3. Moers C, Smits JM, Maathuis MH, et al. Machine perfusion or cold storage in deceased-donor kidney transplantation. *N Engl J Med*. 2009;360:7–19.
4. Moers C, Pirenne J, Paul A, et al. Machine Preservation Trial Study G. Machine perfusion or cold storage in deceased-donor kidney transplantation. *N Engl J Med*. 2012;366:770–771.

5. Jochmans I, Moers C, Smits JM, et al. The prognostic value of renal resistance during hypothermic machine perfusion of deceased donor kidneys. *Am J Transplant*. 2011;11:2214–2220.
6. Gallinat A, Efferz P, Paul A, et al. One or 4 h of "in-house" reconditioning by machine perfusion after cold storage improve reperfusion parameters in porcine kidneys. *Transpl Int*. 2014;27:1214–1219.
7. Bon D, Billault C, Thuillier R, et al. Analysis of perfusates during hypothermic machine perfusion by NMR spectroscopy: a potential tool for predicting kidney graft outcome. *Transplantation*. 2014;97:810–816.
8. Nath J, Smith TB, Patel K, et al. Metabolic differences between cold stored and machine perfused porcine kidneys: A ^{1}H NMR based study. *Cryobiology*. 2017;74:115–120.
9. Guy AJ, Nath J, Cobbold M, et al. Metabolomic analysis of perfusate during hypothermic machine perfusion of human cadaveric kidneys. *Transplantation*. 2015;99:754–759.
10. O'Callaghan JM, Pall KT, Pengel LHM, et al. Supplemental oxygen during hypothermic kidney preservation: a systematic review. *Transplant Rev (Orlando)*. 2017;31:172–179.
11. Thuillier R, Allain G, Celhay O, et al. Benefits of active oxygenation during hypothermic machine perfusion of kidneys in a preclinical model of deceased after cardiac death donors. *J Surg Res*. 2013;184:1174–1181.
12. Gallinat A, Paul A, Efferz P, et al. Role of oxygenation in hypothermic machine perfusion of kidneys from heart beating donors. *Transplantation*. 2012;94:809–813.
13. Buchs JB, Lazeyras F, Ruttimann R, et al. Oxygenated hypothermic pulsatile perfusion versus cold static storage for kidneys from non heart-beating donors tested by in-line ATP resynthesis to establish a strategy of preservation. *Perfusion*. 2011;26:159–165.
14. 't Hart NA, van der Plaats A, Faber A, et al. Oxygenation during hypothermic rat liver preservation: an in vitro slice study to demonstrate beneficial or toxic oxygenation effects. *Liver Transpl*. 2005;11:1403–1411.
15. Lenton KJ, Therriault H, Fulop T, et al. Glutathione and ascorbate are negatively correlated with oxidative DNA damage in human lymphocytes. *Carcinogenesis*. 1999;20:607–613.
16. Will O, Mahler HC, Arrigo AP, et al. Influence of glutathione levels and heat-shock on the steady-state levels of oxidative DNA base modifications in mammalian cells. *Carcinogenesis*. 1999;20:333–337.
17. Sies H. Oxidative stress: from basic research to clinical application. *Am J Med*. 1991;91:31S–38S.
18. Ohkawa H, Ohishi N, Yagi K. Assay for lipid peroxides in animal tissues by thiobarbituric acid reaction. *Anal Biochem*. 1979;95:351–358.
19. Nath J, Smith T, Hollis A, et al. (13)C glucose labelling studies using 2D NMR are a useful tool for determining ex vivo whole organ metabolism during hypothermic machine perfusion of kidneys. *Transplant Res*. 2016;5:7.
20. Nath J, Guy A, Smith TB, et al. Metabolomic perfusate analysis during kidney machine perfusion: the pig provides an appropriate model for human studies. *PLoS One*. 2014;9:e114818.
21. Hosgood SA, Yates PJ, Nicholson ML. 1400W reduces ischemia reperfusion injury in an ex-vivo porcine model of the donation after circulatory death kidney donor. *World J Transplant*. 2014;4:299–305.
22. Kootstra G, Daemen JH, Oomen AP. Categories of non-heart-beating donors. *Transplant Proc*. 1995;27:2893–2894.
23. Ludwig C, Gunther UL. MetaboLab—advanced NMR data processing and analysis for metabolomics. *BMC Bioinformatics*. 2011;12:366.
24. Delaglio F, Grzesiek S, Vuister GW, et al. NMRPipe: a multidimensional spectral processing system based on UNIX pipes. *J Biomol NMR*. 1995;6:277–293.
25. Kazimierczuk K, Orekhov VY. Accelerated NMR spectroscopy by using compressed sensing. *Angew Chem Int Ed Engl*. 2011;50:5556–5559.
26. Orekhov VY, Jaravine VA. Analysis of non-uniformly sampled spectra with multi-dimensional decomposition. *Prog Nucl Magn Reson Spectrosc*. 2011;59:271–292.
27. Chong M, Jayaraman A, Marin S, et al. Combined analysis of NMR and MS spectra (CANMS). *Angew Chem Int Ed Engl*. 2017;56:4140–4144.
28. Hiller K, Hangebrauk J, Jager C, et al. MetaboliteDetector: comprehensive analysis tool for targeted and nontargeted GC/MS based metabolome analysis. *Anal Chem*. 2009;81:3429–3439.
29. Sellevold OF Jynge P, Aarstad K. High performance liquid chromatography: a rapid isocratic method for determination of creatine compounds and adenine nucleotides in myocardial tissue. *J Mol Cell Cardiol*. 1986;18:517–527.
30. Hissin PJ, Hilf R. A fluorometric method for determination of oxidized and reduced glutathione in tissues. *Anal Biochem*. 1976;74:214–226.
31. Bradford MM. A rapid and sensitive method for the quantitation of microgram quantities of protein utilizing the principle of protein-dye binding. *Anal Biochem*. 1976;72:248–254.
32. Taylor MJ, Baicu SC. Current state of hypothermic machine perfusion preservation of organs: The clinical perspective. *Cryobiology*. 2010;60:S20–S35.
33. Southard JH, Belzer FO. Organ preservation. *Annu Rev Med*. 1995;46:235–247.
34. Belzer FO, Southard JH. Organ preservation and transplantation. *Prog Clin Biol Res*. 1986;224:291–303.
35. Minor T, Sitzia M, Dombrowski F. Kidney transplantation from non-heart-beating donors after oxygenated low-flow machine perfusion preservation with histidine-tryptophan-ketoglutarate solution. *Transpl Int*. 2005;17:707–712.
36. Chen Y, Fry BC, Layton AT. Modeling glucose metabolism in the kidney. *Bull Math Biol*. 2016;78:1318–1336.
37. Ganguli M, Tobian L. Does the kidney autoregulate papillary plasma flow in chronic postsalt hypertension? *Am J Physiol*. 1974;226:330–333.
38. Stern MD, Bowen PD, Parma R, et al. Measurement of renal cortical and medullary blood flow by laser-Doppler spectroscopy in the rat. *Am J Physiol*. 1979;236:F80–F87.
39. Chatauret N, Coudroy R, Delpech PO, et al. Mechanistic analysis of nonoxygenated hypothermic machine perfusion's protection on warm ischemic kidney uncovers greater eNOS phosphorylation and vasodilation. *Am J Transplant*. 2014;14:2500–2514.
40. Darius T, Gianello P, Vergauwen M, et al. The effect on early renal function of various dynamic preservation strategies in a preclinical pig ischemia-reperfusion autotransplant model. *Am J Transplant*. 2018;1: DOI:10.1111/ajt.15100.
41. Stuehr DJ. Enzymes of the L-arginine to nitric oxide pathway. *J Nutr*. 2004;134:2748S–2751S; discussion 65S-67S.
42. Zacherl J, Bock S, Feussner H, et al. Periarterial application of papaverine during laparoscopic donor nephrectomy improves early graft function after kidney transplantation in pigs. *Surg Endosc*. 2004;18:417–420.
43. Myagkaya GL, van Veen H, James J. Quantitative analysis of mitochondrial flocculent densities in rat hepatocytes during normothermic and hypothermic ischemia in vitro. *Virchows Arch B Cell Pathol Incl Mol Pathol*. 1985;49:61–72.
44. Trump BF, Berezesky IK. Calcium-mediated cell injury and cell death. *FASEB J*. 1995;9:219–228.
45. Kosieradzki M, Rowinski W. Ischemia/reperfusion injury in kidney transplantation: mechanisms and prevention. *Transplant Proc*. 2008;40:3279–3288.
46. Michel SG, La Muraglia GM 2nd, Madariaga ML, et al. Twelve-hour hypothermic machine perfusion for donor heart preservation leads to improved ultrastructural characteristics compared to conventional cold storage. *Ann Transplant*. 2015;20:461–468.
47. Hoyer DP, Gallinat A, Swoboda S, et al. Influence of oxygen concentration during hypothermic machine perfusion on porcine kidneys from donation after circulatory death. *Transplantation*. 2014;98:944–950.
48. Consortium C The COPE Consortium for organ preservation in Europe. Available at http://cope-eu.com/work%20programme/trials.html. Published 2018.
49. Nath J, Field M, Ebbs SR, et al. Evolution of renal transplant practice over the past decade: a U.K. center experience. *Transplant Proc*. 2015;47:1700–1704.

8.1.2 Discussion

In the attached manuscript, we conclusively demonstrated that the continuous supply of oxygen results in reduced endpoint perfusate and cortical concentrations of [U-^{13}C] lactate and alanine, along with greater cortical tissue concentrations of [4,5-^{13}C] glutamate, when compared to continuous aeration. These metabolic differences, inferences of increased aerobic metabolism(310,312) under continuous perfusate oxygenation were supported by a simultaneous increase in cortical, but not medullary ATP levels.

Maintenance of mitochondrial integrity and decreased lactate production after SCS preservation and during reperfusion coincides with a reduction in the devolvement of DGF(272). Therefore, a switch to aerobic metabolism, or at least enhanced aerobic capacity through greater mitochondrial protection during preservation could be a considerable, clinically beneficial improvement to current organ storage protocols.

Our finding of improvements to ATP content of kidneys caused by perfusate oxygen over aeration has also observed by others(313). Whether the difference in aerobic metabolism stemmed from epigenetic upregulation of aerobic enzymes, or the observed mitochondrial protection imparted by oxygenation is scope for future studies. Collectively, we infer that perfusate oxygenation unequivocally results in improved maintenance of the cortical, cellular energy state, and our work proposes this is through increased TCA cycle activity enabled by the higher oxygen tension(310).

There is however, an alternative explanation. Oxygenation has been reported to reduce vascular resistance during hypothermic preservation (174), although this slight difference is not always observed(313).

We did not observe a significant difference in flow rates between groups, the mean flow rate in oxygenated kidney's was consistently higher than aerated kidneys at all timepoints.

This could indicate that more of the kidney was perfused under oxygenation, i.e. more cells had access to the labelled glucose than under aeration.

When a uniform weight of tissue (i.e. 0.5g) was extracted from both groups, oxygenated kidneys could exhibit an apparent increase in ^{13}C enrichment in glutamate, just because of increased access to labelled substrate. The would be an indirect effect of different fluid flow rates, rather than evidence of metabolic modulation by oxygenation.

Irrespective of the mechanism governing the difference in label incorporation, both possibilities describe a desirable scenario (i.e. increased modulation of aerobic metabolism or greater renal perfusion) and therefore an *ex vivo* beneficial effect of oxygenation over aeration remains.

Since the cell line model is removed from factors related for vascular resistance of flow rates, the *in vitro* evidence in Figure 7.8 supports metabolic modulation of aerobic activity as the mechanism contributing to increased glutamate labelling under oxygenation.

8.1.2.1 Construction of normalised measures of flow rate improvements

The small number of replicates included (n=8) and unpaired nature of the *ex vivo* study may overemphasise biological variability in flow rates between kidneys, making one group (i.e. oxygenation) appear superior to the other in terms of improving flow rates. Factors contributing to the different flow rate observed in otherwise paired kidneys (Appendix 5) could be quality of kidney flush at procurement or thrombus/emboli formation one kidney. To counteract this, a normalised flow rate for each kidney in each condition was assessed. The flow rate measures for each kidney at each time point were normalised to the flow measurement taken shortly after initiation of HMP (i.e. at 5 minutes). These discounts any influence of any other variables on flow parameters, isolating the dilatory potential of oxygen and aeration, purely on a kidney by kidney basis.

As can be observed in Figure 8.1, the percentage improvement in flow rate at each timepoint disappeared in this analysis, and both oxygenation and aeration appeared to have a remarkably equal vasodilatory effect on an isolated kidneys. The impact of this analysis is collated in the final chapter of this thesis (Figure 10.2).

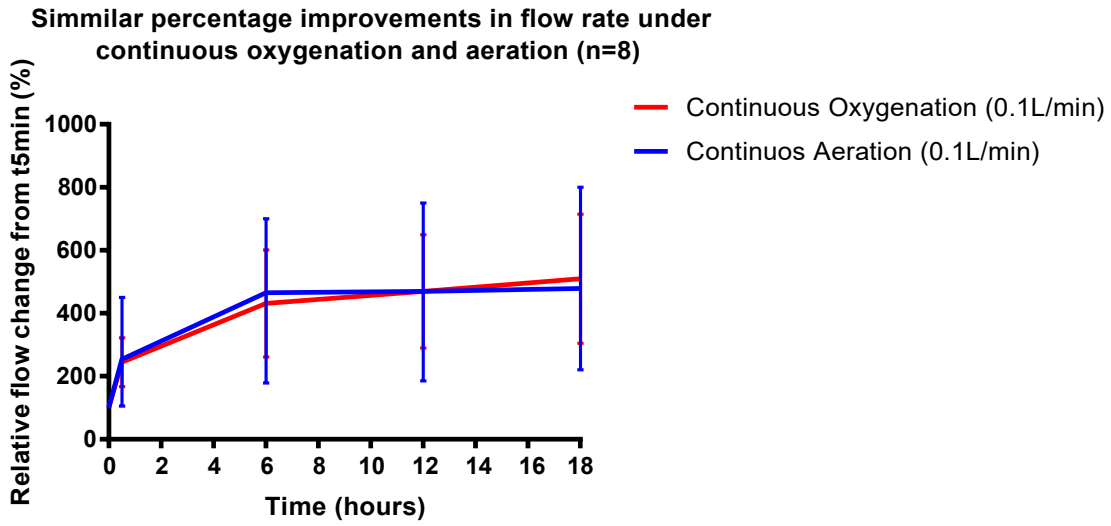

Figure 8.1. Effect of oxygen tension on relative flow change during HMP

Fluid flow rates (see attached manuscript) were normalised to the percentage change from the flow rate detected at initiation of HMP. This allows for the isolated comparison of the therapeutic effect of oxygenation or aeration irrespective of biological differences between replicates.

There was no significant difference determined in the rate of perfusate glucose or glutathione depletion (Figure 8.2), which may be expected if different degrees of kidney permeation by fluid were a considerable mechanism behind the determined metabolic differences. However, the absolute concentrations of key metabolites lactate and glutamate were observed to differ as a function of the oxygenation strategy, albeit only differences in glutamate concentrations were significant.

Perfusate depletion of glucose did not appear to be affected by the oxygenation strategies assessed. The mean lactate concentration was lower at experimental endpoint in

perfusate taken from oxygenated kidneys rather than aerated kidneys (i.e. 1.38 mM (range 0.54-3.22 mM) vs 2.44 mM (range 0.56-3.06 mM). This difference was not significant (p=0.144). Perfusate glutamate concentrations showed similar differences, with mean endpoint concentrations of 1.97 mM (range 0.88-3.26 mM) after aerated HMP and 0.85 mM (range 0.50-2.13 mM) after oxygenated HMP. This difference in glutamate concentrations between oxygenated and aerated kidneys was found to be significant (p=0.0104).

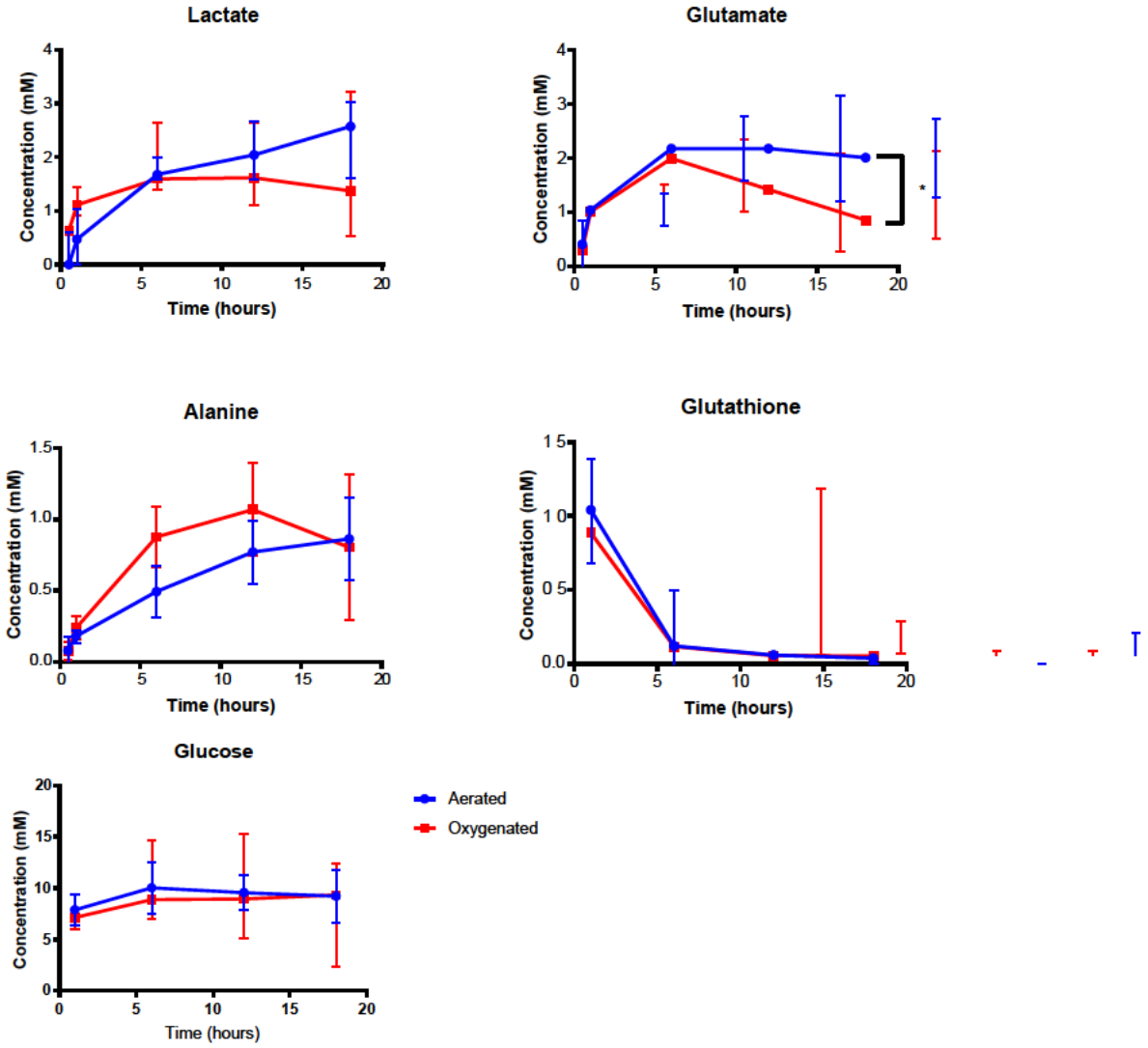

Figure 8.2. Effect of oxygenation and aeration on perfusate metabolic profiles

In addition to the measures of cellular insult inferred by assessment to TBARS and GSH, perfusate LDH was assessed as per Chapter 3. Only samples for 4 replicates remained after the previous analysis, however within these samples no obvious increase in perfusate LDH was found in aerated or oxygenated kidneys (Figure 8.3) echoing the findings of other studies(121) and the absence of deleterious effect *in vitro* (Figure 7.10).

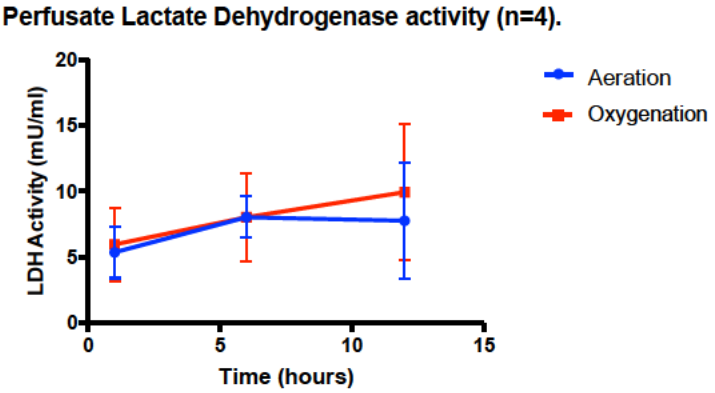

Figure 8.3. LDH release during HMP with continuous oxygenation or aeration

In summary, perfusate oxygenation appears to promote greater ATP regeneration through modulation of TCA cycle activity. There was no detectable deleterious effect of oxygenation over aeration in the porcine model, on the contrary, oxygenation resulted in significant improvements to mitochondrial morphology(274). Lactate and glutamate can be readily identified in the circulating perfusate, and these levels appear to modulated by the oxygen environment.

8.1.2.2 Correlating perfusate metabolic profiles with cortical tissue metabolic profiles.

With both perfusate and tissue available, this experiment allowed for assessment of key questions that is separate from the role of oxygenation in HMP. Perfusate is used as a

surrogate, non-invasive measure of ongoing metabolism when tissue sampling is unavailable as in current clinical practice, or may interfere with perfusion in animal models. However, it has not been characterised whether perfusate metabolic profiles are a good indication of the cortical metabolic profile. To assess this, the metabolic profiles of endpoint perfusate and cortical tissue for 12 kidneys were assessed by ^{1}H NMR and correlations between the two measures were detected using a Spearman's R test.

As shown in Figure 8.4, endpoint perfusate sampling prides a good reflection of the cortical concentrations of key metabolites of interest, with decent correlations observed between cortical profiles for lactate (r=0.75, p=0.005), alanine (r=0.82, p=0.01) and glutamate (r=0.86, p=<0.001). i.e. glutamate, lactate and alanine.

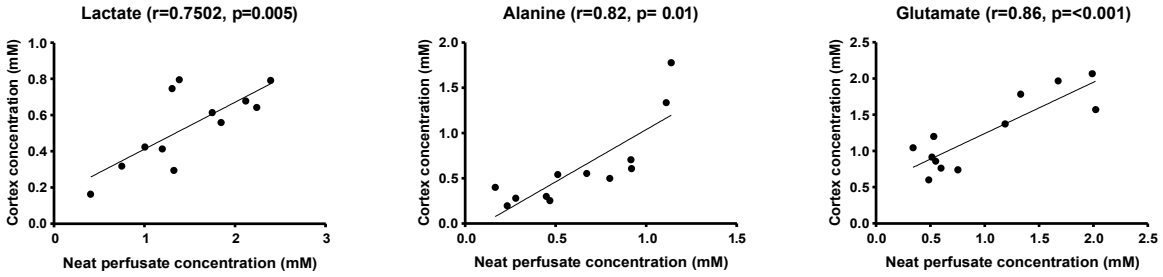

Figure 8.4. Correlation between perfusate and cortical levels of key metabolites.

8.1.3 Limitations of the study

This study was designed to illuminate a metabolic mechanism behind any clinical benefits observed in the current clinical trials. However, key differences between parameters of this experiment and the clinical setting limit this studies application to an illustration of the effects of oxygenation

8.1.3.1 Biological differences between human and porcine kidneys

Structurally, porcine and human kidneys are intrinsically different, with the larger, healthier porcine kidneys potentially utilising more oxygen than the smaller, ischemicly damaged human kidney (Figure 8.5).

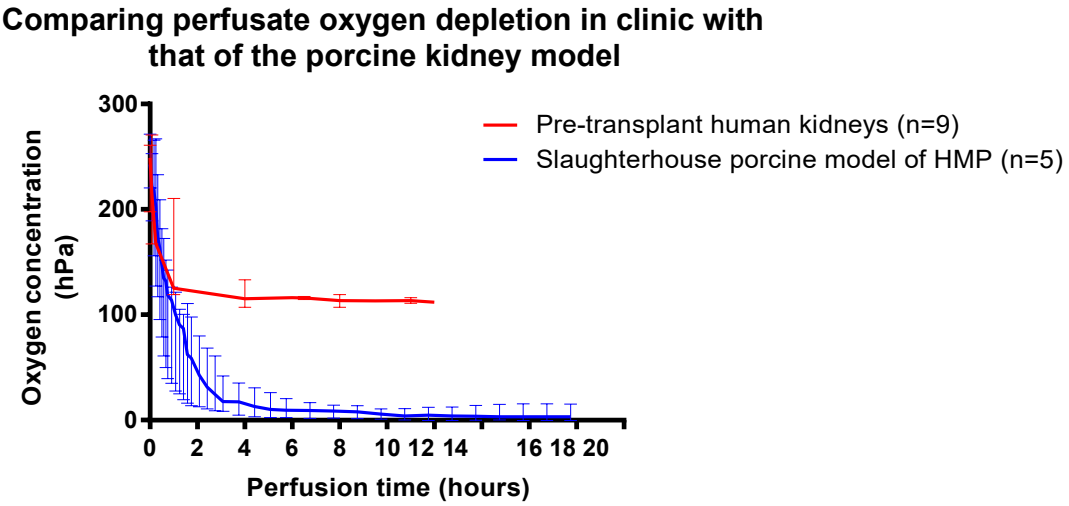

Figure 8.5. Species modulates level of oxygen depletion observed during HMP

Superimposed on the median perfusate oxygen depletion observed in the porcine mode (blue) is data kindly donated by Dr. Kamlesh Patel, who characterised the oxygen levels in HMP stored pretransplant kidneys using a point of care blood gas analyser (red).

As can be visibly observed, there a large difference (i.e. ˜11kPa) in the level at which perfusate oxygen measurements of the porcine and human kidneys plateau

In the porcine model, a gradual but complete depletion of perfusate oxygen was apparent within around 10 hours of perfusion, however this may not be reflective of the human kidney, which we have observed plateaus at roughly 50% of its starting oxygen concentration by 8 hours perfusion.

Therefore, using the porcine kidney to define which the minimal oxygen delivery strategy that fosters metabolic benefit may overestimate that required by the pretransplant human kidney.

An additional limitation is that although we have validated the porcine kidney as a metabolic model of human perfusate profile(109), difficulty in attaining transplant quality human tissue prevented direct comparison with porcine tissues. This is certainly scope for future work given the recent developments involving acquisition of preimplantation biopsies (232).

The porcine model used strictly controlled WIT and CIT prior to submission to HMP. In the clinical setting, these ischemic times are uncontrolled and significantly longer than that simulated in this study(89) and the damage this may limit the number of cells capable of returning to aerobic metabolism after SCS storage.

8.1.3.2 Experimental variation from clinical practice

The COPE POMP trial alluded to earlier uses a consistent oxygen delivery of 100ml/min and primarily focus on the modulation of graft survival after 1-year post transplant, with secondary outputs including DGF and PNF development. However, this study compares oxygenated HMP to SCS, which does not inform of outcome effects that are unique to oxygenation(305).

Additionally, the COPE COMPARE trial is investigating the effect of oxygenated HMP against standard HMP and include similar clinical endpoint(123). Both of these trials utilise the Organ Assist kidney perfusion device, rather than the LifePort® kidney transporter currently used in clinical practice. A key difference between these devices is the perfusion pressure, with the Organ Assist perfusing at 25 mmHg and the LifePort® perfusing at 30 mmHg. These trials will utilise kidneys perfused from source, whereas the kidneys in this

chapter experienced a 2-hour CIT, reflecting the UK practice dictating the routine the usage of SCS during organ transit to the awaiting hospital.

Additionally, the clinical setting will utilise clinical grade UW MPS which contains 10mM glucose. The logistics of obtaining the colloid in UW MPS necessitated supplementation of clinical grade UW MPS with 5mM [$U^{1\text{-}3}C$] glucose to permit downstream tracing of metabolism. Therefore, with additional glucose there is a difference in substrate availability between the clinical environment and that generated experimentally.

For these reasons, the effects of perfusate oxygenation reported herein are not directly comparable to clinical outcome measures irrespective of the biological difference between porcine and pretransplant human kidneys.

8.1.3.3 Further work- defining minimal therapeutic oxygen concentrations

Measurement of perfusate oxygen concentrations using a needle type oxygen sensor revealed that perfusate oxygen using a membrane oxygenator elevates dissolved oxygen far beyond the level possible with active perfusate aeration (Figure 8.6). At experimental endpoint, the mean arterial oxygen measure in the oxygenated perfusate was 54.6 ± 4.83 kPa and the mean oxygen measure in the aerated perfusate was 19.8 ± 4.83 kPa.

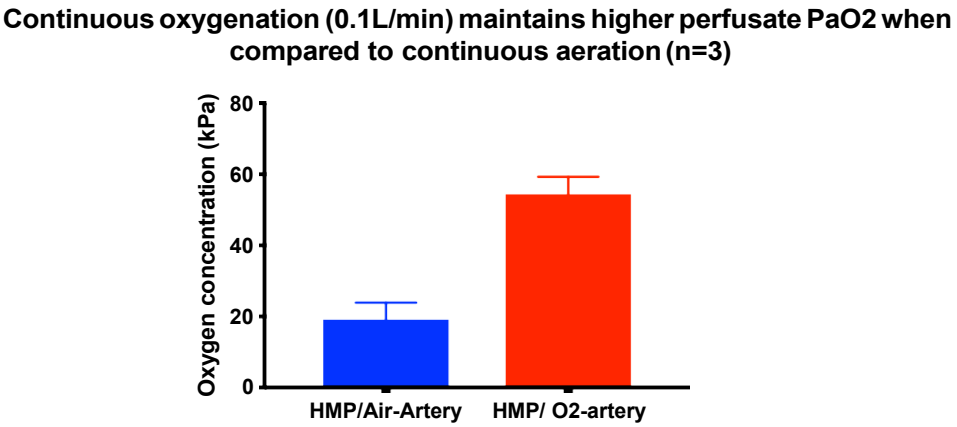

Figure 8.6. continuous aeration does not saturate UWMPS O_2 carrying capacity.

Although this led to evidence of increased aerobic metabolism without evidence of oxidative insult when compared to continuous perfusate aeration, this level of oxygenation may be excessive for the smaller, ischemic injured human kidney.

To illustrate this point, single discarded human kidney was obtained, and perfused as per the methodology described in the attached publication. One modification was made; oxygen flow through sensors were attached to the renal artery and vein, permitting real time assessment of the oxygen levels within these structures (Figure 8.7).

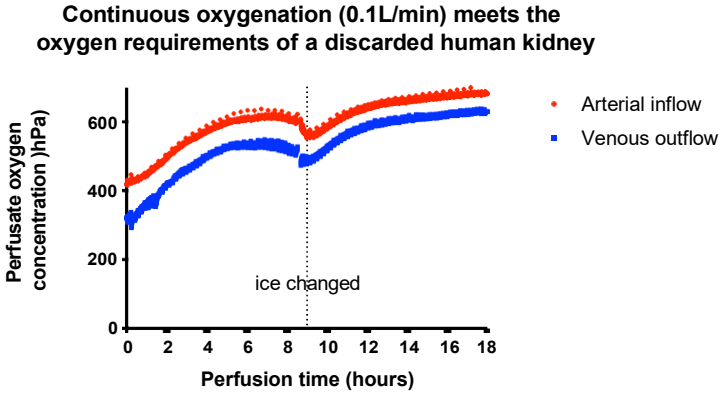

Figure 8.7. Arterial and venous oxygen levels during oxygenation of a human kidney

The dissolved oxygen measured in both arterial and venous oxygen sensors continued to rise over the perfusion period.

Even in the face of gradually increasing arterial oxygen levels, there was a striking linearity between the oxygen concentration of the fluid entering the kidney through the renal artery and that existing via the renal vein.

This is suggestive of one two mechanisms, either the oxygen delivered cannot be fully utilised by that discarded kidney and exits through the renal vein, or oxygen shunting is intact and functioning during preservation. Oxygen shunting has a proposed antioxidative role, diverting arterial oxygen to the venous circulation allowing protection of renal medulla which functions under hypoxia *in vivo*(218).

In both cases, oxygen delivery appears to in excess of what is used by the kidney,

The lower level of oxygen utilised by human kidneys suggested in Figure 8.5 and Figure 8.7 denotes that the clinical translation of porcine oxygenation studies work requires characterisation of the minimal level of oxygen required to exert a beneficial effect on tissue metabolism.

The *in vitro* model has suggested that reducing the oxygen environment by around 20% (i.e. to around 45kPa) still results in increased TCA cycle activity, indicating lower oxygen flowrates may also confer metabolic benefit *ex vivo.*

Additionally, the timing and duration of oxygenation may be varied It Is at this point unclear whether the continuous oxygenation is required. With no evidence of perfusate oxygen depletion during continuous oxygenation, it may be that brief periods of oxygenation can provide sufficient oxygen to support aerobic metabolism over the preservation period. Assessing the benefits fostered by transient oxygenation strategies is the focus of the next chapter.

9 The effects of different oxygen delivery strategies during HMP.

9.1 Introduction

In Chapter 8, an unequivocal increase in the restoration of aerobic activity is observed following continuous oxygenation, when compared to continuous aeration. This coincided with insignificant decreases in vascular resistance and increases in flow rates in the oxygenated group.

While these are promising observations, they do not necessarily correlate with an improvement in kidney quality for a would-be transplant recipient.

Indeed, the continuous perfusion of a single human kidney with the oxygen supplementation utilised in Chapter 8 does indicate that such a strategy may be excessive (Figure 8.7). Evidence of a therapeutic effect with high dose oxygen, delivered for a limited duration would be desirable. Although no deleterious effect of perfusate oxygenation (in terms of LDH, TBARS and GSH) were established in our experiments(274) or similar studies(313), these measures do not predict the significant pathology that occurs during the unavoidable onset of ischemic reperfusion injury following transplantation. The severity of IRI increases with the presence of oxidative insult during preservation(314) and the porcine kidney model of HMP appears to utilise more oxygen than the pretransplant human kidney it is attempting to simulate (Figure 8.5). Therefore, generation of oxygen environments that meet the requirements of the porcine kidney may be excessive for clinical practice.

It is logical to restrict oxygenation, a known driving force behind the generation of oxidative stress(315) to the minimal level capable of driving sufficient therapeutic benefit in the porcine model.

Deployment of continuous oxygenation appears to mask the rate of oxygen utilisation during hypothermic storage (Figure 8.7). As such, it is unknown whether or not transient periods of oxygenation are capable of supporting aerobic metabolism for the entire storage duration.

Hyperoxia in the region of 40-50kPa led to a mean increases in M+2 glutamate labelling *in vitro* (Figure 7.8). There was a visible trend (non-significant) of increasing intracellular ATP concentrations in line with increasing oxygen pressures generated *in vitro* (Figure 7.9). These observations were later conclusively validated in the *ex vivo* whole organ model (Chapter 8). Therefore, an oxygen environment between 21-and 50kPa may be sufficient to drive some restoration of aerobic metabolism. The focus of this chapter is to determine whether similar desirable metabolic or energetic changes can be generated *ex vivo* using transient periods of oxygenation.

This study begins with a whole organ experiment which assesses the metabolic consequences of a brief, non-continuous period of oxygenation at the start of HMP using tracer analysis.

A second experiment focuses on the capacity an initial oxygenation and an additional oxygen period at the end of preservation to replenish cortical ATP. This stemmed from the recognition that maintenance of intracellular ATP stores during preservation may be mitigate cold ischemic insult(313), and that ATP replenishment prior to implantation may be protective against reperfusion injury(309).

Lastly, in a series of studies linked to ours, Dr. Tom Darius of the *Cliniques Universitaires Saint-Luc, Belgium* assessed the post transplantation effects of different oxygen strategies using a porcine auto transplant model, which is unavailable in the UK.

As third author in the publications arising from these auto transplantation experiments, I performed metabolic profiling of samples acquired form Dr. Darius's experiments. The aim of this was collaboration was to determine whether or not metabolic differences that were generated by different oxygenation strategies were associated with clinically relevant post-transplant outcomes using the porcine auto transplant model. My contributions to these studies, have been reanalysed as per Chapter 3, replotted and my conclusions derived exclusively from my analysis are included in this chapter.

9.2 Methods

9.2.1 Experiment 1: The effect of a brief period of oxygen uploading at the start of HMP

A LifePort® perfusion circuit was modified to include a length of perforated tubing submerged in the kidney fluid reservoir, which allows dissolution of supplied gases without the need for a membrane oxygenator.

The circuit was further modified to include a flow through oxygen sensor in the arterial limb which allowed continuous monitoring of the oxygen entering the kidney (Figure 6.1)

As before, UWMPS was supplemented with 5mM [U-^{13}C] glucose (Cambridge Isotopes, UK) and 95% oxygen was bubbled through the UWMPS at a flow rate of 0.1L/m for 15 minutes prior to the kidneys being attached to the circuit. Oxygenation continued for the first 30 minutes of perfusion, after which the oxygen supply was disconnected.

In total, 6 pairs of pig kidneys were submitted to 18-hour hypothermic storage under these conditions (Figure 9.1). Prior to experimentation, organs were procured in line with the methods detailed in Chapter 3, with the slight modification that controlled 30-minute warm ischemic time was used to foster comparability with parallel studies being conducted overseas(125,316).

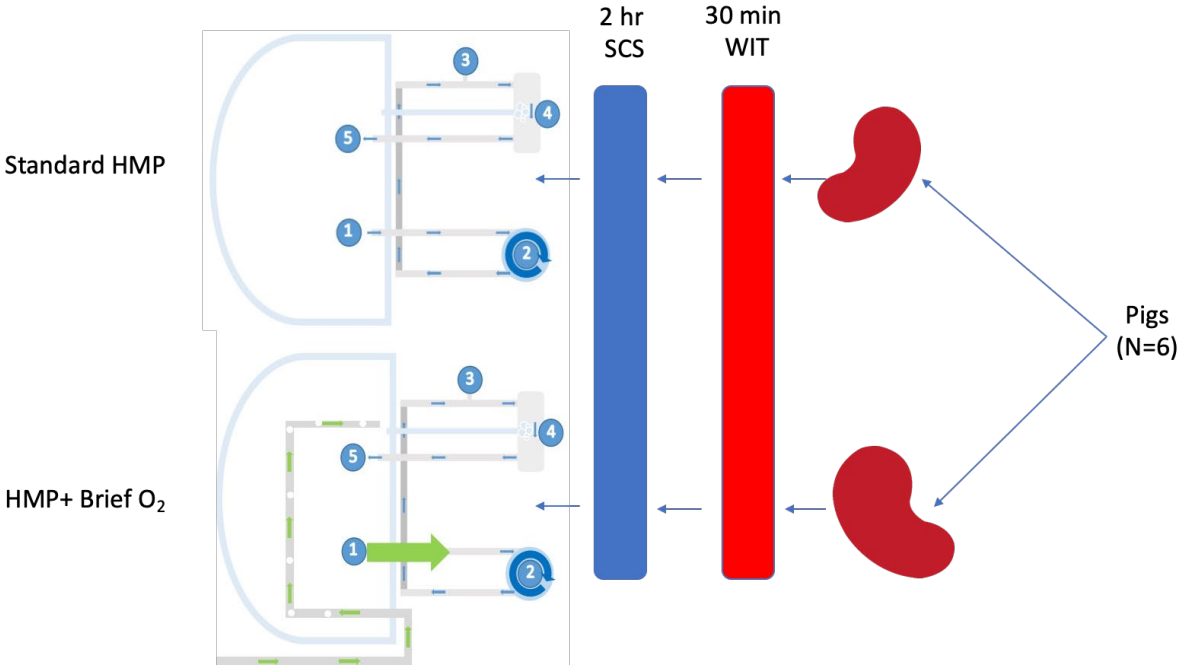

Figure 9.1. Overview of oxygen uploading experiment 1.

Porcine kidneys were subjected to a 30-minute WIT prior to flushing and 2-hour cold storage. With UWMPS supplemented with 5mM [U-^{13}C] glucose, kidneys were either perfused as normal or subjected to a brief period of oxygen supplementation.

Perfusate was sampled at initiation of HMP, and at 1, 2, 6, and 18 hours of perfusion, and assessed for differences in LDH activity as described in Chapter 3. Tissue sampling was restricted to the renal cortex.

The effect of oxygen administration on total endpoint cortical metabolite concentrations was assessed using ^{1}H NMR, and HSQC and GCMS methodologies were used to identify

metabolites with ^{13}C enrichment. Differences were assessed using the Mann Whitney U test, with significance detected at p=<0.05.

922 Experiment 2: The effects of brief initial and end ischemic oxygenation strategies.

Two modified LifePort® cassettes were used per replicate. The UWMPS in both was subjected to 30 minutes of perfusate oxygen uploading at a flow rate of 0.5L/min. After this, the submerged line used for oxygenation was removed, and two porcine kidneys procured form each animal were attached. Both kidneys then subjected to perfusate oxygen using an alternative method, by flowing oxygen across the surface of the perfusate in the sealed cassette (Figure 9.2). After 30 minutes of surface oxygenation at a flow rate of 0.5L/min, the oxygen supply was discontinued for the remainder of the 18-hour preservation period. In one of the kidneys from each pair, atmospheric oxygen was actively flowed over the surface of the fluid over the 18-hour period. At the end an 18hour perfusion time, both kidneys received 0.5L/min oxygenation via surface oxygenation for a period of 1 hour, after which the experiment was terminated.

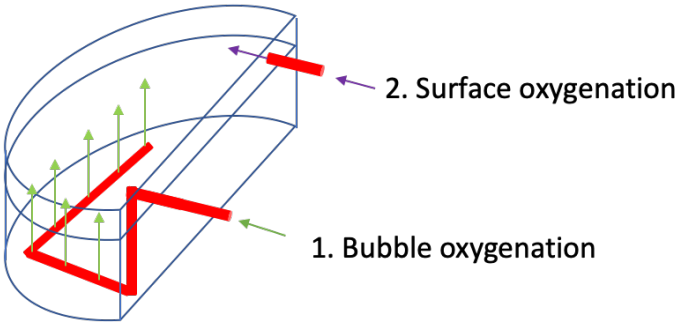

Figure 9.2. Schematic of two oxygen strategies used in uploading experiment 2.

Bubble oxygenation was used to elevate perfusate PaO_2 prior to and for a brief period during HMP. Surface oxygenation, i.e. blowing oxygen or air over the surface of the fluid during perfusion was trialled for its capacity to raise perfusate oxygen content without physical modification to the existing LifePort cassette.

9.2.2.1 Tissue sampling

In line with recent changes in clinical practice, in which a 5mm cortical punch will be used to take a preimplantation biopsy(253), cortical tissue sampling was trialled in the whole organ perfusion model.

Immediately after cessation of oxygen delivered by the bubbling method, a tissue sample was acquired and snap frozen in liquid nitrogen. The biopsy site was sutured shut and perfusion was allowed to commence for 18 hours. At 18 hours HMP, an additional tissue sample was acquired as before, and the cassette was sealed. Surface oxygenation was initiated for 1 hour, after which an endpoint tissue biopsy was collected.

9.2.2.2 ATP quantification.

ATP concentrations in these tissue sections was detected using a colorimetric assay, with methods detailed in Chapter 3. The Mann Whitney U test was used to detect differences in ATP concentrations between paired kidneys (experiment 1) and a paired Wilcoxon test was used on kidneys subjected to serial biopsy (experiment 2). In both cases, differences were deemed significant when $p=<0.05$.

9.2.3 Experiment 3: Profiling the perfusate of kidneys subjected to different oxygenation strategies prior to transplantation.

Using a porcine auto transplantation model, the left kidney from 28 pigs was surgically excised and submitted to either standard HMP (n=7), HMP with continuous 30% oxygen (n=9), HMP with 90% oxygen (n=7), HMP with 2 hours of oxygenation followed by 22 hours of standard non oxygenated HMP or 20 hours of standard HMP with 2 hours of oxygenated HMP. Perfusate was sampled throughout preservations, granting analysis of perfusate metabolic profiles and LDH activity using the methods described in Chapter 3.

The auto transplantation studies were directed and performed by Dr Tom Darius. This chapter includes my own analysis and conclusions, exclusively derived from the data I generated for the above publications.

9.3 Results

9.3.1 Experiment 1: The effect of a brief period of oxygen uploading at the start of HMP

Preloading storage fluid with 95% oxygen at 0.1L/min for 15 minutes resulted in elevation of perfusate O_2 (Figure 9.3). At the end of the 15 minute oxygen uploading period (dark grey) and immediately upon initiation of HMP for both groups, the oxygen concentration in the standard HMP group was 242.73 hPa, (range 220.26-271.46 hPa). The starting oxygen level in the oxygenated group was 311.91 hPa, range 237.38-332.80 hPa.

Continuation of oxygenation (light grey) resulted in elevation of perfusate oxygen concentrations to 414.45 hPa, (range 317.26-642.89 hPa). By this time, the kidney submitted to standard HMP had a mean oxygen concentration of 147.87 hPa, (range 78.93-181.64 hPa). The differences between groups was significant (p=0.0079). By 1.5 hours of perfusion, there was still a significant elevation in perfusate oxygenation caused by oxygen uploading (black line) (0=0.0159), however by 2 hours this differences in dissolved oxygen between oxygenated and standard groups had lost significance (67.46 hPa, (range 34.86-154.42 hPa) and 42.54 hPa, (range 12.52-79.91 hPa) (p=0.222). The oxygen levels in both groups plateaued at around 6 hours both circuits had less than 0.2 kPa oxygen remaining.

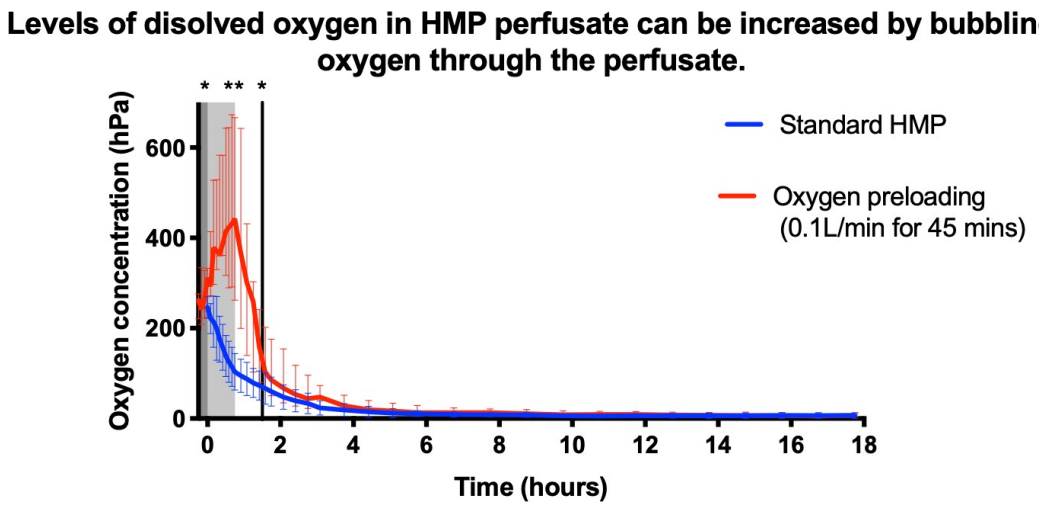

Figure 9.3. Real-time measures of perfusate oxygenation during brief O_2 preloading

9.3.1.1 Effect of oxygen uploading on flow rate

Although the brief period of oxygen preloading did not significantly improve oxygen availability throughout the 18-hour storage period tested, evidence of a persistent increase in mean fluid flow rates, and flow rates relative to that at the first 5 minutes of HMP was observed in kidneys subjected to limited oxygen preloading (Figure 9.4).

In the porcine kidneys perfused using non oxygenated HMP, the mean flow rate at initiation was 42.50 ml/min, range 17.00-78.00 ml/min. The mean flow rate actually decreased by the end of perfusion, with mean measurement of 37.50 ml/min, range 20.00-49.00 ml/min. The mean flow rate at initiation of HMP in kidneys subjected to oxygen uploading was 26.50 ml/min, range 20-49 ml/min. This gradually increased to a mean flow rate of 39.00 ml/min, range 28.00-68.00 ml/min over the 18 hour preservation time.

When the relative flow rates were calculated, the non-oxygenated kidney had a median flowrate increate of 9.89% at 18 hours (i.e. 109.89%, range 25.64-200%), whereas the kidney subjected to oxygen preloading had a mean flowrate increase of 26.97% (i.e.

126.97%, range 93.33-340%) by the end of perseveration. None of these changes attained statistical significance.

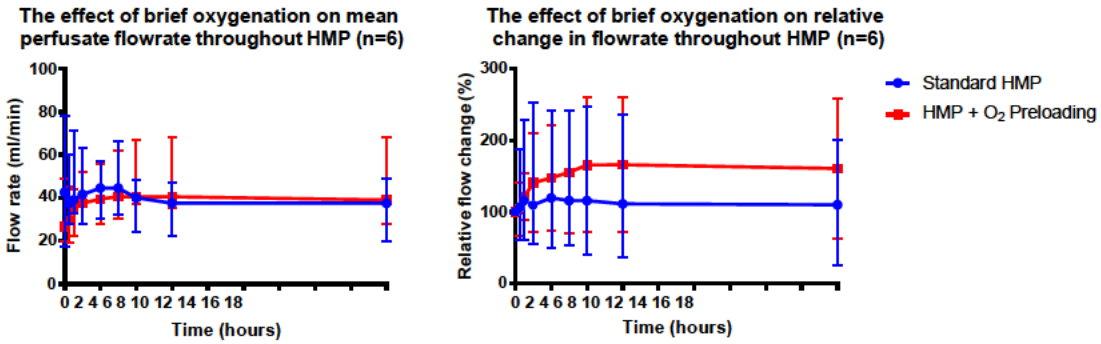

Figure 9.4. Effect of a brief period of oxygenation on perfusate flowrate during HMP

9.3.1.2 Effect on brief oxygen preloading on tissue damage assessed by LDH release

Quantitative assessment of LDH activity in perfusate sampled throughout perfusion demonstrated no effect of oxygen uploading on the release of LDH throughout perfusion. While LDH accumulation over time was evident for both kidneys, there was only a significant difference in LDH activity between 1 and 18 hours of perfusion for kidneys submitted to oxygen preloading (p= 0.0313). (Figure 9.5).

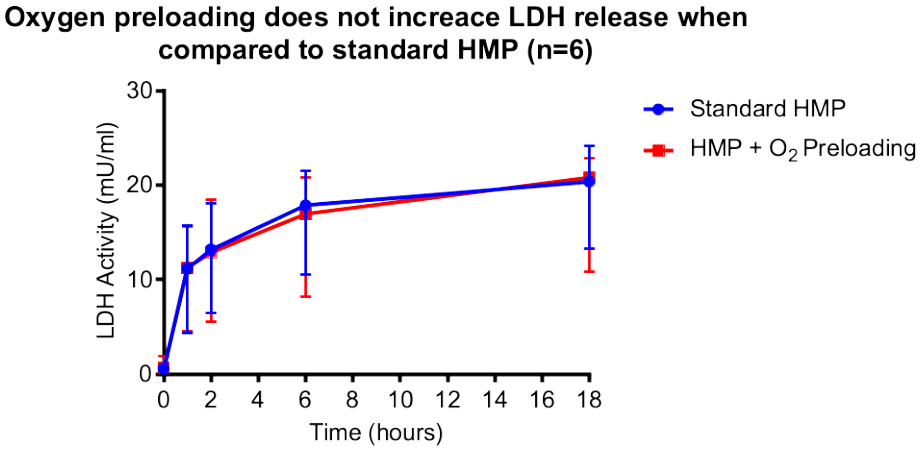

Figure 9.5. The effect of oxygen uploading on perfusate LDH release

9.3.1.3 Effect of oxygen preloading on tissue metabolic profile.

9.3.1.4 Metabolite concentrations

No significant difference was found in cortical levels of lactate alanine, glutamate or succinate between kidneys stored using standard HMP or those that underwent a brief period of oxygenation. The cortical concentrations of all metabolites quantified in these tissues is given in and illustrated in Figure 9.6 and given in Table 6.

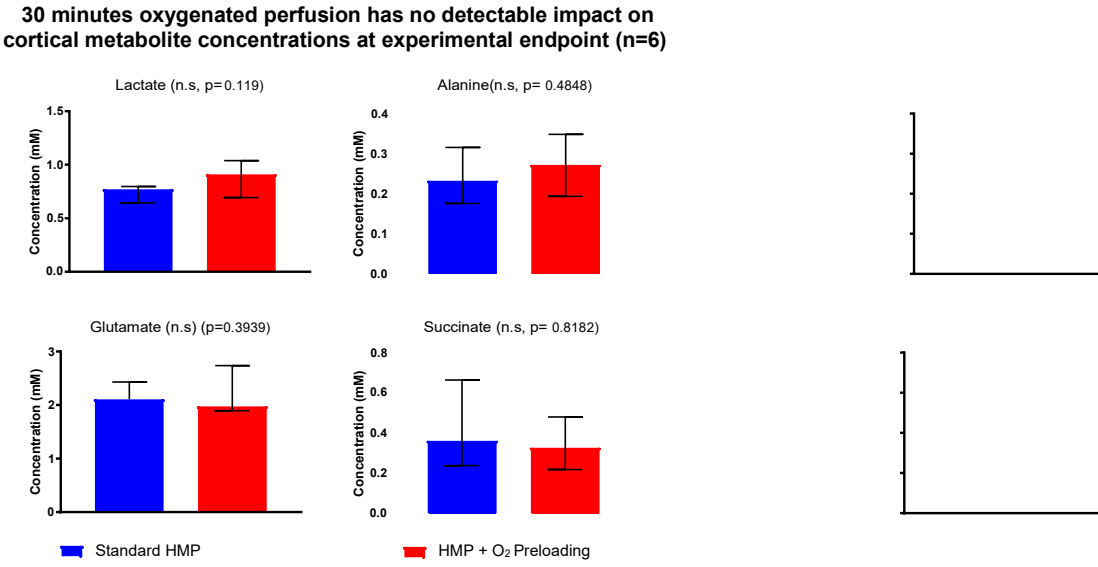

Figure 9.6. Endpoint cortical metabolic profile is unaffected by the brief oxygenation period

	Cortical concentration after standard HMP (mM)	Range (mM)	Cortical concentration after brief oxygen preloading (mM)	Range (mM)
Acetate	0.16	(0.11-0.29)	0.16	(0.12-0.29)
Adenine	1.69	(1.52-2.38)	1.69	(1.23-2.30)
Alanine	0.23	(0.18-0.32)	0.27	(0.19-0.35)
Formate	0.03	(0.03-0.07)	0.03	(0.02-0.07)
Gluconate	18.39	(17.61-23.84)	20.00	(13.32-21.85)
Glutamate	2.06	(1.73-2.71)	1.98	(1.90-2.74)
Glycine	1.78	(1.34-2.34)	1.75	(1.15-2.40)
Hypoxanthine	0.08	(0.06-0.20)	0.08	(0.05-0.14)
Isoleucine	0.03	(0.02-0.04)	0.03	(0.02-0.05)
Lactate	0.77	(0.64-0.80)	0.91	(0.69-1.04)
Leucine	0.03	(0.03-0.07)	0.04	(0.03-0.05)
Mannitol	14.22	(12.41-17.75)	13.99	(11.51-16.23)
myo-Inositol	1.58	(1.31-1.92)	1.70	(1.36-2.17)
Succinate	0.36	(0.24-0.66)	0.33	(0.22-0.48)

Table 3. Cortical metabolic profiles of HMP, and HMP with brief oxygenation kidneys. Data presented as median concentration with range.

9.3.1.5 Characterising de novo metabolism under oxygen preloading

Analysis of the MID of cortical tissue extracts by mass spectrometry revealed evidence of ongoing aerobic *de novo* metabolism in both preloaded and standard HMP experiments. There was detection of ^{13}C enrichment in pyruvate and downstream TCA cycle intermediates such as citrate, alpha ketoglutarate and succinate. Striking homology in the relative contributions of these mass isotopomers to their respective MID was apparent, signifying that neither the provision of limited oxygen nor apparent improvements in fluid flow seen during preloading amount to modified metabolic profiles after 18 hours of hypothermic storage (Figure 9.7). The very little label incorporation is a limitation of this work discussed later. No differences in mass isotopic distribution for any metabolite were observed between groups.

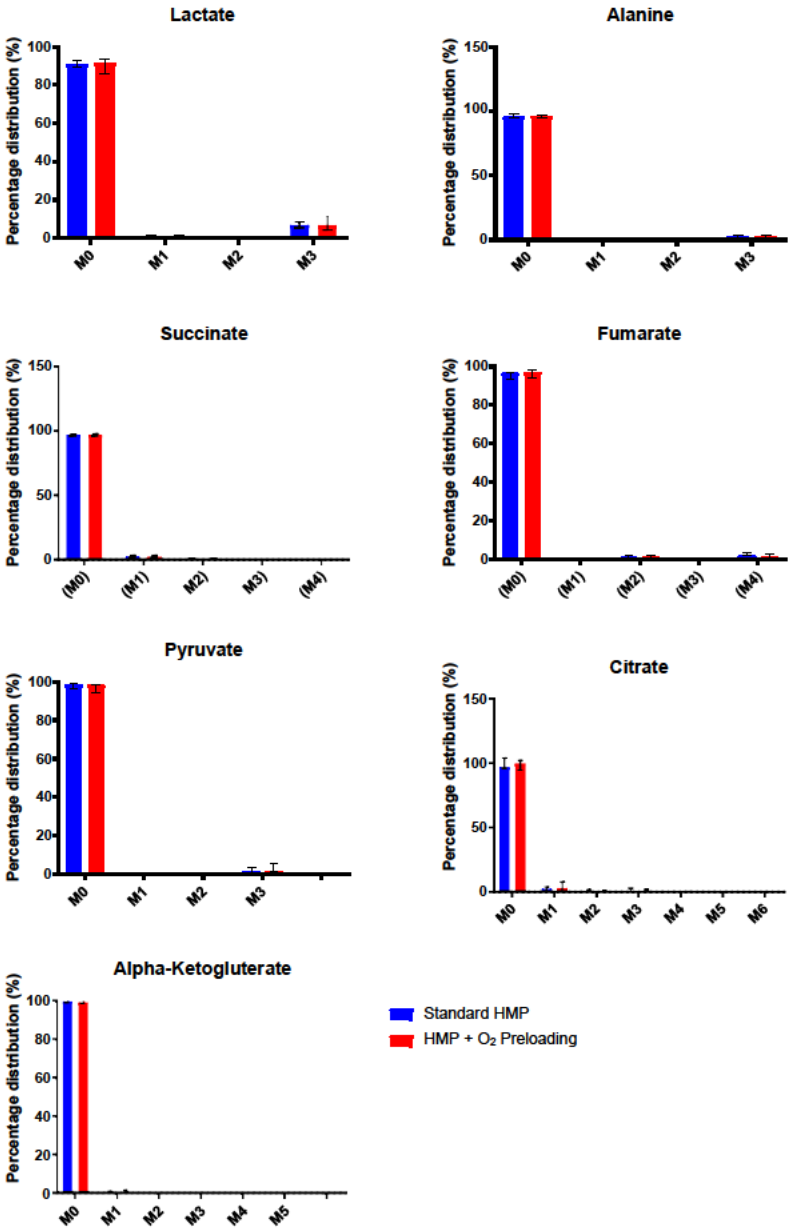

Figure 9.7. *De novo* metabolism is unaffected by oxygen uploading. Data acquired by GCMS

9.3.1.6 HSQC analysis

The 2D NMR analysis corroborates the findings of the MS analysis, of the three metabolites detected (lactate, alanine and glutamate), oxygen preloading did not lead to

any discernible difference is isotopic composition (Figure 9.8). The contribution of fully labelled lactate was 1.94 % (range 1.70-3.97%) under standard HMP and 1.70% (range 0.39-2.27%) under brief preloading. The contribution of fully labelled alanine was 0.35% (range 0.23-0.36%) under standard HMP and 0.33%(range 0.23-0.35%) under oxygen uploading. Glutamate was not found to be labelled in either environment, echoing trends observed in non-oxygenated HMP(235) (Figure 9.8).

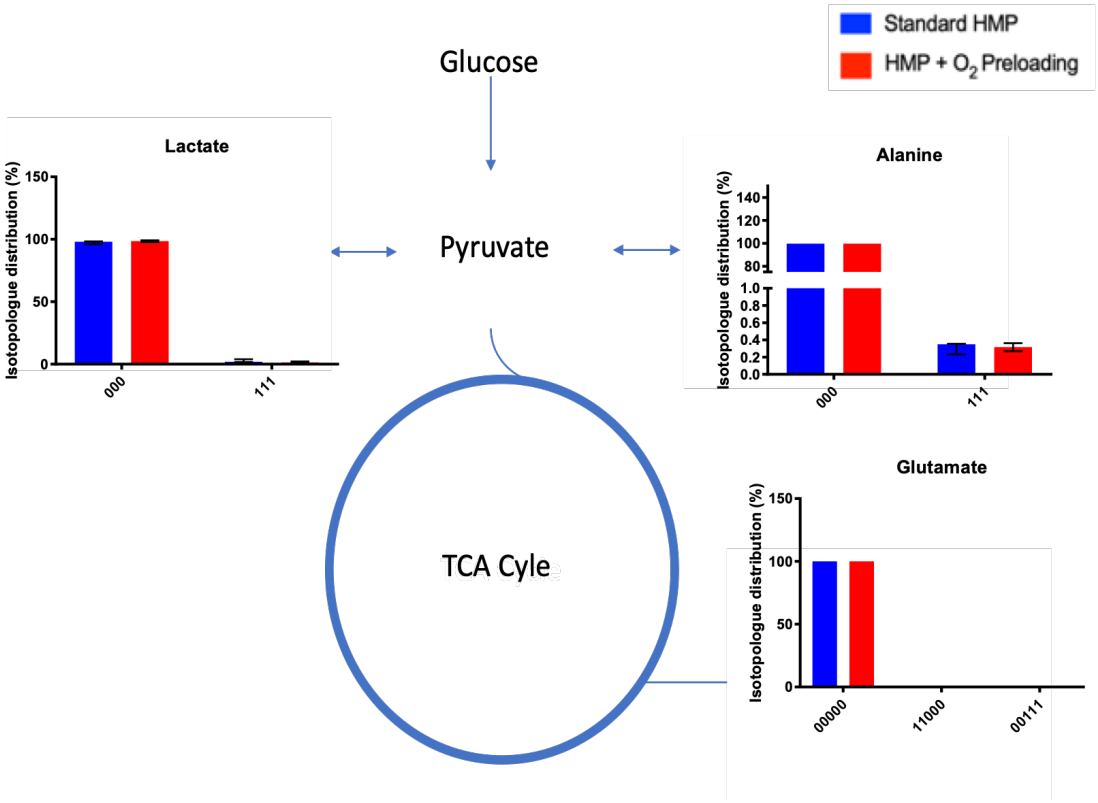

Figure 9.8. HSQC analysis of metabolic flux arising from brief oxygen uploading

9.3.1.7 ATP analysis

Despite the apparent absence of any significant metabolic effects incurred by oxygen preloading (p=0.095), there was evidence of a slight, although insignificant improvement

of cortical ATP concentrations in kidneys subjected to preloading over those stored using standard HMP (Figure 9.9). A suggestion of increased cortical ATP concentrations as a result of oxygen uploading at initiation of HMP was detected, when compared to standard HMP (0.08 nM/μl, range 0.04-0.08 nM/μl) vs 0.04 nM/μl, (range 0.04-0.05 nM/μl) respectively)(p=0.092).

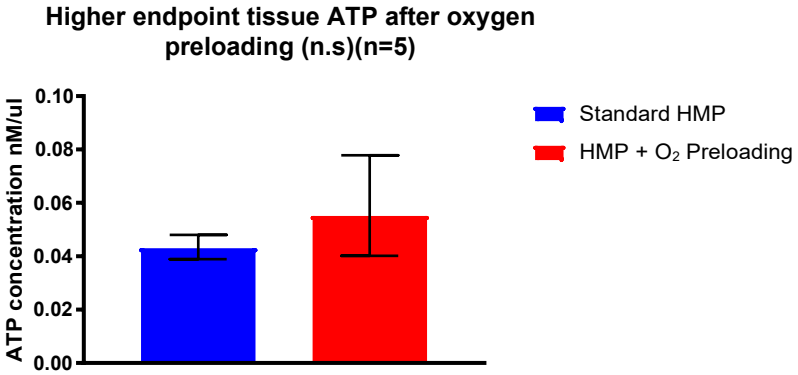

Figure 9.9. Cortical ATP levels after HMP with and without oxygen preloading

9.3.2 Experiment 2: The effects of brief initial and end ischemic oxygenation strategies.

9.3.2.1 Effect of increased oxygen delivery on perfusate oxygen concentrations at the beginning and end of HMP

Thirty minutes of perfusate oxygenation (grey box), prior to initiation of HMP was sufficient to elevate perfusate oxygen to 520.45 hPa (range 410.64-662.24 hPa). This was significantly higher than the dissolved oxygen in available at the start of standard HMP (242.73 hPa, range 220.26-271.46 hPa) (p=0.0025 and preloading at 0.1L/min for 45 minutes (311.91 hPa, range 237.38-332.80 hPa (p=0.005) (Figure 9.10).

At initiation of HMP, surface oxygenation displayed a finite capacity to oxygenate the perfusate, with perfusate oxygen pressure 571.06 hPa (range 210.62-769.05 hPa) by the

end of surface oxygenation. The perfused kidney rapidly removed oxygen from the perfusate, and at 2-hour post initiation of HMP, there was no statistically significant difference in perfusate oxygen levels resulting from oxygen supplementation and those observed in standard HMP (i.e. 128.69 hPa (range 25.48-218.00 hPa) vs 42.54 hPa, (range 12.52-79.91) hPa) respectively, p=0.1389). Despite increased oxygen delivery at the beginning, the median oxygen pressure in oxygen preloaded kidneys between 6-18 hours of perfusion was 18.68 hPa (range 6.10-31.21 hPa).

Neither enhanced oxygen delivery at the beginning of perfusion or continuous surface aeration was able to prevent near complete perfusate oxygen depletion. Endpoint surface oxygenation resulted in a slight but statistically significant increase in perfusate oxygen at 19 hours compared to that at 18 hours (i.e.51.58 hPa (range 44.14-106.2 hPa) vs 16.65 hPa (range 8.38-20.86), p=0.0006).

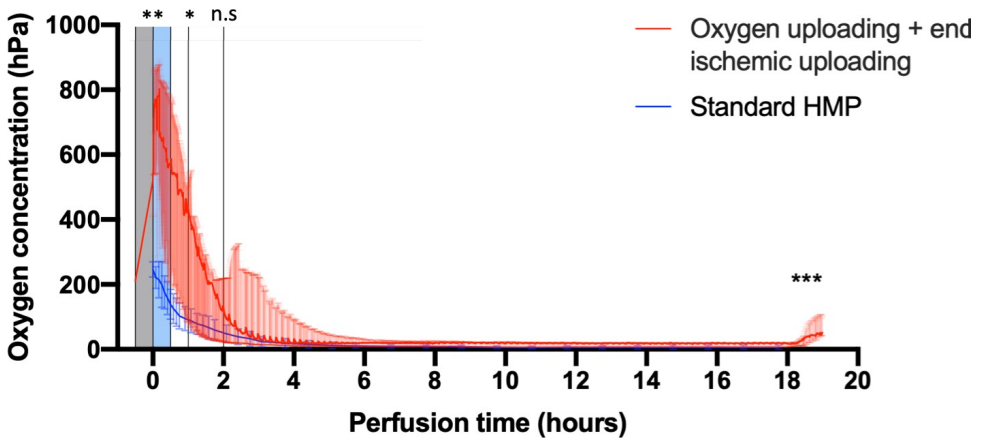

Figure 9.10. Effect of O_2 delivery at the start and end of HMP on perfusate O_2

9.3.2.2 Improvements to flowrate

Calculation of normalised flow rates as described in the previous chapter (Figure 8.1) allows comparison of the relative improvement in perfusate low driven by the application

of higher oxygen tensions and longer durations. As shown in Figure 9.11, Oxygen preloading at 0.5L/minute exerted an improvement in relative flow rate at 2 hours of perfusion (i.e. 350.00%, range 266.67-400.00%). This improvement was significant when compared to that granted by standard HMP (119.73%, range 50.00-241.18%) (p= 0.0022) and preloading at 0.1L/min for 45 minutes (138.33%, range 79.59-280.00%). Much of the relative flow improvement in kidneys granted enhanced oxygen preloading were lost by 8 hours of perfusion (mean flowrate improvement of 131.82%, range 95.45-168.18%).

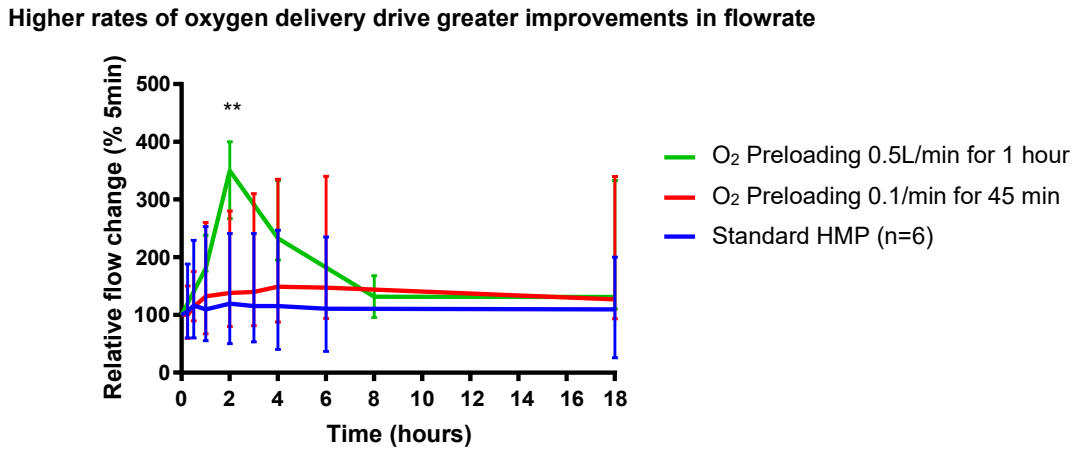

Figure 9.11. Relative renal flow rate improvements by different uploading strategies

9.3.2.3 ATP generation

Serial sampling of kidneys subjected to brief periods of oxygenation yielded a mean increase in cortical ATP concentrations when compared to the 1 hour sample (Figure 9.12). This difference was not found to be significant (p= 0.06). After oxygen uploading, the cortical ATP concentration detected at 1-hour perfusion was 1.34 ng/μl (range 0.23-1.64 ng/μl). This increased to 4.27 ng/μl (range 1.43-5.73 ng/μl) after 18 hours of non-oxygenated perfusion and fell again to 2.22 ng/μl (range 0.84-4.32 at the 19-hour biopsy.

None of these differences attained statistical significance (1hr vs 18 hours p=0.06, 1hr vs 19 hours p= 0.4375).

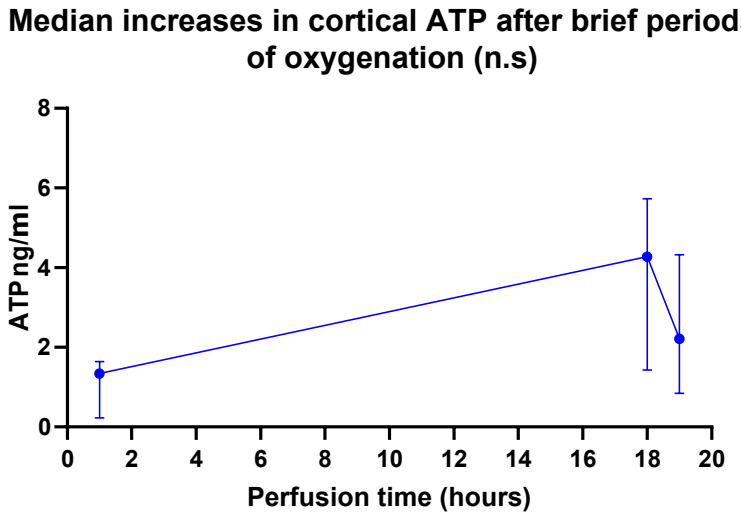

Figure 9.12. ATP levels in serial cortical biopsies during HMP with oxygen uploading

9.3.3 Experiment 3: Profiling the perfusate of kidneys subjected to different oxygenation strategies prior to transplantation.

9.3.3.1 Effect of oxygenation strategy on perfusate lactate concentrations

Both continuous, high-level oxygenation and a brief period of oxygenation at the start of machine perfusion resulted in decreases in the perfusate presence of lactic acid compared to standard HMP (Figure 9.13). As detailed fully in the published manuscript, these coincide with differences in clinical measure of graft function(125) .

Addition of continuos low level oxygenation (i.e 30% O_2) had no detectable effect on endpoint perfusate lactate concentrations when compared to standard HMP (i.e. 0.90 mM (range 0.50-2.27 mM vs 0.72 mM (range 0.61-1.37 mM) respectivly, p=>0.999). Addition of continuous high dose oxygen did significantly lower perfusate lactate concentrations (0.47 mM, range 0.25-0.66 mM) compared to standard HMP (p=0.0023) and oxygenation at 30% (p=0.015). When oxygen delivry was transient, supply of oxygen at the start of

HMP resulted in lactate concentrations of 0.41 mM (range 0.33-0.47). This was significantly lower than that released by standard HMP (p=0.0025), and also when 2 hour oxygenation was delivered at the end of a 20 hour CIT which gave a median perfusate lactate concentration of 0.41 mM (range 0.33-0.47 mM) (p=0.0159).

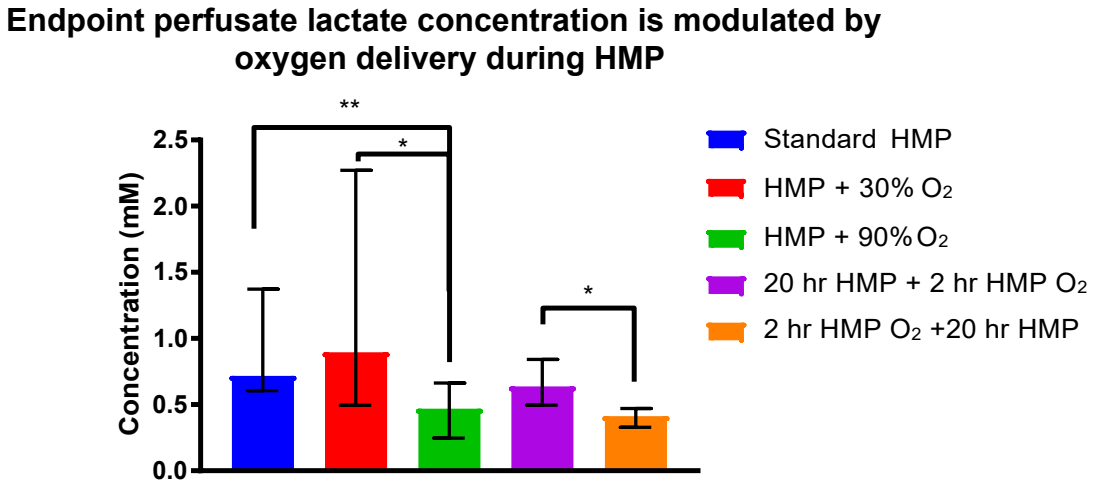

Figure 9.13. Perfusate lactate concentrations vary with oxygenation strategy (125,316)

9.3.3.2 Effect of oxygenation strategy on LDH release

This experiment assessed LDH release after 2 hours of oxygen supplementation either at the beginning of HMP or at the end of a 20 hour CIT. This assessment (Figure 9.14) reproduced our finding that transient oxygenation exerts little to no impact on perfusate LDH release (Figure 9.5). Timings of oxygen delivery did not appear to alter rates of LDH accumulation in the perfusate, with kidneys receiving 2 hours of oxygenation at the start of HMP having LDH activity of 1.31 mU/ml (range 0.76-2.29 mU/ml) , rising to 7.38 mU/ml (range 3.55-12.24 mU/ml) at 2 hours and 27.97 mU/ml (range 19.95-30.88 mU/ml) at experimental endpoint. The rate of accumulation was very similar in kidneys oxygenated for 2 hours after 20 hours of perfusion, with initial measures of LDH activity of 0.73 mU/ml (range 0.54-1.78 mU/ml), rising to 8.72 mU/ml (range 6.38-10.09 mU/ml) at 2 hours and

27.51 mU/ml (range 16.55-30.03 mU/ml at the 22 hour endpoint. No difference in rate or magnitude of LDH release was present between groups.

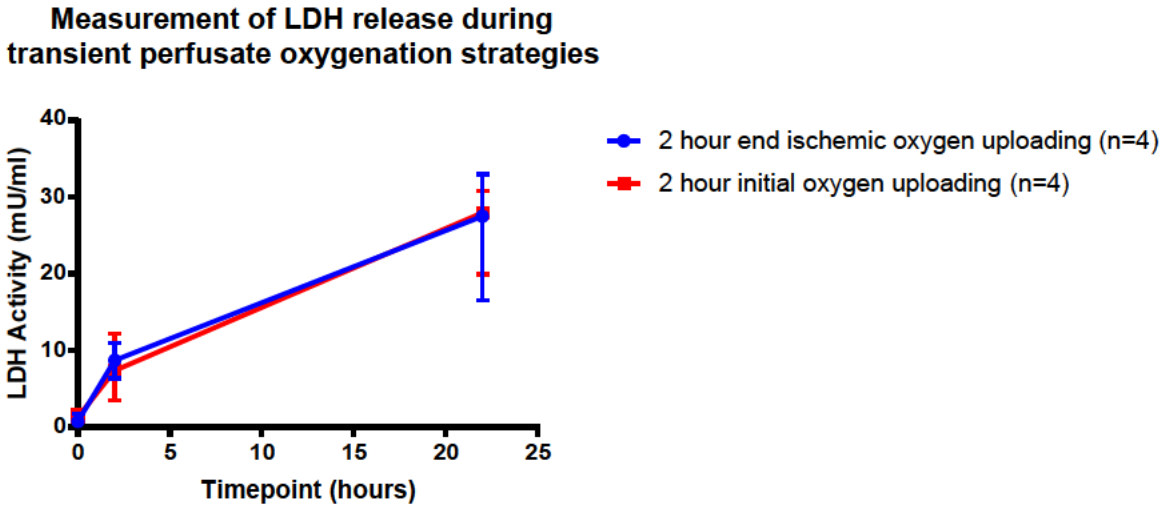

Figure 9.14. Overlay of LDH release between different oxygenation strategies.

However, when oxygenation was continuous, an interaction between the level of oxygenation delivered and perfusate levels of LDH activity after a 22 hour preservation time became apparent (Figure 9.15).

Supplementation of perfusate with 90% oxygen resulted in lower levels of LDH activity (i.e.11.97 mU/ml, range 10.96-16.83 mU/ml)) in the perfusate, when compared to continuous infusion of 30% oxygen (median LDH activity of 19.75 mU/ml, range 11.16-23.72 mU/ml) and standard HMP (16.93 mU/ml, range 14.37-20.01 mU/ml). These differences were found to be significant (p= 0.0379 and p=0.0041 respectively). No difference was found in perfusate LDH activity between standard HMP and HMP supplemented with 30% oxygen (p=0.7104). SCS storage (20 hours) followed by a 2 hour period of low level oxygenated perfusion was found to generate the lowest perfusate LDH activity (5.51 mU/ml range 3.72-7.58 mU/ml) and this was significantly lower than the LDH

release observed after Standard HMP, HMP with 30% oxygen supplementation and HMP with 90% oxygen supplementation (p= 0.0006 for all).

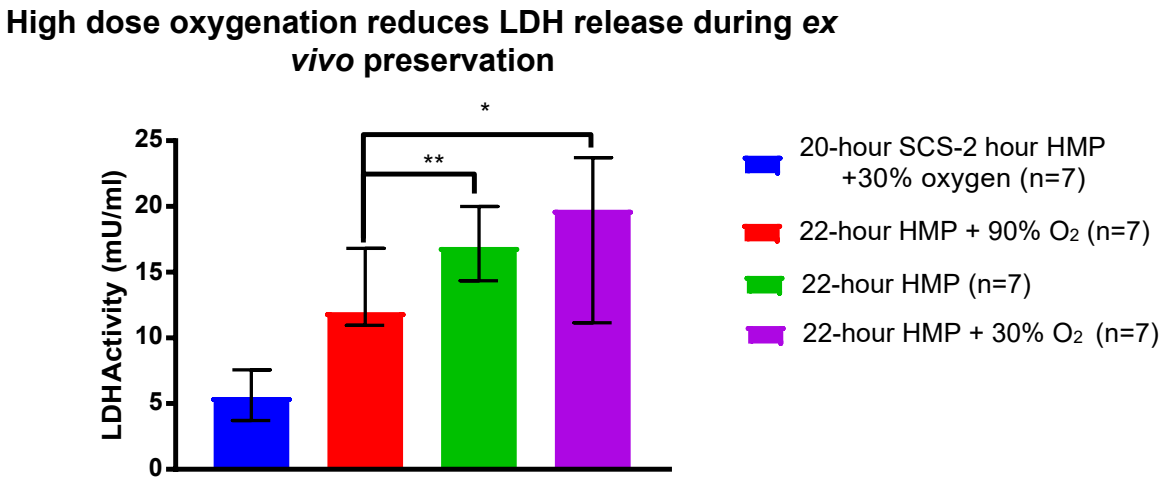

Figure. 9.15. Effect of different oxygen supplementation strategies on perfusate LDH activity

9.4 Discussion:

9.4.1 Efficacy of transient oxygenation strategies in the maintenance of perfusate oxygen levels.

This study served as a screen to assess the merits of a brief period of oxygen preloading in the early stages of HMP. It was found that bubbling oxygen through the perfusate is an effective means with which to raise the concentration of oxygen dissolved in the fluid (Figure 9.3 and Figure 9.10) without the need for oxygen carriers or the membrane oxygenators used elsewhere(274). Bubbling oxygen may therefore be a cost effective mechanism for oxygen supplementation, however mechanistically can lead to microbubble formation may make intrarenal gas emboli more likely(317), a deleterious phenomenon which can impede microvascular perfusion(318).

Despite the demonstrated capacity of transient oxygenation to elevate perfusate PaO_2, maintenance of perfusate oxygen tensions in the porcine model appears to be reliant on

some form of continuous oxygenation. When both oxygen uploading experiments were compared to standard HMP, no significant difference in perfusate oxygen tensions were detectable by 2 hours of perfusion.

These data suggest that at least in the porcine model and with the present UWMPS formulation, oxygenation must be provided continuously, or in bursts in order to prevent hypoxia. Whether this translates to the human setting requires studies using human kidneys, it is possible the oxygen depletion observed in the porcine model is a poor representation of clinical perfusate oxygen depletion (Figure 8.5). However, a modification that could be made to preservation fluid if brief oxygenation is desired is the inclusion of a dedicated oxygen carrier. Studies using the marine worm haemoglobin M101 have described how even with the absence of oxygenation, M101 result in better perfusion parameters and transplant outcomes than standard HMP (174). This may enhance the oxygen carrying capacity of the perfusate, allowing greater retention of oxygen delivered for a short duration.

Surface oxygenation at 0.5L/min slightly elevated perfusate oxygenation when used in the final hour of preservation. However even in this short time frame, there was evidence of a plateau occurring at around 6.3kPa, indicating this may not be a therapeutic intervention (Figure 9.10) Indeed, no elevation in cortical ATP was observed after the 1-hour surface oxygenation period (Figure 9.12).

In order to be effective, surface oxygenation may need to be delivered at a higher rate, at an earlier timepoint or in multiple/continuous doses. These strategies risk generation of a hyperoxic environment in the atmosphere in contact with the kidney, conceivably generating that undesirable oxidative insult .

9.4.2 Effect of oxygen uploading on metabolism.

Continuous perfusate oxygenation at 0.1L/min enhances aerobic metabolism in HMP stored kidneys (Chapter 8). However, it appears that a brief period of oxygenation at this flow rate is incapable of causing metabolic changes that are detectable after 18 hours preservation (Figure 9.7). This is not to say that such changes are not detectable shortly after the period of oxygenation, but these are not directly assessible without taking serial tissue samples, which may impede renal perfusion.

In any case, there was no apparent effect of this oxygen preloading strategy used on cortical metabolic profile. Notably, endpoint cortical lactate concentrations (Figure 9.6) and the ^{13}C labelling of this key metabolite (Figure 9.7) were unaffected by the oxygen environment generated in experiment 1. Furthermore, no differences in the concentration or labelling of metabolites linked to TCA cycle activity were apparent (Figure 9.7). A limitation of this work was the very low level of labelling observed, which may have masked small changes when metabolites were not found to be labelled. If this work was to be repeated- perhaps a greater mass of tissues should be extracted to bolster the quantity of low level metabolites that may contain label.

However, varying oxygen delivery strategy was found to modulate the perfusate presence of lactate in the auto transplantation collaboration (Figure 9.13)

This collaboration demonstrated that kidneys stored by standard HMP, and HMP supplemented with 30% oxygen have very little difference in lactate release, indicating that perfusate supplementation with 30% oxygen may be insufficient to mitigate the anaerobic phenotype, although metabolic tracer studies are required to confirm this.

In any case, perfusate supplementation with 90% oxygen was sufficient to drive a decrease in perfusate lactate concentrations when compared to standard HMP and HMP supplemented with 30% oxygen.

Metabolic analysis of perfusates also revealed the level of lactate in HMP kidneys subjected to 2 hours of oxygenation at initiation of HMP was lower that of kidneys stored by standard HMP with or without end ischemic oxygenation (Figure 9.13), indicating that oxygenation at the start of HMP may be optimal for improved control of anaerobic metabolism at experimental endpoint.

Correlations between perfusate metabolite concentrations and cortical metabolite concentrations demonstrate that at least for lactate, alanine and glutamate, perfusate sampling provides an excellent non-invasive snapshot of the cortical metabolic profile (Figure 8.4).

Because perfusate lactate concentrations in the autotransplant study were observed to differ depending on the oxygenation strategy used, and because the oxygenation strategy used modulated transplant outcomes as assessed by reductions in serum creatinine in the oxygenated kidneys post-transplant(125), this exciting metabolic observation may suggest a functional improvement in kidneys that arises through a reduction in anaerobic metabolism by oxygen delivery. The *ex vivo* experiments described at the start of this chapter failed to resolve any metabolic modulation by brief oxygenation at the start of HMP. Preloading for 2 hours resulted in markedly reduced perfusate lactate concentrations when compared to standard HMP in the autotransplant model. This finding was not replicated in our uploading experiments. However, the interstudy differences recognised here could stem from the fact that in the autotransplant model employed a longer oxygenation period i.e. 2 hours rather than 45minutes. Additionally, prior to HMP, the porcine kidneys used in the auto transplant study did not receive a period of SCS, whereas, all whole organ

experiments conducted in this thesis did. A central rationale behind the interest in metabolic optimisation during organ preservation firmly rests on improvements to cellular energy state, which as described, may confer benefit during hypothermic storage and later during reperfusion (140,307–309).

Figure 9.12 demonstrates that 1 hour of oxygen uploading at 0.5L/min oxygen leads to a median increase in cortical ATP at 18 hours when compared to 1 hour of HMP. Oxygen uploading at 0.1L/min for 45 minutes also appeared to be beneficial to intracellular ATP when compared to non-oxygenated kidneys, though this also narrowly avoided statistical significance (Figure 9.9). However, the trends observed are in line with the recognition that that oxygenation during HMP can support aerobic metabolism(274) and that through these experiments, we are closing in on a minimalistic oxygenation strategy that can replenish cellular energetics which become expended during conventional hypothermic storage. Without tracer studies, it is unclear whether metabolic differences detected in the perfusate denote changes in *de novo* metabolism or arise by other means. An additional collaboration in which porcine kidneys for auto transplantation are perfused using clinical grade [U-^{13}C] glucose UWMPS under different oxygen environments is currently underway. When published, this study will illuminate the preclinical therapeutic impact of optimising *de novo* metabolism through refined perfusate oxygenation strategies.

9.4.3 Chapter conclusion

Oxygen loading prior to start of HMP is incapable of meeting ongoing metabolic demands. In order to provide support for aerobic processes throughout extended CIT the optimal oxygenation strategy is likely to be either be continuous, delivered in bursts or augmented with the use of an oxygen carrier. Oxygen concentrations of 30% and under are unlikely to be optimal conditions for maximal metabolic gains, and high level oxygenation

(i.e.>90%) exerts a protective effect, as ascertained by a significant reduction in perfusate LDH release.

10 Discussion

"Jim, the answer is here; if only we knew what chemicals were right, we could preserve organs perfectly"

-Folkert Belzer to James Southard (319)

Chemical modification of HMP perfusate is technically the simplest modification that can be made to organ preservation protocols. However, with seemingly limitless combinations of possible constituents and concentrations, even resolving an optimised perfusate for otherwise standard HMP protocols would be an almost insurmountable challenge if using whole organ models alone. The painstakingly low throughput nature of whole organ research became personally apparent when assessing metabolic differences between HMP and SCS stored porcine kidneys. This inspired the focus of the first part of this thesis, which was the development of a high throughput *in vitro* model of organ preservation capable of screening the merits of novel whole organ interventions. The role this tiered approach to organ preservation research in this illustrated in Figure 10.1.

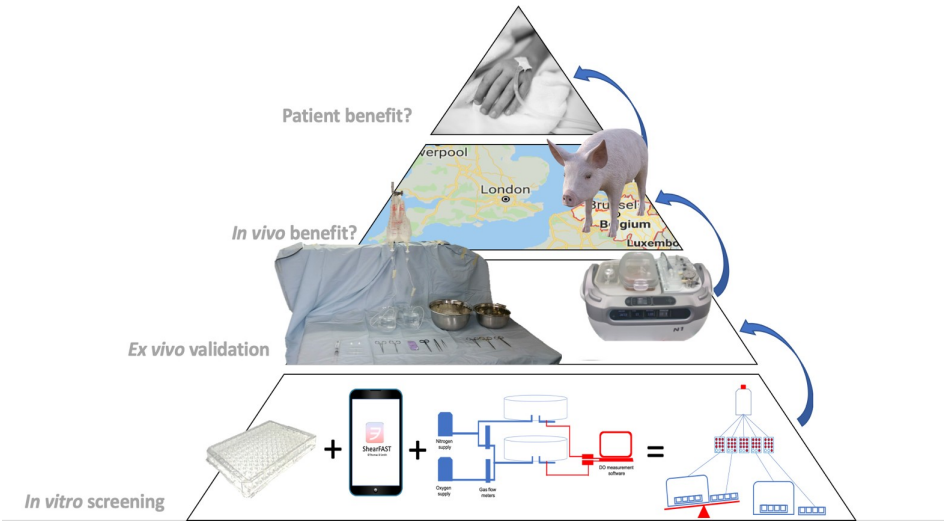

Figure 10.1. illustration of the tiered strategy for organ preservation research.

Please see appendix 5 for image rights

10.1 Proximal tubule metabolism between donor death and transplantation

In the period prior to donor death, functional warm ischemia manifests(320). Within 4 hours, proximal tubule cells exposed to simulated warm ischemia(299) rapidly shift to anaerobic metabolism, characterised by upregulated lactate production and downregulated pyruvate production (Figure 7.2). To mitigate WI injury and slow metabolism, the organ procurement team flush the kidney with chilled solution. *In vitro*, chilling proximal tubule cells results in around a lowers both M+3 lactate (Table 4), whereas M+2 glutamate production (Table.5)

The kidney is submerged in UW to instigate static cold storage, but in all likelihood, this does not enter the proximal tubule (Figure 5.1) If this is the case, the surrounding cortex is still depleting intracellular glucose (Figure 6.14), residual oxygen (Figure 6.3) and producing lactic acid(276), but is not benefiting from antioxidative protection from the

glutathione in UW. If fluid does enter the tubule, it is unlikely to offer optimal protection as a preliminary screen noted storage of PCT cells in UW results in enhanced LDH release over UWMPS and media (Figure 6.5).

The donor donated two kidneys, one is stored by HMP and the other stays in SCS.

If perfusate can pass the glomerulus, the HMP stored proximal tubule may benefit from a time limited respite from hypoxia (Figure 6.3) and from perfusion itself (Figure 6.6) and metabolic support in the provision and metabolism of glucose, although this is level of oxygenation (i.e. at most, that permitted by fluid aeration) is insufficient to drive a measurable switch back to aerobic metabolism Figure 7.7 and Figure 7.8).

If perfusate is able to cross the glomerulus, the presence of fluid flow may generate a protective effect both in the presence (Figure 6.9) and absence (Figure 6.6) of oxygen.

10.1.1 Therapeutic targets for optimisation using the tiered strategy

The *in vitro* data indicates that the hypothermicly stored proximal tubule could be better protected by the presence of low level shear stress and enhanced oxygen replenishment (Figure 6.6) or colloidal alterations (Figure 6.10).

Shear stress in the physiology relevant realm of 1 dyne/cm^2 is likely to be a therapeutic intervention if it can be instigated. This may be facilitated through the usage of increased perfusion pressures- which have been found to be beneficial when applied in moderation, i.e. at 40 mmHg (321) but deleterious at higher levels (120).

An alternative which could aid entry of perfusate into the proximal tubule is selection of a colloid which has a MW that is below the cut off modelled to restrict passage through the glomerulus (i.e.70 kDa)(185). PEG 35kDa falls below this range, whereas HES has a MW that greatly exceeds it (i.e. 250kDa (184). PEG 35kDa has demonstrated beneficial effect on proximal tubule cells *in vitro*(130), While these were not reproduced in this thesis, the

LDH release exhibited by proximal tubule cells stored without any colloid at all, (the potential environment of the non-perfused tubule) was significantly elevated. This indicates the usage of PEG 35kDa may still potentiate enhanced protection of this structure *ex vivo* if it can be delivered to the proximal tubule lumen during storage.

Of these three therapeutic targets, only oxygen supplementation does not depend on the capability of perfusate to cross the glomerulus. While all three agents may traverse the glomeruli, in the absence of tubule perfusion, oxygen may able to access the proximal tubule cells through closely associated peritubular capillaries(322). For this reason, as well as the well evidenced sensitivity of proximal tubule cells to ischemia(134–137) and also because avoidance of hypoxia during cold storage demonstrated the greatest improvement to cell viability (Figure 6.6), much of this thesis focused on identification of an optimised oxygenation strategy.

10.1.2 The effect of oxygen delivery strategy on dissolved oxygen concentrations.

At least in the porcine model, which has been and demonstrated to have a greater oxygen demand than the pretransplant human kidney (Figure 8.5) some form of continuous (Figure 8.6) or repeating oxygenation strategy is required to prevent the onset of hypoxia.

When the oxygen delivery strategy is transient, immediately upon disconnection of the oxygen supply the hypothermicly preserved kidney rapidly depletes the oxygen from the perfusate at a considerable rate (Figure 9.3) and Figure 9.10). By two hours of perfusion. There are no significant differences in oxygen from non-oxygenated kidneys in either study and both strategies maintained hypoxia for around 70% of the perfusion time.

10.1.3 The effect of oxygen delivery strategy on perfusate flowrate improvement

A central finding from this work is that oxygen supply appears to modulate the relative change in perfusate flow rate. The effect of higher oxygen flow rates on perfusate flow improvements has been demonstrated earlier. When the relative change in perfusate flow rates are from all the work contained in this thesis are superimposed on the same graph, a link between the oxygenation pressure or duration with relative flow rate improvements becomes apparent (Figure 10.2). When the relative flow rate improvements driven by preloading at 0.5L/min are compared to those driven by continuous oxygenation strategies, they pale in comparison. Continuous oxygenation, even if room air is used as a source of oxygen appears to be required to generate lasting improvements to flow rate. If the improvements to flow rate denote a greater mass of kidney being perfused or alternatively this may suggest therapeutic action of oxygenation may also result from perfusion itself, which has been shown to be beneficial *in vitro* (Figure 6.6).

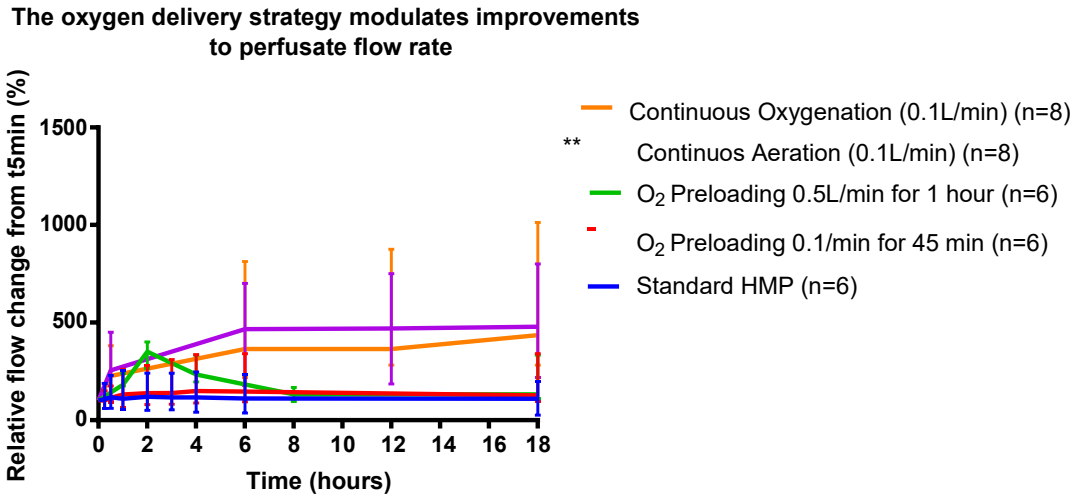

Figure10.2 Oxygenation strategy mediates relative flow rate improvements.

One difference highlighted shows that continuous aeration exerts a more pronounced vasodilatory effect at experimental endpoint than a brief period of high dose oxygenation (0.5L/min for 1 hour) (p= 0.0025).

10.1.4 Effect of oxygenation strategies on tissue damage as assessed by LDH release

The general consensus of this thesis has been that in all the oxygen environments tested, there has not been an association between oxygen availability and cellular LDH release. This was observed in multiple *in vitro* experiments (Figure 6.7, Figure 6.12, and Figure 7.12) and *ex vivo* experiments (Figure 8.3, Figure 9.5 and Figure 9.14).

However, the data in Figure 9.15 demands re-evaluation of this assessment. Continuous delivery of 90% oxygen significantly reduced perfusate LDH activity when compared to standard HMP, and HMP supplemented with low level oxygenation.

This observation takes precedence over all the *in vitro* conclusions, as data derived from the whole organ animal model is far more likely to be representative of the clinical scenario than any *in vitro* model. Furthermore, the single previous assessment of the effect of high level oxygenation on LDH release covered a shorter preservation time (i.e. 12 hours rather than 22) which may have masked accumulating differences in LDH release. Other groups

have demonstrated that when non-oxygenated HMP is compared to kidneys receiving continuous high dose oxygen, the non-oxygenated kidneys release more LDH into the perfusate(121).

10.1.5 The effect of oxygen delivery strategy on metabolism

Continuous oxygen delivery (0.1L/min) using a paediatric membrane oxygenator is sufficient to drive restoration of aerobic metabolism, which manifests primarily as increased concentrations of [4,5-^{13}C glutamate] but also includes morphological improvements to mitochondria and a coinciding increase in cortical ATP levels when compared to continuous perfusate aeration.

These metabolic differences were not observed when oxygen was delivered for a brief period at the start of perfusion.

However, there was consistent (albeit not significant) evidence of an elevation in endpoint 18-hour ATP levels by both initial uploading periods.

Since the increases on ATP were small, and with transient oxygenation being unable to sustain perfusate oxygen pressure for around 67% of the preservation time- it is possible these increases in tissue ATP were at least in part caused by improved flow rates cause by the oxygenation period.

10.2 Further work

10.2.1 In vitro

The *in vitro* work in this thesis was deliberately modelled on practices for industrial drug discovery. High throughput, inexpensive techniques were developed or utilised for controlled simulation of shear stress and oxygen availability, temperature and perfusate composition. High throughput analytical techniques were also employed to determine

modifications to storage environments that were beneficial *in vitro*. The limiting factor in this model was manpower, and for this reason- experiments were performed as screens on a single cell line rather, than a fine tuning of the optimal environment for cell lines representative of multiple key structures in the kidney.

I envisage that the tools described within could be used to define a more protective preservation solution.

My role now revolves around development of automated liquid handing methods using robotics. The *in vitro* model described within is compatible with automation, and such a platform could expiate the discovery of improved organ storage conditions on a cell by cell basis. Further *in vitro* work required assessment of the *in vitro* conclusions of this thesis on cell lines representative of other structures in the kidney.

Interestingly, 20 hours of SCS storage- with a 2 hour period of oxygenated perfusion at the end exhibited the lowest LDH release at experimental endpoint of all preservation environments tested. It has been repeatably observed that in the absence of any effect caused by differences in oxygenation, the LDH present in perfusate accumulates over time during HMP. The fact that the fluid flushed out of the SCS stored kidney in 2 hours did not have comparable levels of LDH to HMP stored kidneys indicates that LDH accumulation is not just consequence of CIT. Some aspect of perfusion may exert a damaging influence over the kidney. It has been demonstrated *in vitro* that storage of proximal tubule cell in UWMPS, rather than UW consistently results in lower release of LDH, suggesting it is not fluid composition driving this change. If greater oxygen availability reduces LDH release, and the standard HMP kidney affords a limited respite from hypoxia when compared to static storage, then mechanical stresses delivered by perfusion may be contributing to the elevation in LDH caused by perfusion, ShearFAST may useful in to characterising the level

of shear stress which is deleterious for cells lines representative of different structures in the kidney.

10.2.2 Ex vivo

Extrapolating from the data presented within, an optimised renal oxygenation strategy can be trialled. At initiation of HMP, perfusate should be preloaded with oxygen since this has been shown to lower endpoint perfusate lactate concentrations (Figure 9.13).

Oxygenation should not be applied once, as this in ineffective at maintaining perfusate PaO_2 (Figure 9.3 and Figure 9.10). Oxygenation should stagger, and the frequency of oxygen supplementation modified based on real time measures of perfusate oxygen consumption to maintain a minimal therapeutic dose. This may result in lower LDH release and improved organ quality.

While interesting, the conclusions gleaned from these *in vitro* and *ex vivo* the whole organ studies fundamentally require the transplantation model in order to assess potential clinical relevance. A tracer-based perfusion of HMP study followed by autotransplant of the kidney is required. Metabolic differences observed could cement the findings of our groups clinical tracer study ^{13}Champion. A key advantage of the of the auto transplant model is the availability of tissue for metabolic analysis, a benefit not afforded to the ^{13}Champion kidneys. In this manner, measures of transplant outcomes could be correlated with unequivocal changes in *de novo* metabolism arising from perfusate oxygenation.

11 Appendices

11.1.1 Appendix 1: High Speed Tracing of Metabolism

This appendix contains an article was published in Wellcome Open research in 2018.

As joint first author, I was responsible for experimental design, execution, analysis and writing/editing of the manuscript. The NMR developments described within were conceived by my supervisor, Christian Ludwig.

11.2 Introduction

Chapter 8 reveals metabolic modulation is possible under simulated hypothermic preservation by increasing oxygen content. The analysis used in this chapter was exclusively assessment of mass isotopomer distribution, a rapid analysis which as described in chapter 1, does not allow analysis of label positioning.

The capacity to identify the position of label incorporation is mandatory in the tracing of the metabolic processes which can be inferred. For example, M2 glutamate observed under fluid oxygenation could infer [4,5-^{13}C] or [1,2-^{13}C labelling] which is indicative of different degrees of TCA cycle progression (310,311).

Our group pioneered the use of HSQC tracer studies in organ preservation, demonstrating the predominance of glycolytic metabolism over aerobic metabolism during standard HMP (235). This is likely to be a vital tool in the determination of whether or not oxygenation unequivocally results in enhanced aerobic metabolism in hypothermicly stored kidneys, but the extended acquisition times required to foster sufficient resolution with which to observe the fine structure of split peaks limits sample throughput

^{13}C NMR isotopologue analysis relies on clear discrimination of coupled peaks, which are informative of isotopic distribution. However as illustrated in the attached manuscript, the standard HSQC may not be able to discern these.

Additionally, optimisation metabolic support of oxygen supplementation will require understanding of the optimal timing, percentage and duration of oxygen delivery. This translates to the need for many experiments and samples, a hefty spectrometer workload and costly analysis.

In light of these issues, a new development is described in which the distance between the splitting's of a ^{13}C signal, caused by the presence of bound homonuclear ^{13}C-^{13}C coupling is increased. This prevents overlap between spin systems and vastly reduces the acquisition time needed to achieve the spectral resolution required for multiplet analysis.

An additional development is described which describes a pulse sequence for high throughput screening of ^{13}C enriched metabolites using a combination of unfiltered and ^{12}C-filtered 1D ^{1}H-NMR spectra. While the application of scaling J-coupling based splittings in 2D-HSQC spectra form the bulk of the metabolic analysis in the following chapters, experiments using the described spectral filtering are an attractive approach for rapid screening of *de novo* metabolism, and may be useful for identification of preservation environments that result in desirable metabolic processes in donated organs in the hours before transplantation.

METHOD ARTICLE

REVISED High-Speed Tracer Analysis of Metabolism (HS-TrAM) [version 2; referees: 4 approved]

Thomas Brendan Smith[1*], Kamlesh Patel[1*], Haydn Munford[1], Andrew Peet[2,3], Daniel A. Tennant [1], Mark Jeeves [2*], Christian Ludwig [1*]

[1]Institute of Metabolism and Systems Research, University of Birmingham, West Midlands, UK
[2]Institute of Cancer and Genomic Sciences, University of Birmingham, West Midlands, UK
[3]Birmingham Children's Hospital NHS Foundation Trust, West Midlands, UK

[*] Equal contributors

v2 First published: 12 Jan 2018, 3:5 (doi: 10.12688/wellcomeopenres.13387.1)
Latest published: 22 Aug 2018, 3:5 (doi: 10.12688/wellcomeopenres.13387.2)

Abstract

Tracing the fate of stable isotopically-enriched nutrients is a sophisticated method of describing and quantifying the activity of metabolic pathways. Nuclear Magnetic Resonance (NMR) spectroscopy offers high resolution data in terms of resolving metabolic pathway utilisation. Despite this, NMR spectroscopy is under-utilised due to length of time required to collect the data, quantification requiring multiple samples and complicated analysis. Here we present two techniques, quantitative spectral filters and enhancement of the splitting of ^{13}C signals due to homonuclear ^{13}C,^{13}C or heteronuclear ^{13}C,^{15}N J-coupling in ^{1}H,^{13}C-HSQC NMR spectra. Together, these allow the rapid collection of NMR spectroscopy data in a quantitative manner on a single sample. The reduced duration of HSQC spectra data acquisition opens up the possibility of real-time tracing of metabolism including the study of metabolic pathways *in vivo*. We show how these techniques can be used to trace the fate of labelled nutrients in a whole organ model of kidney preservation prior to transplantation using a porcine kidney as a model organ. In addition, we show how the use of multiple nutrients, differentially labelled with ^{13}C and ^{15}N, can be used to provide additional information with which to profile metabolic pathways.

eywords

NMR, stable-isotope tracing, 13C, 15N, splitting enhancement, metabolism, tracer

Open Peer Review

Referee Status:

	Invited Referees 1	2	3	4
REVISED version 2 published 22 Aug 2018	✓ report	✓ report		✓ report
version 1 published 12 Jan 2018	? report	? report	✓ report	? report

1 Sebastien Serres , University of Nottingham, UK

2 Paul C. Driscoll , Francis Crick Institute, UK

3 ulian L. riffin, University of Cambridge, UK

4 Hector C. eun , Imperial College London, UK

Discuss this article

Comments (0)

Corresponding authors: **Mark Jeeves** **Christian Ludwig**

Author roles: Smith TB: **Data Curation, Formal Analysis, Investigation, Methodology, Validation, Writing - Original Draft Preparation, Writing - Review & Editing;** Patel : **Data Curation, Formal Analysis, Investigation, Methodology, Validation, Writing - Original Draft Preparation, Writing - Review & Editing;** Munford H: **Data Curation, Investigation, Methodology, Writing - Original Draft Preparation, Writing - Review & Editing;** Peet A: **Funding Acquisition, Resources, Supervision, Writing - Original Draft Preparation, Writing - Review & Editing;** Tennant DA: **Funding Acquisition, Resources, Supervision, Writing - Original Draft Preparation, Writing - Review & Editing;** eeves M: **Data Curation, Formal Analysis, Investigation, Methodology, Supervision, Validation, Writing - Original Draft Preparation, Writing - Review & Editing;** Ludwig C: **Conceptualization, Data Curation, Formal Analysis, Funding Acquisition, Investigation, Methodology, Project Administration, Resources, Software, Supervision, Validation, Visualization, Writing - Original Draft Preparation, Writing - Review & Editing**

Competing interests: **No competing interests were disclosed.**

rant information: **This work was supported by the Wellcome Trust [099185] and through an Institutional Strategic Support Award given to the University of Birmingham; the National Institute for Health Research [13-0053]; Help Harry Help Others [HelpCU09]; UHB Charitable Funds [17-3-846] and the metabolic tracer analysis core (MTAC) at the University of Birmingham.**
The funders had no role in study design, data collection and analysis, decision to publish, or preparation of the manuscript.

How to cite this article: **Smith TB, Patel K, Munford H** *et al.* High-Speed Tracer Analysis of Metabolism (HS-TrAM) [version 2; referees: 4 approved] **Wellcome Open Research 2018, 3:5 (doi: 10.12688/wellcomeopenres.13387.2)**

First published: **12 Jan 2018, 3:5 (doi: 10.12688/wellcomeopenres.13387.1)**

REVISED **Amendments from Version 1**

This version addresses all major and most minor criticisms of the reviewers. We simplified the biological models and concentrated mostly on renal metabolism, by adding new experimental data. We also removed 900 MHz data and are now using NMR data acquired at 600 MHz only. We redesigned most figures to exclude spectral overlays to improve clarity and added line shape simulations. We also added a new figure, which is now Figure 5, so that the previous Figure 5 and Figure 6 are now Figure 6 and Figure 7, respectively.

See referee reports

Introduction

Investigations of metabolism in health and disease increasingly rely on tracing the use of stable isotope-enriched nutrients through the cell's metabolic pathways. The most widely utilised technology platform to analyse the resulting complex patterns of labelling in multiple cellular metabolites is mass spectrometry (MS), due to its high sensitivity, short run times and a resulting low-cost operation[1–12]. Conversely, NMR spectroscopy is relatively under-utilised, despite being able to provide higher resolution information on the conversion of synthetically produced stable isotopes of nutrients are incorporated into cellular metabolites[12–19]. This is because NMR spectroscopy has historically suffered from low sensitivity, long acquisition times and the need for complex analytical tools.

NMR spectroscopy is, however, ideally suited to answering some of the more pressing questions about metabolic control in health and disease. We currently have limited knowledge about the compartmentalisation of metabolic pathways in metabolically-active organelles, such as mitochondria, and therefore whether the same metabolite is selectively utilised for distinct purposes in different compartments[20]. Given the recent drive to target metabolism in various diseases, understanding the control of metabolism by different tissues is critical to the ability to select specific therapies which target the desired pathways within appropriate cellular compartments. While sample analysis by high-resolution NMR spectroscopy is performed *ex vivo* or *in vitro*, the data obtained provide information on metabolic pathways *in vivo*.

Stable isotope-enriched metabolic precursors, such as glucose or glutamine, are employed as metabolic tracers. These synthetically produced nutrients are enriched in isotopes with a low natural abundance, such as ^{13}C or ^{15}N. Despite the fact that metabolites can arise from multiple sources, the contribution of the different metabolic pathways to the synthesis of this metabolite can be determined through the analysis of the ^{13}C and/or ^{15}N distribution within the metabolite (Figure 1). The couplings

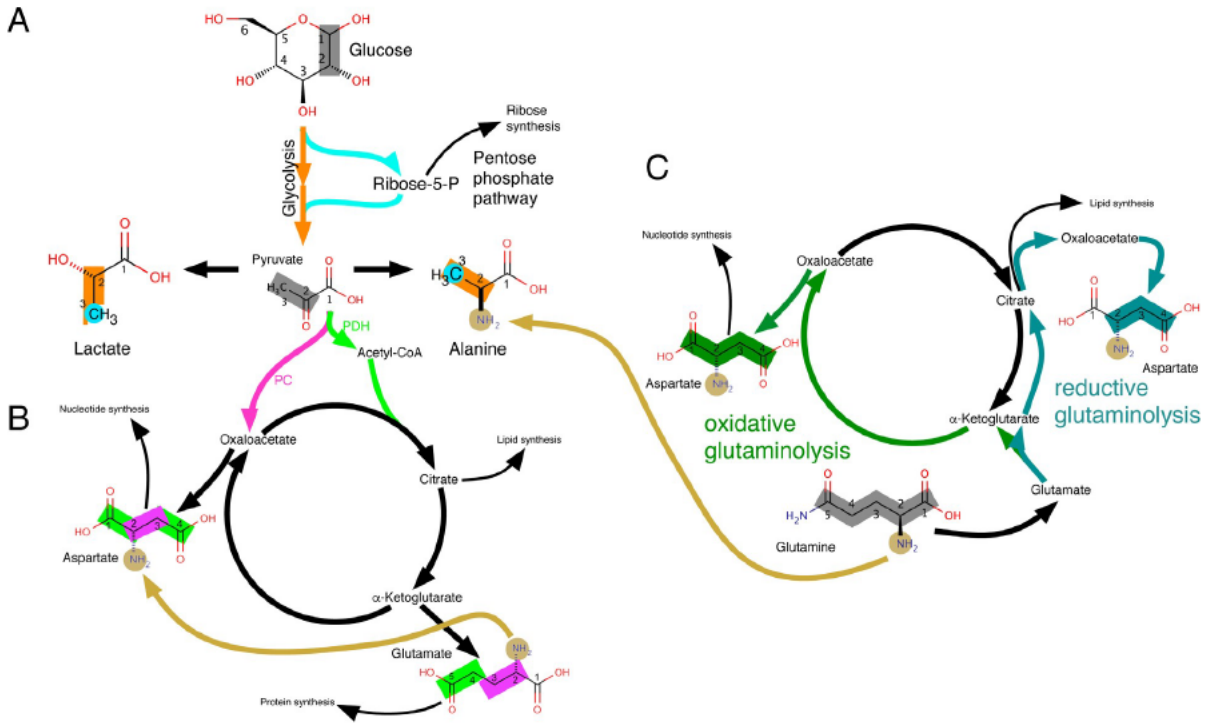

Figure 1. Tracing of metabolic pathways. The labelling patterns arising from [1,2-^{13}C] glucose (**A** & **B**) as well as from [U-^{13}C,^{15}N] glutamine (**C** for ^{13}C labelling and **A**–**C** for ^{15}N labelling) are shown. Metabolism of [1,2-^{13}C] glucose leads to distinctive labelling patterns in lactate and alanine ([2,3-^{13}C] lactate/alanine when using glycolysis and [3-^{13}C] lactate/alanine when using the pentose phosphate shunt, PPP) (Panel **A**). Similarly, glutamate and aspartate express different labelling patterns from [1,2-^{13}C] glucose, depending whether they were synthesised via pyruvate dehydrogenase (PDH; resulting in [4,5-^{13}C] glutamate) or via the pyruvate carboxylase (PC; resulting in [2,3-^{13}C] aspartate) route (Panel **B**). Metabolisation of labelled glutamine can reveal other anaplerotic pathway activities such as reductive carboxylation (Panel **C**).

are visualised in the indirect dimension of an HSQC spectrum allowing the determination of the percentage incorporation of isotopic label into adjacent nuclei. While MS data does not need a reference sample to distinguish between labelled and unlabelled metabolites, it is not always possible to derive the exact distribution of labelled nuclei within a molecule. In contrast, NMR spectroscopy data can resolve label distribution at the atomic level, enabling a clearer picture of the label distribution in metabolites.

Our recently published combined NMR spectroscopy and MS approach (CANMS) harnesses the strengths of both modalities to produce highly-resolved metabolism information in the form of metabolite isotopomers[19]. The detailed interpretation of MS isotopologue data, when using MS data in isolation, requires use of a pre-defined metabolic model. In contrast, the integrated analysis of NMR spectroscopy and MS data makes fewer assumptions about the metabolic network, providing a more accurate insight into relative pathway contributions than is possible with current established methods or the independent analysis of MS or NMR spectroscopy data alone. For example, proton-less carbon atoms do not give rise to a signal in 2D-HSQC NMR spectra, although incomplete information on those carbons is available via splitting of adjacent carbon nucleus signals. The combination of NMR spectroscopy and MS analysis fills this gap as the MS data provides informa- tion on the amount of single carbon labelling into those carbon nuclei via "m+x" isotopologues. [1,2-^{13}C] glucose is the optimal tracer to assess metabolic flux through glycolysis vs pentose phosphate pathway (PPP) shunting back into glycolysis. While the glycolytically derived isotopomer of lactate is [2,3-^{13}C] lactate, the PPP derived isotopomers can be [3-^{13}C], [1-^{13}C] or [1,3-^{13}C] lactate. Although the first isotopomer can be assessed with NMR spectroscopy data, the other two isotopomers include labelling in C(1), which HSQC NMR spectroscopy is "blind" to. In these cases, MS data adds new information to the NMR spectroscopy data by contributing the isotopo- logues NMR spectroscopy is not able to detect, while NMR spectroscopy adds to the MS data by differentiating between [1,3-^{13}C] and [2,3-^{13}C] lactate.

A major drawback of utilising ^{13}C-^{13}C scalar coupling information to derive isotopomer distributions is the time required to acquire spectra. For example, around four hours are required for the acquisition of a 2D-HSQC NMR spectrum with high-resolution in the ^{13}C dimension, even when using fast, state-of-the-art non-uniform sampling (NUS) techniques.

Here we describe two developments, quantitative spectral filters and signal splitting enhancement, to facilitate and speed-up the acquisition of NMR spectra for tracer-based analysis of metabolism. Such techniques permit high throughput metabolic pathway profiling, increasing access, affordability and sensitivity when using NMR spectroscopy as an investigative modality. Additionally, these developments facilitate fast detection of ^{15}N labelling, especially when combined with ^{13}C tracing, thus providing extra information allowing more accurate metabolic pathway profiling.

Methods and results

Quantitative spectral filters for ^{13}C tracer observation: 1D Spectral filters

Experimental setup. A porcine kidney was procured from a slaughterhouse (FA Gill, Wolverhampton) following approximately 14 minutes warm ischaemic time (WIT) as per previous experimental methodology[18]. No animal was killed solely for experimental purposes; all were due for human consumption, therefore no ethical approval was required. After 2 hours cold ischaemic time, kidneys were subject to 18 hours of hypothermic machine perfusion. The perfusate sample was collected after 6 hrs of perfusion and prepared for NMR analysis.

1D NMR spectra were acquired using a Bruker Avance III 600 MHz NMR spectrometer equipped with a 5mm z-PFG TCI Cryoprobe. 128 transients were acquired for each spectrum with a 5 s interscan relaxation delay. A total of 32768 data points with a spectral width of 12 ppm was acquired for each FID using an adiabatic bi-level decoupling scheme to suppress ^{1}H, ^{13}C J-coupling during acquisition[21]. While decoupling for this long (2.25 s) was possible because of the cryogenic probe and may potentially work with a room temperature probe, care must be taken as there will be significant sample heating. The sample heating can be significantly reduced, with only very minor reduction in resolution, by acquiring for only 1.125 s. In order to estimate whether a specific spectrometer with a cryoprobe can tolerate the power dissipation originating from the decoupling sequence specific attention should be paid to the cryogas heater current, which should never fall below its system specific lower limit.

The spectra were processed within the MetaboLab software package (version 2018.07182055)[22]. A 0.5 Hz line broadening was applied with zero-filling of the data up to 131072 real data points prior to Fourier transformation. The resulting spectra were referenced using DSS and manually phase corrected. Subsequently the spectral baseline was corrected using MetaboLab's spline baseline correction before the spectra were exported to Bruker format for metabolites to be quantified in the Chenomx software package (version 8.2, http://www.chenomx.com).

NMR methodology. Despite their relative simplicity and limited resolution, 1D-NMR spectra are highly sensitive tools with which to identify and quantify metabolites. Spectral filters enable the acquisition of spectra which filter out certain signals, thereby reducing ambiguity in 1D spectra associated with attributing peaks to nuclei within metabolites. For example, one can acquire 1D ^{1}H NMR spectra of protons bound to ^{13}C only, simplifying signal assignment and analysis of the acquired spectra. The simplest approach to collect such spectra would be to acquire the first increment of a 2D-^{1}H, ^{13}C-HSQC spectrum. However, signal intensities are not directly comparable with those in standard 1D-^{1}H NMR spectra. It is therefore not possible to directly derive ^{13}C percentages based on a comparison of those spectra with standard proton 1D spectra unless only a small subset of molecules is labelled with ^{13}C and one accompanying spectrum is scaled so that

the majority of signals within the two spectra are of same intensity[23]. Spectral filters such as BIRD, TANGO and POCE[24–28] originated in protein NMR spectroscopy to filter out certain parts of the magnetisation and therefore quantitative data cannot be gained from resultant output spectra. Quantitative comparisons between unfiltered and filtered spectra are usually unnecessary, except for tracer-based analysis. Here we present a novel spectral filter which enables quantitative analysis of resultant spectra from single samples, enriched with ^{13}C tracer.

Panels A-1 and B-1 in Figure 2 show the pulse sequences implementing the quantitative spectral filter. While the central

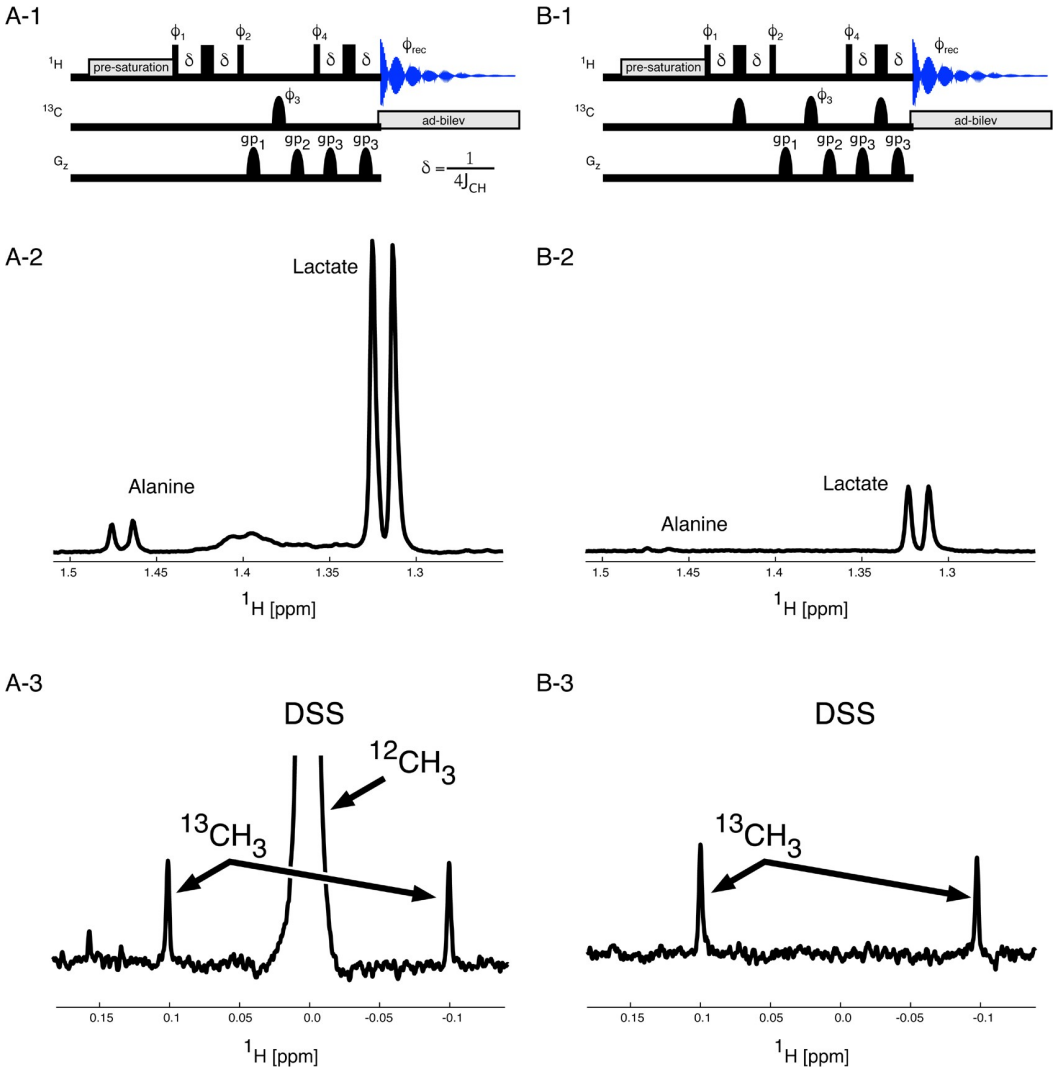

Figure 2. Spectral Filters in 1D spectroscopy. To determine percentage ^{13}C incorporation two spectra are acquired per sample. One spectrum (**A**) contains ^{1}H signals originating from all protons (all ^{1}H spectrum), while the second spectrum (**B**) only contains signals from protons attached to a ^{13}C nucleus. The central ^{13}C Π–pulse with phase Φ_3 is executed every second transient in both experiments. The proton magnetisation in the all ^{1}H pulse sequence is the same for ^{12}C and for ^{13}C bound protons and as a consequence, all ^{1}H magnetisation is longitudinal during the interval between ^{1}H pulses with the phases Φ_2 and Φ_4. Because of the additional ^{13}C Π–pulses in the ^{13}C bound ^{1}H pulse sequence, the magnetisation for the two different kinds of protons develops differently. Here only the ^{13}C bound ^{1}H magnetisation is longitudinal in the interval between the ^{1}H pulses with the phases Φ_2 and Φ_4. Therefore, the ^{12}C bound ^{1}H magnetisation can be destroyed using the two pulse field gradients labelled gp_1 and gp_2. A recovery delay of 200 µs was used after each gradient. The central ^{13}C Π–pulse with phase Φ_4 improves magnetisation selection as it is accompanied by phase changes of the ^{1}H pulses and the receiver. All ^{13}C Π-pulses are adiabatic Chirp pulses with ΓB_{1max} = 10 kHz. ^{1}H,^{13}C J-coupling is suppressed during acquisition using adiabatic bilevel decoupling (ad-bilev)[21]. The pulse phases are: Φ_1 = x, x, -x, -x; Φ_2 = x, x, -x, -x for the all ^{1}H spectrum (**A-1**) and y, y, y, y for the ^{13}C bound ^{1}H spectrum (**B-1**), Φ_3 = x, y, -x, -y, Φ_4 = x, -x, -x, x, y, -y, -y, y for the all ^{1}H spectrum (**A-1**) and y, -y, -y, y, -x, x, x, -x for the ^{13}C bound ^{1}H spectrum (**B-1**). Panels **A-2** and **B-2** show the peaks from Alanine and Lactate methyl protons in the all ^{1}H spectrum (**A-2**) and the ^{13}C bound ^{1}H spectrum (**B-2**). The scaling of the two spectra is identical allowing easy determination of the percentage incorporation of ^{13}C metabolites. Panels **A-3** and **B-3** demonstrate the complete removal of the ^{12}C bound proton signal from the ^{13}C edited spectrum (**B-3**) leaving only the natural abundance ^{13}C signals to be observed.

^{13}C Π-pulse (phase Φ_3) is used only in odd numbered transients and replaced with a delay of the same length during even numbered transients, the two other ^{13}C Π-pulses are only used in the ^{12}C filtering experiment (B-1), where ^{1}H magnetisation to ^{12}C neighbours is filtered out, so that only ^{13}C bound ^{1}H magnetisation contributes to the signal intensities in the 1D spectrum. The phase cycle Φ_1 changes as well between the 2 experiments, as indicated in the figure legend.

Panels A-2 and B-2 in Figure 2 depict two sample spectra from a perfusate sample where a cadaveric porcine kidney was perfused with modified University of Wisconsin machine perfusion solution (UW MPS) during a period of hypothermic machine perfusion. The standard unlabelled glucose constituent (10 mM) within classical UW MPS was replaced with 10 mM universally labelled glucose, for use as a metabolic tracer during the 18 hour perfusion.

While filters such as BIRD utilise relaxation to minimise the unwanted part of the magnetisation, methods such as TANGO or POCE generate magnetisation where ^{12}C bound ^{1}H atoms possess either the same or the opposite phase compared to the magnetisation of ^{13}C bound ^{1}H atoms, generating two different spectra. By subtraction of these two spectra, the magnetisation of ^{13}C bound ^{1}H atoms can then be calculated. In case of low ^{13}C incorporation, as with any difference technique, subtracting two very large signals in presence of a small signal can lead to substantial artefacts. The quantitative spectral filter works slightly differently compared to TANGO and POCE as the pulse sequence depicted in Figure 2, panel B-1 makes use of two gradient pulses (gp_1 and gp_2) to destroy unwanted magnetisation. As an example, panels A-3 and B3 in Figure 2 show a variant of the pulse sequences where the adiabatic bilevel decoupling (ad-bilev)[21] has been omitted, so that the ^{12}C and the ^{13}C bound ^{1}H signals appear separated in the spectrum. The $^{12}CH_3$ signal in A-3 has been truncated to be able to visualise the ^{13}C satellites, which appear with 0.5% of the peak height of the $^{12}CH_3$ signal. As can be seen in panel B-3, the $^{12}CH_3$ signal is completely suppressed without leaving an artefact, so that even signals from naturally occurring ^{13}C alone are easily detectable in a ^{13}C decoupled spectrum.

The quantitative spectral filter is invariant with respect to differential ^{1}H relaxation rates or signal multiplicities. As with any J-coupling based filtering approach, the ^{12}C filtered spectrum will be scaled with a factor that is proportional to $\sin(2\Pi\Delta J_{CH})^2$, where Δ is the delay during the first and last spin echo. Δ is usually set to $¼J_{CH}$ with J_{CH} = 145 Hz. Assuming a minimum J_{CH} of 120 Hz and a maximum J_{CH} of 165 Hz, results in a maximum downscaling of 7.2%.

J-Coupling based splitting enhancement in 2D-NMR spectra

Experimental setup. Slaughterhouse porcine kidneys (WIT-15 minutes) were cannulated and flushed with chilled Soltran solution (Baxter) as performed in clinical practice. Kidneys were placed in static cold storage en route to our laboratory, where they were immediately perfused with modified KPS-1 using the Lifeport Kidney Transporter 1.0 (Organ Recovery Systems), which has been modified to include a paediatric oxygenator. Oxygen was supplied at a flow rate of 0.7 L/min for the duration of the 24 hours perfusion period.

At the end of the perfusion period, the kidney was removed from the perfusion circuit and laterally bisected. Sections of cortex and medulla were isolated and snap frozen in liquid nitrogen. These tissues were powdered, also under liquid nitrogen, and 0.5 g was placed in 7 ml homogenisation tube (Precellys, CK28), containing 5.1 ml of HPLC grade methanol (−80°C) to quench metabolism. These were homogenised using the Precellys 24 dual homogeniser (8x 5000 rpm for 15 s). The samples were mixed with 4.65 ml deionised water and 5.1 ml HPLC grade chloroform and vigorously agitated. Biphasic separation of polar and non-polar solvents was performed by centrifugation (1300 g, 15 minutes, 4°C), after which 4.5 ml of the polar layer was aspirated and dried overnight at 35°C.

The dried extracts were resuspended in 60 µl NMR buffer (0.1 M phosphate buffer, 0.5 mM 4,4-dimethyl-4-silapen- tane-1-sulfonic acid, 2 mM imidazole and 10% D_2O). These suspensions were sonicated to dissolve micro particles and then 35 µl of this solution was added to 1.7 mm NMR tubes.

$^{1}H,^{13}C$-HSQC spectra were acquired using a Bruker Avance III 600 MHz NMR spectrometer equipped with a 1.7 mm z-PFG TCI Cryoprobe. The HSQC spectra were acquired using 2 transients per increment with echo/anti-echo gradient coherence selection and an additional pre-saturation for suppressing the water resonance during the 1.5 s interscan relaxation delay. The ^{1}H dimension was acquired with a spectral width of 13 ppm using 512 complex data points. The ^{13}C dimension was acquired with a spectral width of 160 ppm using 25% (2048) of 8192 data points using a non-uniform sampling scheme. The non-uniformly sampled spectra were reconstructed via the compressed sensing algorithm within the MDDNMR (version 2.5)[29] and processed using NMRPipe (version 9.2)[30]. All spectra were processed without baseline correction to avoid complications in the multiplet analysis procedure.

NMR methodology. The relatively long acquisition times of 2D-HSQC spectra are necessary to generate the spectral resolution required to resolve complex multiplet patterns[19]. Here we present a technique to manipulate the appearance of NMR multiplets in the indirect dimension of 2D-HSQC spectra. The ability to expand the splitting caused by J-coupling has previously been reported[31,32]. Here we apply this technique in order to negate the requirement for the collection of large number of increments in the ^{13}C dimension, which, together with methods such as non-uniform sampling[29,33] and variation of the repetition time[34] significantly reduces the time required to acquire 2D-HSQC spectra with sufficient resolution. It also means that at increasingly higher magnetic fields, the advantages of extra sensitivity and increased ^{1}H chemical shift resolution are not negated by the increased ^{13}C increments needed in in order to resolve J-couplings. Enhancement of the splitting due to J-coupling can be achieved by incrementing the spin echo delay after the period where chemical shift of ^{13}C evolves in parallel with the chemical shift evolution (Figure 3). This spin

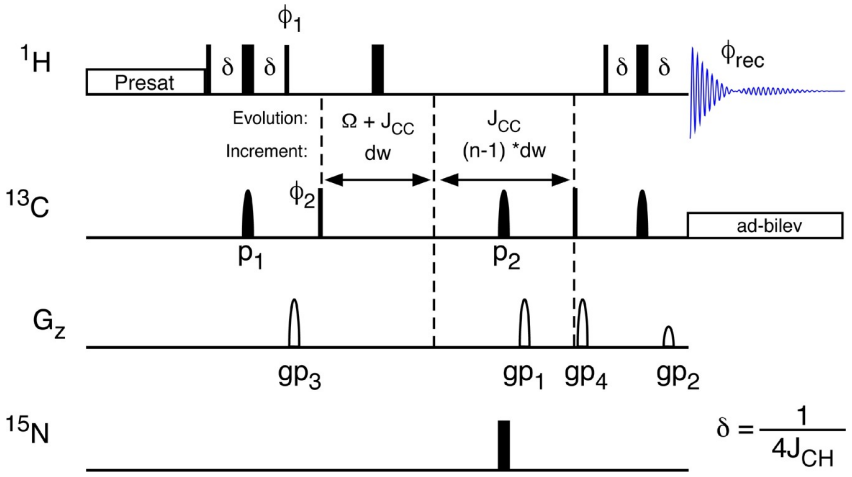

Figure 3. Splitting Enhanced HSQC Spectroscopy. The splitting enhancement due to J-coupling is achieved using an additional spin echo subsequent to the ^{13}C evolution period. The delays in the spin-echo for the J-coupling enhancement are multiples of the dwell time (dw). While the chemical shift evolves with dw, which is determined by setting the spectral width of the spectrum, splittings are enhanced depending on the increment of the ^{13}C gradient selection spin-echo. The HSQC spectrum is acquired using echo/anti-echo for quadrature detection to allow for efficient removal of artefacts in only two scans per increment. Optionally, the ^{13}C,^{15}N-couplings can be scaled by the introduction of the ^{15}N Π-pulse simultaneously with the ^{13}C Π-pulse (labelled p2). ^{1}H,^{13}C J-coupling is suppressed during acquisition using adiabatic bilevel decoupling (ad-bilev)[21]. The pulse phases are: Φ_1 = y; Φ_2 = x, -x; Φ_{rec} = x, -x.

echo refocuses the ^{13}C chemical shift and the ^{1}H-^{13}C coupling, but allows the ^{13}C-^{13}C coupling to evolve further. The delays in the spin echo are proportional to those in the $\Omega+J_{CC}$ evolution period with the amount of extra coupling achieved being defined by the stretch of the J_{CC} increment compared to the $\Omega+J_{CC}$ increment. Thus, the ^{13}C-^{13}C J-couplings can be expanded as required (Figure 4). The ability to scale the signal splittings to varying extents means that the experiment can be tuned to the requirements of the sample and which metabolites are present, and of interest. Figure 4 demonstrates the effect of J-coupling splitting enhancement on 2D HSQC spectra, displaying C(6) of ^{13}C enriched glucose. The ^{13}C trace through the left-most signal (Figure 4D), demonstrates clearly that while the singlet in the middle of the multiplet does not change, the splitting due to the $^{1}J_{CC}$ coupling increases and in fact splits into multiple signals as the splittings of previously unresolved long-range couplings are amplified so that they are large enough to become resolved in the spectrum. These splittings can easily be simulated (Figure 4E), thereby providing additional information with which to model metabolic pathways.

Large expansion of J-coupling also allows for rapid collection of data, as the resolution required to resolve them becomes diminished (Figure 5). However, this should be tempered by the need to avoid unnecessary overlap of signals. To date, the authors have acquired 2D spectra with up to eight fold enhanced ^{13}C J-couplings, combined with shortening the acquisition by using variable pulse sequence repetition times[34], leading to an overall decrease in acquisition time by a factor larger than 10 (Figure 5). Panels A to D show the spectral region of the methyl groups of lactate and alanine. Panel E shows a cross section, as marked in the 2D spectra, from alanine, whereas panel F shows the corresponding simulations of those multiplets. The acquisition times for the different spectra were 233, 110, 51 and 24 minutes (Table 1). Whilst the lines in the spectrum become broader due to the shorter acquisition times, this is negated by the increase in splittings, allowing the analysis of the multiplets with similar precision. Shorter acquisition times may be achieved by including spectral folding in the acquisition protocol or by incorporating new fast acquisition schemes such as ASAP- or ALSOFAST-HSQC[35].

^{15}N tracing

Experimental setup. *2D ^{14}N spectral filter* - Sample preparation is described elsewhere[16]. 2D ^{1}H ^{13}C-HSQC NMR spectra with and without ^{14}N filtering were acquired using a Bruker Avance III 600 MHz NMR spectrometer equipped with a 1.7 mm z-PFG TCI Cryoprobe. The HSQC spectra were acquired using 2 transients per increment with echo/anti-echo gradient coherence selection and an additional pre-saturation during the 1.5 s interscan relaxation delay to suppress the water resonance. The ^{1}H dimension was acquired with a spectral width of 13 ppm using 512 complex data points. The ^{13}C dimension was acquired with a spectral width of 160 ppm using 2048 data points. The spectra were processed with quadratic cosine window functions and without baseline correction to avoid complications in the multiplet analysis procedure.

^{13}C, ^{15}N J-coupling splitting enhancement. The human Renal Proximal tubule cell line (RPTEC/TERT1, supplied by Evercyte GmBH, Austria) was used to investigate the metabolic fates of both carbon from glucose, and carbon and nitrogen from glutamine. Cells were expanded as described elsewhere[36], with population doubling level (PDL) routinely tracked using in-house software (PDL calculator, EcoCyto). Cells with PDL between 43 and 45 were collated and seeded at a density of $4\times10^4/cm^2$ in 75 cm^2 flasks containing 240 µl/cm^2 flux media (Zenbio, cat DMEMf12-NGG002), supplemented as above with the addition of 17.5 mM [1,2-^{13}C] D-Glucose (sigma 453188) and 2 mM [U-^{13}C,U-^{15}N] L-Glutamine (sigma, 607983). Cell

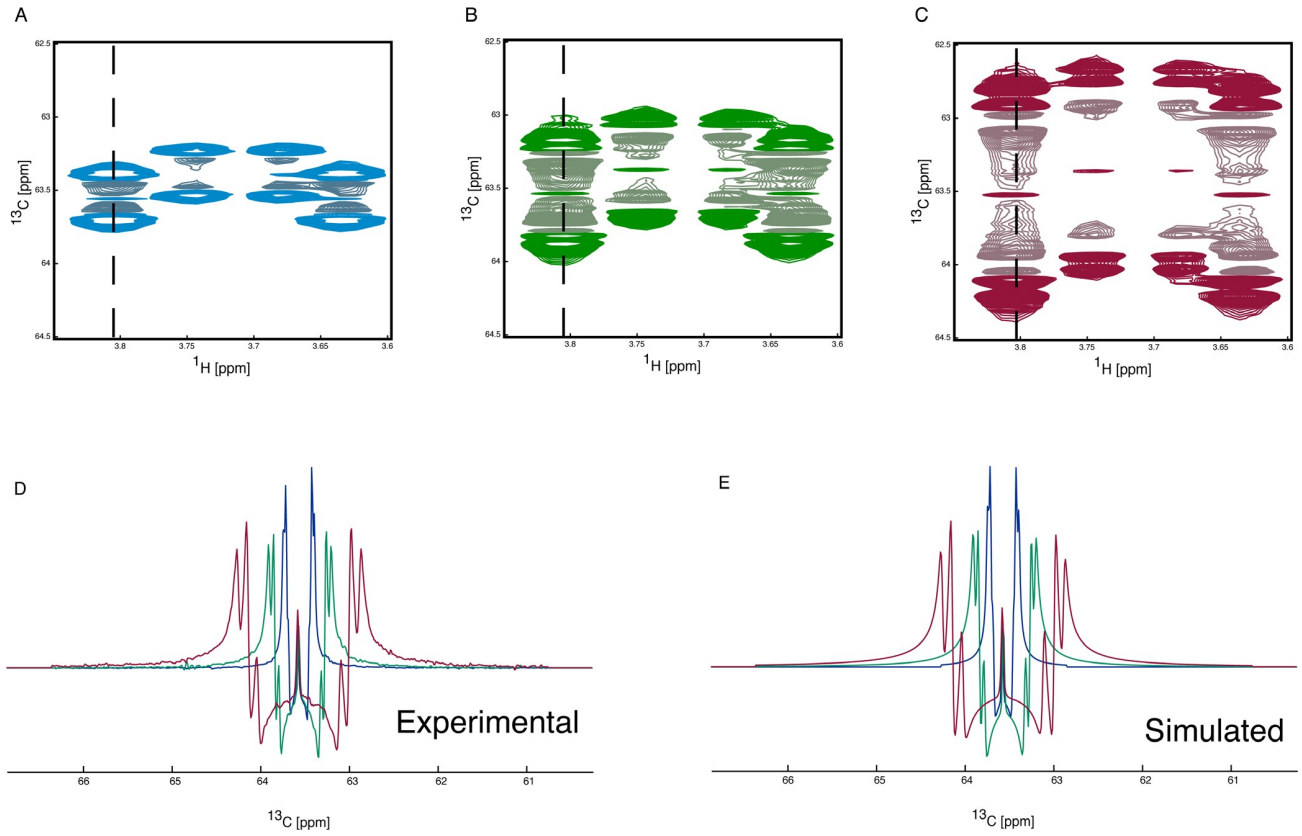

Figure 4. J-coupling splitting enhancement HSQC spectroscopy. ^{1}H,^{13}C HSQC spectra showing the C(6) of glucose are shown (**A**, **B** and **C**). The spectrum with no J-coupling splitting enhancement is shown in blue (**A**), with an enhancement of two in green (**B**) and with an enhancement of four in red (**C**). The ^{13}C trace of the HSQC spectra (**D**), taken from the ^{1}H frequency as depicted by the dashed line, clearly shows the increase in observed splitting. The J-coupling splitting enhancement is achieved using an additional spin echo subsequent to the ^{13}C evolution period. The delays to achieve the scaling of the splittings are multiples of dw such the use of a delay of 3*dw will result in a J-coupling splitting enhancement of 4 (one from the t_1 evolution and three from the J-coupling splitting enhancement spin echo). The observed splitting can be simulated (**E**) giving the following incorporation percentages. From the no J-coupling splitting enhancement spectrum 6.8% / 41.2% / 52 % for [6-^{13}C] / [5,6-^{13}C] / [U-^{13}C], from the two-fold J-coupling splitting enhancement 6.3% /41.4% / 52.3 % for [6-^{13}C] / [5,6-^{13}C] / [U-^{13}C] and from the four-fold J-coupling splitting enhancement 5.9% / 41.6% / 52.5 % for [6-^{13}C] / [5,6-^{13}C] / [U-^{13}C].

culture was continued for 48 hours to allow isotopic labelling, after which cells were washed with ice-cold saline solution (0.9%) and collected by scraping into 2 ml pre-chilled methanol (-20°C), 2 ml water (4°C) and 2 ml chloroform (-20°C). The solution was vigorously mixed for 10 minutes, after which lysates were centrifuged at 15,000 *g* for 15 min at 4°C. 1 ml of the sample was aspirated for NMR analysis. Samples were dried using a Savant (SPD1010) speedvac concentrator and then resuspended in 60 µL of 100 mM sodium phosphate buffer, containing 0.5 mM DSS, 2 mM Imidazole in D_2O, pH 7.0. The samples were vortexed and subsequently sonicated for 10 min and then centrifuged at 15000 *g* for 30 seconds to collate the fluid. Finally 35 µl of the samples were transferred to 1.7 mm NMR tubes.

2D-^{1}H,^{13}C-HSQC and 2D-^{1}H,^{15}N-HSQC NMR spectra were acquired using a Bruker Avance III 600 MHz NMR spectrometer equipped with a 1.7 mm z-PFG TCI Cryoprobe. The HSQC spectra were acquired using 2 transients per increment with echo/anti-echo gradient coherence selection with an additional pre-saturation to suppress the water resonance during the 1.5 s interscan relaxation delay. The ^{1}H dimension of the ^{1}H, ^{13}C-HSQC spectra was acquired with a spectral width of 12 ppm using 512 complex data points. The ^{13}C dimension was acquired with a spectral width of 160 ppm using 25% (2048) of 8192 data points using a non-uniform sampling scheme. The ^{1}H dimension of the ^{1}H,^{15}N-HSQC spectra was acquired with a spectral width of 12 ppm using 1024 complex data points. The ^{15}N dimension was acquired with a spectral width of 40 ppm using 256 data. All non-uniformly sampled spectra were reconstructed via the compressed sensing algorithm within MDDNMR (version 2.5)[29] and processed using NMRpipe (version 9.2)[30]. All spectra were processed without baseline correction to avoid complications in the multiplet analysis procedure especially with regards to the negative peaks caused by the echo/anti-echo coherence selection with gradients.

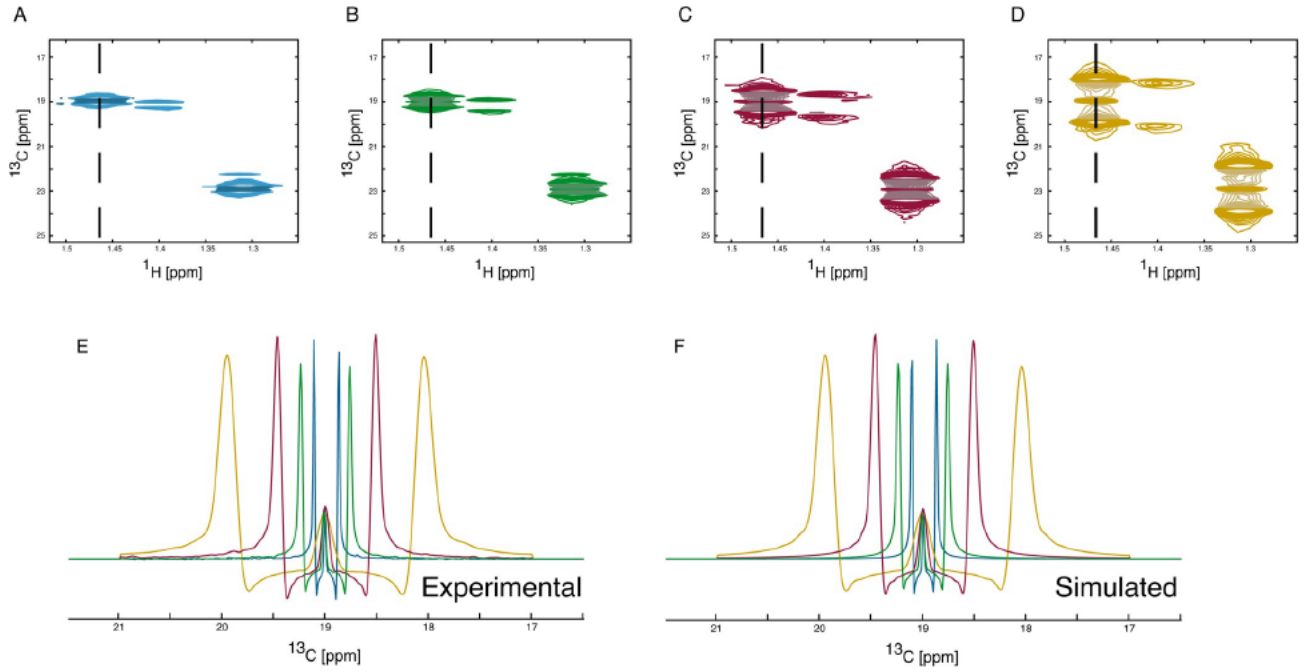

Figure 5. Simulation of J-coupling splitting enhanced spectra. ^{1}H,^{13}C HSQC spectra showing the C(3) of alanine are shown (**A**, **B**, **C** and **D**). The enhancement of J-coupling in the ^{1}H,^{13}C-HSQC spectra leads to increased separation of coupled peaks and allows the collection of data with reduced numbers of increments in the ^{13}C dimension resulting in shorter acquisition times. The number of points collected in the ^{13}C dimension can be reduced to match the increase in J-coupling enhancement as the loss of resolution will be counteracted by the increase in separation of the coupled peaks. Spectra with no enhancement (**A**), two-fold enhancement (**B**), four-fold enhancement (**C**) and eight-fold enhancement (**D**) were collected. The overlay of the differently enhanced spectra clearly shows the effect of the enhancement (**E**). The enhancement can be tailored to meet the need in order to maximise separation without significantly increasing signal overlap whilst achieving the maximum reduction in acquisition time possible. The splitting enhancement can easily be included in the simulation parameters (**F**) resulting in no adverse effects on the simulated spectra. The simulation gives the following incorporation percentages. From the no J-coupling splitting enhancement spectrum 12.1% / 87.9% for [3-^{13}C] / [2,3-^{13}C], from the two-fold J-coupling splitting enhancement 12.0% / 88.0% for [3-^{13}C] / [2,3-^{13}C], from the four-fold J-coupling splitting enhancement 12.0% / 88.0% for [3-^{13}C] / [2,3-^{13}C] and from the eight-fold J-coupling splitting enhancement 12.1% / 87.9% for [3-^{13}C] / [2,3-^{13}C].

Table 1. Comparison of spectroscopic techniques. The acquisition time and signal to noise ratios of various experiments used in this study. A good signal to noise ratio can be achieved using the spectral filtering allowing rapid measurement of quantitative spectra. The signal to noise benefit of the HSQC over the 1D ^{13}C acquisition is clearly seen. The effect of increasing the J-coupling splitting enhancement whilst simultaneously reducing the number of increments on the acquisition time of ^{1}H,^{13}C-HSQC spectra is also shown.

Experiment	Acquisition time [mins]	Signal to noise ratio (CH_3 of lactate)	Transients	TD	SW [ppm]	Splitting enhancement
^{1}H 1D (all ^{1}H)	2	327.31	8	16384	12	1
^{1}H 1D (^{13}C bound ^{1}H)	2	66.13	8	16384	12	1
^{1}H,^{13}C-HSQC	233	823.86	2	1024/8192	12/160	1
^{1}H,^{13}C-HSQC	110	770.98	2	1024/4096	12/160	2
^{1}H,^{13}C-HSQC	51	426.41	2	1024/2048	12/160	4
^{1}H,^{13}C-HSQC	24	283.38	2	1024/1024	12/160	8
^{13}C 1D (30v excitation)	1414	59.95	16384	65538	239	1

All NMR spectra in this article were processed within the MetaboLab software package (version 2018. 07182055; http://metabolab.uk)[22].

NMR methodology. Both aforementioned methods can be used to detect ^{15}N labelling in metabolites, which alongside ^{13}C isotope incorporation can provide additional much-needed information

on the overlapping activity of multiple metabolic pathways. 2D spectroscopic filters are an extension of the 1D concept and as such can be used to simplify increasingly complex 2D spectra by selectively observing a subset of metabolites in which nuclei of interest have been incorporated. For example, the analysis of the ^{13}C nuclei that are adjacent to ^{15}N nuclei using 2D spectra permits a simplified unequivocal description of the nature in which two metabolic pathways converge.

Similar to the 1D method, the acquisition of two spectra is required in order to enable a quantitative analysis of the amount of ^{15}N labelling in the presence of ^{13}C labelling within the metabolite. If spectral simplification is the goal, a single spectrum is sufficient[16]. The pulse sequence (Figure 6) is a gradient selected $^{1}H,^{13}C$-HSQC spectrum with the spectral filter added once the ^{1}H magnetisation has been transferred to the ^{13}C nucleus. The spectrum collected with the ^{14}N spectral filter (Panel C-2,

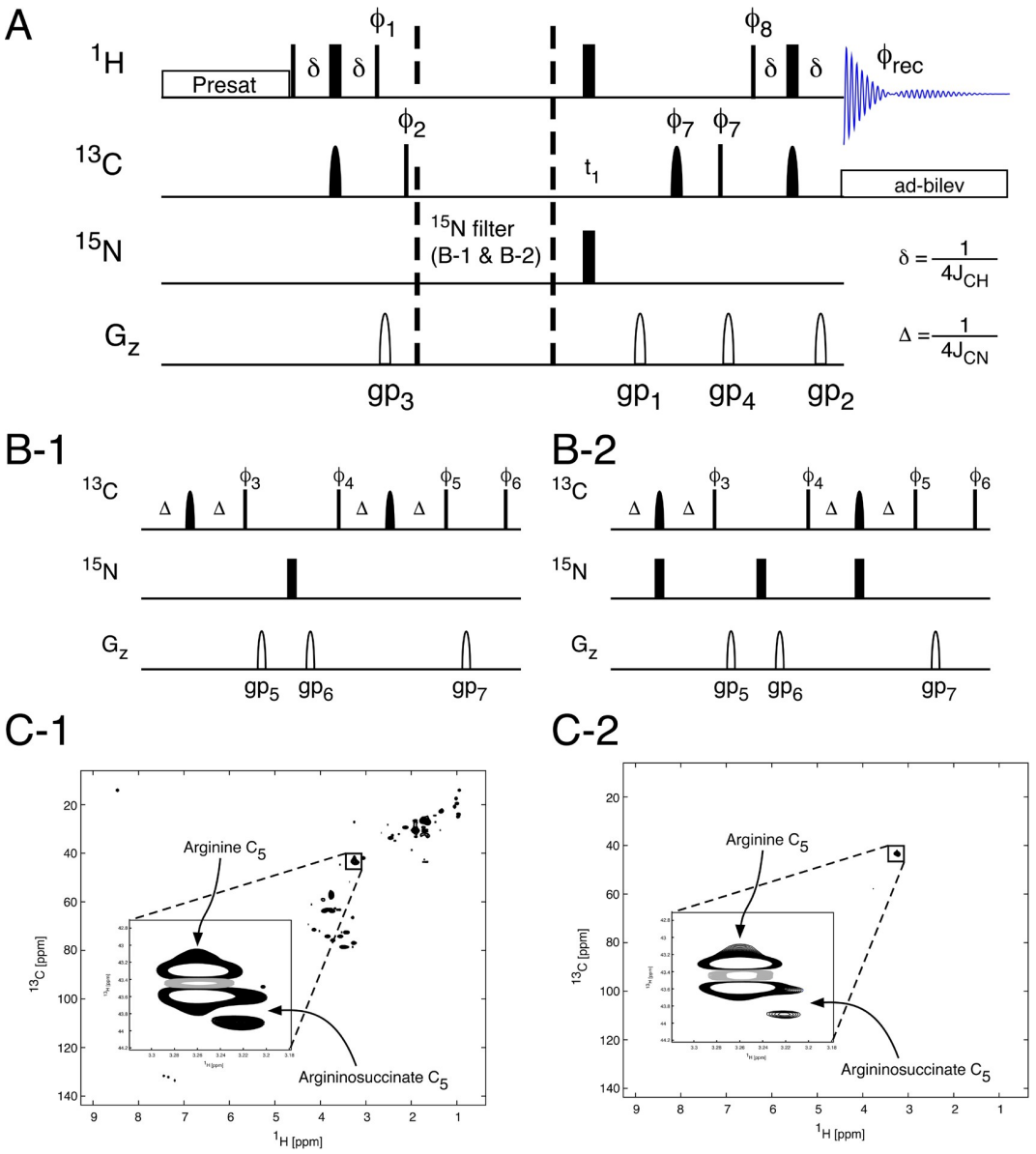

Figure 6. Filtered HSQC spectroscopy. The application of a ^{15}N filtering block in the $^{1}H,^{13}C$-HSQC pulse sequence (**A**) allows the observation of $^{1}H,^{13}C$ groups directly coupled to ^{15}N nuclei. In the sequence in panel **B-1** no filtering will be observed and the resulting spectrum (**C-1**) will contain all ^{1}H, ^{13}C groups adjacent to either ^{14}N or ^{15}N nuclei. The use of a ^{15}N filter (**B-2**) will result in only those ^{1}H, ^{13}C groups adjacent to a ^{15}N nuclei being observed in the resulting ^{1}H, ^{13}C HSQC spectrum (**C2**). $^{1}H,^{13}C$ J-coupling is suppressed during acquisition using adiabatic bilevel decoupling (ad-bilev)[21]. The pulse phases are: Φ_1 = y; Φ_2 = x, -x; Φ_3 = x for the no filter sequence (panel **B-1**) and y for the ^{15}N filtered sequence (panel **B-2**); Φ_4 = y, –y for the no filter sequence and y, y for the ^{15}N filtered sequence; Φ_5 = y, -y for the no filter sequence x, -x for the ^{15}N filtered sequence; Φ_6 = x, x, -x, -x; Φ_7 = x, x, x, x, -x, -x, -x, -x; Φ_8 = x, x, x, x, y, y, y, y; Φ_{rec} = x, -x, -x, x, y, -y, -y, y.

Figure 6) contains only two visible NMR signals, corresponding to arginine and arginosuccinate, clearly showing how the filter can simplify complex spectra for easier analysis.

While 2D spectral filters serve a purpose, their quantitative usage is limited by the variability of the $^{1}J_{CN}$ constant. J-coupling splitting enhancement on the other hand can be easily extended to include ^{13}C-^{15}N J- coupling splitting enhancement. Indeed, the addition of a single ^{15}N Π–pulse simultaneous with the central ^{13}C Π–pulse (Figure 3) is sufficient to enhance the apparent ^{13}C-^{15}N J-coupling splitting in ^{1}H,^{13}C-HSQC spectra, an example of which is given in Figure 7. The 2D signals for the J_{CN} splitting scaled spectrum are shown in panel A. Panels B and C show traces of the ^{13}C multiplets for carbon atoms 2 and 3 of alanine. While the J_{CC} splittings are enhanced by a factor of 4 in both spectra, the apparent J_{CN} splittings are unchanged in the spectrum in panel B, whereas they are enhanced by a factor of 4 in the spectra in panel C. Because the $^{2}J_{CN}$ coupling between C(3) and N is negligible, both traces for C(3) overlap perfectly. C(2) on the other hand experiences a $^{1}J_{CN}$ coupling,

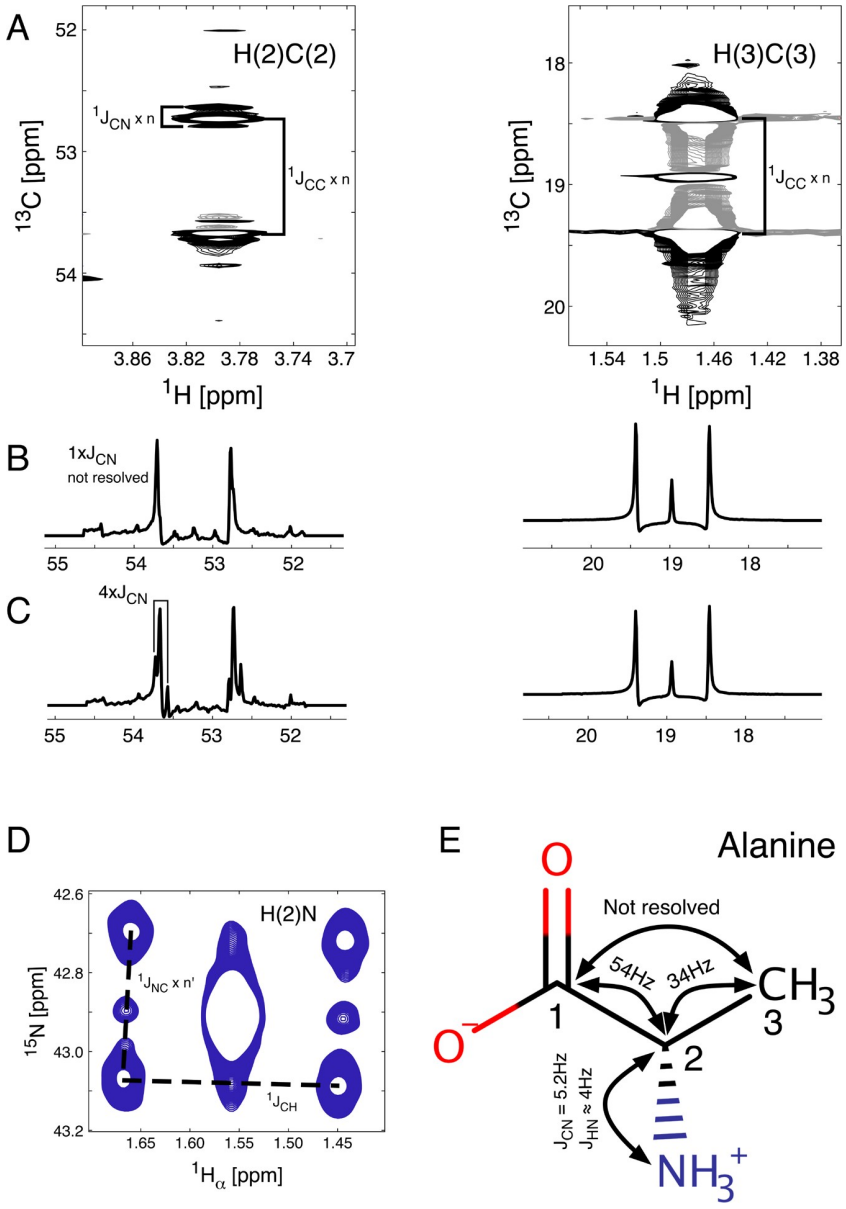

Figure 7. Splitting due to ^{15}N and ^{13}C incorporation. Regions of the ^{1}H,^{13}C-HSQC spectrum containing signals from alanine (panels **A** & **B**). The ^{13}C traces of the alanine signals are shown with either no J_{CN}-coupling splitting enhancement (**B**) or four-fold J_{CN}-coupling splitting enhancement (**C**). The signals are split by either $^{1}J_{CC}$ or $^{1}J_{CN}$ coupling contributions. The long range ^{1}H,^{15}N-HSQC spectrum (**D**) is composed of unlabelled alanine (central peak) and $^{13}C/^{15}N$ labelled alanine (6 outer signals, 4 split by $^{2}J_{HC}$ and $^{1}J_{NC}$ couplings and 2 only split by $^{1}J_{HC}$ (values for the coupling constants are shown in panel **E**)).

which is too small to be resolved when the J_{CN} splitting is not enhanced and is only detectable in panel C.

J_{CN} coupling, as any J-coupling, works in two directions, therefore a similar approach can be followed from the opposite direction. While amine groups of small molecules are notoriously difficult to observe due to chemical exchange of amine protons with solvent molecules, a long-range HSQC spectrum can be acquired. In such a spectrum proton magnetisation is transferred from H_A (the proton bound to C(2)) via the $^2J_{HN}$ coupling. The splitting due to the J_{NC} coupling then can be enhanced to show the appearance of ^{13}C labelling in molecules which contain ^{15}N next to those labelled carbon nuclei. As in this case, where the ^{13}C nucleus is also bound to the proton determining the chemical shift on the horizontal axis, that same proton signal will be split by the $^1J_{CH}$ coupling constant. The result in this case is therefore a signal split into 7 2D components (Figure 7, panel D), demonstrating that alanine was either recycled from unlabelled alanine which was incorporated into proteins, synthesised *de-novo* from [U-^{13}C] glucose and ^{15}N labelled glutamate which originated from [U-^{13}C, U-^{15}N] glutamine that was added to the growth medium in addition to the [U-^{13}C] glucose or just synthesised *de novo* from [U-^{13}C] glucose with an unlabelled amino group trans- ferred to form alanine. In conjunction with MS data, this complementarity between the 2D-^1H,^{13}C- and the 2D- ^1H,^{15}N-HSQC spectra enables a model-free metabolism analysis using multiple nutrients as tracer sources in a single sample.

Discussion

Changes in metabolism are increasingly being recognised as central to the pathogenesis of a number of different diseases. Although metabolomic studies have helped determine aspects of disease phenotype, tracing the changing use of specific metabolic pathways using stable isotope-enriched nutrients provides higher resolution information on altered metabolic pathway activity that may lead to the identification of specific novel therapeutic targets. Over the last few years, development of magnet and probe technology, including innovative ultra-sensitive microprobes, has enabled the study of systems that were not previously amenable to NMR spectroscopy. Parallel advancement in the methods used to acquire and analyse data from samples will increase the amount of information we can gain from such samples.

In this paper, we describe how spectral filters and J-splitting enhancement can be used in tracer-based metabolism studies. These techniques overcome some of the major hurdles in the use of NMR spectroscopy. A challenge in the analysis of NMR HSQC spectroscopy data has been the need for an additional "unlabelled" sample in order to determine absolute per carbon ^{13}C incorporation percentages. However, samples cannot be assumed to be biologically identical, thus making analyses problematic due to the inability to determine accurate ^{13}C isotope incorporation values. Systems that demonstrate greater inter-sample variation, such as *in vivo* tracer studies, are even more prone to these analytical issues. The use of spectral filters negates the requirement for two samples and instead a single sample can be used to determine absolute percentage ^{13}C incorporation and thus allow the scaling of multiplets.

The 2D HSQC spectrum is a powerful tool in the study of metabolism as it takes advantage of the increased sensitivity of the ^1H nucleus over ^{13}C and using the splitting due to J-coupling in the ^{13}C dimension allows the indirect visualisation of the ^{13}C incorporation into quaternary carbons. However, long acquisitions times, even when using the latest NUS techniques, limits the number of samples that can be acquired. Reducing the experimental time makes the use of HSQC spectra a much more attractive method in the study of tracer-based metabolism. The use of echo/anti-echo for quadrature detection ensures efficient elimination of unwanted artefacts, whilst using only two scans per increment in the indirect dimension. The changes observed in line shape due to the quadrature detection are predictable and can be easily incorporated into line fitting analysis. As described elsewhere[19], the simulation procedure assumes weak coupling between the different carbon nuclei. The simulation is implemented as a spin echo before the acquisition of a ^{13}C-FID to allow the evolution of ^{13}C,^{13}C spin coupling prior to the first increment.

The ability to scale the visualised splittings due to J-coupling allows HSQC spectra to be acquired in time equivalent to that of a 1D ^1H spectrum, but the HSQC spectrum contains significantly more information. The reduced time required to acquire HSQC spectra means that it is feasible to apply 2D methods to *in vivo* tracer-based metabolism studies, as well as allowing the use of greater sensitivity of higher field spectrometers while avoiding longer experiment times (Table 1). Expansion of the splitting due to J-coupling can also bring out smaller long-range couplings that were not apparent in a normal HSQC spectrum. Thus, the scaling of splittings can either be used to decrease acquisition imes by allowing data collection at lower resolution or to bring out smaller couplings not previously visible. These small couplings include the $^1J_{CN}$ couplings that are found in many metabolites after the addition of metabolites labelled ^{15}N in conjugation with ^{13}C. This increases the information available and allows more in-depth analysis of complex metabolic pathways. In the example shown (Figure 6), the cells used for this experiment were deficient in the expression of fumarate hydratase[16] and therefore contained high fumarate levels. One hypothesis was that argininosuccinate is synthesised from fumarate and arginine to minimise intracellular fumarate. In order to ascertain the signal assignment, we used [U-^{13}C, U-^{15}N] arginine and were able to show that ^{15}N labelled argininosuccinate was being produced in the cells containing the knock out, but not in wild-type cells[16]. This shows the utility of using multiple labelled nutrients to answer fundamental questions in metabolism.

In summary, the spectroscopic tools presented here open up new avenues for tracer-based metabolism studies. Scaling of signal splittings due to J-coupling leads to faster data collection of samples supplemented with nutrients enriched in stable isotopes, such as ^{13}C and ^{15}N. This enables profiling of metabolic pathways and can also be used to enhance sensitivity beyond current technical developments whilst maintaining reasonable data acquisition times. Ultimately, the use of 1D spectral filters

as well as the fast acquisition of HSQC spectra leads to the possibility of tracing metabolism in real-time. In addition, simultaneous tracing with multiple nutrients will lead to unprecedented insight into the interplay of converging and intersecting metabolic pathways, both *in vitro* and *in vivo*[37].

Data availability

All experimental data for this article is available at: http://doi.org/10.17605/OSF.IO/EQHN3[38].

Experimental NMR datasets for HS-TrAM: ^{12}C filtered (subdirectory 2) ^{1}H spectrum, both of which are ^{13}C decoupled during acquisition. Subdirectories 3 and 4 contain an unfiltered (3) and a ^{12}C filtered (4) spectrum, both without ^{13}C decoupling during acquisition. Subdirectories 5 and 6 contain POCE spectra, either with ^{12}C- and ^{13}C-bound ^{1}H with same phase (subdirectory 5), or with opposite phase (subdirectory 6), both without ^{13}C decoupling during acquisition. Subdirectory 7 contains a 30 degree excitation 1D ^{13}C spectrum, acquired using a TXO Cryoprobe. The file jEnhanced_13C_HSQC.zip contains the ^{1}H, ^{13}C-HSQC spectra with different J-coupling splitting enhancements.

The file 13C_HSQC_14N_filter_and_15N_HSQC.zip contains an unfiltered (subdirectory 1) and a ^{14}N filtered (subdirectory 2) ^{1}H,^{13}C-HSQC spectrum. The file jEnhanced_13C_15N_HSQC.zip contains the following spectra: 4 x ^{13}C,^{13}C splitting enhancement ^{1}H,^{13}C-HSQC in subdirectory 1, 4 x ^{13}C,^{13}C splitting enhancement and 4 x ^{13}C,^{15}N splitting enhancement ^{1}H,^{13}C-HSQC in subdirectory 2 and 4 x ^{13}C,^{15}N splitting enhancement ^{1}H,^{15}N-HSQC in subdirectory 3.

Grant information

This work was supported by the Wellcome Trust [099185] and through an Institutional Strategic Support Award given to the University of Birmingham; the National Institute for Health Research [13-0053]; Help Harry Help Others [HelpCU09]; UHB Charitable Funds [17-3-846] and the metabolic tracer analysis core (MTAC) at the University of Birmingham.

The funders had no role in study design, data collection and analysis, decision to publish, or preparation of the manuscript.

Acknowledgements

We thank HWB-NMR at the University of Birmingham for providing open access to their Wellcome Trust-funded spectrometers. Organ Recovery Systems donated perfusion equipment.

References

1. Frezza C, Zheng L, Folger O, *et al.*: **Haem oxygenase is synthetically lethal with the tumour suppressor fumarate hydratase.** *Nature.* 2011; **477**(7363): 225–228.
PubMed Abstract | Publisher Full Text

2. Walther JL, Metallo CM, Zhang J, *et al.*: **Optimization of ^{13}C isotopic tracers for metabolic flux analysis in mammalian cells.** *Metab Eng.* 2012; **14**(2): 162–171.
PubMed Abstract | Publisher Full Text | Free Full Text

3. Hiller K, Metallo CM: **Profiling metabolic networks to study cancer metabolism.** *Curr Opin Biotechnol.* 2013; **24**(1): 60–68.
PubMed Abstract | Publisher Full Text

4. Gravel SP, Andrzejewski S, Avizonis D, *et al.*: **Stable isotope tracer analysis in isolated mitochondria from mammalian systems.** *Metabolites.* 2014; **4**(2): 166–183.
PubMed Abstract | Publisher Full Text | Free Full Text

5. Huang X, Chen YJ, Cho K, *et al.*: **X^{13}CMS global tracking of isotopic labels in untargeted metabolomics.** *Anal Chem.* 2014; **86**(3): 1632–1639.
PubMed Abstract | Publisher Full Text | Free Full Text

6. Chouchani ET, Pell VR, Gaude E, *et al.*: **Ischaemic accumulation of succinate controls reperfusion injury through mitochondrial ROS.** *Nature.* 2014; **515**(7527): 431–435.
PubMed Abstract | Publisher Full Text | Free Full Text

7. Buescher JM, Antoniewicz MR, Boros LG, *et al.*: **A roadmap for interpreting ^{13}C metabolite labeling patterns from cells.** *Curr Opin Biotechnol.* 2015; **34**: 189–201.
PubMed Abstract | Publisher Full Text | Free Full Text

8. Mackay GM, Zheng L, van den Broek NJ, *et al.*: **Analysis of Cell Metabolism Using LC-MS and Isotope Tracers.** *Methods Enzymol.* Elsevier, 2015; **561**: 171–196.
PubMed Abstract | Publisher Full Text

9. Jiang L, Shestov AA, Swain P, *et al.*: **Reductive carboxylation supports redox homeostasis during anchorage-independent growth.** *Nature.* 2016; **532**(7598): 255–258.
PubMed Abstract | Publisher Full Text | Free Full Text

10. Quek LE, Liu M, Joshi S, *et al.*: **Fast exchange fluxes around the pyruvate node a leaky cell model to explain the gain and loss of unlabelled and labelled metabolites in a tracer experiment.** *Cancer Metab.* 2016; **4**: 13.
PubMed Abstract | Publisher Full Text | Free Full Text

11. Zhang H, Badur MG, Divakaruni AS, *et al.*: **Distinct Metabolic States Can Support Self-Renewal and Lipogenesis in Human Pluripotent Stem Cells under Different Culture Conditions.** *Cell Rep.* 2016; **16**(6): 1536–1547.
PubMed Abstract | Publisher Full Text | Free Full Text

12. Sauer U: **Metabolic networks in motion ^{13}C-based flux analysis.** *Mol Syst Biol.* 2006; **2**(1): 62.
PubMed Abstract | Publisher Full Text | Free Full Text

13. Lane AN, Fan TW, Higashi RM: **Isotopomer-based metabolomic analysis by NMR and mass spectrometry.** *Methods Cell Biol.* 2008; **84**: 541–588.
PubMed Abstract | Publisher Full Text

14. Lane AN, Fan TW, Bousamra M 2nd, *et al.*: **Stable isotope-resolved metabolomics (SIRM) in cancer research with clinical application to nonsmall cell lung cancer.** *OMICS.* 2011; **15**(3): 173–182.
PubMed Abstract | Publisher Full Text | Free Full Text

15. Yang Y, Lane AN, Ricketts CJ, *et al.*: **Metabolic reprogramming for producing energy and reducing power in fumarate hydratase null cells from hereditary leiomyomatosis renal cell carcinoma.** *PLoS One.* 2013; **8**(8): e72179.
PubMed Abstract | Publisher Full Text | Free Full Text

16. Adam J, Yang M, Bauerschmidt C, *et al.*: **A role for cytosolic fumarate hydratase in urea cycle metabolism and renal neoplasia.** *Cell Rep.* 2013; **3**(5): 1440–1448.
PubMed Abstract | Publisher Full Text | Free Full Text

17. Lussey-Lepoutre C, Hollinshead KE, Ludwig C, *et al.*: **Loss of succinate dehydrogenase activity results in dependency on pyruvate carboxylation for cellular anabolism.** *Nat Commun.* 2015; **6**: 8784.
PubMed Abstract | Publisher Full Text | Free Full Text

18. Nath J, Smith T, Hollis A, *et al.*: **^{13}C glucose labelling studies using 2D NMR are a useful tool for determining ex vivo whole organ metabolism during hypothermic machine perfusion of kidneys.** *Transpl Res.* 2016; **5**: 7.
PubMed Abstract | Publisher Full Text | Free Full Text

19. Chong M, Jayaraman A, Marin S, *et al.*: **Combined Analysis of NMR and MS Spectra (CANMS).** *Angew Chem Int Ed Engl.* 2017; **56**(15): 4140–4144.
PubMed Abstract | Publisher Full Text

20. Banke NH, Lewandowski ED: **Impaired cytosolic NADH shuttling and elevated UCP3 contribute to inefficient citric acid cycle flux support of postischemic cardiac work in diabetic hearts.** *J Mol Cell Cardiol.* 2015; **79**: 13–20.
PubMed Abstract | Publisher Full Text | Free Full Text

21. Kupce Ê, Freeman R, Wider G, *et al.*: **Suppression of Cycling Sidebands Using Bi-level Adiabatic Decoupling.** *J Magn Reson A.* 1996; **122**: 81–84.
Reference Source

22. Ludwig C, Günther UL: **MetaboLab--advanced NMR data processing and analysis for metabolomics.** *BMC Bioinformatics.* 2011; **12**: 366.
PubMed Abstract | Publisher Full Text | Free Full Text

23. Howe PW, Ament Z, Knowles K, *et al.*: **Combined use of filtered and edited ^{1}H NMR spectroscopy to detect ^{13}C-enriched compounds in complex mixtures.** *NMR Biomed.* 2012; **25**(11): 1217–1223.
PubMed Abstract | Publisher Full Text

24. Garbow JR, Weitekamp DP, Pines A: **Bilinear rotation decoupling of homonuclear scalar interactions.** *Chem Phys Lett.* 1982; **93**(5): 504–509.
Publisher Full Text

25. Wimperis S, Freeman R: **An excitation sequence which discriminates between direct and long-range CH coupling.** *J Magn Reson 1969.* 1984; **58**(2): 348–353.
Publisher Full Text

26. Uhrin D, Liptaj T, Kover KE: **Modified BIRD Pulses and Design of Heteronuclear Pulse Sequences.** *J Magn Reson A.* 1993; **101**(1): 41–46.
Publisher Full Text

27. Briand J, Sørensen OW: **Simultaneous and independent rotations with arbitrary flip angles and phases for I, ISalpha, and ISbeta spin systems.** *J Magn Reson.* 1998; **135**(1): 44–49.
PubMed Abstract | Publisher Full Text

28. Henry PG, Marjanska M, Walls JD, *et al.*: **Proton-observed carbon-edited NMR spectroscopy in strongly coupled second-order spin systems.** *Magn Reson Med.* 2006; **55**(2): 250–257.
PubMed Abstract | Publisher Full Text

29. Kazimierczuk K, Orekhov VY: **Accelerated NMR spectroscopy by using compressed sensing.** *Angew Chem Int Ed.* 2011; **50**(24): 5556–5559.
PubMed Abstract | Publisher Full Text

30. Delaglio F, Grzesiek S, Vuister GW, *et al.*: **NMRPipe a multidimensional spectral processing system based on UNIX pipes.** *J Biomol NMR.* 1995; **6**(3): 277–93.
PubMed Abstract | Publisher Full Text

31. Willker W, Flögel U, Leibfritz D, *et al.*: **Ultra-high-resolved HSQC spectra of multiple- ^{13}C-labeled biofluids.** *J Magn Reson.* 1997; **125**(1): 216–219.
PubMed Abstract | Publisher Full Text

32. Furihata K, Tashiro M: **BASHD-J-resolved-HMBC, an efficient method for measuring proton-proton and heteronuclear long-range coupling constants.** *Magn Reson Chem.* 2014; **52**(1–2): 27–31.
PubMed Abstract | Publisher Full Text

33. Kazimierczuk K, Zawadzka A, Koźmiński W: **Optimization of random time domain sampling in multidimensional NMR.** *J Magn Reson.* 2008; **192**(1): 123–30.
PubMed Abstract | Publisher Full Text

34. Macura S: **Accelerated multidimensional NMR data acquisition by varying the pulse sequence repetition time.** *J Am Chem Soc.* 2009; **131**(28): 9606–9607.
PubMed Abstract | Publisher Full Text

35. Schulze-Sünninghausen D, Becker J, Koos MRM, *et al.*: **Improvements, extensions, and practical aspects of rapid ASAP-HSQC and ALSOFAST-HSQC pulse sequences for studying small molecules at natural abundance.** *J Magn Reson.* 2017; **281**: 151–161.
PubMed Abstract | Publisher Full Text

36. Aschauer L, Gruber LN, Pfaller W, *et al.*: **Delineation of the key aspects in the regulation of epithelial monolayer formation.** *Mol Cell Biol.* 2013; **33**(13): 2535–2550.
PubMed Abstract | Publisher Full Text | Free Full Text

37. Nilsson R, Jain M: **Simultaneous tracing of carbon and nitrogen isotopes in human cells.** *Mol Biosyst.* 2016; **12**(6): 1929–1937.
PubMed Abstract | Publisher Full Text | Free Full Text

38. Ludwig C: **HS-TrAM.** 2017.
http //www.doi.org/10.17605/OSF.IO/EQHN3

11.2.1.1 Appendix 2: Discussion on the glomerular filtration of HES (personal communication

included with permission

From: Rutger Ploeg [redacted] >
Date: Friday, 2 September 2016 at 11:26
To: Thomas Brendan Smith <[redacted]
Subject: Re: degrees of low MW pentafraction entry into the proximal tubule during Hypothermic Machine perfusion- your thoughts?

Dear Thomas

Interesting question. The HES used in UW, either the static cold storage K-Lactobionate or the Na-Gluconate machine perfusion solution, concerns as you say a pentafraction. This ought to be a dialysed fraction of HES with a molecular weight of around 250.000 Dalton. This fraction was used taking out too big molecules of 500.000 and over as they may cause injury, but also remove the smaller components below 100.000 as too many of those could induce a rebound effect with oedema (as you see with albumen).The idea is that HES stays in the vasculature to create the colloid osmotic pressure – also upholding the perfusability of the vessels. For reduction of oedema in the interstitium and cell, the anion (gluconate) and saccharide was added as 'impermeants'.
Of the top of my head I do not know exactly whether HES crosses the glom, I would say not … The combined effect of anion, saccharide and HES results in a 20% with reduction during preservation with a regain of weight at time of reperfusion.
Early experiments with renal tubules exposed to prolonged periods of cold ischaemia demonstrated that the combination of anion and saccharide (e.g. lactobionate and raffinose or gluconate and mannitol) significantly reduced oedema when compared
to Collins' components or citrate and glucose as in HOC Marshalls. You should come and visit our group, giving a talk if you want.

Hope this helps.

Rutger

Rutger J. Ploeg, MD PhD FRCS
Professor of Transplant Biology | Consultant Transplant Surgeon
Director of Clinical and Translational Research | Oxford Transplant Centre
Nuffield Department of Surgical Sciences | University of Oxford
Churchill Hospital | Oxford OX3 7LE | United Kingdom
EA: Susan Louineau | T: +44 (0)1865 226100 | E: susan.louineau@nds.ox.ac.uk

---

From: Thomas Brendan Smith <[redacted]>
Date: Friday, 2 September 2016 at 10:33
To: Rutger Ploeg <[redacted]>
Subject: Degrees of low MW pentafraction entry into the proximal tubule during Hypothermic Machine perfusion- your thoughts?

Good morning Professor Ploeg,

I am currently researching proximal tubule metabolism during cold storage in UW MPS. I was hoping to pick your brains about whether or not you think low molecular weight molecules of Pentastarch/Pentafraction do cross the glomerulus during HMP? Obviously, the high mean molecular weight would intuitively limit entry into the proximal tubule, I am interested discerning the effect of variable low molecular weight fractions within bags of UW MPS.

Any thoughts would be most appreciated!
Tom

[BOS452] THE EFFECTS OF GLUTATHIONE SUPPLEMENTATION ON KIDNEYS UNDERGOING HYPOTHERMIC MACHINE PERFUSION (FR) (NFR)

Charlotte Turnbull [Birmingham,UNITED KINGDOM][1], Willam Ries [UNITED KINGDOM][1], Kamlesh Patel [UNITED KINGDOM][2], Tom Smith [UNITED KINGDOM][3], Andrew Ready [UNITED KINGDOM][2], Jay Nath [UNITED KINGDOM][2], Christian Ludwig [UNITED KINGDOM][3]

University Of Birmingham[1], Queen Elizabeth Hospital, Birmingham[2], Institute Of Metabolism And Systems Research, University Of Birmingham[3]

Background

Reduced glutathione is a constituent of perfusion fluids commonly used for hypothermic machine perfusion (HMP) of kidneys prior to transplantation (e.g. KPS-1). Glutathione acts to reduce damage to tissue by scavenging free radicals produced during ischaemia. Previous research by our unit suggests reduced glutathione levels are depleted quickly during HMP and are almost undetectable after 12 hours.

The aim of this study was to investigate the effect of supplemental reduced glutathione on perfusate metabolite concentrations over 18 hours of hypothermic machine perfusion.

Methods

This study utilised a paired study design, using porcine kidneys (n=7) in a donation after cardiac death (DCD) model of renal transplantation. Machine perfusion fluid in the experimental arm was supplemented with 7mM additional reduced glutathione (i.e. 10mM total vs 3mM).

The metabolic profile of kidneys perfused with standard (S) vs reduced glutathione-supplemented (GS) perfusion fluid was characterised using one-dimensional nuclear magnetic resonance spectroscopy (1D-^{1}H NMR).

Results

As expected, the reduced glutathione concentration in the perfusion fluid was higher at all timepoints in the GS group, compared with the controls ($p<0.01$), with easily detectable levels even after 18hrs of HMP (mean 0.24mM). In addition, fifteen metabolites demonstrated significant differences between the two arms of the experiment. Citrate, glutamate and glycine concentrations were higher in the GS group ($p<0.05$), whereas lactate concentrations were higher in the S group ($p<0.05$).

Conclusion

The protective antioxidant glutathione was present in the perfusion fluid even following periods of prolonged HMP when supplemented initially. Furthermore, the perfusate of kidneys perfused with GS fluid displayed a different metabolic profile to control kidneys. This indicates that the presence of more reduced glutathione in the perfusion solution modifies metabolic pathways in the kidney during HMP.

11.2.3 Appendix 4- Differences in organ characteristics in paired kidneys.

Kidney 1	Kidney 2	Percentage difference	average difference in flow rate (%)	SD
24	23	4.16666667	22.9319292	20.0762029
13	11	15.3846154		
14	7	50		
18	14	22.2222222		
19	19	0		
16	13	18.75		
8	4	50		

Table 4. Different flow rates between pairs of kidneys during initiation of HMP

Kidney 1	Kidney 2	Percentage difference	average difference in weight (%)	SD (%)
217	195	10.1382488	12.0848873	5.79095167
285	252	11.5789474		
234	199	14.957265		
300	246	18		
218	214	1.83486239		
300	252	16		

Table 5. Differences in weight between paired kidneys prior to initiation HMP

11.2.3.1 Appendix 5- links to public domain images used in tiered strategy diagram

Sourced images for tiered strategy model. These are public domain

Patient: https://www.piqsels.com/en/public-domain-photo-zkteb
Pig: https://pixabay.com/illustrations/pig-farm-piglet-animals-cute-pigs-3961588/

1124 Appendix 6 –ShearFAST supplementary data

Supplementary data.

Image J detected angle (°)	ShearFAST detected angle (°)	Difference (°)	Mean Difference (°)
0.87	0.86709	0.00291	0.291± 0.254
1.8	2.172	0.372	
4.52	4.023	0.497	
5.79	5.128	0.662	
6.53	6.142	0.388	
7.04	6.932	0.108	
9.05	9.063	0.013	

Table S1. ShearFAST measurement of rocker angle vs ImageJ analysis determination of rocker angle.

Motion capture (°)	Shear FAST (°)	Difference (°)	Mean Difference (°)
0.424	0.02	0.404	0.544 ± 0.162
2.046	2.648	0.602	
2.23	2.5	0.27	
3.18	3.58	0.4	
3.35	3.786	0.436	
4.08	4.644	0.564	
4.396	5.034	0.638	
6.15	6.56782	0.41782	
7.2	7.73382	0.53382	
7.56	8.34682	0.78682	
9.19	9.93	0.74	
9.68	10.421	0.741	

Table S2. Comparisons between in rocker pitch detection measurements between ShearFAST and the motion capture analysis.

11.2.4.1 Appendix 8- Mass isotopic distribution in RPTEC/TERT1

Metabolite	Mean MID	Standard deviation	Metabolite	Mean MID	Standard deviation
Pyruvate			Succinate		
174 (M0)	0.3977	0.0660	289 (M0)	0.8956	0.0153
175 (M1)	0.0298	0.0009	290 (M1)	0.0525	0.0051
176 (M2)	0.0460	0.0084	291 (M2)	0.0444	0.0074
177 (M3)	0.5368	0.0535	292 (M3)	0.0060	0.0022
Glycine			293 (M4)	0.0032	0.0013
246 (M0)	0.6632	0.0019	Fumarate		
247 (M1)	0.0711	0.0016	287 (M0)	0.7729	0.0227
248 (M2)	0.2665	0.0026	288 (M1)	0.0900	0.0065
Citrate-			289 (M2)	0.0781	0.0087
591 (M0)	0.5589	0.0197	290 (M3)	0.0570	0.0071
592 (M1)	0.2149	0.0013	291 (M4)	0.0032	0.0009
593 (M2)	0.1212	0.0074	Aspartate		
594 (M3)	0.0756	0.0065	418 (M0)	0.7337	0.0182
595 (M4)	0.0233	0.0032	419 (M1)	0.1051	0.0051
596 (M5)	0.0050	0.0013	420 (M2)	0.0901	0.0063
597 (M6)	0.0014	0.0002	421 (M3)	0.0641	0.0055
Lactate			422 (M4)	0.0043	0.0009
261 (M0)	0.5231	0.0846	Serine		
262 (M1)	0.0196	0.0034	390 (M0)	0.3986	0.0022
263 (M2)	0.0426	0.0066	391 (M1)	0.2458	0.0012
264 (M3)	0.4153	0.0744	392 (M2)	0.1507	0.0007
Alanine			393 (M3)	0.2020	0.0033
260 (M0)	0.4403	0.0065	Glutamate		
261 (M1)	0.0234	0.0000	432 (M0)	0.7314	0.0225
262 (M2)	0.0467	0.0009	433 (M1)	0.1092	0.0066
263 (M3)	0.4914	0.0051	434 (M2)	0.1144	0.0100
Glycerol-3-phosphate			435 (M3)	0.0366	0.0040
571 (M0)	0.7813	0.0209	436 (M4)	0.0063	0.0014
572 (M1)	0.1190	0.0028	437 (M5)	0.0021	0.0006
573 (M2)	0.0101	0.0033			
574 (M3)	0.0816	0.0159			
Malate					
419 (M0)	0.7259	0.0234			
420 (M1)	0.1077	0.0078			
421 (M2)	0.0944	0.0091			
422 (M3)	0.0688	0.0057			

11.2.5 Appendix 9: ^{1}H-NMR spectra from a renal cortex

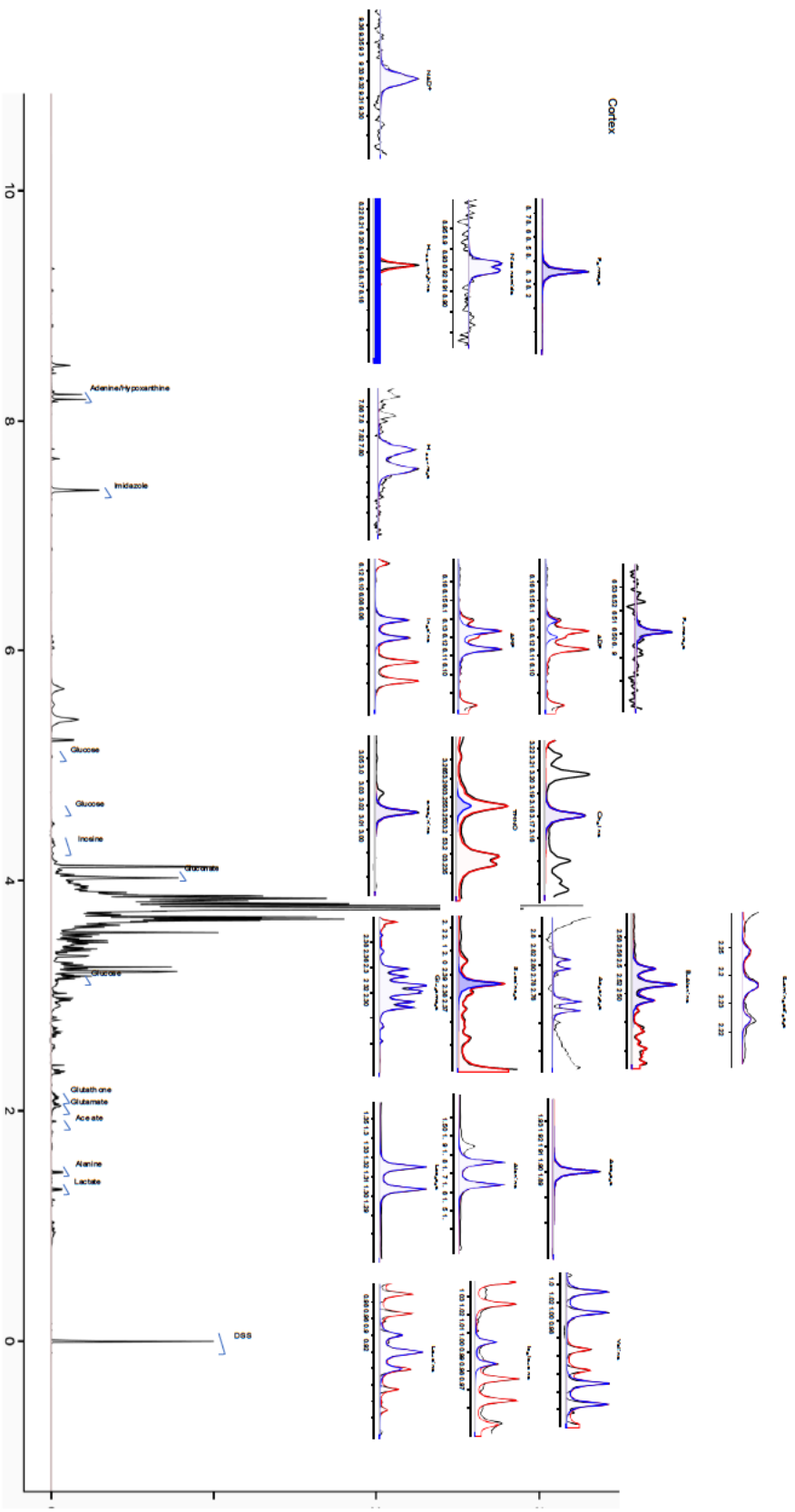

11.2.6 1H-NMR spectra from HMP perfusate

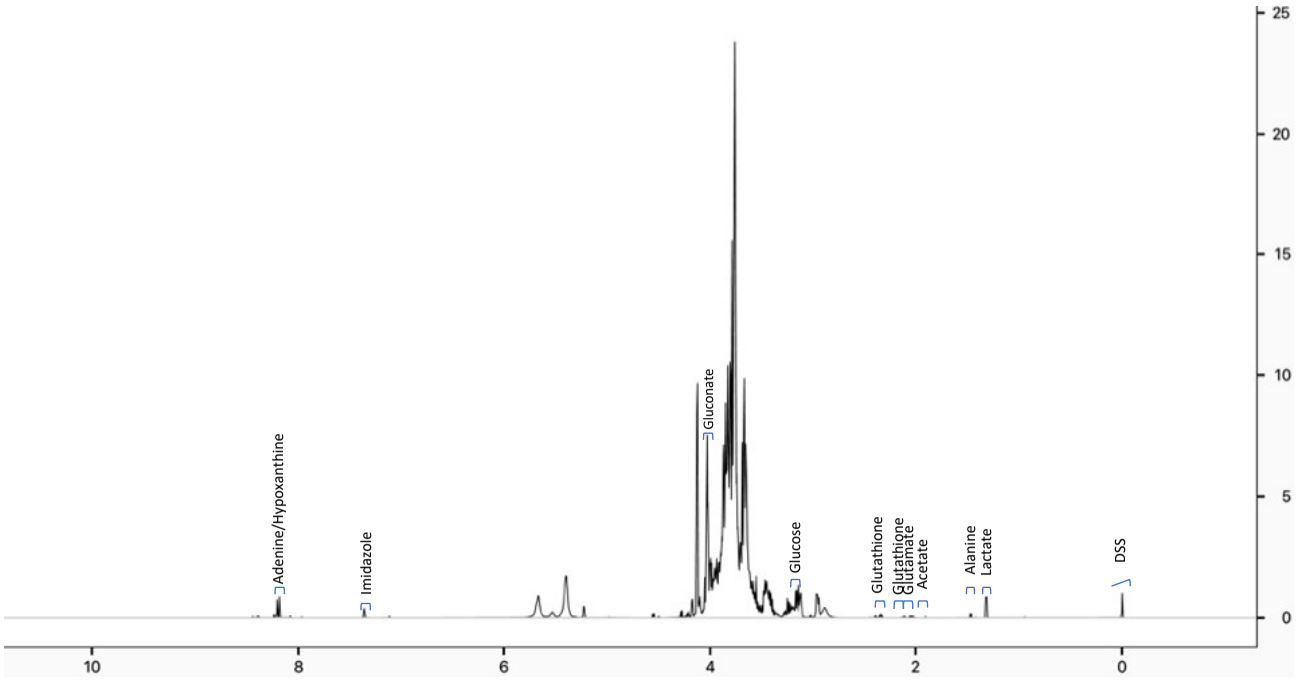

12 References

1. Farsijani NM, Liu Q, Kobayashi H, Davidoff O, Sha F, Fandrey J, et al. Renal epithelium regulates erythropoiesis via HIF-dependent suppression of erythropoietin. J Clin Invest [Internet]. 2016 Apr 1 [cited 2016 Sep 14];126(4):1425–37. Available from: http://www.ncbi.nlm.nih.gov/pubmed/26927670
2. Atherton JC. Regulation of fluid and electrolyte balance by the kidney. Anaesth Intensive Care Med [Internet]. 2006 Jul 1 [cited 2020 Feb 8];7(7):227–33. Available from: https://www.sciencedirect.com/science/article/pii/S1472029906000063
3. Koeppen BM. The kidney and acid-base regulation. Adv Physiol Educ [Internet]. 2009 Dec [cited 2020 Feb 8];33(4):275–81. Available from: https://www.physiology.org/doi/10.1152/advan.00054.2009
4. Webster AC, Nagler E V, Morton RL, Masson P. Chronic Kidney Disease. Lancet [Internet]. 2017 Mar 25 [cited 2019 Nov 17];389(10075):1238–52. Available from: https://www.sciencedirect.com/science/article/pii/S0140673616320645?via%3Dihub
5. Zemaitis MR, Foris LA, Chandra S, Bashir K. Uremia [Internet]. StatPearls. StatPearls Publishing; 2019 [cited 2019 Nov 18]. Available from: http://www.ncbi.nlm.nih.gov/pubmed/28722889
6. Pasala S, Carmody JB. How to use… serum creatinine, cystatin C and GFR. Arch Dis Child - Educ Pract Ed [Internet]. 2017 Feb [cited 2019 Nov 17];102(1):37–43. Available from: http://www.ncbi.nlm.nih.gov/pubmed/27647862
7. Sterner G, Frennby B, Mansson S, Nyman U, Van Westen D, Almén T. Determining 'true' glomerular filtration rate in healthy adults using infusion of inulin and comparing it with values obtained using other clearance techniques or prediction equations. Scand J Urol Nephrol [Internet]. 2008 Jan 9 [cited 2019 Nov 17];42(3):278–85. Available from: http://www.ncbi.nlm.nih.gov/pubmed/17943640
8. Torres VE, Harris PC. Autosomal dominant polycystic kidney disease: the last 3 years. Kidney Int [Internet]. 2009 Jul [cited 2015 Nov 26];76(2):149–68. Available from: http://www.pubmedcentral.nih.gov/articlerender.fcgi?artid=2812475&tool=pmcentrez&rendertype=abstract
9. Low S, Chi LS, Yeoh LY, Liu JJ, Fun S, Su C, et al. Long-term diabetes outcomes in multi-ethnic Asians living in Singapore. Diabetes Res Clin Pract [Internet]. 2015 Oct [cited 2015 Nov 5]; Available from: http://www.sciencedirect.com/science/article/pii/S0168822715004118
10. Rees F, Doherty M, Grainge M, Lanyon P, Davenport G, Zhang W. The burden of co-morbidity in Systemic Lupus Erythematosus in the United Kingdom 1999-2012. Arthritis Care Res (Hoboken) [Internet]. 2015 Oct 16 [cited 2015 Dec 3]; Available from: http://www.ncbi.nlm.nih.gov/pubmed/26473719
11. Plantinga L, Lim SS, Patzer R, McClellan W, Kramer M, Klein M, et al. Incidence of End-Stage Renal Disease among Newly Diagnosed Systemic Lupus Erythematosus Patients: The Georgia Lupus Registry. Arthritis Care Res (Hoboken) [Internet]. 2015 Aug 3 [cited 2015 Dec 3]; Available from: http://www.ncbi.nlm.nih.gov/pubmed/26239749
12. Nasri H, Mubarak M. Extracapillary proliferation in IgA nephropathy; recent findings and new ideas. J Nephropathol [Internet]. 2015 Jan [cited 2015 Dec 3];4(1):1–5. Available from: http://www.pubmedcentral.nih.gov/articlerender.fcgi?artid=4316579&tool=pmcentrez&rendertype=abstract
13. Banaga ASI, Mohammed EB, Siddig RM, Salama DE, Elbashir SB, Khojali MO, et al. Causes of end stage renal failure among haemodialysis patients in Khartoum State/Sudan. BMC Res Notes [Internet]. 2015 Jan 29 [cited 2015 Dec 3];8(1):502. Available from: http://www.biomedcentral.com/1756-0500/8/502
14. Levey AS, Coresh J. Chronic kidney disease. Lancet [Internet]. 2012 Jan 14 [cited 2014 Jul 11];379(9811):165–80. Available from: http://www.sciencedirect.com/science/article/pii/S0140673611601785
15. Murtagh FE, Addington-Hall J, Edmonds P, Donohoe P, Carey I, Jenkins K, et al. Symptoms in

the month before death for stage 5 chronic kidney disease patients managed without dialysis. J Pain Symptom Manage [Internet]. 2010 Sep 1 [cited 2019 Nov 18];40(3):342–52. Available from: http://www.ncbi.nlm.nih.gov/pubmed/20580200
16. Ellis H. The Kolff Artificial Kidney. J Perioper Pract [Internet]. 2007 Aug 10 [cited 2019 Nov 18];17(8):398–398. Available from: http://journals.sagepub.com/doi/10.1177/175045890701700805
17. MISRA M. Basic mechanisms governing solute and fluid transport in hemodialysis. Hemodial Int [Internet]. 2008 Oct [cited 2020 Feb 16];12:S25–8. Available from: http://doi.wiley.com/10.1111/j.1542-4758.2008.00320.x
18. Hoenich NA, Ronco C. Haemodialysis Fluid: Composition and Clinical Importance. Blood Purif [Internet]. 2007 [cited 2019 Nov 18];25(1):62–8. Available from: http://www.ncbi.nlm.nih.gov/pubmed/17170540
19. Mehrotra R, Devuyst O, Davies SJ, Johnson DW. The current state of peritoneal dialysis. Vol. 27, Journal of the American Society of Nephrology. American Society of Nephrology; 2016. p. 3238–52.
20. Takahashi A, Kubota T, Shibahara N, Terasaki J, Kagitani M, Ueda H, et al. The mechanism of hypoglycemia caused by hemodialysis. Clin Nephrol. 2004 Nov;62(5):362–8.
21. Kessler M. Erythropoietin and erytbropoiesis in renal transplantation. Nephrol Dial Transplant [Internet]. 1995 Jan 1 [cited 2019 Nov 18];10(supp6):114–6. Available from: http://www.ncbi.nlm.nih.gov/pubmed/8524479
22. Coronado Daza J, Martí-Carvajal AJ, Ariza García A, Rodelo Ceballos J, Yomayusa González N, Páez-Canro C, et al. Early versus delayed erythropoietin for the anaemia of end-stage kidney disease. Cochrane Database Syst Rev [Internet]. 2015 Dec 16 [cited 2019 Nov 18];(12):CD011122. Available from: http://www.ncbi.nlm.nih.gov/pubmed/26671531
23. O'Connor NR, Dougherty M, Harris PS, Casarett DJ. Survival after dialysis discontinuation and hospice enrollment for ESRD. Clin J Am Soc Nephrol [Internet]. 2013 Dec 6 [cited 2015 Dec 9];8(12):2117–22. Available from: http://cjasn.asnjournals.org/content/8/12/2117.full
24. Mailloux LU, Bellucci AG, Napolitano B, Mossey RT, Wilkes BM, Bluestone PA. Death by withdrawal from dialysis: a 20-year clinical experience. J Am Soc Nephrol [Internet]. 1993 [cited 2019 Nov 18];3(9). Available from: https://jasn.asnjournals.org/content/3/9/1631
25. Bianchi S, Aucella F, De Nicola L, Genovesi S, Paoletti E, Regolisti G. Management of hyperkalemia in patients with kidney disease: a position paper endorsed by the Italian Society of Nephrology. J Nephrol [Internet]. 2019 Aug [cited 2019 Nov 18];32(4):499–516. Available from: http://www.ncbi.nlm.nih.gov/pubmed/31119681
26. Plantinga LC, Fink NE, Levin NW, Jaar BG, Coresh J, Levey AS, et al. Early, Intermediate, and Long-Term Risk Factors for Mortality in Incident Dialysis Patients: The Choices for Healthy Outcomes in Caring for ESRD (CHOICE) Study. Am J Kidney Dis [Internet]. 2007 Jun [cited 2016 Jan 11];49(6):831–40. Available from: http://www.ncbi.nlm.nih.gov/pubmed/17533026
27. Smith C, Da Silva-Gane M, Chandna S, Warwicker P, Greenwood R, Farrington K. Choosing not to dialyse: evaluation of planned non-dialytic management in a cohort of patients with end-stage renal failure. Nephron Clin Pract [Internet]. 2003 Jan 17 [cited 2015 Nov 12];95(2):c40-6. Available from: http://www.karger.com/Article/FullText/73708
28. Collins AJ, Foley RN, Herzog C, Chavers BM, Gilbertson D, Ishani A, et al. Excerpts From the US Renal Data System 2009 Annual Data Report. Am J Kidney Dis [Internet]. 2010 Jan [cited 2019 Nov 18];55(1):A6–7. Available from: https://linkinghub.elsevier.com/retrieve/pii/S0272638609013225
29. Chertow GM, Johansen KL, Lew N, Lazarus JM, Lowrie EG. Vintage, nutritional status, and survival in hemodialysis patients. Kidney Int [Internet]. 2000 Mar [cited 2019 Nov 18];57(3):1176–81. Available from: http://www.ncbi.nlm.nih.gov/pubmed/10720970
30. Mumford L, Parsons J. ANNUAL REPORT ON KIDNEY TRANSPLANTATION REPORT FOR 2017/2018 (1 APRIL 2008 – 31 MARCH 2018) [Internet]. 2018 [cited 2019 Nov 18]. Available from: https://nhsbtdbe.blob.core.windows.net/umbraco-assets-corp/12256/nhsbt-kidney-transplantation-annual-report-2017-2018.pdf
31. Kaballo MA, Canney M, O'Kelly P, Williams Y, O'Seaghdha CM, Conlon PJ. A comparative analysis of survival of patients on dialysis and after kidney transplantation. Clin Kidney J [Internet]. 2018 Jun [cited 2019 Nov 18];11(3):389–93. Available from: http://www.ncbi.nlm.nih.gov/pubmed/29942504

32. Yoo KD, Kim CT, Kim M-H, Noh J, Kim G, Kim H, et al. Superior outcomes of kidney transplantation compared with dialysis: An optimal matched analysis of a national population-based cohort study between 2005 and 2008 in Korea. Medicine (Baltimore) [Internet]. 2016 Aug [cited 2019 Nov 18];95(33):e4352. Available from: http://www.ncbi.nlm.nih.gov/pubmed/27537562
33. Wolfe RA, Ashby VB, Milford EL, Ojo AO, Ettenger RE, Agodoa LYC, et al. Comparison of Mortality in All Patients on Dialysis, Patients on Dialysis Awaiting Transplantation, and Recipients of a First Cadaveric Transplant. N Engl J Med [Internet]. 1999 Dec 2 [cited 2019 Nov 18];341(23):1725–30. Available from: http://www.nejm.org/doi/abs/10.1056/NEJM199912023412303
34. Santos AH, Casey MJ, Wen X, Zendejas I, Rehman S, Womer KL, et al. Survival With Dialysis Versus Kidney Transplantation in Adult Hemolytic Uremic Syndrome Patients. Transplantation [Internet]. 2015 Dec [cited 2019 Nov 18];99(12):2608–16. Available from: http://content.wkhealth.com/linkback/openurl?sid=WKPTLP:landingpage&an=00007890-201512000-00028
35. Purnell TS, Auguste P, Crews DC, Lamprea-Montealegre J, Olufade T, Greer R, et al. Comparison of life participation activities among adults treated by hemodialysis, peritoneal dialysis, and kidney transplantation: a systematic review. Am J Kidney Dis [Internet]. 2013 Nov [cited 2015 Dec 9];62(5):953–73. Available from: http://www.pubmedcentral.nih.gov/articlerender.fcgi?artid=3809150&tool=pmcentrez&rendertype=abstract
36. NHSBT. Fact sheet 7: Cost-effectiveness of transplantation [Internet]. 2009 [cited 2019 Nov 18]. Available from: https://nhsbtmediaservices.blob.core.windows.net/organ-donation-assets/pdfs/Organ_Donation_Registry_Fact_Sheet_7_21337.pdf
37. Laupacis A, Keown P, Pus N, Krueger H, Ferguson B, Wong C, et al. A study of the quality of life and cost-utility of renal transplantation. Kidney Int. 1996;50(1):235–42.
38. Caskey F, Dawnay CC, Farrington A, Fogarty K, Kumwenda FS, Macphee M, et al. UK Renal Registry UK Renal Registry 18th Annual Report of the Renal Association. Nephron [Internet]. 2016 [cited 2016 Sep 14];132(suppl1). Available from: www.renalreg.org
39. Summers DM, Watson CJE, Pettigrew GJ, Johnson RJ, Collett D, Neuberger JM, et al. Kidney donation after circulatory death (DCD): state of the art. Kidney Int [Internet]. 2015 Aug [cited 2016 Nov 25];88(2):241–9. Available from: http://www.ncbi.nlm.nih.gov/pubmed/25786101
40. Ojo AO. Expanded Criteria Donors: Process and Outcomes. Semin Dial [Internet]. 2005 Nov 29 [cited 2016 Jun 14];18(6):463–8. Available from: http://doi.wiley.com/10.1111/j.1525-139X.2005.00090.x
41. Bradbury L, Brown C. ANNUAL REPORT ON KIDNEY TRANSPLANTATION REPORT FOR 2015/2016 (1 APRIL 2006 – 31 MARCH 2016) [Internet]. 2016 [cited 2019 Nov 18]. Available from: http://odt.nhs.uk/pdf/organ_specific_report_kidney_2016.pdf
42. Raghavan V, Weisz OOA, Alexander L, Alagarsamy S, Douglas J, Ashworth S, et al. Discerning the role of mechanosensors in regulating proximal tubule function. Am J Physiol Renal Physiol [Internet]. 2016 Jan 1 [cited 2016 Feb 29];310(1):F1-5. Available from: http://www.ncbi.nlm.nih.gov/pubmed/26662200
43. Yarlagadda SG, Coca SG, Garg AX, Doshi M, Poggio E, Marcus RJ, et al. Marked variation in the definition and diagnosis of delayed graft function: a systematic review. Nephrol Dial Transplant [Internet]. 2008 Sep [cited 2016 Jan 4];23(9):2995–3003. Available from: http://www.pubmedcentral.nih.gov/articlerender.fcgi?artid=2727302&tool=pmcentrez&rendertype=abstract
44. Nagaraja P, Roberts GW, Stephens M, Horvath S, Fialova J, Chavez R, et al. Influence of Delayed Graft Function and Acute Rejection on Outcomes After Kidney Transplantation From Donors After Cardiac Death. Transplant J [Internet]. 2012 Dec 27 [cited 2019 Nov 18];94(12):1218–23. Available from: http://www.ncbi.nlm.nih.gov/pubmed/23154212
45. Balaz P, Rokosny S, Wohlfahrtova M, Wohlfahrt P, Bartonova A, Pokorna E, et al. Identification of Expanded-Criteria Donor Kidney Grafts at Lower Risk of Delayed Graft Function. Transplant J [Internet]. 2013 Oct 15 [cited 2019 Nov 18];96(7):633–8. Available from: http://www.ncbi.nlm.nih.gov/pubmed/23912171
46. Martínez-Vaquera S, Navarro Cabello MD, López-Andreu M, Jurado JMD, Haad CR, Salas RO, et al. Outcomes in Renal Transplantation with Expanded-Criteria Donors. Transplant Proc

[Internet]. 2013 Dec [cited 2019 Nov 18];45(10):3595–8. Available from: http://www.ncbi.nlm.nih.gov/pubmed/24314969
47. Khurram MA, Wilson C, Vasdev N, Manas D, Talbot D, Rix D. Therapeutic kidney donation: A potential source of precious organs. Br J Med Surg Urol [Internet]. 2012 Jun 1 [cited 2015 Nov 9];6(6):424–6. Available from: http://uro.sagepub.com/content/6/6/424.short
48. Sapir-Pichhadze R, Young A, Joseph Kim S. Living donor age and kidney transplant outcomes: an assessment of risk across the age continuum. Transpl Int [Internet]. 2013 May [cited 2019 Nov 18];26(5):493–501. Available from: http://doi.wiley.com/10.1111/tri.12069
49. Chkhotua AB, Klein T, Shabtai E, Yussim A, Bar-Nathan N, Shaharabani E, et al. Kidney transplantation from living-unrelated donors: comparison of outcome with living-related and cadaveric transplants under current immunosuppressive protocols. Urology [Internet]. 2003 Dec [cited 2019 Nov 18];62(6):1002–6. Available from: http://www.ncbi.nlm.nih.gov/pubmed/14665344
50. NHSBT. Organ Donation Activity [Internet]. 2019 [cited 2019 Nov 18]. Available from: https://nhsbtdbe.blob.core.windows.net/umbraco-assets-corp/16420/section-3-organ-donation-activity.pdf
51. Watson CJE, Dark JH. Organ transplantation: historical perspective and current practice. Br J Anaesth [Internet]. 2012 Jan 1 [cited 2019 Nov 18];108(suppl_1):i29–42. Available from: https://linkinghub.elsevier.com/retrieve/pii/S0007091217321645
52. UK.Renal.Registry. UK Renal Registry 21st Annual Report: Data to 31/12/2017 [Internet]. 2019 [cited 2019 Nov 18]. Available from: https://www.renalreg.org/wp-content/uploads/2019/05/21st_UKRR_Annual_Report.pdf
53. Public.Health.England. Chronic kidney disease prevalence model [Internet]. 2014 [cited 2019 Nov 18]. Available from: https://assets.publishing.service.gov.uk/government/uploads/system/uploads/attachment_data/file/612303/ChronickidneydiseaseCKDprevalencemodelbriefing.pdf
54. Mannon RB. Delayed Graft Function: The AKI of Kidney Transplantation. Nephron [Internet]. 2018 [cited 2019 Nov 16];140(2):94–8. Available from: http://www.ncbi.nlm.nih.gov/pubmed/30007955
55. Tennankore KK, Kim SJ, Alwayn IPJ, Kiberd BA. Prolonged warm ischemia time is associated with graft failure and mortality after kidney transplantation. Kidney Int [Internet]. 2016 Mar 1 [cited 2019 Nov 16];89(3):648–58. Available from: https://www.sciencedirect.com/science/article/pii/S0085253815000642
56. Khan TFT, Ahmad N, Serageldeen AS, Fourtounas K. Implantation Warm Ischemia Time in Kidney Transplant Recipients: Defining Its Limits and Impact on Early Graft Function. Ann Transplant [Internet]. 2019 Jul 23 [cited 2019 Nov 16];24:432–8. Available from: https://www.annalsoftransplantation.com/abstract/index/idArt/916012
57. Ponticelli C. Ischaemia-reperfusion injury: a major protagonist in kidney transplantation. Nephrol Dial Transplant [Internet]. 2014 Jun 1 [cited 2019 Nov 16];29(6):1134–40. Available from: http://www.ncbi.nlm.nih.gov/pubmed/24335382
58. Spoelstra-de Man AME, Oudemans-van Straaten HM. Acute kidney injury after cardiac arrest: the role of coronary angiography and temperature management. Crit Care [Internet]. 2019 Dec 30 [cited 2019 Nov 16];23(1):193. Available from: https://ccforum.biomedcentral.com/articles/10.1186/s13054-019-2476-8
59. Van Erp AC, Rebolledo RA, Hoeksma D, Jespersen NR, Ottens PJ, Nørregaard R, et al. Organ-specific responses during brain death: increased aerobic metabolism in the liver and anaerobic metabolism with decreased perfusion in the kidneys. Sci Rep [Internet]. 2018 [cited 2019 Nov 16];8(1):4405. Available from: http://www.ncbi.nlm.nih.gov/pubmed/29535334
60. Stiegler P, Sereinigg M, Puntschart A, Seifert-Held T, Zmugg G, Wiederstein-Grasser I, et al. A 10 min “no-touch” time - is it enough in DCD? A DCD Animal Study. Transpl Int [Internet]. 2012 Apr 1 [cited 2019 Nov 16];25(4):481–92. Available from: http://doi.wiley.com/10.1111/j.1432-2277.2012.01437.x
61. Bradley JA, Pettigrew GJ, Watson CJ. Time to death after withdrawal of treatment in donation after circulatory death (DCD) donors. Curr Opin Organ Transplant [Internet]. 2013 Apr [cited 2019 Nov 16];18(2):133–9. Available from: http://content.wkhealth.com/linkback/openurl?sid=WKPTLP:landingpage&an=00075200-201304000-00003

62. Dünser MW, Takala J, Ulmer H, Mayr VD, Luckner G, Jochberger S, et al. Arterial blood pressure during early sepsis and outcome. Intensive Care Med [Internet]. 2009 Jul 3 [cited 2019 Nov 16];35(7):1225–33. Available from: http://link.springer.com/10.1007/s00134-009-1427-2
63. Law J, Hornby K, Payne C, Sener A, Luke PP. Missed opportunities for DCD kidney donors: Evaluation of warm ischemic time and associated functional warm ischemic time. Clin Transplant [Internet]. 2019 Nov 22 [cited 2020 Feb 27];33(11). Available from: https://onlinelibrary.wiley.com/doi/abs/10.1111/ctr.13724
64. Hollis A, Patel K, Smith T, Nath J, Tennant D, Ready A, et al. Manipulating the HIF Pathway in Renal Transplantation, Current Progress and Future Developments. J Clin Exp Transplant [Internet]. 2016 Nov 7 [cited 2018 Apr 3];1(2):1–6. Available from: https://www.omicsonline.org/open-access/manipulating-the-hif-pathway-in-renal-transplantation-current-progressand-future-developments-.php?aid=81542
65. Schiffer TA, Gustafsson H, Palm F. Kidney outer medulla mitochondria are more efficient compared with cortex mitochondria as a strategy to sustain ATP production in a suboptimal environment. Am J Physiol Physiol [Internet]. 2018 Sep 1 [cited 2019 Nov 16];315(3):F677–81. Available from: https://www.physiology.org/doi/10.1152/ajprenal.00207.2018
66. Kaminski J, Delpech P-O, Kaaki-Hosni S, Promeyrat X, Hauet T, Hannaert P. Oxygen Consumption by Warm Ischemia-Injured Porcine Kidneys in Hypothermic Static and Machine Preservation. J Surg Res [Internet]. 2019 Oct 1 [cited 2019 Nov 16];242:78–86. Available from: http://www.ncbi.nlm.nih.gov/pubmed/31071608
67. Weinberg JM, Venkatachalam MA, Roeser NF, Saikumar P, Dong Z, Senter RA, et al. Anaerobic and aerobic pathways for salvage of proximal tubules from hypoxia-induced mitochondrial injury. Am J Physiol Physiol [Internet]. 2000 Nov 1 [cited 2019 Nov 17];279(5):F927–43. Available from: https://www.physiology.org/doi/10.1152/ajprenal.2000.279.5.F927
68. Belzer FO, Southard JH. PRINCIPLES OF SOLID-ORGAN PRESERVATION BY COLD STORAGE. Transplantation [Internet]. 1988 Apr [cited 2019 Nov 17];45(4):673–6. Available from: https://insights.ovid.com/crossref?an=00007890-198804000-00001
69. Hochachka P. Defense strategies against hypoxia and hypothermia. Science (80-) [Internet]. 1986 Jan 17 [cited 2019 Nov 17];231(4735):234–41. Available from: http://www.ncbi.nlm.nih.gov/pubmed/2417316
70. Bienholz A, Walter B, Pless-Petig G, Guberina H, Kribben A, Witzke O, et al. Characterization of injury in isolated rat proximal tubules during cold incubation and rewarming. Lesnefsky EJ, editor. PLoS One [Internet]. 2017 Jul 3 [cited 2019 Nov 17];12(7):e0180553. Available from: https://dx.plos.org/10.1371/journal.pone.0180553
71. Kellerman PS. Exogenous adenosine triphosphate (ATP) preserves proximal tubule microfilament structure and function in vivo in a maleic acid model of ATP depletion. J Clin Invest [Internet]. 1993 Oct 1 [cited 2019 Nov 17];92(4):1940–9. Available from: http://www.ncbi.nlm.nih.gov/pubmed/8408646
72. Yin M, Currin RT, Peng X-X, Mekeel HE, Schoonhoven R, Lemasters JJ. Different patterns of renal cell killing after warm and cold ischemia. Ren Fail [Internet]. 2002 Mar [cited 2016 Jun 29];24(2):147–63. Available from: http://www.ncbi.nlm.nih.gov/pubmed/12071589
73. Lieberthal W, Menza SA, Levine JS. Graded ATP depletion can cause necrosis or apoptosis of cultured mouse proximal tubular cells. Am J Physiol Physiol [Internet]. 1998 Feb 1 [cited 2019 Nov 17];274(2):F315–27. Available from: https://www.physiology.org/doi/10.1152/ajprenal.1998.274.2.F315
74. Stubenitsky BM, Ametani M, Danielewicz R, Southard JH, Belzer FO. Regeneration of ATP in kidney slices after warm ischemia and hypothermic preservation. Transpl Int [Internet]. 1995 Jul [cited 2019 Nov 16];8(4):293–7. Available from: http://doi.wiley.com/10.1111/j.1432-2277.1995.tb01524.x
75. Han WK, Bailly V, Abichandani R, Thadhani R, Bonventre J V. Kidney Injury Molecule-1 (KIM-1): a novel biomarker for human renal proximal tubule injury. Kidney Int [Internet]. 2002 Jul [cited 2015 Jul 24];62(1):237–44. Available from: http://dx.doi.org/10.1046/j.1523-1755.2002.00433.x
76. Patel K, Nath J, Hodson J, Inston N, Ready A. Outcomes of donation after circulatory death kidneys undergoing hypothermic machine perfusion following static cold storage: A UK

population-based cohort study. Am J Transplant [Internet]. 2018 Jun 1 [cited 2019 May 5];18(6):1408–14. Available from: http://doi.wiley.com/10.1111/ajt.14587
77. Peters-Sengers H, Houtzager JHE, Idu MM, Heemskerk MBA, van Heurn ELW, Homan van der Heide JJ, et al. Impact of Cold Ischemia Time on Outcomes of Deceased Donor Kidney Transplantation: An Analysis of a National Registry. Transplant direct [Internet]. 2019 May [cited 2020 Feb 16];5(5):e448. Available from: http://www.ncbi.nlm.nih.gov/pubmed/31165083
78. Barba J, Zudaire JJ, Robles JE, Tienza A, Rosell D, Berián JM, et al. Is there a safe cold ischemia time interval for the renal graft? Actas Urológicas Españolas (English Ed [Internet]. 2011 Sep 1 [cited 2020 Feb 18];35(8):475–80. Available from: https://www.sciencedirect.com/science/article/pii/S2173578611000618
79. Halazun KJ, Al-Mukhtar A, Aldouri A, Willis S, Ahmad N. Warm Ischemia in Transplantation: Search for a Consensus Definition. Transplant Proc [Internet]. 2007 Jun 1 [cited 2019 Nov 17];39(5):1329–31. Available from: https://www.sciencedirect.com/science/article/pii/S0041134507002771?via%3Dihub
80. Schröppel B, Legendre C. Delayed kidney graft function: from mechanism to translation. Kidney Int [Internet]. 2014 Aug [cited 2019 Nov 17];86(2):251–8. Available from: http://www.ncbi.nlm.nih.gov/pubmed/24522494
81. Zhao H, Alam A, Soo AP, George AJT, Ma D. Ischemia-Reperfusion Injury Reduces Long Term Renal Graft Survival: Mechanism and Beyond. EBioMedicine [Internet]. 2018 Feb [cited 2020 Feb 27];28:31–42. Available from: http://www.ncbi.nlm.nih.gov/pubmed/29398595
82. Francis A, Baynosa R. Ischaemia-reperfusion injury and hyperbaric oxygen pathways: a review of cellular mechanisms. Diving Hyperb Med [Internet]. 2017 Jun [cited 2019 Nov 17];47(2):110–7. Available from: http://www.ncbi.nlm.nih.gov/pubmed/28641323
83. Li C, Jackson RM. Reactive species mechanisms of cellular hypoxia-reoxygenation injury. Am J Physiol Physiol [Internet]. 2002 Feb 1 [cited 2019 Nov 17];282(2):C227–41. Available from: http://www.ncbi.nlm.nih.gov/pubmed/11788333
84. Kalogeris T, Baines CP, Krenz M, Korthuis RJ. Cell Biology of Ischemia/Reperfusion Injury. In: International review of cell and molecular biology [Internet]. 2012 [cited 2019 Nov 17]. p. 229–317. Available from: http://www.ncbi.nlm.nih.gov/pubmed/22878108
85. Salvadori M, Rosso G, Bertoni E. Update on ischemia-reperfusion injury in kidney transplantation: Pathogenesis and treatment. World J Transplant [Internet]. 2015 Jun 24 [cited 2019 Nov 21];5(2):52–67. Available from: http://www.ncbi.nlm.nih.gov/pubmed/26131407
86. Lan R, Geng H, Singha PK, Saikumar P, Bottinger EP, Weinberg JM, et al. Mitochondrial Pathology and Glycolytic Shift during Proximal Tubule Atrophy after Ischemic AKI. J Am Soc Nephrol [Internet]. 2016 Mar 21 [cited 2016 Mar 27];27(11):ASN.2015020177-. Available from: http://jasn.asnjournals.org/content/early/2016/03/18/ASN.2015020177.abstract
87. Hosgood SA, Thompson E, Moore T, Wilson CH, Nicholson ML. Normothermic machine perfusion for the assessment and transplantation of declined human kidneys from donation after circulatory death donors. Br J Surg [Internet]. 2018 [cited 2019 Nov 16];105(4):388–94. Available from: http://www.ncbi.nlm.nih.gov/pubmed/29210064
88. Southard, M.D JH, Belzer, M.D FO. ORGAN PRESERVATION. Annu Rev Med [Internet]. 1995 Feb [cited 2016 Sep 14];46(1):235–47. Available from: http://www.annualreviews.org/doi/10.1146/annurev.med.46.1.235
89. Patel K, Nath J, Hodson J, Inston N, Ready A. Outcomes of Donation after Circulatory Death kidneys undergoing Hypothermic Machine Perfusion following Static Cold Storage: A UK population-based cohort study. Am J Transplant [Internet]. 2017 Nov 14 [cited 2017 Nov 28]; Available from: http://doi.wiley.com/10.1111/ajt.14587
90. Lee CY, Mangino MJ. Preservation methods for kidney and liver. 2009 [cited 2019 Nov 16]; Available from: https://www.tandfonline.com/action/journalInformation?journalCode=kogg20
91. Englesbe MJ, Mulholland MW. Operative techniques in transplantation surgery. 384 p.
92. Belzer F, Ashby BS, Dunphy JE. 24-HOUR AND 72-HOUR PRESERVATION OF CANINE KIDNEYS. Lancet [Internet]. 1967 Sep 9 [cited 2019 Nov 16];290(7515):536–9. Available from: https://www.sciencedirect.com/science/article/pii/S0140673667904989?via%3Dihub
93. Jochmans I, Moers C, Smits JM, Leuvenink HGD, Treckmann J, Paul A, et al. Machine Perfusion Versus Cold Storage for the Preservation of Kidneys Donated After Cardiac Death. Ann Surg [Internet]. 2010 Nov [cited 2016 Sep 3];252(5):756–64. Available from: http://content.wkhealth.com/linkback/openurl?sid=WKPTLP:landingpage&an=00000658-

201011000-00007
94. Moers C, Pirenne J, Paul A, Ploeg RJ, Machine Preservation Trial Study Group. Machine perfusion or cold storage in deceased-donor kidney transplantation. N Engl J Med [Internet]. 2012 Feb 23 [cited 2015 Nov 3];366(8):770–1. Available from: http://www.ncbi.nlm.nih.gov/pubmed/22356343
95. Moers C, Smits JM, Maathuis M-HJ, Treckmann J, van Gelder F, Napieralski BP, et al. Machine perfusion or cold storage in deceased-donor kidney transplantation. N Engl J Med [Internet]. 2009 Jan 1 [cited 2015 Dec 30];360(1):7–19. Available from: http://www.ncbi.nlm.nih.gov/pubmed/19118301
96. D'Alessandro AM, Hoffmann RM, Southard JH. Solution development in organ preservation: The University of Wisconsin perspective. Transplant Rev. 1999;13(2):67–77.
97. Organ Preservation Solutions | Organ Recovery Systems [Internet]. [cited 2019 Nov 16]. Available from: https://www.organ-recovery.com/organ-preservation-solutions
98. Wu WK, Famure O, Li Y, Kim SJ. Delayed graft function and the risk of acute rejection in the modern era of kidney transplantation. Kidney Int [Internet]. 2015 Oct [cited 2016 Sep 1];88(4):851–8. Available from: http://www.ncbi.nlm.nih.gov/pubmed/26108067
99. Weber S, Dienemann T, Jacobi J, Eckardt K-U, Weidemann A. Delayed graft function is associated with an increased rate of renal allograft rejection: A retrospective single center analysis. Remuzzi G, editor. PLoS One [Internet]. 2018 Jun 21 [cited 2019 Nov 16];13(6):e0199445. Available from: https://dx.plos.org/10.1371/journal.pone.0199445
100. Yarlagadda SG, Coca SG, Formica RN, Poggio ED, Parikh CR. Association between delayed graft function and allograft and patient survival: a systematic review and meta-analysis. Nephrol Dial Transplant [Internet]. 2008 Oct 8 [cited 2019 Nov 16];24(3):1039–47. Available from: https://academic.oup.com/ndt/article-lookup/doi/10.1093/ndt/gfn667
101. Tingle SJ, Figueiredo RS, Moir JA, Goodfellow M, Talbot D, Wilson CH. Machine perfusion preservation versus static cold storage for deceased donor kidney transplantation. Cochrane Database Syst Rev [Internet]. 2019 Mar 15 [cited 2019 Nov 16];3:CD011671. Available from: http://www.ncbi.nlm.nih.gov/pubmed/30875082
102. Kox J, Moers C, Monbaliu D, Strelniece A, Treckmann J, Jochmans I, et al. The Benefits of Hypothermic Machine Preservation and Short Cold Ischemia Times in Deceased Donor Kidneys. Transplantation [Internet]. 2018 Aug [cited 2019 May 5];102(8):1344–50. Available from: http://www.ncbi.nlm.nih.gov/pubmed/29570164
103. Jochmans I, Moers C, Smits JM, Leuvenink HGD, Treckmann J, Paul A, et al. The prognostic value of renal resistance during hypothermic machine perfusion of deceased donor kidneys. Am J Transplant [Internet]. 2011 Oct [cited 2016 Feb 15];11(10):2214–20. Available from: http://doi.wiley.com/10.1111/j.1600-6143.2011.03685.x
104. Featherstone RL, Kelly FJ, Shattock MJ, Hearse DJ, Chambers DJ. Hypothermic preservation of isolated rat lungs in modified bicarbonate buffer, EuroCollins solution or St Thomas' Hospital cardioplegic solution. Eur J Cardio-Thoracic Surg [Internet]. 1998 Nov 1 [cited 2019 Nov 16];14(5):508–15. Available from: https://academic.oup.com/ejcts/article-lookup/doi/10.1016/S1010-7940(98)00188-2
105. Jochmans I, O'Callaghan JM, Pirenne J, Ploeg RJ. Hypothermic machine perfusion of kidneys retrieved from standard and high-risk donors. Transpl Int [Internet]. 2015 Jun 1 [cited 2019 Nov 16];28(6):665–76. Available from: http://doi.wiley.com/10.1111/tri.12530
106. von Horn C, Minor T. Improved approach for normothermic machine perfusion of cold stored kidney grafts. Am J Transl Res [Internet]. 2018 [cited 2019 Nov 17];10(6):1921–9. Available from: http://www.ncbi.nlm.nih.gov/pubmed/30018731
107. Reznik ON, Bagnenko SF, Loginov I V., Iljina VA, Ananyev AN, Eremich S V., et al. Machine Perfusion as a Tool to Select Kidneys Recovered From Uncontrolled Donors After Cardiac Death. Transplant Proc. 2008 May;40(4):1023–6.
108. Reznik ON, Bagnenko SF, Loginov I V, Moisiuk YG. Increasing kidneys donor's pool by machine perfusion with the LifePort--pilot Russian study. Ann Transplant [Internet]. 2006 [cited 2019 Nov 16];11(3):46–8. Available from: http://www.ncbi.nlm.nih.gov/pubmed/17494299
109. Guy AJ, Nath J, Cobbold M, Ludwig C, Tennant DA, Inston NG, et al. Metabolomic Analysis of Perfusate During Hypothermic Machine Perfusion of Human Cadaveric Kidneys. Transplantation [Internet]. 2015 Apr [cited 2015 Oct 5];99(4):754–9. Available from: http://www.ncbi.nlm.nih.gov/pubmed/25222017

110. Bon D, Chatauret N, Giraud S, Thuillier R, Favreau F, Hauet T. New strategies to optimize kidney recovery and preservation in transplantation. Nat Rev Nephrol [Internet]. 2012 [cited 2016 Jul 1];8(6):339–47. Available from: http://dx.doi.org/10.1038/nrneph.2012.83
111. Nayak L, Lin Z, Jain MK. "Go with the flow": how Krüppel-like factor 2 regulates the vasoprotective effects of shear stress. Antioxid Redox Signal [Internet]. 2011 Sep 1 [cited 2019 Nov 16];15(5):1449–61. Available from: http://www.ncbi.nlm.nih.gov/pubmed/20919941
112. Gallinat A, Fox M, L?er B, Efferz P, Paul A, Minor T. Role of Pulsatility in Hypothermic Reconditioning of Porcine Kidney Grafts by Machine Perfusion After Cold Storage. Transplant J [Internet]. 2013 Sep [cited 2017 Jun 14];96(6):538–42. Available from: http://content.wkhealth.com/linkback/openurl?sid=WKPTLP:landingpage&an=00007890-201309270-00006
113. Ries W, Marie Y, Patel K, Turnbull C, Smith T, Jamil N, et al. A simple ex vivo model of human renal allograft preservation using the gonadal vein. Ann R Coll Surg Engl [Internet]. 2019 Nov [cited 2019 Nov 16];101(8):609–16. Available from: http://www.ncbi.nlm.nih.gov/pubmed/31508984
114. Wu H, Chen G, Wyburn KR, Yin J, Bertolino P, Eris JM, et al. TLR4 activation mediates kidney ischemia/reperfusion injury. J Clin Invest [Internet]. 2007 Oct 1 [cited 2016 Feb 15];117(10):2847–59. Available from: http://www.jci.org/articles/view/31008
115. Marshak-Rothstein A. Toll-like receptors in systemic autoimmune disease. Nat Rev Immunol [Internet]. 2006 Nov [cited 2019 Nov 16];6(11):823–35. Available from: http://www.nature.com/articles/nri1957
116. Beg AA. Endogenous ligands of Toll-like receptors: implications for regulating inflammatory and immune responses. Trends Immunol [Internet]. 2002 Nov [cited 2019 Nov 16];23(11):509–12. Available from: http://www.ncbi.nlm.nih.gov/pubmed/12401394
117. Hua F, Ha T, Ma J, Li Y, Kelley J, Gao X, et al. Protection against Myocardial Ischemia/Reperfusion Injury in TLR4-Deficient Mice Is Mediated through a Phosphoinositide 3-Kinase-Dependent Mechanism. J Immunol [Internet]. 2007 May 18 [cited 2016 Feb 16];178(11):7317–24. Available from: http://www.jimmunol.org/content/178/11/7317.full
118. Gallinat A, Paul A, Efferz P, Lüer B, Kaiser G, Wohlschlaeger J, et al. Hypothermic reconditioning of porcine kidney grafts by short-term preimplantation machine perfusion. Transplantation [Internet]. 2012 Apr 27 [cited 2016 Feb 5];93(8):787–93. Available from: http://www.ncbi.nlm.nih.gov/pubmed/22441320
119. Tozzi M, Franchin M, Soldini G, Ietto G, Chiappa C, Maritan E, et al. Impact of static cold storage VS hypothermic machine preservation on ischemic kidney graft: inflammatory cytokines and adhesion molecules as markers of ischemia/reperfusion tissue damage. Our preliminary results. Int J Surg [Internet]. 2013 Dec 1 [cited 2019 Nov 16];11:S110–4. Available from: https://www.sciencedirect.com/science/article/pii/S1743919113600291
120. Maathuis M-HJ, Manekeller S, van der Plaats A, Leuvenink HGD, 't Hart NA, Lier AB, et al. Improved kidney graft function after preservation using a novel hypothermic machine perfusion device. Ann Surg [Internet]. 2007 Dec [cited 2016 May 16];246(6):982–8; discussion 989-91. Available from: http://content.wkhealth.com/linkback/openurl?sid=WKPTLP:landingpage&an=00000658-200712000-00010
121. Hoyer DP, Gallinat A, Swoboda S, Wohlschlaeger J, Rauen U, Paul A, et al. Influence of oxygen concentration during hypothermic machine perfusion on porcine kidneys from donation after circulatory death. Transplantation [Internet]. 2014 Nov 15 [cited 2016 Feb 15];98(9):944–50. Available from: http://www.ncbi.nlm.nih.gov/pubmed/25369373
122. Gallinat A, Paul A, Efferz P, Lüer B, Swoboda S, Hoyer D, et al. Role of Oxygenation in Hypothermic Machine Perfusion of Kidneys From Heart Beating Donors. Transplant J [Internet]. 2012 Oct [cited 2016 Sep 5];94(8):809–13. Available from: http://content.wkhealth.com/linkback/openurl?sid=WKPTLP:landingpage&an=00007890-201210270-00005
123. Hofker Groningen S. COPE -COMPARE Trial. Consort organ Preserv Eur. 2015;
124. Hsieh T-J, Zhang S-L, Filep JG, Tang S-S, Ingelfinger JR, Chan JSD. High Glucose Stimulates Angiotensinogen Gene Expression via Reactive Oxygen Species Generation in Rat Kidney Proximal Tubular Cells. Endocrinology [Internet]. 2013 Jul 1 [cited 2016 Jan 12]; Available from: http://press.endocrine.org/doi/full/10.1210/endo.143.8.8931

125. Darius T, Vergauwen M, Smith TB, Patel K, Craps J, Joris V, et al. Influence of different partial pressures of oxygen during continuous hypothermic machine perfusion in a pig kidney ischemia-reperfusion autotransplant model. Transplantation [Internet]. 2019 Nov [cited 2019 Nov 27];1. Available from: http://insights.ovid.com/crossref?an=00007890-900000000-95853
126. Grundmann R, Raab M, Meusel E, Kirchhoff R, Pichlmaier H. Analysis of the optimal perfusion pressure and flow rate of the renal vascular resistance and oxygen consumption in the hypothermic perfused kidney. Surgery [Internet]. 1975 Mar [cited 2020 Jan 26];77(3):451–61. Available from: http://www.ncbi.nlm.nih.gov/pubmed/1092016
127. Giraud S, Favreau F, Chatauret N, Thuillier R, Maiga S, Hauet T, et al. Contribution of large pig for renal ischemia-reperfusion and transplantation studies: the preclinical model. J Biomed Biotechnol [Internet]. 2011 [cited 2016 Oct 17];2011:532127. Available from: http://www.ncbi.nlm.nih.gov/pubmed/21403881
128. Tolstykh GP, Gelineau JF, Maier LM, Bunegin L. Novel portable hypothermic pulsatile perfusion preservation technology: Improved viability and function of rodent and canine kidneys. Ann Transplant [Internet]. [cited 2019 Nov 16];15(3):35–43. Available from: http://www.ncbi.nlm.nih.gov/pubmed/20877265
129. Chanda SK, Caldwell JS. Fulfilling the promise: drug discovery in the post-genomic era. Drug Discov Today [Internet]. 2003 Feb 15 [cited 2019 Nov 16];8(4):168–74. Available from: https://www.sciencedirect.com/science/article/pii/S1359644602025953
130. Dutheil D, Rioja-Pastor I, Tallineau C, Goujon J-MJ-M, Hauet T, Mauco G, et al. Protective Effect of PEG 35 000 Da on Renal Cells: Paradoxical Activation of JNK Signaling Pathway During Cold Storage. Am J Transplant [Internet]. 2006 Jul [cited 2015 Sep 30];6(7):1529–40. Available from: http://doi.wiley.com/10.1111/j.1600-6143.2006.01343.x
131. Yu N, Fu S, Liu Y, Fu Z, Meng J, Xu Z, et al. Benign and Malignant Renal Cells Are Differentially Inhibited during Prolonged Organ Preservation. Bueno V, editor. PLoS One [Internet]. 2013 Dec 9 [cited 2016 Aug 26];8(12):e81745. Available from: http://dx.plos.org/10.1371/journal.pone.0081745
132. Healy DA, Daly PJ, Docherty NG, Murphy M, Fitzpatrick JM, Watson RWG. Heat Shock-Induced Protection of Renal Proximal Tubular Epithelial Cells from Cold Storage and Rewarming Injury. J Am Soc Nephrol [Internet]. 2006 Jan 18 [cited 2016 Aug 26];17(3):805–12. Available from: http://www.jasn.org/cgi/doi/10.1681/ASN.2005090980
133. Daly PJ, Docherty NG, Healy DA, McGuire BB, Fitzpatrick JM, Watson RWG. The single insult of hypoxic preconditioning induces an antiapoptotic response in human proximal tubular cells, *in vitro,* across cold storage. BJU Int [Internet]. 2009 Jan 1 [cited 2019 Nov 16];103(2):254–9. Available from: http://doi.wiley.com/10.1111/j.1464-410X.2008.08010.x
134. Hollenberg NK, Epstein M, Rosen SM, Basch RI, Oken DE, Merrill JP. Acute oliguric renal failure in man: evidence for preferential renal cortical ischemia. Medicine (Baltimore) [Internet]. 1968 Nov [cited 2016 Jan 28];47(6):455–74. Available from: http://www.ncbi.nlm.nih.gov/pubmed/5715692
135. Gobé G, Willgoss D, Hogg N, Schoch E, Endre Z. Cell survival or death in renal tubular epithelium after ischemia-reperfusion injury. Kidney Int [Internet]. 1999 Oct [cited 2015 Oct 15];56(4):1299–304. Available from: http://dx.doi.org/10.1046/j.1523-1755.1999.00701.x
136. Fine LG. The Breathing Kidney. J Am Soc Nephrol [Internet]. 2002 Jul 1 [cited 2016 Mar 21];13(7):1974–6. Available from: http://jasn.asnjournals.org/content/13/7/1974
137. Neuhofer W, Beck F-X. Cell survival in the hostile environment of the renal medulla. Annu Rev Physiol [Internet]. 2005 Jan 17 [cited 2016 Mar 21];67:531–55. Available from: http://www.annualreviews.org/doi/abs/10.1146/annurev.physiol.67.031103.154456
138. Wong G, Teixeira-Pinto A, Chapman JR, Craig JC, Pleass H, McDonald S, et al. The Impact of Total Ischemic Time, Donor Age and the Pathway of Donor Death on Graft Outcomes After Deceased Donor Kidney Transplantation. Transplantation [Internet]. 2017 [cited 2020 Feb 17];101(6):1152–8. Available from: http://www.ncbi.nlm.nih.gov/pubmed/27479168
139. Osband AJ, James NT, Segev DL. Extraction Time of Kidneys From Deceased Donors and Impact on Outcomes. Am J Transplant [Internet]. 2016 Feb 1 [cited 2020 Feb 17];16(2):700–3. Available from: http://doi.wiley.com/10.1111/ajt.13457
140. Ravaioli M, Baldassare M, Vasuri F, Pasquinelli G, Laggetta M, Valente S, et al. Strategies to Restore Adenosine Triphosphate (ATP) Level After More than 20 Hours of Cold Ischemia Time in Human Marginal Kidney Grafts. Ann Transplant [Internet]. 2018 Jan 12 [cited 2019 Nov

17];23:34–44. Available from: http://www.ncbi.nlm.nih.gov/pubmed/29326416
141. Asderakis A, Dyer P, Augustine T, Worthington J, Campbell B, Johnson RW. Effect of cold ischemic time and HLA matching in kidneys coming from "young" and "old" donors: do not leave for tomorrow what you can do tonight. Transplantation [Internet]. 2001 Aug 27 [cited 2016 Jul 14];72(4):674–8. Available from: http://www.ncbi.nlm.nih.gov/pubmed/11544430
142. Mitchell HH, Hamilton TS, Steggerda FR, Bean HW. THE CHEMICAL COMPOSITION OF THE ADULT HUMAN BODY AND ITS BEARING ON THE BIOCHEMISTRY OF GROWTH. J Biol Chem [Internet]. 1945 May 1 [cited 2015 Nov 12];158(3):625–37. Available from: http://www.jbc.org/content/158/3/625.citation
143. Bökenkamp A, Ludwig M. Disorders of the renal proximal tubule. Nephron Physiol [Internet]. 2011 Jan 11 [cited 2016 Mar 4];118(1):p1-6. Available from: http://www.karger.com/Article/FullText/320880
144. Runembert I, Couette S, Federici P, Colucci-Guyon E, Babinet C, Briand P, et al. Recovery of Na-glucose cotransport activity after renal ischemia is impaired in mice lacking vimentin. Am J Physiol Renal Physiol [Internet]. 2004 Nov [cited 2016 Jul 14];287(5):F960-8. Available from: http://www.ncbi.nlm.nih.gov/pubmed/15238351
145. Norden AGW, Lapsley M, Unwin RJ. Urine retinol-binding protein 4: a functional biomarker of the proximal renal tubule. Adv Clin Chem [Internet]. 2014 [cited 2016 Jul 19];63:85–122. Available from: http://www.ncbi.nlm.nih.gov/pubmed/24783352
146. Câmara NOS, Silva MS, Nishida S, Pereira AB, Pacheco-Silva A. Proximal Tubular Dysfunction is Associated with Chronic Allograft Nephropathy and Decreased Long-Term Renal-Graft Survival. Transplant J [Internet]. 2004 Jul [cited 2016 Jul 14];78(2):269–75. Available from: http://content.wkhealth.com/linkback/openurl?sid=WKPTLP:landingpage&an=00007890-200407270-00018
147. Lee YJ, Lee YJ, Han HJ. Regulatory mechanisms of Na(+)/glucose cotransporters in renal proximal tubule cells. Kidney Int Suppl [Internet]. 2007 Aug [cited 2016 Mar 9];(106):S27-35. Available from: http://www.ncbi.nlm.nih.gov/pubmed/17653207
148. Wright EM. Renal Na+-glucose cotransporters. Am J Physiol Ren Physiol [Internet]. 2001 Jan 1 [cited 2016 Mar 14];280(1):F10-18. Available from: http://ajprenal.physiology.org/content/280/1/F10.short
149. Vogetseder A, Picard N, Gaspert A, Walch M, Kaissling B, Le Hir M. Proliferation capacity of the renal proximal tubule involves the bulk of differentiated epithelial cells. Am J Physiol Cell Physiol [Internet]. 2008 Jan 1 [cited 2015 Nov 10];294(1):C22-8. Available from: http://ajpcell.physiology.org/content/294/1/C22.long
150. Kusaba T, Lalli M, Kramann R, Kobayashi A, Humphreys BD. Differentiated kidney epithelial cells repair injured proximal tubule. Proc Natl Acad Sci U S A [Internet]. 2014 Jan 28 [cited 2015 Nov 9];111(4):1527–32. Available from: http://www.pubmedcentral.nih.gov/articlerender.fcgi?artid=3910580&tool=pmcentrez&rendertype=abstract
151. MJ R, G J, J K, SM F, RA Z, B T-S. HK-2: an immortalized proximal tubule epithelial cell line from normal adult human kidney. Kidney Int [Internet]. 1994 [cited 2020 Aug 16];45(1). Available from: https://pubmed.ncbi.nlm.nih.gov/8127021/
152. Pei XF. CANCER BIOLOGY: The human papillomavirus E6/E7 genes induce discordant changes in the expression of cell growth regulatory proteins. Carcinogenesis [Internet]. 1996 Jul 1 [cited 2016 Apr 12];17(7):1395–401. Available from: http://carcin.oxfordjournals.org/content/17/7/1395
153. Aschauer L, Gruber LN, Pfaller W, Limonciel A, Athersuch TJ, Cavill R, et al. Delineation of the key aspects in the regulation of epithelial monolayer formation. Mol Cell Biol [Internet]. 2013 Jul [cited 2015 Nov 10];33(13):2535–50. Available from: http://www.pubmedcentral.nih.gov/articlerender.fcgi?artid=3700122&tool=pmcentrez&rendertype=abstract
154. Jenkinson SE, Chung GW, van Loon E, Bakar NS, Dalzell AM, Brown CDA. The limitations of renal epithelial cell line HK-2 as a model of drug transporter expression and function in the proximal tubule. Pflügers Arch Eur J Physiol [Internet]. 2012 Dec [cited 2016 Apr 12];464(6):601–11. Available from: http://www.ncbi.nlm.nih.gov/pubmed/23014881

155. Wieser M, Stadler G, Jennings P, Streubel B, Pfaller W, Ambros P, et al. hTERT alone immortalizes epithelial cells of renal proximal tubules without changing their functional characteristics. AJP Ren Physiol [Internet]. 2008 Aug 20 [cited 2015 Jun 29];295(5):F1365–75. Available from: http://www.ncbi.nlm.nih.gov/pubmed/18715936
156. Lee KM, Choi KH, Ouellette MM. Use of exogenous hTERT to immortalize primary human cells. Cytotechnology [Internet]. 2004 Jun [cited 2016 Feb 23];45(1–2):33–8. Available from: http://www.pubmedcentral.nih.gov/articlerender.fcgi?artid=3449956&tool=pmcentrez&rendertype=abstract
157. Aschauer L, Carta G, Vogelsang N, Schlatter E, Jennings P. Expression of xenobiotic transporters in the human renal proximal tubule cell line RPTEC/TERT1. Toxicol In Vitro [Internet]. 2014 Dec 10 [cited 2015 Nov 10]; Available from: http://www.sciencedirect.com/science/article/pii/S0887233314002434
158. Balaban RS, Mandel LJ. Metabolic substrate utilization by rabbit proximal tubule. An NADH fluorescence study. Am J Physiol [Internet]. 1988 Mar [cited 2016 Jul 12];254(3 Pt 2):F407-16. Available from: http://www.ncbi.nlm.nih.gov/pubmed/3348418
159. Mandel LJ. Metabolic substrates, cellular energy production, and the regulation of proximal tubular transport. Annu Rev Physiol [Internet]. 1985 Jan [cited 2016 Mar 4];47:85–101. Available from: http://www.ncbi.nlm.nih.gov/pubmed/3888090
160. Wieser M, Francisci T, Lackner D, Buerckstuemmer T, Wasner K, Eilenberg W, et al. CD46 knock-out using CRISPR/Cas9 editing of hTERT immortalized human cells modulates complement activation. Saretzki G, editor. PLoS One [Internet]. 2019 Apr 8 [cited 2019 Nov 20];14(4):e0214514. Available from: http://www.ncbi.nlm.nih.gov/pubmed/30958843
161. Lee JH, Okuno Y, Cavagnero S. Sensitivity enhancement in solution NMR: emerging ideas and new frontiers. J Magn Reson [Internet]. 2014 Apr [cited 2019 Nov 20];241:18–31. Available from: http://www.ncbi.nlm.nih.gov/pubmed/24656077
162. Van der Hauwaert C, Savary G, Gnemmi V, Glowacki F, Pottier N, Bouillez A, et al. Isolation and characterization of a primary proximal tubular epithelial cell model from human kidney by CD10/CD13 double labeling. Abe H, editor. PLoS One [Internet]. 2013 Jan 14 [cited 2015 Sep 30];8(6):e66750. Available from: https://dx.plos.org/10.1371/journal.pone.0066750
163. Stein A. Decreasing variability in your cell culture. Biotechniques [Internet]. 2007 Aug [cited 2019 Nov 20];43(2):228–9. Available from: http://www.ncbi.nlm.nih.gov/pubmed/17824391
164. Tang MJ, Tannen RL. Metabolic substrates alter attachment and differentiated functions of proximal tubule cell culture. J Am Soc Nephrol [Internet]. 1994 May [cited 2019 Nov 20];4(11):1908–11. Available from: http://www.ncbi.nlm.nih.gov/pubmed/7919143
165. Homan KA, Kolesky DB, Skylar-Scott MA, Herrmann J, Obuobi H, Moisan A, et al. Bioprinting of 3D Convoluted Renal Proximal Tubules on Perfusable Chips. Sci Rep [Internet]. 2016 Dec 11 [cited 2019 Nov 20];6(1):34845. Available from: http://www.nature.com/articles/srep34845
166. Lee DW, Choi N, Sung JH. A microfluidic chip with gravity-induced unidirectional flow for perfusion cell culture. Biotechnol Prog [Internet]. 2019 Jan 1 [cited 2019 Nov 18];35(1):e2701. Available from: http://doi.wiley.com/10.1002/btpr.2701
167. Wang B, Wang H-W, Guo H, Anderson E, Tang Q, Wu T, et al. Optical coherence tomography and computer-aided diagnosis of a murine model of chronic kidney disease. J Biomed Opt [Internet]. 2017 Dec [cited 2020 Feb 18];22(12):1–11. Available from: http://www.ncbi.nlm.nih.gov/pubmed/29197178
168. Zhou X, Liu D, You L, Wang L. Quantifying fluid shear stress in a rocking culture dish. J Biomech [Internet]. 2010 May 28 [cited 2016 Apr 26];43(8):1598–602. Available from: http://www.pubmedcentral.nih.gov/articlerender.fcgi?artid=2866761&tool=pmcentrez&rendertype=abstract
169. Voigt W. Sulforhodamine B Assay and Chemosensitivity. In: Chemosensitivity [Internet]. New Jersey: Humana Press; 2005 [cited 2019 Nov 20]. p. 039–48. Available from: http://www.ncbi.nlm.nih.gov/pubmed/15901925
170. Orellana EA, Kasinski AL. Sulforhodamine B (SRB) Assay in Cell Culture to Investigate Cell Proliferation. Bio-protocol [Internet]. 2016 Nov 5 [cited 2019 Nov 20];6(21). Available from: http://www.ncbi.nlm.nih.gov/pubmed/28573164
171. Kumar P, Nagarajan A, Uchil PD. Analysis of Cell Viability by the Lactate Dehydrogenase Assay. Cold Spring Harb Protoc [Internet]. 2018 Jun 1 [cited 2019 Nov 20];2018(6):pdb.prot095497. Available from: http://www.ncbi.nlm.nih.gov/pubmed/29858337

172. Navarro Suay R, Escolán Gonzalvo MN, de Nicolás Álvarez MA, Brinquis Crespo MÁ. Oxygen dissolved in plasma does matter. Tissue oxygen monitoring to assess the feasability of a microvascular flap in a patient undergoing hyperbaric oxygen therapy. Rev Española Anestesiol y Reanim (English Ed [Internet]. 2018 Feb 1 [cited 2019 Nov 16];65(2):119–20. Available from: https://www.sciencedirect.com/science/article/pii/S2341192917302032
173. Clarke A, Fraser KPP. Why does metabolism scale with temperature? Funct Ecol [Internet]. 2004 Apr 1 [cited 2019 Nov 16];18(2):243–51. Available from: http://doi.wiley.com/10.1111/j.0269-8463.2004.00841.x
174. Kasil A, Giraud S, Couturier P, Amiri A, Danion J, Donatini G, et al. Individual and Combined Impact of Oxygen and Oxygen Transporter Supplementation during Kidney Machine Preservation in a Porcine Preclinical Kidney Transplantation Model. Int J Mol Sci [Internet]. 2019 Apr 23 [cited 2019 Nov 16];20(8):1992. Available from: http://www.ncbi.nlm.nih.gov/pubmed/31018558
175. Drumond MC, Deen WM. Analysis of pulsatile pressures and flows in glomerular filtration. Am J Physiol [Internet]. 1991 Sep [cited 2016 May 16];261(3 Pt 2):F409-19. Available from: http://www.ncbi.nlm.nih.gov/pubmed/1887905
176. Raghavan V, Weisz OA. Discerning the role of mechanosensors in regulating proximal tubule function. Am J Physiol Renal Physiol [Internet]. 2016 Jan 1 [cited 2016 May 24];310(1):F1-5. Available from: http://ajprenal.physiology.org/content/310/1/F1.full
177. Satchell SC, Braet F. Glomerular endothelial cell fenestrations: an integral component of the glomerular filtration barrier. Am J Physiol Renal Physiol [Internet]. 2009 May [cited 2016 Apr 14];296(5):F947-56. Available from: http://www.pubmedcentral.nih.gov/articlerender.fcgi?artid=2681366&tool=pmcentrez&rendertype=abstract
178. Ohlson M, Sorensson J, Haraldsson B. A gel-membrane model of glomerular charge and size selectivity in series. Am J Physiol Ren Physiol [Internet]. 2001 Mar 1 [cited 2016 May 27];280(3):F396-405. Available from: http://ajprenal.physiology.org/content/280/3/F396?ijkey=1731e78e64152a2ff319c3c712b13b57a308e0f1&keytype2=tf_ipsecsha
179. Haraldsson B, Nyström J, Deen WM. Properties of the glomerular barrier and mechanisms of proteinuria. Physiol Rev [Internet]. 2008 Apr [cited 2016 Aug 4];88(2):451–87. Available from: http://www.ncbi.nlm.nih.gov/pubmed/18391170
180. Wuerzner G, Firsov D, Bonny O. Circadian glomerular function: from physiology to molecular and therapeutical aspects. Nephrol Dial Transplant [Internet]. 2014 Aug 1 [cited 2019 Nov 16];29(8):1475–80. Available from: https://academic.oup.com/ndt/article-lookup/doi/10.1093/ndt/gft525
181. Bhaskar A, Oommen V. A simple model for demonstrating the factors affecting glomerular filtration rate. Adv Physiol Educ [Internet]. 2018 Jun 1 [cited 2019 Nov 16];42(2):380–2. Available from: https://www.physiology.org/doi/10.1152/advan.00195.2017
182. Thomson SC, Blantz RC. Glomerulotubular balance, tubuloglomerular feedback, and salt homeostasis. J Am Soc Nephrol [Internet]. 2008 Dec 1 [cited 2019 Nov 16];19(12):2272–5. Available from: http://www.ncbi.nlm.nih.gov/pubmed/18322161
183. Bevan HS, Slater SC, Clarke H, Cahill PA, Mathieson PW, Welsh GI, et al. Acute laminar shear stress reversibly increases human glomerular endothelial cell permeability via activation of endothelial nitric oxide synthase. Am J Physiol Renal Physiol [Internet]. 2011 Oct [cited 2019 Nov 16];301(4):F733-42. Available from: http://www.ncbi.nlm.nih.gov/pubmed/21775480
184. Henry SD, van der Wegen P, Metselaar HJ, Scholte BJ, Tilanus HW, van der Laan LJW. Hydroxyethyl starch-based preservation solutions enhance gene therapy vector delivery under hypothermic conditions. Liver Transplant [Internet]. 2008 Dec 1 [cited 2019 Nov 16];14(12):1708–17. Available from: http://doi.wiley.com/10.1002/lt.21623
185. Lote C. Glomerular filtration. In: Principles of Renal Physiology [Internet]. Dordrecht: Springer Netherlands; 2000 [cited 2019 Nov 16]. p. 34–46. Available from: http://link.springer.com/10.1007/978-94-011-4086-7_3
186. Lo S, Byrum SD, Tackett AJ, Parajuli N. Cold Storage Increases Albumin and Advanced Glycation-End Product-Albumin Levels in Kidney Transplants. Transplant Direct [Internet]. 2019 Jun [cited 2019 Nov 16];5(6):e454. Available from: http://insights.ovid.com/crossref?an=01845228-201906000-00004

187. Lambert R, Henry M, Howden B, Jablonski P, Rae D, Tavanlis G, et al. GLOMERULAR DAMAGE AFTER KIDNEY PRESERVATION. Transplantation [Internet]. 1986 Aug [cited 2019 Nov 16];42(2):125–9. Available from: http://www.ncbi.nlm.nih.gov/pubmed/3738974
188. Curthoys NP, Moe OW. Proximal tubule function and response to acidosis. Clin J Am Soc Nephrol [Internet]. 2014 Sep 5 [cited 2016 Jan 25];9(9):1627–38. Available from: http://www.pubmedcentral.nih.gov/articlerender.fcgi?artid=4152816&tool=pmcentrez&rendertype=abstract
189. Du Z, Duan Y, Yan Q, Weinbaum S, Weinstein AM, Wang T. Flow-activated proximal tubule function underlies glomerulotubular balance. Kitasato Med J [Internet]. 2016 [cited 2019 Nov 16];46(1):105–17. Available from: http://www.ncbi.nlm.nih.gov/pubmed/31105444
190. Gilbert RE. Proximal Tubulopathy: Prime Mover and Key Therapeutic Target in Diabetic Kidney Disease. Diabetes [Internet]. 2017 Apr 1 [cited 2019 Nov 16];66(4):791–800. Available from: http://www.ncbi.nlm.nih.gov/pubmed/28325740
191. Chevalier RL. The proximal tubule is the primary target of injury and progression of kidney disease: role of the glomerulotubular junction. Am J Physiol Ren Physiol Am J Physiol -Renal Physiol [Internet]. 2016 [cited 2016 Aug 5];311:145–61. Available from: http://ajprenal.physiology.org/content/311/1/F145.full#ref-list-1
192. Weinberg JM, Davis JA, Abarzua M, Kiani T. Relationship between cell adenosine triphosphate and glutathione content and protection by glycine against hypoxic proximal tubule cell injury. J Lab Clin Med [Internet]. 1989 May 1 [cited 2019 Dec 3];113(5):612–22. Available from: https://www.translationalres.com/article/0022-2143(89)90031-0/fulltext
193. Gardiner BS, Thompson SL, Ngo JP, Smith DW, Abdelkader A, Broughton BRS, et al. Diffusive oxygen shunting between vessels in the preglomerular renal vasculature: anatomic observations and computational modeling. Am J Physiol Renal Physiol [Internet]. 2012 Sep [cited 2016 Aug 26];303(5):F605-18. Available from: http://www.ncbi.nlm.nih.gov/pubmed/22674022
194. Evans RG, Gardiner BS, Smith DW, O'Connor PM. Intrarenal oxygenation: unique challenges and the biophysical basis of homeostasis. Am J Physiol Physiol [Internet]. 2008 Nov [cited 2019 Nov 16];295(5):F1259–70. Available from: http://www.ncbi.nlm.nih.gov/pubmed/18550645
195. Haberle DA, von Baeyer H. Characteristics of glomerulotubular balance. Am J Physiol Physiol [Internet]. 1983 Apr 1 [cited 2019 Nov 16];244(4):F355–66. Available from: http://www.ncbi.nlm.nih.gov/pubmed/6340526
196. Dave RA, Morris ME. Semi-mechanistic kidney model incorporating physiologically-relevant fluid reabsorption and transporter-mediated renal reabsorption: pharmacokinetics of γ-hydroxybutyric acid and L-lactate in rats. J Pharmacokinet Pharmacodyn [Internet]. 2015 Oct [cited 2016 May 2];42(5):497–513. Available from: http://link.springer.com/article/10.1007/s10928-015-9441-1/fulltext.html
197. Bonvalet JP, de Rouffignac C. Distribution of ferrocyanide along the proximal tubular lumen of the rat kidney: its implications upon hydrodynamics. J Physiol [Internet]. 1981 Sep [cited 2016 May 17];318:85–98. Available from: http://www.pubmedcentral.nih.gov/articlerender.fcgi?artid=1245479&tool=pmcentrez&rendertype=abstract
198. Duan Y, Gotoh N, Yan Q, Du Z, Weinstein AM, Wang T, et al. Shear-induced reorganization of renal proximal tubule cell actin cytoskeleton and apical junctional complexes. Proc Natl Acad Sci U S A [Internet]. 2008 Aug 12 [cited 2016 May 17];105(32):11418–23. Available from: http://www.pnas.org/content/105/32/11418.long
199. Chou C, Marsh D. Measurement of flow rate in rat proximal tubules with a nonobstructing optical method. Am J Physiol … [Internet]. 1987 [cited 2016 May 20]; Available from: http://ajprenal.physiology.org/content/253/2/F366.short
200. Maunsbach A. Effects of flow rate on proximal tubule ultrastructure. Am J … [Internet]. 1987 [cited 2016 May 20]; Available from: http://ajprenal.physiology.org/content/253/3/F582.short
201. Raghavan V, Rbaibi Y, Pastor-Soler NM, Carattino MD, Weisz OA. Shear stress-dependent regulation of apical endocytosis in renal proximal tubule cells mediated by primary cilia. Proc Natl Acad Sci U S A [Internet]. 2014 Jun 10 [cited 2016 Apr 27];111(23):8506–11. Available from: http://www.pubmedcentral.nih.gov/articlerender.fcgi?artid=4060694&tool=pmcentrez&renderty

pe=abstract
202. Essig M, Friedlander G. Shear-stress-responsive signal transduction mechanisms in renal proximal tubule cells. Curr Opin Nephrol Hypertens [Internet]. 2003 Jan [cited 2016 Apr 14];12(1):31–4. Available from: http://www.ncbi.nlm.nih.gov/pubmed/12496663
203. Parr A, Parr A. Fundamental Principles. Hydraul Pneum [Internet]. 2011 Jan 1 [cited 2019 Nov 16];1–29. Available from: https://www.sciencedirect.com/science/article/pii/B978008096674800001X
204. Lauga E, Squires TM. Brownian motion near a partial-slip boundary: A local probe of the no-slip condition. Phys Fluids [Internet]. 2005 Oct 19 [cited 2019 Nov 16];17(10):103102. Available from: http://scitation.aip.org/content/aip/journal/pof2/17/10/10.1063/1.2083748
205. Myers TG, Charpin JPF, Tshehla MS. The flow of a variable viscosity fluid between parallel plates with shear heating. Appl Math Model [Internet]. 2006 Sep 1 [cited 2019 Nov 16];30(9):799–815. Available from: https://www.sciencedirect.com/science/article/pii/S0307904X05001125
206. Laliberté* M. Model for Calculating the Viscosity of Aqueous Solutions. 2007 [cited 2019 Nov 16]; Available from: https://pubs.acs.org/doi/abs/10.1021/je0604075
207. Raghavan V, Weisz OA. Discerning the role of mechanosensors in regulating proximal tubule function. Am J Physiol Renal Physiol [Internet]. 2016 Jan 1 [cited 2016 Feb 29];310(1):F1-5. Available from: http://ajprenal.physiology.org/content/310/1/F1.long
208. Wang T, Weinbaum S, Weinstein AM. Regulation of glomerulotubular balance: flow-activated proximal tubule function. 1960 [cited 2018 Sep 16]; Available from: https://link.springer.com/content/pdf/10.1007%2Fs00424-017-1960-8.pdf
209. Vrhovac I, Balen Eror D, Klessen D, Burger C, Breljak D, Kraus O, et al. Localizations of Na(+)-D-glucose cotransporters SGLT1 and SGLT2 in human kidney and of SGLT1 in human small intestine, liver, lung, and heart. Pflügers Arch Eur J Physiol [Internet]. 2015 Sep [cited 2016 Mar 14];467(9):1881–98. Available from: http://www.ncbi.nlm.nih.gov/pubmed/25304002
210. Jang K-J, Mehr AP, Hamilton GA, McPartlin LA, Chung S, Suh K-Y, et al. Human kidney proximal tubule-on-a-chip for drug transport and nephrotoxicity assessment. Integr Biol [Internet]. 2013 Aug 19 [cited 2015 Oct 15];5(9):1119. Available from: http://pubs.rsc.org/en/content/articlehtml/2013/ib/c3ib40049b
211. Layton AT, Vallon V, Edwards A. Modeling oxygen consumption in the proximal tubule: effects of NHE and SGLT2 inhibition. Am J Physiol Renal Physiol [Internet]. 2015 Jun 15 [cited 2016 Mar 4];308(12):F1343-57. Available from: http://www.ncbi.nlm.nih.gov/pubmed/25855513
212. Essig M. Tubular Shear Stress and Phenotype of Renal Proximal Tubular Cells. J Am Soc Nephrol [Internet]. 2003 Jun 1 [cited 2016 Apr 14];14(90001):33S – 35. Available from: http://jasn.asnjournals.org/content/14/suppl_1/S33.full
213. Timsit M-OO, Adams WJ, Laguna-Fernandez A, Ichimura T, Bonventre J V., García-Cardeña G, et al. Flow is critical for maintaining a protective phenotype in renal proximal tubular cells [Internet]. American Journal of Transplantation Jun, 2013 p. 1617–8. Available from: http://www.ncbi.nlm.nih.gov/pubmed/23617882
214. Layton AT. Recent advances in renal hypoxia: insights from bench experiments and computer simulations. Am J Physiol Renal Physiol [Internet]. 2016 [cited 2019 Nov 16];311(1):F162-5. Available from: http://www.ncbi.nlm.nih.gov/pubmed/27147670
215. Lee C-J, Gardiner BS, Ngo JP, Kar S, Evans RG, Smith DW. Accounting for oxygen in the renal cortex: a computational study of factors that predispose the cortex to hypoxia. Am J Physiol Physiol [Internet]. 2017 Aug 1 [cited 2019 Nov 16];313(2):F218–36. Available from: https://www.physiology.org/doi/10.1152/ajprenal.00657.2016
216. Levy MN. Influence of variations in blood flow and of dinitrophenol on renal oxygen consumption. Am J Physiol Content [Internet]. 1959 Mar 31 [cited 2019 Nov 16];196(4):937–42. Available from: http://www.ncbi.nlm.nih.gov/pubmed/13637249
217. Kuo W;, Kurtcuoglu V. Renal arteriovenous oxygen shunting. Curr Opin Nephrol Hypertens [Internet]. 2017 [cited 2019 Nov 16];26(4):290–5. Available from: www.zora.uzh.chyear:2017URL:https://doi.org/10.5167/uzh
218. O'Connor PM, Anderson WP, Kett MM, Evans RG. RENAL PREGLOMERULAR ARTERIAL-VENOUS O2 SHUNTING IS A STRUCTURAL ANTI-OXIDANT DEFENCE MECHANISM OF THE RENAL CORTEX. Clin Exp Pharmacol Physiol [Internet]. 2006 Jul [cited 2019 Nov 16];33(7):637–41. Available from: http://www.ncbi.nlm.nih.gov/pubmed/16789933

219. Lindell SL, Muir H, Brassil J, Mangino MJ. Hypothermic Machine Perfusion Preservation of the DCD Kidney: Machine Effects. J Transplant. 2013;2013.
220. Weegman BP, Kirchner VA, Scott WE, Avgoustiniatos ES, Suszynski TM, Ferrer-Fabrega J, et al. Continuous real-time viability assessment of kidneys based on oxygen consumption. Transplant Proc [Internet]. 2010 [cited 2016 Sep 19];42(6):2020–3. Available from: http://www.ncbi.nlm.nih.gov/pubmed/20692397
221. Bunegin L, Tolstykh GP, Gelineau JF, Cosimi AB, Anderson LM. Oxygen Consumption During Oxygenated Hypothermic Perfusion as a Measure of Donor Organ Viability. ASAIO J [Internet]. 2013 [cited 2016 Sep 20];59(4):427–32. Available from: http://content.wkhealth.com/linkback/openurl?sid=WKPTLP:landingpage&an=00002480-201307000-00013
222. Ow CPC, Ngo JP, Ullah MM, Hilliard LM, Evans RG. Renal hypoxia in kidney disease: Cause or consequence? Acta Physiol [Internet]. 2018 Apr 1 [cited 2019 Nov 16];222(4):e12999. Available from: http://doi.wiley.com/10.1111/apha.12999
223. Wan C, Wang C, Liu T, Wang H, Yang Z. Experimental study on the cryopreservation of LLC-PK1 epithelial cells with hypoxic UW solution. J Huazhong Univ Sci Technolog Med Sci [Internet]. 2007 Aug [cited 2016 Aug 26];27(4):426–8. Available from: http://www.ncbi.nlm.nih.gov/pubmed/17828502
224. Summers DM, Johnson RJ, Allen J, Fuggle S V, Collett D, Watson CJ, et al. Analysis of factors that affect outcome after transplantation of kidneys donated after cardiac death in the UK: a cohort study. Lancet [Internet]. 2010 Oct 16 [cited 2019 Nov 18];376(9749):1303–11. Available from: https://www.sciencedirect.com/science/article/pii/S0140673610608276
225. Oniscu GC, Plant W, Pocock P, Forsythe JLR, Scotland-Northern Ireland Alliance in conjunction with UK Transplant, United Kingdom. Does a kidney-sharing alliance have to sacrifice cold ischemic time for better HLA matching? Transplantation [Internet]. 2002 May 27 [cited 2019 Nov 18];73(10):1647–52. Available from: http://www.ncbi.nlm.nih.gov/pubmed/12042654
226. Kute VB, Patel H V, Shah PR, Modi PR, Shah VR, Rizvi SJ, et al. International kidney paired donation transplantations to increase kidney transplant of O group and highly sensitized patient: First report from India. World J Transplant [Internet]. 2017 Feb 24 [cited 2019 Nov 18];7(1):64–9. Available from: http://www.ncbi.nlm.nih.gov/pubmed/28280697
227. Cabral PD, Hong NJ, Garvin JL. Shear stress increases nitric oxide production in thick ascending limbs. Am J Physiol Physiol [Internet]. 2010 Nov [cited 2019 Nov 16];299(5):F1185–92. Available from: http://www.ncbi.nlm.nih.gov/pubmed/20719980
228. Ernandez T, Udwan K, Chassot A, Martin P-Y, Feraille E. Uninephrectomy and apical fluid shear stress decrease ENaC abundance in collecting duct principal cells. Am J Physiol Physiol [Internet]. 2018 May 1 [cited 2019 Nov 16];314(5):F763–72. Available from: http://www.ncbi.nlm.nih.gov/pubmed/28877879
229. Cai Z, Xin J, Pollock DM, Pollock JS. Shear stress-mediated NO production in inner medullary collecting duct cells. Am J Physiol Physiol [Internet]. 2000 Aug 1 [cited 2019 Nov 16];279(2):F270–4. Available from: http://www.ncbi.nlm.nih.gov/pubmed/10919845
230. Verschuren EHJ, Hoenderop JGJ, Peters DJM, Arjona FJ, Bindels RJM. Tubular flow activates magnesium transport in the distal convoluted tubule. FASEB J [Internet]. 2019 Apr [cited 2019 Nov 16];33(4):5034–44. Available from: http://www.ncbi.nlm.nih.gov/pubmed/30596515
231. Schödel J, Bohr D, Klanke B, Schley G, Schlötzer-Schrehardt U, Warnecke C, et al. Factor inhibiting HIF limits the expression of hypoxia-inducible genes in podocytes and distal tubular cells. Kidney Int [Internet]. 2010 Nov 1 [cited 2020 Jan 26];78(9):857–67. Available from: https://www.sciencedirect.com/science/article/pii/S0085253815546668?via%3Dihub
232. Husted RF, Lu H, Sigmund RD, Stokes JB. Oxygen regulation of the epithelial Na channel in the collecting duct. Am J Physiol Physiol [Internet]. 2011 Feb [cited 2020 Jan 26];300(2):F412–24. Available from: https://www.physiology.org/doi/10.1152/ajprenal.00245.2010
233. Zhou DH, Shah G, Mullen C, Sandoz D, Rienstra CM. Proton-detected solid-state NMR spectroscopy of natural-abundance peptide and protein pharmaceuticals. Angew Chem Int Ed Engl [Internet]. 2009 [cited 2020 Jan 26];48(7):1253–6. Available from: http://www.ncbi.nlm.nih.gov/pubmed/19130513
234. Butler LG. An Introduction to Solution, Solid-State, and Imaging NMR Spectroscopy. In: Handbook of Spectroscopy: Second, Enlarged Edition. Wiley Blackwell; 2014. p. 193–224.

235. Nath J, Smith T, Hollis A, Ebbs S, Canbilen SW, Tennant DA, et al. 13C glucose labelling studies using 2D NMR are a useful tool for determining ex vivo whole organ metabolism during hypothermic machine perfusion of kidneys. Transplant Res [Internet]. 2016 Dec 5 [cited 2016 Nov 16];5(1):7. Available from: http://transplantationresearch.biomedcentral.com/articles/10.1186/s13737-016-0037-0
236. James TL. Chapter 1 Fundamentals of NMR.
237. Onwu OS. Physics and mathematics of magnetic resonance imaging for nanomedicine: An overview. World J Transl Med. 2014;3(1):17.
238. Reynolds WF. NMR Pulse Sequences. In: Encyclopedia of Spectroscopy and Spectrometry. Elsevier; 1999. p. 1554–67.
239. Mills E, O'Neill LAJ, Janeway CA, Medzhitov R, Pearce EL, Pearce EJ, et al. Succinate: a metabolic signal in inflammation. Trends Cell Biol [Internet]. 2014 May [cited 2016 Jun 27];24(5):313–20. Available from: http://www.ncbi.nlm.nih.gov/pubmed/24361092
240. Mckay RT. How the 1D-NOESY suppresses solvent signal in metabonomics NMR spectroscopy: An examination of the pulse sequence components and evolution. Concepts Magn Reson Part A [Internet]. 2011 Sep [cited 2020 Jan 27];38A(5):197–220. Available from: http://doi.wiley.com/10.1002/cmr.a.20223
241. Keeler J. Wiley-VCH - Keeler, James - Understanding NMR Spectroscopy [Internet]. 2nd editio. Wiley-VCH; 2010 [cited 2020 Jan 30]. Available from: http://www.wiley-vch.de/publish/en/books/bySubjectCH00/newTitles201004/0-470-74608-4/?sID=os3g8aepd1n93d8ifednj3b3s7
242. Perrin CL. Polynomial coefficients. Application to spin-spin splitting by *N* equivalent nuclei of spin *I* > 1/2. Magn Reson Chem [Internet]. 2018 Sep 1 [cited 2020 Jan 31];56(9):798–798. Available from: http://doi.wiley.com/10.1002/mrc.4785
243. Farmer S, Kennepohl D. 3.2: The Nature of NMR Absorptions [Internet]. 2020 [cited 2020 Jan 30]. Available from: https://chem.libretexts.org/link?31534
244. Freeman R. A handbook of nuclear magnetic resonance. Longman; 1997. 344 p.
245. Mandal PK, Majumdar A. A comprehensive discussion of HSQC and HMQC pulse sequences. Concepts Magn Reson [Internet]. 2004 Jan 1 [cited 2020 Jan 31];20A(1):1–23. Available from: http://doi.wiley.com/10.1002/cmr.a.10095
246. Rahman A-, Choudhary MI, Wahab A. Solving problems with NMR spectroscopy. Elsevier Academic Press; 2016. 522 p.
247. Szakács Z, Sánta Z. NMR Methodological Overview. Anthr Aware [Internet]. 2015 Jan 1 [cited 2020 Jan 31];257–89. Available from: https://www.sciencedirect.com/science/article/pii/B9780124199637000079
248. Vinaixa M, Rodríguez MA, Aivio S, Capellades J, Gómez J, Canyellas N, et al. Positional Enrichment by Proton Analysis (PEPA): A One-Dimensional ^{1}H-NMR Approach for ^{13}C Stable Isotope Tracer Studies in Metabolomics. Angew Chemie Int Ed [Internet]. 2017 Mar 20 [cited 2020 Aug 16];56(13):3531–5. Available from: http://doi.wiley.com/10.1002/anie.201611347
249. Smith TB, Patel K, Munford H, Peet A, Tennant DA, Jeeves M, et al. High-Speed Tracer Analysis of Metabolism (HS-TrAM). Wellcome Open Res [Internet]. 2018 Jan 12 [cited 2018 Apr 3];3:5. Available from: https://wellcomeopenresearch.org/articles/3-5/v1
250. Lane AN, Fan TW-M, Bousamra M, Higashi RM, Yan J, Miller DM. Stable Isotope-Resolved Metabolomics (SIRM) in Cancer Research with Clinical Application to NonSmall Cell Lung Cancer. Omi A J Integr Biol [Internet]. 2011 Mar 6 [cited 2020 Aug 16];15(3):173–82. Available from: http://www.liebertpub.com/doi/10.1089/omi.2010.0088
251. Stem cell technologies. Hypoxia Incubator Chamber Handling / Directions For Use. 2017 [cited 2016 Oct 6];27310–1. Available from: https://cdn.stemcell.com/media/files/pis/29829-PIS_2_2_1.pdf?_ga=2.5490677.71075206.1498145027-1639741903.1494225990
252. Phillips BL, Kassimatis T, Atalar K, Wilkinson H, Kessaris N, Simmonds N, et al. Chronic histological changes in deceased donor kidneys at implantation do not predict graft survival: a single-centre retrospective analysis. Transpl Int [Internet]. 2019 May 8 [cited 2019 Nov 20];32(5):523–34. Available from: https://onlinelibrary.wiley.com/doi/abs/10.1111/tri.13398
253. Ayorinde JO, Summers DM, Pankhurst L, Laing E, Deary AJ, Hemming K, et al. PreImplantation Trial of Histopathology In renal Allografts (PITHIA): a stepped-wedge cluster randomised controlled trial protocol. BMJ Open [Internet]. 2019 Jan 17 [cited 2019 Nov 20];9(1):e026166. Available from: http://www.ncbi.nlm.nih.gov/pubmed/30659043

254. Ludwig C, Günther U. MetaboLab - advanced NMR data processing and analysis for metabolomics [Internet]. Vol. 12, BMC Bioinformatics. 2011. Available from: http://beregond.bham.ac.uk/~ludwigc/metabolab/
255. Willker W, Flögel U, Leibfritz D. Ultra-high-resolved HSQC spectra of multiple- 13C-labeled biofluids. J Magn Reson [Internet]. 1997 Mar [cited 2020 Aug 16];125(1):216–9. Available from: http://www.ncbi.nlm.nih.gov/pubmed/9245385
256. Delaglio F, Grzesiek S, Vuister G, Zhu G, Pfeifer J, Bax A. NMRPipe: A multidimensional spectral processing system based on UNIX pipes. J Biomol NMR [Internet]. 1995 Nov [cited 2020 Jan 25];6(3). Available from: http://link.springer.com/10.1007/BF00197809
257. Kazimierczuk K, Orekhov VY. Accelerated NMR Spectroscopy by Using Compressed Sensing. Angew Chemie Int Ed [Internet]. 2011 Jun 6 [cited 2020 Jan 25];50(24):5556–9. Available from: http://doi.wiley.com/10.1002/anie.201100370
258. Orekhov VY, Jaravine VA. Analysis of non-uniformly sampled spectra with multi-dimensional decomposition. Prog Nucl Magn Reson Spectrosc [Internet]. 2011 Oct [cited 2020 Jan 25];59(3):271–92. Available from: https://linkinghub.elsevier.com/retrieve/pii/S0079656511000161
259. Hiller K, Hangebrauk J, Jäger C, Spura J, Schreiber K, Schomburg D. MetaboliteDetector: Comprehensive Analysis Tool for Targeted and Nontargeted GC/MS Based Metabolome Analysis. Anal Chem [Internet]. 2009 May 1 [cited 2019 Nov 20];81(9):3429–39. Available from: http://www.ncbi.nlm.nih.gov/pubmed/19358599
260. Yang N-C, Ho W-M, Chen Y-H, Hu M-L. A Convenient One-Step Extraction of Cellular ATP Using Boiling Water for the Luciferin–Luciferase Assay of ATP. Anal Biochem [Internet]. 2002 Jul 15 [cited 2019 Nov 20];306(2):323–7. Available from: http://www.ncbi.nlm.nih.gov/pubmed/12123672
261. Herrmann H, Lebeau P. ATP LEVEL, CELL INJURY, AND APPARENT EPITHELIUM-STROMA INTERACTION IN THE CORNEA. Br Notes [Internet]. 1962 [cited 2019 Nov 20];465–7. Available from: http://jcb.rupress.org/content/jcb/13/3/465.full.pdf
262. Zhou L, Xue X, Zhou J, Li Y, Zhao J, Wu L. Fast Determination of Adenosine 5′-Triphosphate (ATP) and Its Catabolites in Royal Jelly Using Ultraperformance Liquid Chromatography. J Agric Food Chem [Internet]. 2012 Sep 12 [cited 2019 Nov 20];60(36):8994–9. Available from: https://pubs.acs.org/doi/10.1021/jf3022805
263. Curtis MJ, Bond RA, Spina D, Ahluwalia A, Alexander SPA, Giembycz MA, et al. Experimental design and analysis and their reporting: new guidance for publication in BJP. Br J Pharmacol [Internet]. 2015 Jul [cited 2019 Nov 20];172(14):3461–71. Available from: http://www.ncbi.nlm.nih.gov/pubmed/26114403
264. Ghasemi A, Zahediasl S. Normality tests for statistical analysis: a guide for non-statisticians. Int J Endocrinol Metab [Internet]. 2012 [cited 2019 Nov 20];10(2):486–9. Available from: http://www.ncbi.nlm.nih.gov/pubmed/23843808
265. Lew M. Good statistical practice in pharmacology. Problem 2. Br J Pharmacol [Internet]. 2007 Oct [cited 2019 Nov 20];152(3):299–303. Available from: http://www.ncbi.nlm.nih.gov/pubmed/17618310
266. Marco Durante., Francis A. Cucinotta., Jay S. Loeffler. Charged Particles in Oncology [Internet]. Frontiers Media S.A; [cited 2020 Feb 12]. Available from: https://books.google.co.uk/books?id=YMxJDwAAQBAJ&pg=PA51&lpg=PA51&dq=wilcoxon+matched+pairs+signed+rank+test+normalised+to+100%25&source=bl&ots=GRGXUsVLmU&sig=ACfU3U3bcWuoWad5lGH3vOYFxtC-agR5nw&hl=en&sa=X&ved=2ahUKEwixlt-pgKDnAhUHZcAKHQzpDS0Q6AEwDHoECAsQAQ#v=onepage&q=wilcoxon matched pairs signed rank test normalised to 100%25&f=false
267. Steele AK, Lee EJ, Manuzak JA, Dillon SM, Beckham J, McCarter MD, et al. Microbial exposure alters HIV-1-induced mucosal CD4+ T cell death pathways Ex vivo. Retrovirology [Internet]. 2014 Feb 4 [cited 2020 Feb 12];11(1):14. Available from: http://retrovirology.biomedcentral.com/articles/10.1186/1742-4690-11-14
268. Watanabe A, St. Clair W, Kelsoe G. Self-tolerance curtails the B cell repertoire to microbial epitopes. JCL insight [Internet]. 2019 [cited 2020 Feb 12];4(10). Available from: https://df6sxcketz7bb.cloudfront.net/manuscripts/122000/122551/cache/122551.2-20190716111500-covered-253bed37ca4c1ab43d105aefdf7b5536.pdf
269. Pucino V, Bombardieri M, Pitzalis C, Mauro C. Lactate at the crossroads of metabolism,

inflammation, and autoimmunity. Eur J Immunol [Internet]. 2017 Jan [cited 2017 Nov 7];47(1):14–21. Available from: http://www.ncbi.nlm.nih.gov/pubmed/27883186
270. Wiegand A, Ritter A, Graf N, Arampatzis S, Sidler D, Hadaya K, et al. Preservation of kidney function in kidney transplant recipients by alkali therapy (Preserve-Transplant Study): rationale and study protocol. BMC Nephrol [Internet]. 2018 [cited 2019 Nov 22];19(1):177. Available from: http://www.ncbi.nlm.nih.gov/pubmed/30001705
271. Bellomo R. Bench-to-bedside review: Lactate and the kidney. Crit Care [Internet]. 2002 [cited 2019 Nov 22];6(4):322. Available from: http://ccforum.biomedcentral.com/articles/10.1186/cc1518
272. Wijermars LGM, Schaapherder AF, de Vries DK, Verschuren L, Wüst RCI, Kostidis S, et al. Defective postreperfusion metabolic recovery directly associates with incident delayed graft function. Kidney Int [Internet]. 2016 Jul 1 [cited 2019 Nov 23];90(1):181–91. Available from: https://www.sciencedirect.com/science/article/pii/S0085253816300497?via%3Dihub
273. Patel K, Nath J, Hodson J, Inston N, Ready A. Outcomes of donation after circulatory death kidneys undergoing hypothermic machine perfusion following static cold storage: A UK population-based cohort study. Am J Transplant [Internet]. 2018 Jun [cited 2019 Nov 16];18(6):1408–14. Available from: http://doi.wiley.com/10.1111/ajt.14587
274. Patel K, Smith TB, Neil DAH, Thakker A, Tsuchiya Y, Higgs EB, et al. The Effects of Oxygenation on Ex Vivo Kidneys Undergoing Hypothermic Machine Perfusion. Transplantation [Internet]. 2019 Feb [cited 2019 Mar 3];103(2):314–22. Available from: http://www.ncbi.nlm.nih.gov/pubmed/30461718
275. Bon D, Claire B, Thuillier R, Hebrard W, Boildieu N, Celhay O, et al. Analysis of Perfusates During Hypothermic Machine Perfusion by NMR Spectroscopy. Transplantation [Internet]. 2014 Apr [cited 2020 Feb 9];97(8):810–6. Available from: http://content.wkhealth.com/linkback/openurl?sid=WKPTLP:landingpage&an=00007890-201404270-00006
276. Nath J, Smith TB, Patel K, Ebbs SR, Hollis A, Tennant DA, et al. Metabolic differences between cold stored and machine perfused porcine kidneys: A 1H NMR based study. Cryobiology [Internet]. 2017 Feb [cited 2017 Mar 28];74:115–20. Available from: http://linkinghub.elsevier.com/retrieve/pii/S0011224016304394
277. Juarez-Moreno K, Ayala M, Vazquez-Duhalt R. Antioxidant Capacity of Poly(Ethylene Glycol) (PEG) as Protection Mechanism Against Hydrogen Peroxide Inactivation of Peroxidases. Appl Biochem Biotechnol [Internet]. 2015 Nov 26 [cited 2019 Dec 6];177(6):1364–73. Available from: http://www.ncbi.nlm.nih.gov/pubmed/26306530
278. Neuhaus W, Schick MA, Bruno RR, Schneiker B, Förster CY, Roewer N, et al. The effects of colloid solutions on renal proximal tubular cells in vitro. Anesth Analg [Internet]. 2012 Feb [cited 2016 Aug 4];114(2):371–4. Available from: http://www.ncbi.nlm.nih.gov/pubmed/22025492
279. Schick MA, Baar W, Bruno RR, Wollborn J, Held C, Schneider R, et al. Balanced Hydroxyethylstarch (HES 130/0.4) Impairs Kidney Function In-Vivo without Inflammation. Latus J, editor. PLoS One [Internet]. 2015 Sep 4 [cited 2016 Aug 4];10(9):e0137247. Available from: http://dx.plos.org/10.1371/journal.pone.0137247
280. Daly PJA, Power RE, Healy DA, Hickey DP, Fitzpatrick JM, Watson RWG. Delayed graft function: a dilemma in renal transplantation. BJU Int [Internet]. 2005 Sep 1 [cited 2020 Feb 11];96(4):498–501. Available from: http://doi.wiley.com/10.1111/j.1464-410X.2005.05673.x
281. Vodenicharov A, Simoens P. Morphologic Peculiarities of the Renal Cortical Vasculature Connected with Blood Redistribution in the Kidney of the Domestic Pig. Anat Histol Embryol J Vet Med Ser C [Internet]. 1998 Aug [cited 2019 Nov 29];27(4):257–62. Available from: http://doi.wiley.com/10.1111/j.1439-0264.1998.tb00190.x
282. Wan C, Wang C, Liu T, Wang H, Yang Z. Experimental study on the cryopreservation of LLC-PK1 epithelial cells with hypoxic UW solution. J Huazhong Univ Sci Technol [Internet]. 2007 Aug [cited 2019 Nov 22];27(4):426–8. Available from: http://www.ncbi.nlm.nih.gov/pubmed/17828502
283. Ardakani AG, Cheema U, Brown RA, Shipley RJ. Quantifying the correlation between spatially defined oxygen gradients and cell fate in an engineered three-dimensional culture model. J R Soc Interface [Internet]. 2014 Sep 6 [cited 2019 Nov 22];11(98):20140501. Available from: https://royalsocietypublishing.org/doi/10.1098/rsif.2014.0501
284. Jovanovic P, Zoric L, Stefanovic I, Dzunic B, Djordjevic-Jocic J, Radenkovic M, et al. Lactate

dehydrogenase and oxidative stress activity in primary open-angle glaucoma aqueous humour. Bosn J basic Med Sci [Internet]. 2010 Feb [cited 2019 Dec 1];10(1):83–8. Available from: http://www.ncbi.nlm.nih.gov/pubmed/20192938
285. Visarius TM, Putt DA, Schare JM, Pegouske DM, Lash LH. Pathways of glutathione metabolism and transport in isolated proximal tubular cells from rat kidney. Biochem Pharmacol [Internet]. 1996 Jul 26 [cited 2020 Feb 14];52(2):259–72. Available from: https://www.sciencedirect.com/science/article/pii/0006295296002031?via%3Dihub
286. Cutrín JC, Zingaro B, Camandola S, Boveris A, Pompella A, Poli G. Contribution of γ glutamyl transpeptidase to oxidative damage of ischemic rat kidney. Kidney Int [Internet]. 2000 Oct 1 [cited 2020 Feb 14];57(2):526–33. Available from: https://www.sciencedirect.com/science/article/pii/S0085253815467687
287. Shang Y, Siow YL, Isaak CK, O K. Downregulation of Glutathione Biosynthesis Contributes to Oxidative Stress and Liver Dysfunction in Acute Kidney Injury. Oxid Med Cell Longev [Internet]. 2016 [cited 2020 Feb 23];2016:1–13. Available from: https://www.hindawi.com/journals/omcl/2016/9707292/
288. Kostidis S, Bank JR, Soonawala D, Nevedomskaya E, van Kooten C, Mayboroda OA, et al. Urinary metabolites predict prolonged duration of delayed graft function in DCD kidney transplant recipients. Am J Transplant [Internet]. 2019 [cited 2020 Feb 24];19(1):110–22. Available from: http://www.ncbi.nlm.nih.gov/pubmed/29786954
289. Malek M, Nematbakhsh M. Renal ischemia/reperfusion injury; from pathophysiology to treatment. J Ren Inj Prev [Internet]. 2015 Jan [cited 2016 Feb 17];4(2):20–7. Available from: http://www.ncbi.nlm.nih.gov/pubmed/26060833
290. Zhang G, Darshi M, Sharma K. The Warburg Effect in Diabetic Kidney Disease. Semin Nephrol [Internet]. 2018 [cited 2020 Feb 24];38(2):111. Available from: https://www.ncbi.nlm.nih.gov/pmc/articles/PMC5973839/
291. Ren Q, Gliozzi ML, Rittenhouse NL, Edmunds LR, Rbaibi Y, Locker JD, et al. Shear stress and oxygen availability drive differential changes in opossum kidney proximal tubule cell metabolism and endocytosis. Traffic [Internet]. 2019 Jun 9 [cited 2019 Nov 24];20(6):448–59. Available from: https://onlinelibrary.wiley.com/doi/abs/10.1111/tra.12648
292. Park JS, Burckhardt CJ, Lazcano R, Solis LM, Isogai T, Li L, et al. Mechanical regulation of glycolysis via cytoskeleton architecture. Nature [Internet]. 2020 Feb 12 [cited 2020 Feb 21];1–6. Available from: http://www.nature.com/articles/s41586-020-1998-1
293. Ning X-H, Chen S-H, Xu C-S, Hyyti OM, Qian K, Krueger JJ, et al. Hypothermia preserves myocardial function and mitochondrial protein gene expression during hypoxia. Am J Physiol Circ Physiol [Internet]. 2003 Jul [cited 2019 Nov 24];285(1):H212–9. Available from: https://www.physiology.org/doi/10.1152/ajpheart.01149.2002
294. Schulte PM. The effects of temperature on aerobic metabolism: Towards a mechanistic understanding of the responses of ectotherms to a changing environment. Vol. 218, Journal of Experimental Biology. Company of Biologists Ltd; 2015. p. 1856–66.
295. Boutilier RG. Mechanisms of cell survival in hypoxia and hypothermia. J Exp Biol [Internet]. 2001 Sep [cited 2019 Nov 24];204(Pt 18):3171–81. Available from: http://www.ncbi.nlm.nih.gov/pubmed/11581331
296. Cohen JJ, Kamm DE. Renal metabolism: relation to renal function. Vol. 1, The kidney. Philidephia:Saunders; 1981. 147 p.
297. Juriasingani S, Akbari M, Chan JY, Whiteman M, Sener A. H2S supplementation: A novel method for successful organ preservation at subnormothermic temperatures. Nitric Oxide [Internet]. 2018 Dec 1 [cited 2019 Nov 24];81:57–66. Available from: http://www.ncbi.nlm.nih.gov/pubmed/30393129
298. Maassen H, Hendriks KDW, Venema LH, Henning RH, Hofker SH, van Goor H, et al. Hydrogen sulphide-induced hypometabolism in human-sized porcine kidneys. Gallyas F, editor. PLoS One [Internet]. 2019 Nov 19 [cited 2019 Nov 29];14(11):e0225152. Available from: https://dx.plos.org/10.1371/journal.pone.0225152
299. Meldrum KKK, Meldrum DRR, Hile KLL, Burnett ALL, Harken AHH. A novel model of ischemia in renal tubular cells which closely parallels in vivo injury. J Surg Res [Internet]. 2001 Aug [cited 2016 Mar 21];99(2):288–93. Available from: http://www.ncbi.nlm.nih.gov/pubmed/11469899
300. Szabo C, Ransy C, Módis K, Andriamihaja M, Murghes B, Coletta C, et al. Regulation of mitochondrial bioenergetic function by hydrogen sulfide. Part I. Biochemical and physiological

mechanisms. Br J Pharmacol [Internet]. 2014 Apr [cited 2019 Nov 24];171(8):2099–122. Available from: http://www.ncbi.nlm.nih.gov/pubmed/23991830
301. Baicu SC, Taylor MJ, Brockbank KG. The role of preservation solution on acid-base regulation during machine perfusion of kidneys. Clin Transplant [Internet]. 2006 Jan 1 [cited 2020 Aug 16];20(1):113–21. Available from: http://doi.wiley.com/10.1111/j.1399-0012.2005.00451.x
302. Jiang J, Chan A, Ali S, Saha A, Haushalter KJ, Lam W-LM, et al. Hydrogen Sulfide--Mechanisms of Toxicity and Development of an Antidote. Sci Rep [Internet]. 2016 Feb 15 [cited 2020 Feb 24];6:20831. Available from: http://www.ncbi.nlm.nih.gov/pubmed/26877209
303. Mullarky E, Cantley LC. Diverting Glycolysis to Combat Oxidative Stress [Internet]. Innovative Medicine: Basic Research and Development. Springer; 2015 [cited 2020 Aug 16]. Available from: http://www.ncbi.nlm.nih.gov/pubmed/29787184
304. Nalos M, Parnell G, Robergs R, Booth D, McLean AS, Tang BM. Transcriptional reprogramming of metabolic pathways in critically ill patients. Intensive Care Med Exp [Internet]. 2016 Dec 7 [cited 2020 Aug 16];4(1):21. Available from: http://icm-experimental.springeropen.com/articles/10.1186/s40635-016-0094-1
305. Ploeg R, Paul A, Kocabayoglu P. “In house” Pre-implantation Oxygenated Hypothermic Machine Perfusion Reconditioning after Cold Storage versus Cold Storage alone in ECD Kidneys from Brain Dead Donors Acronym: COPE-POMP trial. COPE WP3 (POMP Trial) Protoc. 2014;
306. Darius T, Gianello P, Buemi A, de Meyer M, Mourad M. High Oxygen Pressure during Continuous Hypothermic Machine Perfusion is Associated with a Better Ex Vivo Renal Blood Flow and Early Graft Function in a Porcine DCD Auto-Transplant Model. Transplantation [Internet]. 2018 Jul [cited 2020 Feb 24];102:S701. Available from: http://insights.ovid.com/crossref?an=00007890-201807001-01130
307. Lutz J, Thurmel K, Heemann U. Anti-inflammatory treatment strategies for ischemia/reperfusion injury in transplantation. J Inflamm [Internet]. 2010 May 28 [cited 2019 Nov 23];7(1):27. Available from: http://journal-inflammation.biomedcentral.com/articles/10.1186/1476-9255-7-27
308. Kim J-S, He L, Qian T, Lemasters JJ. Role of the Mitochondrial Permeability Transition in Apoptotic and Necrotic Death After Ischemia / Reperfusion Injury to Hepatocytes. Curr Mol Med [Internet]. 2003 Sep 1 [cited 2019 Nov 23];3(6):527–35. Available from: http://www.ncbi.nlm.nih.gov/pubmed/14527084
309. Szeto HH, Liu S, Soong Y, Birk A V. Improving mitochondrial bioenergetics under ischemic conditions increases warm ischemia tolerance in the kidney. Am J Physiol Physiol [Internet]. 2015 Jan 1 [cited 2019 Nov 23];308(1):F11–21. Available from: http://www.ncbi.nlm.nih.gov/pubmed/25339695
310. Bak LK, Waagepetersen HS, Melø TM, Schousboe A, Sonnewald U. Complex Glutamate Labeling from [U-13C]glucose or [U-13C]lactate in Co-cultures of Cerebellar Neurons and Astrocytes. Neurochem Res [Internet]. 2007 Mar 22 [cited 2019 Nov 23];32(4–5):671–80. Available from: http://link.springer.com/10.1007/s11064-006-9161-4
311. Izquierdo-Garcia JL, Cai LM, Chaumeil MM, Eriksson P, Robinson AE, Pieper RO, et al. Glioma Cells with the IDH1 Mutation Modulate Metabolic Fractional Flux through Pyruvate Carboxylase. Scemes E, editor. PLoS One [Internet]. 2014 Sep 22 [cited 2020 Jan 25];9(9):e108289. Available from: http://dx.plos.org/10.1371/journal.pone.0108289
312. Metallo CM, Walther JL, Stephanopoulos G. Evaluation of 13C isotopic tracers for metabolic flux analysis in mammalian cells. J Biotechnol [Internet]. 2009 Nov [cited 2016 May 20];144(3):167–74. Available from: http://www.pubmedcentral.nih.gov/articlerender.fcgi?artid=3026314&tool=pmcentrez&rendertype=abstract
313. Venema LH, Brat A, Moers C, ‘t Hart NA, Ploeg RJ, Hannaert P, et al. Effects of Oxygen During Long-term Hypothermic Machine Perfusion in a Porcine Model of Kidney Donation After Circulatory Death. Transplantation [Internet]. 2019 Oct [cited 2019 Nov 23];103(10):2057–64. Available from: http://insights.ovid.com/crossref?an=00007890-201910000-00018
314. Shi S, Xue F. Current Antioxidant Treatments in Organ Transplantation. Oxid Med Cell Longev [Internet]. 2016 [cited 2019 Nov 24];2016:8678510. Available from: http://www.ncbi.nlm.nih.gov/pubmed/27403232
315. Alcaraz-García MJ, Albaladejo MD, Acevedo C, Olea A, Zamora S, Martínez P, et al. Effects of

hyperoxia on biomarkers of oxidative stress in closed-circuit oxygen military divers. J Physiol Biochem [Internet]. 2008 Jun [cited 2019 Nov 24];64(2):135–41. Available from: http://www.ncbi.nlm.nih.gov/pubmed/19043983
316. Darius T, Vergauwen M, Smith T, Gerin I, Joris V, Mueller M, et al. Brief O2 uploading during continuous hypothermic machine perfusion is simple yet effective oxygenation method to improve initial kidney function in a porcine autotransplant model. Am J Transplant [Internet]. 2020 Feb 3 [cited 2020 Feb 7];ajt.15800. Available from: https://onlinelibrary.wiley.com/doi/abs/10.1111/ajt.15800
317. Grefe C, Ayisi K, Krebber J-J. Emission of Micro-Bubbles in Bubble (BO) and Membrane-Oxygenators (MO): A Comparative Investigation. In: Impact of Cardiac Surgery on the Quality of Life [Internet]. Boston, MA: Springer US; 1990 [cited 2019 Dec 1]. p. 273–8. Available from: http://link.springer.com/10.1007/978-1-4613-0647-4_33
318. Izamis M-L, Efstathiades A, Keravnou C, Georgiadou S, Martins PN, Averkiou MA. Effects of air embolism size and location on porcine hepatic microcirculation in machine perfusion. Liver Transplant [Internet]. 2014 May 1 [cited 2019 Dec 1];20(5):601–11. Available from: http://doi.wiley.com/10.1002/lt.23838
319. Southard JH. Coffee creamer, the bionic man, and organ preservation. Surgery [Internet]. 2002 Feb 1 [cited 2019 Nov 19];131(2):228–9. Available from: http://www.ncbi.nlm.nih.gov/pubmed/11854706
320. British Transplantation society. Transplantation From Donors AfterDeceased Circulatory Death British Transplantation Society Guidelines [Internet]. 2015 [cited 2020 Feb 26]. Available from: www.bts.org.uk
321. Ding C-G, Tian P-X, Ding X-M, Xiang H-L, Li Y, Tian X-H, et al. Beneficial Effect of Moderately Increasing Hypothermic Machine Perfusion Pressure on Donor after Cardiac Death Renal Transplantation. Chin Med J (Engl) [Internet]. 2018 Nov 20 [cited 2019 Nov 23];131(22):2676–82. Available from: http://www.ncbi.nlm.nih.gov/pubmed/30425194
322. Fine LG, Bandyopadhay D, Norman JT. Is there a common mechanism for the progression of different types of renal diseases other than proteinuria? Towards the unifying theme of chronic hypoxia. Kidney Int [Internet]. 2000 Apr 1 [cited 2020 Feb 27];57:S22–6. Available from: https://www.sciencedirect.com/science/article/pii/S0085253815470590